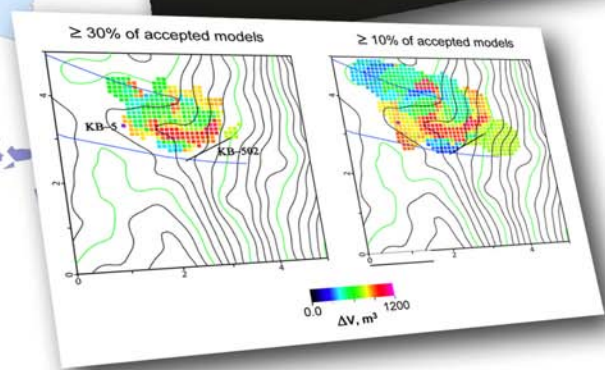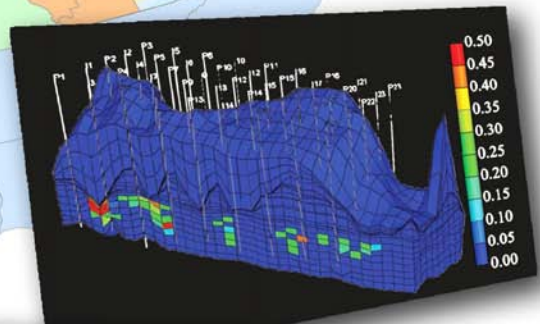the **ENERGY** lab

Regional Carbon Sequestration Partnerships' Simulation and Risk Assessment Case Histories

Addendum to Best Practices for Risk Analyses and Simulation for Geologic Storage of CO$_2$

NETL

≥ 30% of accepted models   ≥ 10% of accepted models

0.0   Δ*V*, m³   1200

Version 1.0

NATIONAL ENERGY TECHNOLOGY LABORATORY

U.S. DEPARTMENT OF **ENERGY**

Disclaimer

Regional Carbon Sequestration Partnerships' Simulation and Risk Assessment Case Histories

Addendum to Best Practices for
Risk Analysis and Simulation for Geologic Storage of CO$_2$

DOE/NETL-2011/1459

March 2011

National Energy Technology Laboratory
www.netl.doe.gov

Table of Contents

List of Tables

List of Figures

List of Figures (cont.)

List of Figures (cont.)

Big Sky Carbon Sequestration Partnership

Pre-Injection Characterization and Modeling for the Big Sky Carbon Sequestration Partnership Basalt Sequestration Pilot Test

B. P. McGrail, D. H. Bacon, M. D. White, F. A. Spane, E. C. Sullivan
Battelle Pacific Northwest Division, Richland, Washington

The Big Sky Carbon Sequestration Partnership is undertaking a field pilot to demonstrate CO_2 storage in deep basalt formations. The field test is designed to assess the mineralogical, geochemical, and hydrologic impact of injected CO_2 within a mafic basalt formation, and will incorporate site monitoring and verification activities. Periodic groundwater and gas sampling and core sample extraction approximately 1.5 years after injection are planned to verify laboratory and computer simulation studies that show rapid onset of carbonate mineralization.

The basalt pilot well was drilled to a depth of 1,250 m during 2009 on the Boise Whitepaper mill site near Wallula, in southeastern Washington. Based on hydrogeologic characterization results obtained during drilling, three prospective Grande Ronde flow top breccia zones (Slack Canyon flow #1 and #2 and uppermost Ortley flow) were identified between the depth interval of 827.8 and 887 m below ground surface (bgs) as being a suitable injection reservoir. The targeted injection reservoir lies stratigraphically below the 24 m thick flow interior of the Slack Canyon #3, which forms the primary seal, and below the massive Umtanum Member of the Grande Ronde Basalt, whose flow-interior section possesses regionally recognized low-permeability characteristics, making it a secondary seal. Reservoir modeling of a 1,000 metric ton injection shows that most of the CO_2 will flow into the more permeable Slack Canyon Flow #2. Radius of the CO_2 bubble is projected to extend approximately 200 ft from the injection well.

An injection permit for the pilot test was issued in October 2010 by the Washington State Department of Ecology. Injection of CO_2 is anticipated in early 2011.

Introduction

Continental flood basalts represent some of the largest geologic structures on the planet but have received comparatively little attention for geologic storage of CO_2. Eastern Washington State and a large portion of the entire Pacific Northwest east of the Cascade Mountain Range belong to the Columbia Plateau Province, which hosts world-class continental flood basalt deposits. The Miocene Columbia River Basalt Group (CRBG) covers over 168,000 km^2 of portions of eastern Washington, northeastern Oregon and western Idaho (Figure 1), with a total estimated volume of more than 220,000 km^3 (REIDEL et al., 2002). Collectively, over 300 individual CRBG flows have been mapped within the region, with a composite thickness of greater than 5 km within the central portion of the Columbia Basin. The brecciated flow tops and bases of the CRBG form regional aquifers, and are targets for storage of anthropogenic CO_2 in areas where the basalts contain unpotable water and are at depths greater than 800 m. Conservative estimates of CO_2 storage capacity in the CRBG are approximately 10 to 50 $GtCO_2$ (MCGRAIL et al., 2006).

Because flood basalt formations exist in regions of the United States (and other countries such as India) where sedimentary basin storage capacity is limited, demonstration of commercial-scale storage in deep flood basalts is important in meeting global CO_2 emissions targets. That fact is now being increasingly recognized. Since the original concepts for storage in basalts were proposed (McGrail et al., 2003; McGrail et al., 2006), interest has grown rapidly with laboratory (White et al., 2006; Matter et al., 2007; Flaathen et al., 2008; Goldberg et al., 2008; Gysi and Stefansson, 2008; Prasad et al., 2009; Schaef and McGrail,
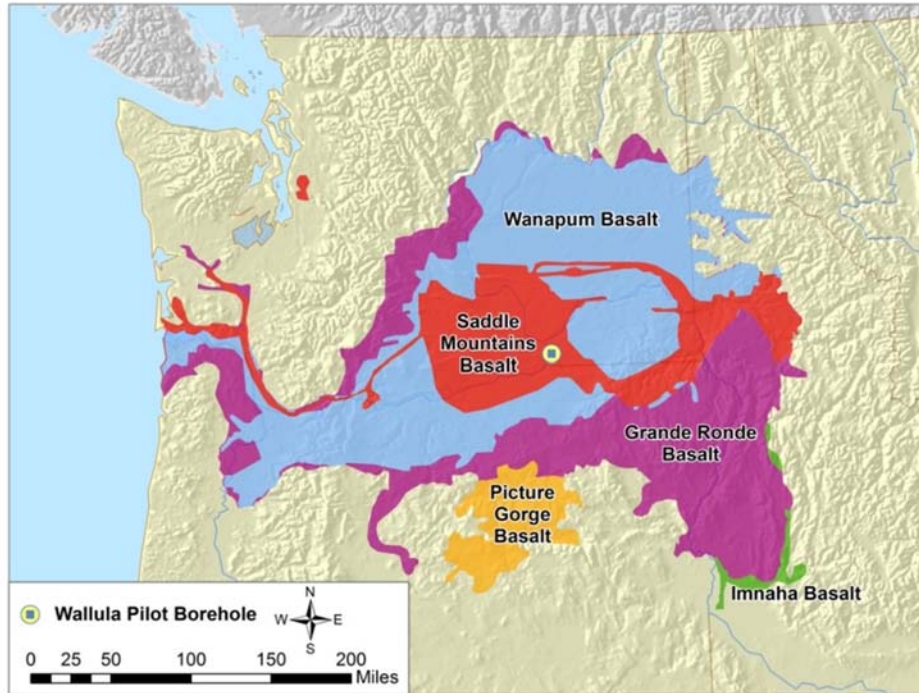
Figure 1: Surface Areal Extent of Basalt Formations of the Columbia River Basalt Group (modified from Reidel et al. 2002) (location of the pilot well is shown as green dot).

2009) and other field trials (Alfredsson et al., 2008; Khalilabad et al., 2008) now underway around the world. Nevertheless, the field pilot study undertaken by the BSCSP remains unique in the world for confirming the feasibility of permanently and safely storing large quantities of supercritical CO_2 within deep flood basalt formations.

The Columbia River flood basalts are grouped into four basalt formations, from oldest to youngest: Imnaha, Grande Ronde, Wanapum, and Saddle Mountains. The Grande Ronde flows are the most voluminous, comprising some 148,600 cubic kilometers and extending from eastern Idaho to the Pacific Ocean (Reidel et al., 1989) (Figure 1). Younger flows cover more limited areas, with flows of the Saddle Mountains Formation filling paleo-canyons cut into older flows (Hooper, 1982). Interbed layers between the Grande Ronde flows are thinner and less common than in the younger formations, which contain both sedimentary siliciclastics and silica-rich volcaniclastic materials. Groundwater within the Grande Ronde Basalt and

below in this region of the Columbia Basin has high pH and contains high concentrations of fluoride that exceed maximum concentration limits (MCL) as specified in National Primary Drinking Water Regulations (40 CFR 141.62). Exceedance of MCLs listed in 40 CFR 141.62[1] is the standard adopted in Washington State for permitting geologic storage projects under WAC 173-218-115.

Typical CRBG basalts are pahoehoe flows that display a massive base with columns at right angles to the cooling surfaces. An upper colonnade portion may be present with columns that are smaller and less well developed than in lower colonnades (Figure 2). Both upper and lower colonnade may contain zones of platy fracturing. Upper crustal portions of individual flows are fractured, glassy, highly vesiculated, and may be brecciated or ropey. The entablature is a zone of irregular horizontal fractures between the upper and lower colonnade or under the upper surface crust. Basal portions of individual CRBG flows may locally contain features such as pillow palagonite complexes that reflect

---

[1] 40 CFR 141.62. 2009. "National Primary Drinking Water Regulations, Maximum Contaminant Levels for Inorganic Contaminants." Code of Federal Regulations, U.S. Environmental Protection Agency.
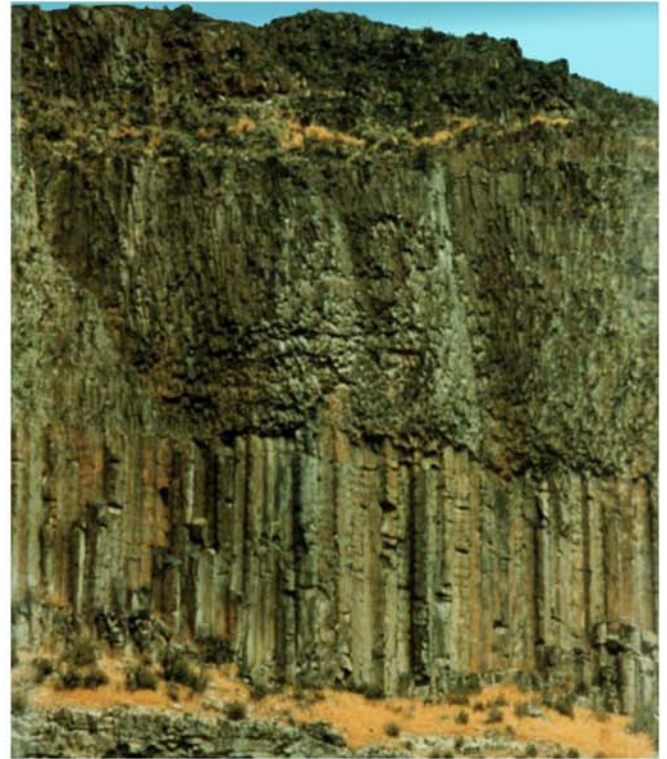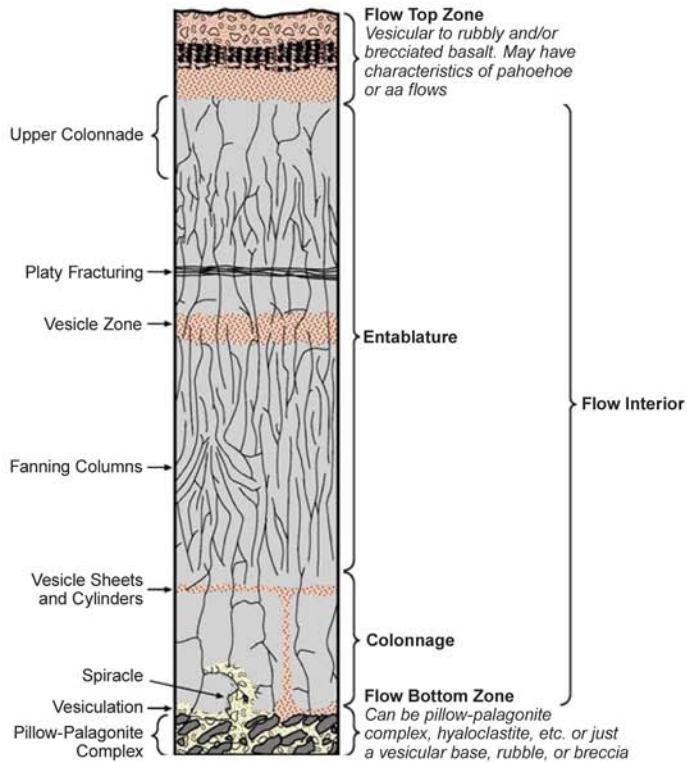
Figure 2: Features of an Idealized Single Flow (left) and an Outcrop Photo of a Saddle Mountain Basalt Flow near the Wallula Well Site with Colonnade and Thick Entablature

extrusion of lava into water or onto saturated substrates. Lower Tertiary sedimentary rocks also are widespread beneath the basalt cover and these formations are presently the target of natural gas exploration activities in western and northern parts of the Columbia Basin (Montgomery, 2008). The presence of natural gas plays (as well as distinct hydrologic and isotopic signatures across basalt flows) in the Columbia Basin confirms the regional sealing properties of the CRBG.

Site Characterization

In 2007, the BSCSP initiated a multi-year field test of capacity, integrity, and geochemical reactivity of Columbia River Basalt reservoirs. Details of the site characterization program are provided in a Topical Report (McGrail et al., 2009). Only a brief summary will be provided here.

A basalt pilot well was drilled to a depth of 1,250 m during 2009 on the Boise Whitepaper mill site near Wallula, in southeastern Washington and was logged with cased-hole tools to 335 m and with open-hole tools below 335 m. Basalt cutting samples taken at key points in drilling and sent to Eastern Washington University in Washington State for X-ray fluorescence (XRF) analyses provided whole rock geochemistry and stratigraphic control for the well. Interpretation of the wellbore data indicates that no faults were cut within the well, and that the stratigraphic level at total depth (1250 m) is within the Wapshilla Ridge 1 basalt flow (Table 1).

Based on well logs and extensive hydrogeologic testing results obtained during drilling, three prospective flow top breccia zones were identified within the Grande Ronde Basalt formation between 827.8 and 887 m below ground surface. Flow top zones within

Table 1: Stratigraphy of the Wallula Basalt Pilot (depths are in feet)

Geologic Unit	Depth to Top of Unit, (ft below ground surface)
Surficial Sediment	0
Saddle Mountain Basalt Formation	44
Ice Harbor Member	44
Levy Sedimentary Interbed	140
Elephant Mountain Member	206
Rattlesnake Ridge Interbed	307
Pomona Member	365
Selah Interbed	515
Umatilla Member	527
Wanapum Basalt Formation	1058
Priest Rapids Member	1058
Frenchman Springs Member (FSM)	1135
FSM Flow 1	1135
FSM Flow 2	1256
FSM Flow 3	1328
FSM Flow 4	1449
Vantage Interbed	1588
Grande Ronde Basalt Formation	1594
Sentinel Bluffs Member (SBM)	1594
SBM Flow 1	1594
SBM Flow 2	1755
SBM Flow 3	1838
SBM Flow 4	1932
SBM Flow 5	2010

Geologic Unit	Depth to Top of Unit, (ft below ground surface)
SBM Flow 6	2085
SBM Flow 7	2139
SBM Flow 8	2250
Winterwater Member	2320
Umtanum Member	2418
Slack Canyon Member (SC)	2590
SC Flow 1	2590
SC Flow 2	2730
SC Flow 3	2808
Ortley Member (OM)	2850
OM Flow 1	2850
OM Flow 2	2940
OM Flow 3	3219
OM Flow 4	3385
Grouse Creek Member (GCM) (tentative ID)	3463
GCM Flow 1	3463
GCM Flow 2	3607
Wapshilla Ridge Member (WRM) (tentative ID)	3810
WRM Flow 1	3810
WRM Flow 2	4068
Borehole – Total Depth	4110.5

the 59.1 m open-well completion zone contain Slack Canyon flow #2, Slack Canyon flow #1, and the Ortley flow top. Because of the relatively thin intervening basalt flow interior sections between the Slack Canyon flow tops #1 and #2, and between the lower Slack Canyon and underlying Ortley basalts, this composite open zone completion is considered to be a single, hydraulically communicative, hydrogeologic unit. The targeted injection reservoir lies stratigraphically below a primary Slack Canyon seal and below the massive Umtanum Member of the Grande Ronde Basalt, whose flow-interior section possesses regionally recognized low-permeability characteristics. Hydrologic testing of these isolated flow interior sections revealed extremely low permeability (<1 microDarcy). As part of the well-completion design required under State regulation, the lower borehole section of the pilot borehole was cemented back to 887 m. Final well completion is illustrated in Figure 3.

Injection Simulation Analysis

Simulations of a pilot-scale CO_2 injection into the flow tops of individual basalt flows in the Grande Ronde Basalt at Wallula, Washington, were performed using the STOMP-H_2O-CO_2-NaCl model simulator (White and Oostrom, 2006). The model for the CO_2 injection simulations included three injection horizons: the Ortley flow top (OFT), the Slack Canyon #1 flow top (SCFT1) and the Slack Canyon #2 flow top (SCFT2). The injection zone flow top intervals possess moderately high permeabilities and are overlain by two thick-flow interior/caprock intervals (i.e., the Umtanum and Slack Canyon #3) exhibiting low-permeability, confining-layer conditions. Separating the individual injection zone flow tops are relatively thin, intervening flow interiors that have expected low-permeability conditions.

Hydraulic Properties

Hydraulic properties for each model layer were determined from hydraulic test results conducted at the Wallula site. Horizontal hydraulic conductivities for each layer are shown in Table 2. The hydraulic conductivity for the SCFT2 is the highest, at 6.35×10^{-5} cm/sec, while hydraulic conductivities for the SCFT1 and OFT are 8 times lower, at 8.2×10^{-6} cm/sec. Vertical hydraulic conductivities were assumed to be one order of magnitude lower than the horizontal hydraulic conductivities. Flow tops were assumed to have 10% porosity and flow interiors to have 1% porosity.
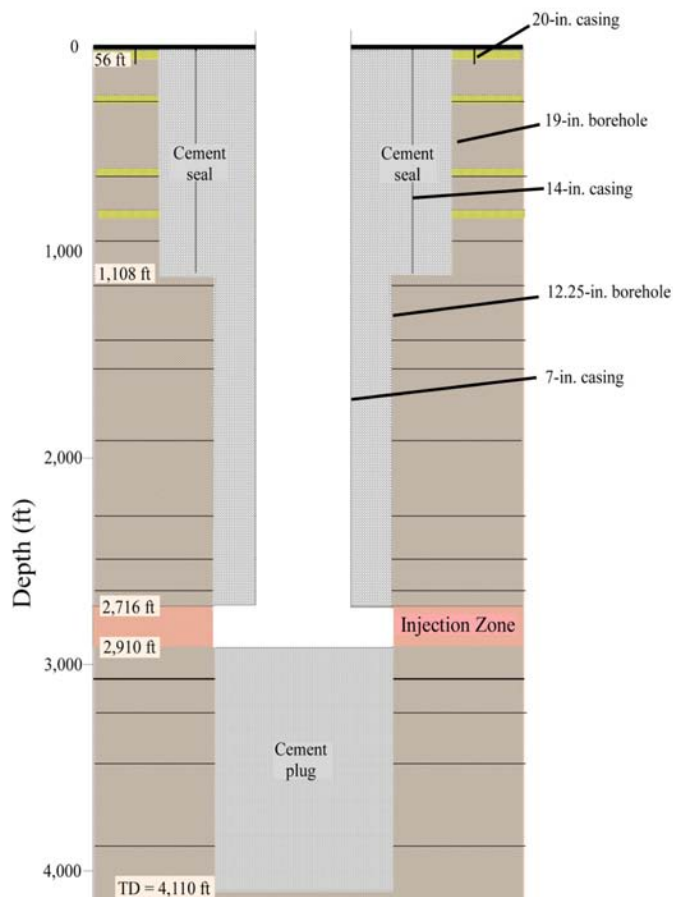
Figure 3: As-Built Completion for the Wallula Pilot Borehole

Unsaturated flow properties of the basalt flows intersected by the Wallula pilot borehole have not been measured and were assumed for each of the materials (White., 2006), as listed in Table 3. The unsaturated hydraulic properties for the flow tops are similar to those of gravel, whereas the flow interiors were assigned higher air-entry pressure to reflect the smaller pore size inherent for their lower permeability.

A hydrostatic gradient of 0.435 psi/ft was assumed based on observed formation pressure versus depth measurements exhibited for a deep Hanford Site characterization borehole, RRL-2, as reported in Strait and Spane (1982). Formation temperature was assumed to be 94.59 °F (34.8° C) at a depth of 2930.5 ft (893 m), with a geothermal gradient of –0.0147 °F/ft, based on observed measurements within the Wallula pilot borehole.

Table 2: Hydraulic Properties and Depth in Feet of Basalt Flows at the Wallula Pilot

Abbreviation	Model Layer	Top, ft	Bottom, ft	Thickness, ft	K, cm/sec	Porosity, %
UFI	Umtanum flow interior (secondary seal)	2442.5	2577.5	135	1.00×10^{-12}	1
SCFT3	Slack Canyon #3 porosity zone (no injection)	2577.5	2645.5	68	1.47×10^{-4}	10
SCFI3	Slack Canyon #3 flow interior (primary seal)	2645.5	2720.5	75	3.00×10^{-12}	1
SCFT2	Slack Canyon #2 flow top porosity zone (injection)	2720.5	2768.5	48	6.53×10^{-5}	10
SCFI2	Slack Canyon #2 flow interior (seal)	2768.5	2797.5	29	3.00×10^{-11}	1
SCFT1	Slack Canyon #1 flow top porosity zone (injection)	2797.5	2811.5	14	8.20×10^{-6}	10
SCFI1	Slack Canyon #1 flow interior (seal)	2811.5	2837.5	26	3.00×10^{-11}	1
OFT	Ortley flow top porosity zone (injection)	2837.5	2866.5	29	8.20×10^{-6}	10
OFI	Ortley flow interior (lower confining zone)	2866.5	2930.5	64	1.00×10^{-12}	1

Table 3: Brooks-Corey Function Parameters

	Air-Entry Pressure, cm	λ	Residual Saturation
UFI	154	4.033	0.01
SCFT3	54	4.033	0.01
SCFI3	154	4.033	0.01
SCFT2	54	4.033	0.01
SCFI2	154	4.033	0.01
SCFT1	54	4.033	0.01
SCFI1	154	4.033	0.01
OFT	54	4.033	0.01
OFI	154	4.033	0.01

Two-dimensional simulations with a cylindrical coordinate grid were developed for the model simulations. The model domain extended from 2930.5 ft (893 m) in depth to 2442.5 ft (744 m) in depth (488 ft [148 m] total), with a radial width of 1,000 ft (305 m) surrounding the injection well. A vertical grid spacing of 0.6 m (2 ft) was used, with a radial grid spacing set at 5 ft (1.5 m). Homogeneous layers were assumed throughout (Figure 4). Simulations were limited in scope to include only multiphase flow behaviour and did not include chemical reactions with the basalts to provide the most conservative plume dimensions for permitting.
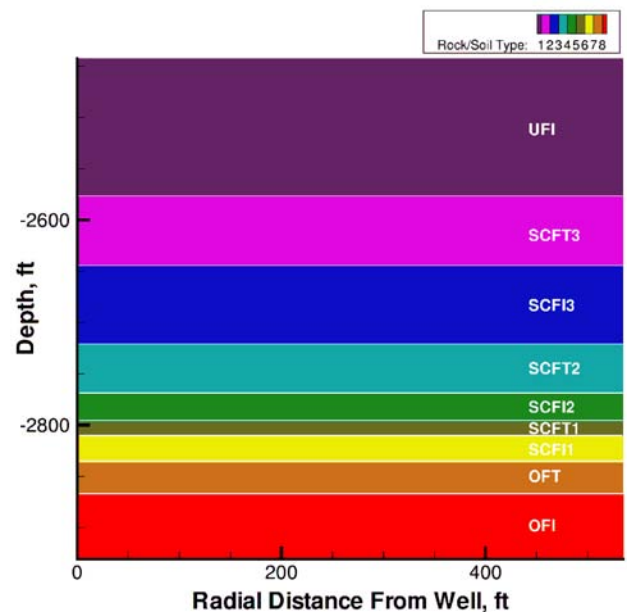
Figure 4: Lithologic Units for Simulation of Pilot-Scale CO_2 Injection at Wallula

Simulation Results

The total mass of CO_2 modelled for the injection simulations was 1,000 metric tons (MT), which was injected over a time period of either 14 or 30 days. For possible pilot study design considerations, three different injection scenarios were considered:

- **Scenario 1**: simultaneous injection into the OFT, SCFT1, and SCFT2 over a period of 14 days.

- **Scenario 2**: injection only into the SCFT2 over a period of 14 days.

- **Scenario 3**: injection only into the OFT over a period of 30 days.

Only results from injection Scenario 1 will be presented here.

Simulation results for the composite, open-borehole injection into the OFT, SCFT1, and SCFT2 (Scenario 1) indicate that most of the injected CO_2 flows into the SCFT2 (Figure 5). This zonal preferential injection of CO_2 is a result of the higher permeability exhibited by SCFT2. The density of the injected supercritical CO_2 is 66% of that exhibited by groundwater at the prevailing formation temperature and pressure conditions. Because supercritical CO_2 does not displace all of the groundwater within the formation pore space, the average fluid-density contrast is 75% to 100% of that exhibited by the initial formation water (Figure 6). The radius of the injected supercritical CO_2 from the Wallula pilot borehole well increases from 100 ft after the active 2 weeks of injection to 180 ft at 1 year after the start of injection (Figure 7 and Figure 8). The simulated increase in downhole pressure within the injection zone/well bore is less than 110 psi (Figure 9). One year after the start of injection, 18% of the injected CO_2 has dissolved into the aqueous-groundwater phase (Figure 10).
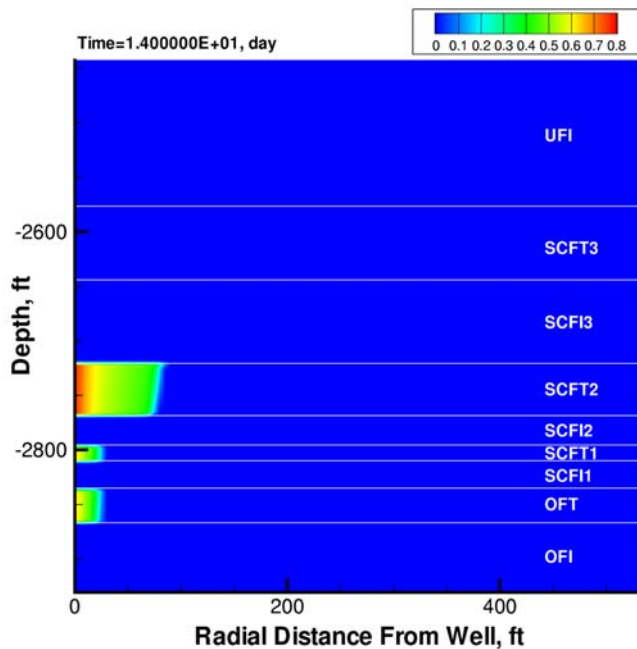
Figure 5: CO_2 Saturation in the Ortley, Slack Canyon #1 and Slack Canyon #2 Flow Tops Immediately after 1,000 MT Supercritical CO_2 Injection
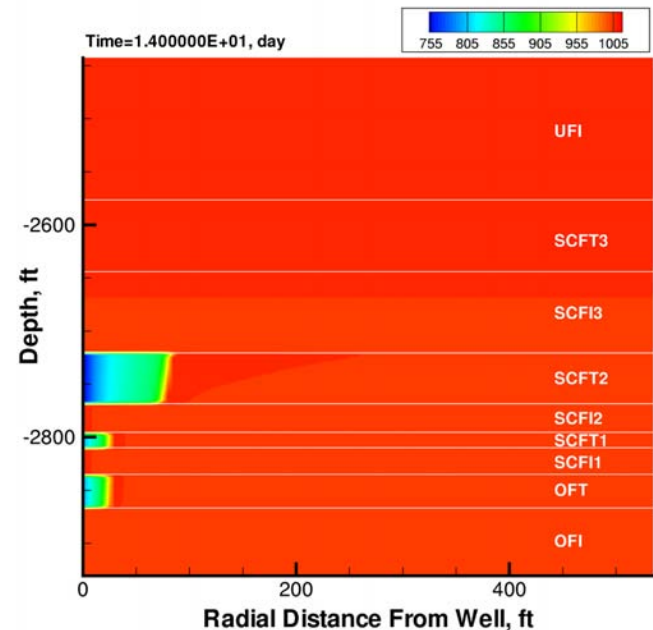
Figure 6: Fluid Density (kg/m^3) in the Ortley, Slack Canyon #1, and Slack Canyon #2 Flow Tops Immediately after 1,000 MT Supercritical CO_2 Injection
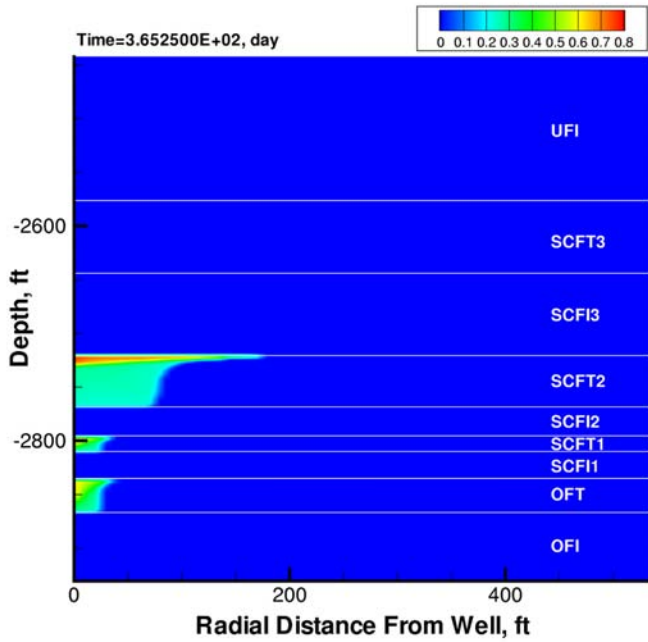
Figure 7: CO$_2$ Saturation in the Ortley, Slack Canyon #1 and Slack Canyon #2 Flow Tops 1 Year after Start of 1,000 MT Supercritical CO$_2$ Injection
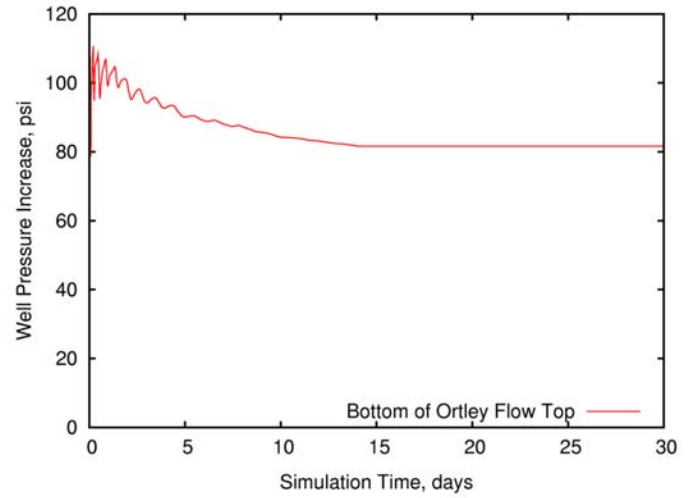
Figure 9: Increase in Well Pressure Over Hydrostatic During Injection of Supercritical CO$_2$ into the Ortley, Slack Canyon #1, and Slack Canyon #2 Flow Tops
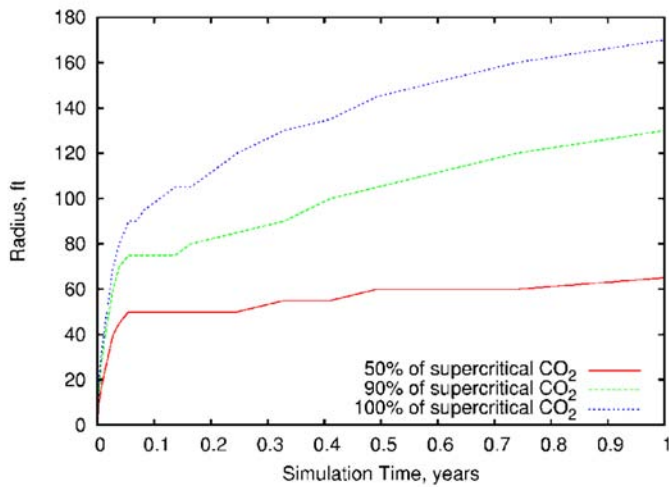
Figure 8: Radii Containing 50%, 90%, and 100% of 1,000 MT of Supercritical CO$_2$ Injected into the Ortley, Slack Canyon #1, and Slack Canyon #2 Flow Tops
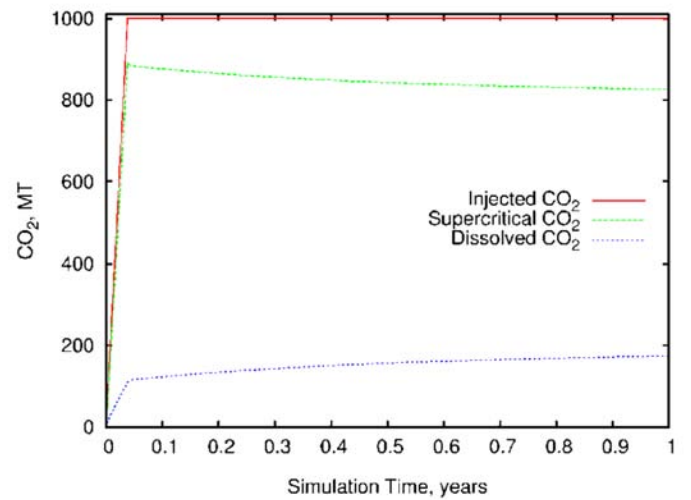
Figure 10: Phase Distribution of 1,000 MT of Supercritical CO$_2$ Injected into the Ortley, Slack Canyon #1, and Slack Canyon #2 Flow Tops

Conclusion

The borehole configuration established at the Wallula pilot site provides a unique and attractive opportunity to scientifically study the reservoir behavior of three connected reservoir intervals below primary and secondary caprock zones. Simulations of a 1,000 MT open-borehole injection over a period of 14 days into the three brecciated zones show that most of the injected CO_2 flows into the Slack Canyon #2 flow top due to its higher permeability. The increase in pressure in the well bore is less than 110 psi over hydrostatic to achieve this injection rate and the radius of the injected supercritical CO_2 increases to a maximum of 180 ft one year after the start of injection. No CO_2 migration into the overlying Slack Canyon flow interior is predicted even after 1 year of simulation time. Based on the cumulative analyses completed to date, the Wallula basalt pilot borehole is well suited to conduct the world's first supercritical CO_2 injection test into a continental flood basalt formation.

References

Alfredsson, H. A., B. S. Hardarson, H. Franzson, and S. R. Gislason, 2008, CO_2 sequestration in basaltic rock at the Hellisheidi site in SW Iceland: Stratigraphy and chemical composition of the rocks at the injection site: Mineralogical Magazine, v.72, no. 1, p.1-5.

Flaathen, T. K., E. H. Oelkers, and S. R. Gíslason, 2008, The effect of aqueous sulphate on basaltic glass dissolution rates: Mineralogical Magazine, v. 72, no. 1, p.39-41.

Goldberg, D. S., T. Takahashi, and A. L. Slagle, 2008, Carbon dioxide sequestration in deep-sea basalt: Proceedings of the National Academy of Sciences of the United States of America, v.105, no. 29, p.9920-9925, 10.1073/pnas.0804397105.

Gysi, A. P. and A. Stefansson, 2008, Numerical modeling of CO_2-water-basalt interaction: Mineralogical Magazine, v.72, no. 1, p.55-59.

Hooper, P. R, 1982, The Columbia River Basalts. In *Basalts* (ed. P. C. Ragland and J. J. W. Rogers), pp. 353-358. Van Reinhold Company, New York.

Khalilabad, M. R., G. Axelsson, and S. R. Gislason, 2008, Aquifer characterization with tracer test technique; Permanent CO_2 sequestration into basalt, SW Iceland: Mineralogical Magazine, v. 72, no. 1, p.121-125.

Matter, J. M., T. Takahashi, and D. Goldberg, 2007, Experimental evaluation of in situ CO_2-water-rock reactions during CO_2 injection in basaltic rocks: Implications for geological CO_2 sequestration: Geochemistry, Geophysics, Geosystems, v. 8, Q02001.

McGrail, B. P., A. M. Ho, S. P. Reidel, and H. T. Schaef, 2003, Use and features of basalt formations for geologic sequestration. In *Proceedings of the Sixth International Conference on Greenhouse Gas Control Technologies*, Vol. II (ed. J. Gale and Y. Kaya), pp. 1637-1640. Elsevier Science Limited, Kidlington, Oxford, United Kingdom.

McGrail, B. P., H. T. Schaef, A. M. Ho, Y. J. Chien, J. J. Dooley, and C. L. Davidson, 2006, Potential for Carbon Dioxide Sequestration in Flood Basalts, Journal of Geophysical Research - Solid Earth, v. 111(B12), doi:10.1029/2005JB004169.

McGrail, B. P., E. C. Sullivan, F. A. Spane, D. H. Bacon, G. Hund, P. D. Thorne, C. J. Thompson, S. P. Reidel, and F. S. Colwell, 2009, Preliminary hydrogeologic characterization results from the Wallula Basalt Pilot study, PNWD-4129, Battelle Pacific Northwest Division, Richland, Washington.

Montgomery, S. L., 2008, New exploration concepts highlight Columbia River Basin's potential: Oil & Gas Journal, v. 106, no. 2, p.35-42.

Prasad, P. S. R., D. S. Sarma, L. Sudhakar, U. Basavaraju, R. S. Singh, Z. Begum, K. B. Archana, C. D. Chavan, and S. N. Charan, 2009, Geological sequestration of carbon dioxide in Deccan Basalts: Preliminary laboratory study, Current Science, v. 96, no. 2, p.288-291.

Reidel, S. P., T. L. Tolan, P. R. Hooper, M. H. Beeson, K. R. Fecht, R. D. Bentley, and J. L. Anderson, 1989, The Grande Ronde Basalt, Columbia River Basalt Group; Stratigraphic descriptions and correlations in Washington, Oregon, and Idaho. In *Volcanism and Tectonism in the Columbia River Flood-Basalt Province* (ed. S. P. Reidel and P. R. Hooper), pp. 21-45. The Geological Society of America, Boulder, CO.

Reidel, S. P., V. G. Johnson, and F. A. Spane, 2002, Natural gas storage in basalt aquifers of the Columbia Basin, Pacific Northwest USA: A guide to site characterization, PNNL-13962, Pacific Northwest National Laboratory, Richland, Washington.

Schaef, H. T. and B. P. McGrail, 2009, Dissolution of Columbia River Basalt under mildly acidic conditions as a function of temperature: Experimental results relevant to the geological sequestration of carbon dioxide: Applied Geochemistry, v. 24, no. 5, p.980-987, 10.1016/j.apgeochem.2009.02.025.

White, M. D., B. P. McGrail, H. T. Schaef, and D. H. Bacon, 2006, Numerically simulating carbonate mineralization of basalt with injection of carbon dioxide into deep saline formations: In Proceedings of *XVI International Conference on Computational Methods in Water Resources*, Technical University of Denmark, Available at http://proceedings.cmwr-xvi.org/contributionDisplay.py?contribId=246&sessionId=3&confId=a051.

White, M. D. and M. Oostrom, 2006, STOMP Subsurface Transport over Multiple Phases, Version 4.0, User's Guide, PNNL-15782, Pacific Northwest National Laboratory, Richland, Washington.

Midwest Geological Sequestration Consortium

Tanquary Enhanced Coal Bed Methane Project

Scott M. Frailey and David G. Morse
Illinois State Geological Survey

The purpose of the Tanquary Enhanced Coal Bed Methane (ECBM) project was to evaluate the CO_2 injection and storage potential of Illinois Basin coal seams and to evaluate the methane recovery potential in response to CO_2 injection. The plan was to inject up to 100 tons of CO_2 into the Pennsylvanian Springfield Coal seam. An injection site was selected on the Tanquary Farms in southeast Illinois between Albion and Mt. Carmel.

During Phase I a general purpose model of Illinois Basin coal was developed using COMET3 E/CBM software to assess CO_2 storage potential. The input parameters were based on data specific to the Basin coals, the published literature, and staff experience with coalbed methane production. A rigorous study of the parameters was performed to develop high, medium and low estimates of each parameter. These input parameters and the COMET3 software were the basis for the coal simulation model used to aid in the design of the MGSC Phase II Tanquary ECBM project.

Since relatively deeper and thicker coals were of interest, the southern part of the Illinois Basin where this trend is exhibited was targeted for the site location. During the site screening process a number of oilfield operators were contacted with an invitation to participate in an ECBM pilot study. At the time, the price of crude oil was relatively high and oilfield activities in the region were correspondingly elevated. This likely explains why the oilfield operators who were contacted did not express interest in participating. However, one oil company drilling in the deeper part of the Basin did provide access for collecting cores and performing a drill stem test (DST) on one of the coal seams that lay above their drilling target. Analyses demonstrated that the permeability of this coal seam was much greater than anticipated. Unfortunately, this company declined to participate further in an ECBM pilot study. Eventually, a farm cooperative interested in learning more about the coals underlying their land agreed to participate and provide a suitable site.

Due to the large number of oil well penetrations in the Basin, data on the thickness, depth and structure of the Basin's coals seams were abundant. These data, along with the permeability data obtained from the DST, were used to generate model inputs. A grid sensitivity analysis was also conducted to find the smallest grid size that would have negligible effect on the pressure response and saturation profile at potential monitoring well locations. It was found that the primary influence on grid sensitivity was the size of each well's grid cell and, to a much lesser degree, the size of cells between wells. Two hybrid grids (2.5 x 2.5 ft and 5 x 5 ft) were used (Figure 11). Because of the vast expanse of coals in the Basin, the finely gridded model was surrounded by a few rows of larger cells and an analytical aquifer function was assigned to the outer cells to provide an open-boundary. The properties of the aquifer function were assigned the same values as that of the coal seam. The coals seams in the Basin are relatively thin (5-10 ft) and encased vertically between shale beds, so a single model layer was used to represent the coal.

After the grid and coal properties were selected, projected pilot injection rates and duration were simulated as part of a parametric study. Variables in the study were matrix and pore compressibility, cleat spacing, initial gas concentration, stress dependent permeability, porosity, skin, matrix swelling, methane and CO_2 sorption time, differential permeability (k_x/k_y), methane Langmuir constants, and relative permeability. Thirty-six scenarios based on the most likely values were simulated. The wellbores were simulated with rate and pressure constraints; however, the designated CO_2 injection rates were chosen so that the maximum pressure constraint (90% of the projected fracture gradient) would be invoked. The results of these simulations indicated a minimum distance of 150 ft between injector and observation wells was necessary to observe a detectable pressure (≥ 5 psi) and saturation ($\geq 10\%$) change during the planned injection period (Figure 12).
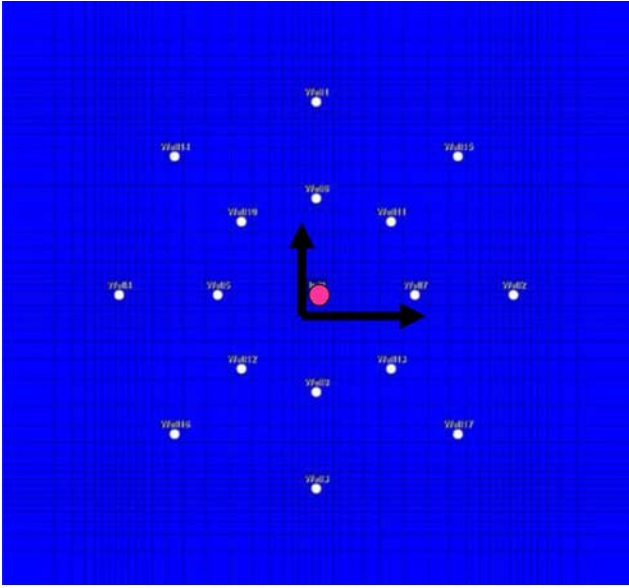
Figure 11: Example of one of the models used for pilot design and well spacing. Cleat orientation is along the x-y grid direction. Sixteen monitoring wells were placed around the central injector in 150 and 300 ft diameter rings. Wells were placed on diagonals in case the orientation of the cleats determined from a nearby mine did not match up well with the location of the wells drilled. (Well locations were required in the model to allow simple determination of pressure and saturation at these locations.)
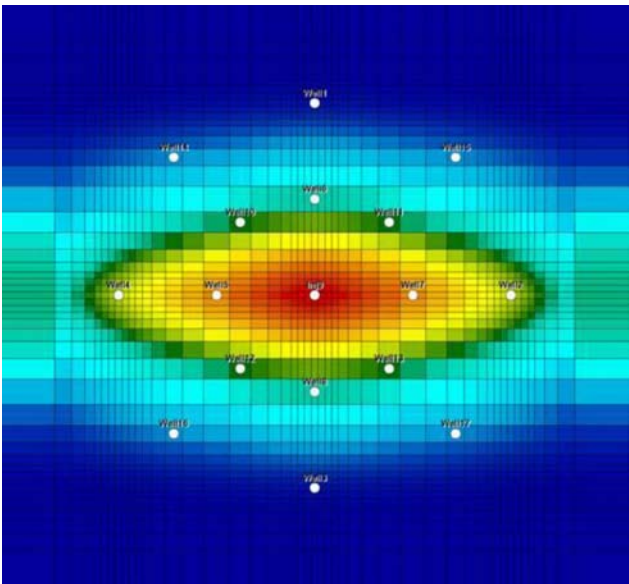
Figure 12: Example of one of the models used for pilot design and well spacing showing that the outer ring of monitoring wells (300 ft) would not have detectable gas saturation. Consequently, for the initial pilot design, the 150 ft well spacing was used. The face cleat direction is left to right and the butt cleat direction is top to bottom. Light blue is 10% and the red is up to 50% gas saturation.

In the summer of 2007, two wells (M-1 and M-3) were drilled 150 ft apart in the butt cleat direction. (Cleat orientation was available from regional maps and direct measurements from an underground coal mine in the area.) The Springfield coal was one of the thickest coals in these wells (Figure 13). DST interpretations of the Springfield coal in these wells gave permeability of 2 and 7 mD and skin +6 and +9, which was lower than the values used in the pilot design simulations (pre-drill). Real-time simulations were made with these reduced permeability values, and the model results indicated that 150 ft monitoring well spacing in the butt cleat direction would have no saturation response and relative low pressure response during the CO_2 injection period. Consequently, drilling operations ceased until pressure transient tests (falloff and pulse tests) with controlled injection rates could be conducted between the first two wells to confirm the DST permeability. (These tests were considered more reliable than DSTs.)
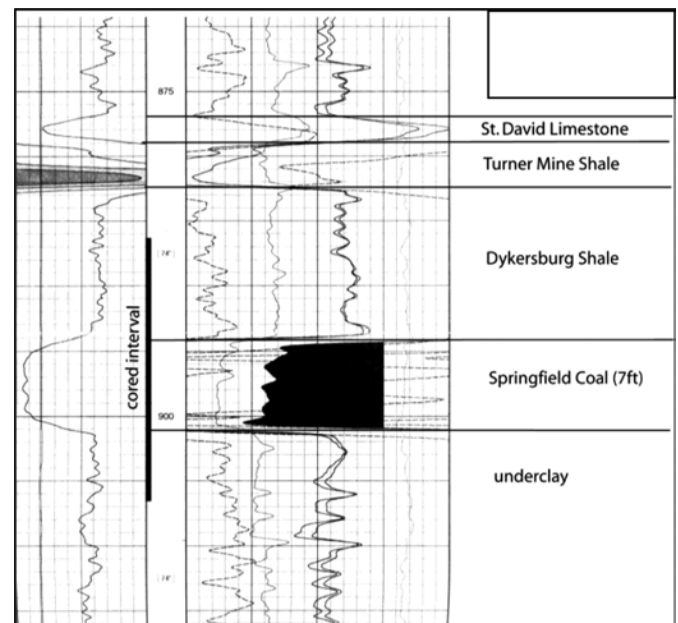
Figure 13: Gamma ray (track 1) and porosity logs (track 2 and 3) showing Springfield coal and vertical confinement of coal. The cored interval is shown in the depth track.

M-1 and M-3 were cased and cemented to surface. The Springfield coal was perforated with 6 shots per foot, 60° phasing, and 3/8 inch diameter. A 250 gallon, 9% formic acid treatment was used to breakdown the perfs; the acid was displaced with 1,000 gallons water. The wells were swabbed (removing liquid volume adequate to return the acid and displacing water) and methane gas was brought to surface. The wells were shut-in to achieve static pressure prior to the pressure transient tests. The coal cleat pressure supported a water level to surface with a small positive pressure at the wellhead.

Bottomhole pressure gauges with surface readout were placed in both wells during all tests. A step rate test was conducted in the first well. Injection rates were maintained for about two hours for each rate. The step rate test gave a fracture pressure gradient of 0.96 psi/ft so injection rate and pressure could be maximized without fracturing the coal. The Illinois Oil and Gas Division permitted injection at up to 90% of this fracture gradient.

During the step rate test of M-3, pressure in M-1 was recorded. The butt cleat direction permeability was estimated at 3.3 mD. An injection period of nine hours followed the injection periods of the step rate test at a rate below the parting pressure. Afterwards, the first well was shut-in for a 24-hour falloff test. Because the coal pressure supported a water level to the surface, the well was shut-in at the surface and little wellbore storage occurred. The M-3 falloff gave a permeability of 4.0 mD and skin of -1.5. After the falloff test, a two-cycle pulse test with 10 hour flow and 10 hour shut-in periods was conducted. For each injection pulse, a pressure increase of 5-6 psi after about 10 hours was measured at the M-1 well. An interwell permeability of 3.3 mD was calculated, which was in good agreement with the analyses of the pulse created during the step rate test. Lastly a falloff of M-1 gave a permeability of 4.4 mD and skin of -3.0.

The skin was reduced substantially from the DST to the falloff test indicating the effectiveness of the acid treatment. The interference and pulse tests showed pressure communication between the wells. Falloff tests confirmed the lower DST permeability estimates. A comparison of the single well permeability and interwell permeability gave little difference suggesting that the face and butt cleat permeability may not be different. (The single well PTA tests provide an equivalent permeability which is equal to the square root of the face and butt cleat permeability product. The permeability from the pulse tests is either the face or butt cleat permeability depending on the orientation of the wells with respect to the cleat orientation.) The coal model's permeability and skin factors were updated with these results and new simulations indicated that a 100 ft well spacing was required to achieve measurable results at the monitoring wells during the planned injection period. Consequently, two additional wells (M-2 and I-1) were drilled to complete this pilot (Figure 14). The injection well (I-1) was drilled in the butt cleat direction between the first two wells: 50 feet from M-1 and 100 feet from M-3. The face cleat monitoring well (M-2) was drilled 100 ft from the injection well, orthogonal to the butt cleat direction aligned wells (M-1, I-1, and M-3).

After these wells were drilled, another series of pulse tests and falloff tests were completed on M-2 and I-1. The objective of the reservoir modeling of the pre-CO_2 water injection pressure transient tests was to define the baseline permeability of the coal seam. A match of the pressure transient responses of all of the wells was not easily accomplished. Numerous variations on grid size, grid orientation, face and butt cleat permeability, coal compressibility, and aquifer strength (outer boundary) were conducted but a good simultaneous match of the measured pressure of all wells was not possible. After these futile attempts, the only option was to move the well locations within the model. Small changes of 3-10 feet were required to get a good match of the water injection period. For larger spaced wells, 3-10 feet is likely negligible but due to the close proximity of these wells, this small amount was important to the history match. Discussions with drilling companies and oilfield operators confirmed that a 900 ft well could easily have a bottomhole location offset 10-15 ft from its surface location. However from a modeling perspective, it was recognized that any pressure history could be matched if a modeler used well locations as a variable. Therefore, well locations were checked with bottomhole surveys conducted as part of the post-CO_2 injection cased hole logging program. The bottomhole survey revealed two well locations at the coal seam were off 2 and 11 ft from the surface location, which validated the history match of the water pressure transient tests.
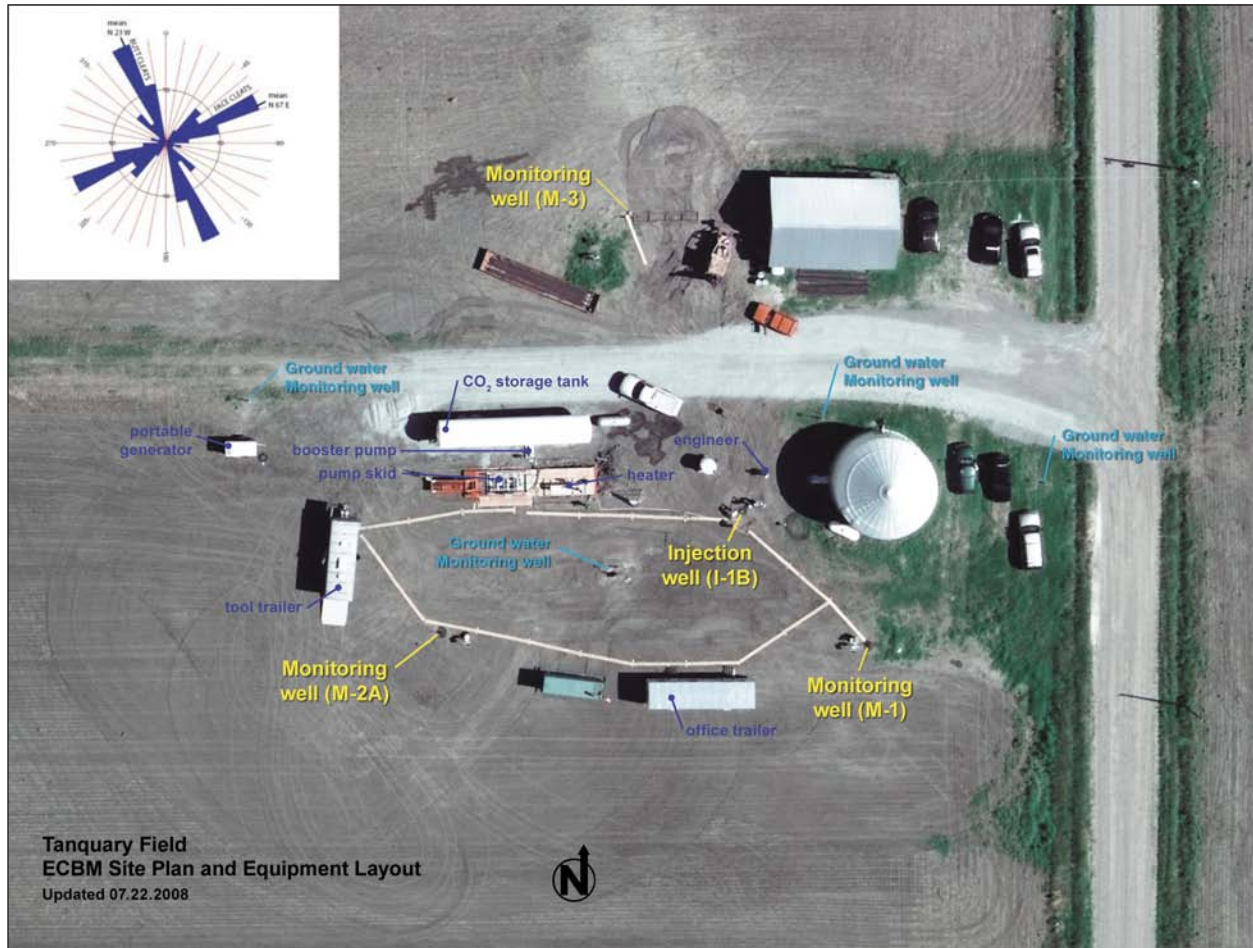
Figure 14: Layout of wells and equipment at the Tanquary site. The cleat orientation is represented in the rose diagram in the upper left. The butt cleat direction is SE-NW and the face cleat direction is SW-NE.

CO_2 delivery was by 20 ton liquid CO_2 tanker trucks. On site, the CO_2 was transferred to a 60 ton storage tank and pumped through an inline heater to ensure the CO_2 is in the gas phase before entering the coal seam. Gaseous CO_2, which has lower viscosity than liquid CO_2, was expected to improve injectivity in the cleat system of the coal. Moreover, low density CO_2 (gas) was expected to be less reactive with coal compared to relatively higher density CO_2 (liquid or supercritical).

Initially, all wells were at static equilibrium pressure and no withdrawal (shut-in) occurred at the observation wells. Because the objective of this pilot is to account for free methane gas due to CO_2 injection, the observation wells' bottomhole pressure was maintained above the methane desorption pressure to ensure that any free methane gas is a result of CO_2 injection and not pressure depletion. This reduced the ambiguity of the source of free methane gas detected at the observation wells, and has a direct field indication of ECBM.

After a few hours of CO_2 injection at I-1, methane gas was detected at M-1 and M-3, the butt cleat monitoring wells. The methane gas head continued to increase at these wells for the next month until CO_2 was detected at M-1. At that time the gas head was slowly produced and metered until water from the coal seam again filled both wellbores. The face cleat monitoring well, M-2, did not have any indication of gas during this time period. Also during this first month, several CO_2 pressure transient tests were completed during the first month of injection so that changes to permeability might be determined in the early part of the pilot.

After each shut-in period, CO_2 injection rates would start at 2-4 tons/day and stabilized after a few days at 0.5-1.0 tons/day. There was no direct evidence of changes to permeability from the CO_2 injection data. Gas head continued to build in M-1 and M-3, but water only was present in the M-2 wellbore. After four months of CO_2 injection, the M-2 bottomhole pressure was lowered to check if a pressure decrease would cause gas to enter the well from the coal. The well was opened at the surface, and the surface pressure slowly decreased. Initially only a small stream of water flowed. Within a few minutes, methane gas flowed from M-2. This continued for about two hours until the well was shut-in. At that time, M-1 and M-3 gas heads were produced by opening the wells and lowering surface pressure. However, water did not return to surface for these two wells, and the gas head remained in these wells as additional gas entered the wellbore via the coal. M-2 was opened and flowed for about two hours every few days during the next two weeks after this first production period until CO_2 was detected at this well. After about six months of interrupted operations, 100 tons of CO_2 was injected.

Presently, water is being injected into the coal seam to provide a post-CO_2 estimate of cleat permeability and compressibility. Step-rate tests are planned for each well to observe any changes in mechanical strength of the coal as a consequence of CO_2 injection. Lastly, to provide additional modeling matching criteria and direct evidence of the ECBM and CO_2 storage of Basin coals, controlled gas withdrawal at incremental reductions in water level are planned. These tests will provide in-situ gas content and composition as a function of coal seam pressure. Specifically, direct information will be acquired to assess if the current condition of the coal has changed compared to the initial gas desorption pressure and if the sorbed gas composition is predominantly methane, CO_2, or a mixture of these two gases.

The modeling completed to date was a necessary and effective part of the pilot design and coal pilot characterization but only reflects single phase (water) flow at pressure above the methane gas desorption pressure of the coal. The general purpose model input parameters have been replaced with site specific depth, thickness, porosity, cleat permeability, and isotherm data. The gas physical properties, two phase flow parameters, and desorption features of the COMET3 software and the associated input parameters (e.g. gas-water relative permeability, Langmuir isotherm, and coal swelling factors) have not been calibrated to field measurements or observations. Following the calibration of the Tanquary COMET3 model to the CO_2 injection, post-CO_2 water injection rates and all wells' pressure responses, the remaining modeling is expected to provide CO_2 plume size and distribution, estimate storage efficiency and capacity of Basin coals, assess ECBM potential, and detect any reduction in cleat permeability.

Acknowledgements:

Midwest Regional Carbon Sequestration Partnership

Models Used to Simulate Supercritical CO_2 Injection at MRCSP Phase II Test Sites

Joel Sminchak
Battelle

Introduction

Models were used to simulate supercritical CO_2 injection at MRCSP Phase II test sites in the Appalachian Basin, Cincinnati Arch, and Michigan Basin (Figure 15). Model development evolved through three different stages:

1. The first stage was a general model developed before the site characterization well had been drilled. A homogeneous formation was assumed as a target for all sites. This model was based on regional data and involved many assumptions. However, it did provide valuable information for planning the injection tests.

2. The second stage conceptual model was completed after core data were available from the characterization well, but before hydraulic tests were performed.

3. The final conceptual model was revised based on hydraulic test data and actual time-varying injection rates and temperatures in the injection well. The STOMP-WCSE simulator was validated against observed values of pressure in the injection and observation wells.
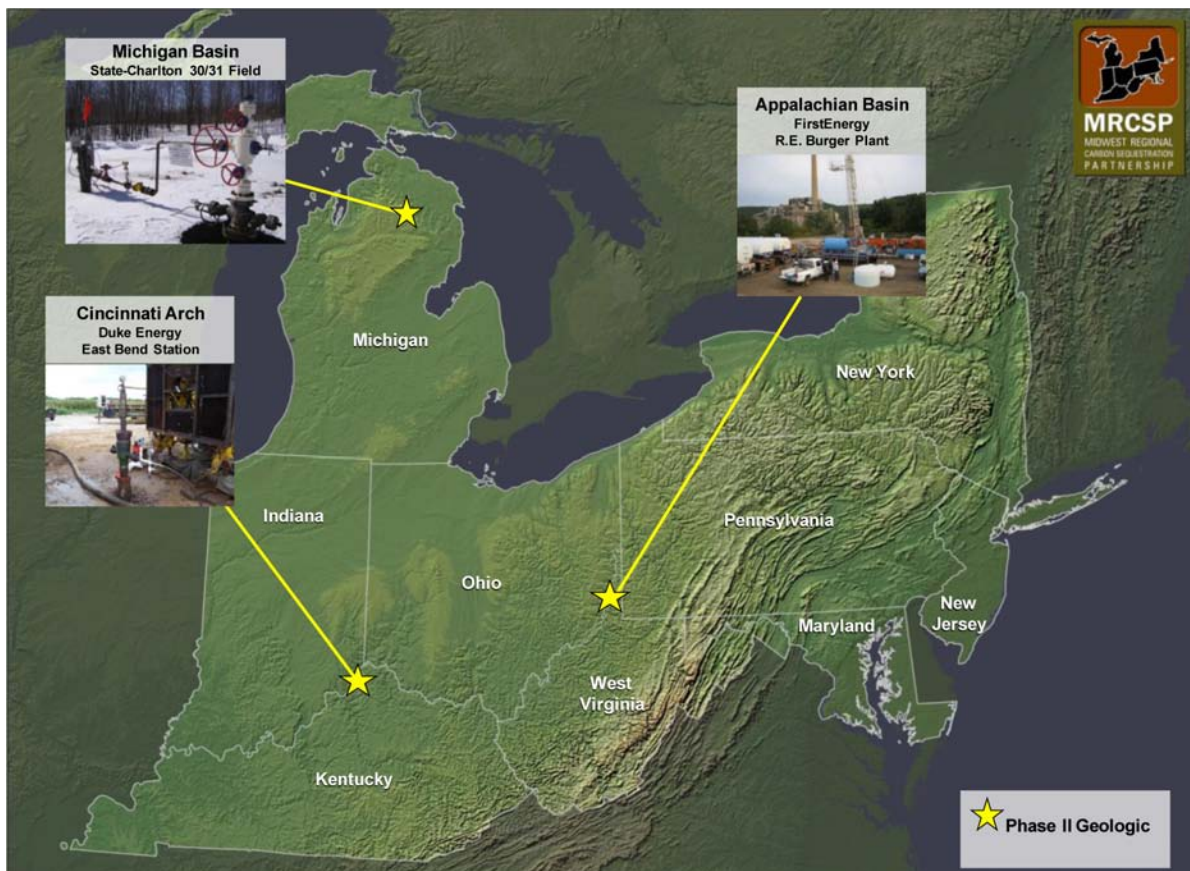
Figure 15: MRCSP Phase II Geological CO_2 Injection Test Sites

The MRCSP Phase II sites emphasized integration of modeling with field data. For the Michigan Basin site, approximately 60,000 metric tons CO_2 was injected over 6 months, and a large amount of monitoring data was collected (Figure 16). Consequently, a fairly rigorous model calibration was completed to assess model accuracy. The Appalachian Basin site involved limited injection testing, so analytical models were used estimate pressure buildup. For the Cincinnati Arch site, a limited amount of CO_2 injection was completed into the Mt. Simon sandstone. However, advanced numerical models were used to calibrate to test results and better understand large scale injection in the Mt. Simon Sandstone.

MRCSP Models for Geologic Storage

Simulations for the MRCSP Phase II sites were executed with the STOMP-WCSE (Subsurface Transport Over Multiple Phases- water, CO_2, salt, energy) simulator. Partial differential conservation equations for fluid mass, energy, and salt mass comprise the fundamental equations for STOMP-WCSE. The STOMP simulator's fundamental purpose is to produce numerical predictions of thermal and hydrogeologic flow and transport phenomena in variably saturated subsurface environments (White and Oostrom, 2006). The STOMP simulator is written in the FORTRAN 77 and 90 languages, following American National Standards Institute (ANSI) standards.

STOMP was verified against other codes used for simulation of geologic disposal of CO_2 as part of the GeoSeq code intercomparison study (Pruess et al., 2002). Coefficients within the fundamental equations are related to the primary variables through a set of constitutive relations. The conservation equations for fluid mass and energy are solved simultaneously, whereas the salt transport equations are solved sequentially after the coupled flow solution. The fundamental coupled flow equations are solved following an integral volume finite-difference approach with the nonlinearities in the discretized equations resolved through Newton-Raphson iteration. The dominant nonlinear functions within the STOMP simulator are the relative permeability-saturation-capillary pressure (k-s-p) relations. The STOMP simulator allows the user to specify these relations through a large variety of popular and classic functions. Two-phase (gas-aqueous) k-s-p relations can be specified with hysteretic or nonhysteretic functions or nonhysteretic tabular data. Entrapment of CO_2 with imbibing water conditions can be modeled with the hysteretic two-phase k-s-p functions. Two-phase k-s-p relations span both saturated and unsaturated conditions. The aqueous phase is assumed to never completely disappear through extensions to the s-p function below the residual saturation and a vapor pressure-lowering scheme. Supercritical CO_2 has the role of a gas in these two-phase k-s-p relations. A well model in STOMP-WCSE was used to simulate the
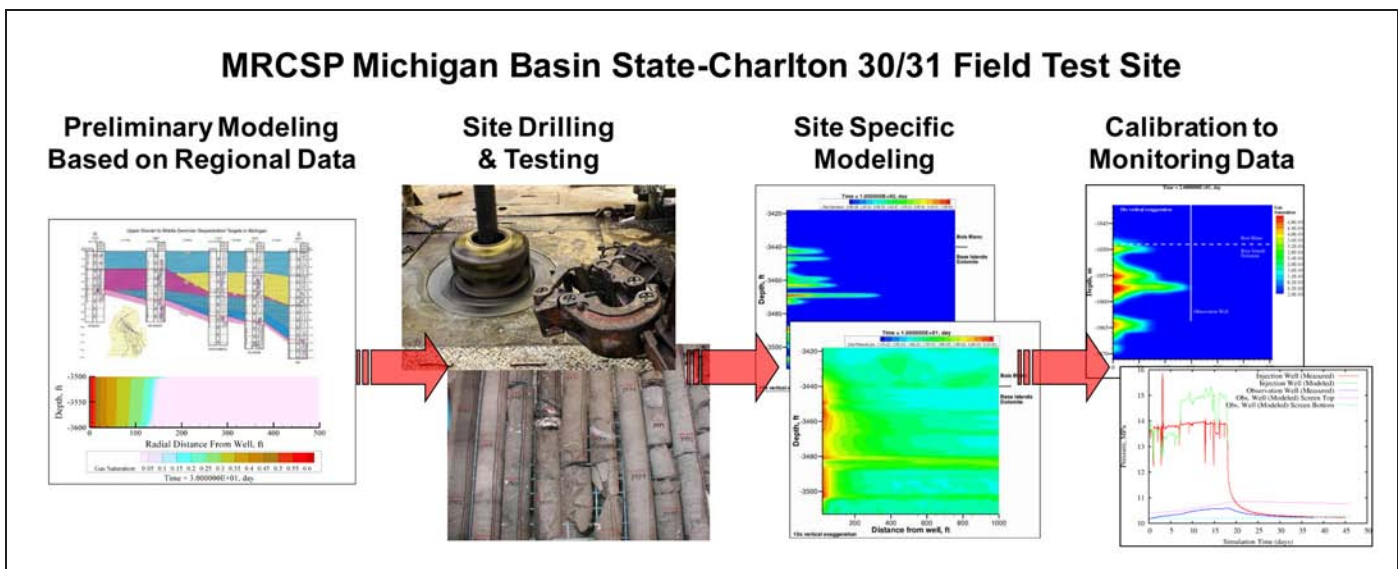
Figure 16: Example of the Modeling Process for MRCSP Michigan Basin Phase II Test Site

injection of supercritical CO_2. A well model is defined as a type of source term that extends over multiple grid cells, where the well diameter is smaller than the grid cell. The CO_2 injection rate is proportional to the pressure gradient between the well and surrounding formation in each grid cell. A bottomhole pressure is calculated iteratively until either the maximum borehole pressure or the desired injection rate is reached.

Case Study MRCSP Phase II Michigan Basin Site

Background

The MRCSP Phase II Michigan Basin site was located in Otsego County, Michigan. The CO_2 injection was completed in the Bass Islands dolomite, a carbonate deep saline rock formation. A test well, identified as State-Charlton #4-30, was drilled at the field site in November 2006. Full rock coring, rotary sidewall coring, and wireline logging were completed in the borehole to define the CO_2 storage reservoir and confining layers. In addition, a nearby well named State-Charlton #3-30a was recompleted and logged in the Bass Islands to allow monitoring of the injection process. This information was used to define specifications of the injection tests and develop a suitable monitoring, verification and accounting (MVA) program for the project. In February-March 2008, approximately 10,000 metric tons CO_2 was injected at the test well, followed by another injection test of approximately 50,000 metric tons CO_2 in February-July 2009.

The site is located in the northern portion of the Michigan Basin, a large, mature sedimentary basin that covers most of Lower Michigan. Paleozoic sedimentary rocks up to approximately 10,000 ft in total thickness underlie a 600 to 800 ft thick glacial layer in the study area. Precambrian crystalline basement rocks underlie the Paleozoic rocks. The target CO_2 storage interval included rocks at a depth of 3,190 to 3,515 ft. This interval includes the porous portions of the Bois Blanc to the Bass Islands Dolomite Formation (Figure 17).

The actual interval for injection was within the Bass Islands Dolomite at 3442 to 3515 ft, the most permeable section of the target storage zone (Harrison et al., 2008). Rocks in the overlying Amherstburg Group are considered the immediate overlying confining interval. Rock formations in the interval of interest dip toward the south at approximately 50 ft/mile. While some anticlines and arch trends have been identified in the region, there does not appear to be any clear structure near the site.
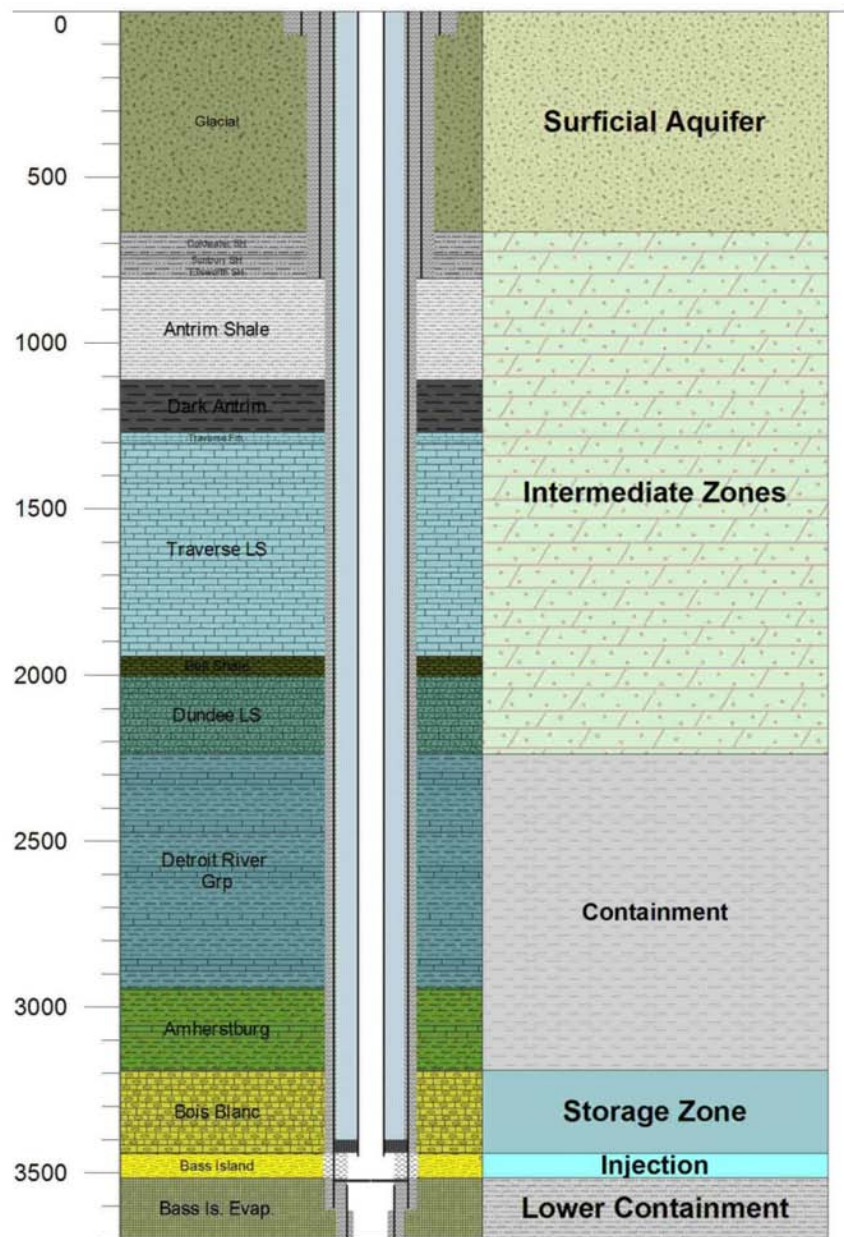
Figure 17: Schematic Diagram Illustrating CO_2 Storage and Containment Zones at MRCSP Phase II Michigan Basin Site

Pre-Injection Analyses

Before the injection and monitoring wells were drilled, information on the target formations was limited. A simple, homogeneous sandstone formation was assigned in these preliminary simulations as summarized in Table 4.

The injection was simulated as a radial model with STOMP-WCSE. Injection of supercritical CO_2 was assumed to occur over a period of 61 days, at a rate of 200 metric tons per day, for a total injected mass of 12,200 metric tons. The predicted radius containing 100% of injected supercritical CO_2 was 272 ft after 61 days of injection. Near the end of the injection period, the supercritical CO_2 concentrations are highest near the injection well (Figure 18), with some upward movement due to buoyancy forces. CO_2 dissolves into the brine up to a mass fraction of 0.042, which is the solubility limit of CO_2 at the specified temperature, pressure and salinity. Formation gas pressures near the end of the injection period are increased by approximately 80 psi relative to the ambient hydrostatic pressure.

During Injection Analyses

After the injection (State Charlton #4-30) and monitoring (State Charlton #3-30) wells were drilled, hydraulic properties from core samples were analyzed using geostatistical methods. Based on an analysis of porosity and permeability from core samples, the Bass Islands Dolomite was identified as an injection target. For the Bass Islands Dolomite core samples, the mean porosity was 13 percent and the mean permeability was 22.6 mD. A spherical semivariogram model was fit to the core data, using a vertical range of 3.4 feet. The porosity was assumed to be normally distributed and the intrinsic permeability was assumed to be log-normally distributed. In the model, the Bass Islands Dolomite, the Bois Blanc and Amherstberg formations geology were represented by spatially correlated random fields of porosity and intrinsic permeability that maintained the mean and variance of the data collected from the formation core samples (Figure 19). The random fields were generated using the SGSIM sequential Gaussian simulator (Deutsch and Journel, 1998).

Table 4: Pre-Characterization Model Input Parameters

Saturated Intrinsic Permeability	100 mD
Porosity	15%
Formation Thickness	100 ft
Rock Type	Homogeneous, Isotropic Sandstone
Saturation Function	Berea Sandstone, Brooks and Corey extended
Aqueous/Gas Relative Permeability	Burdine pore distribution function
Injection Rate	200 metric tons/day for 2 months
Simulation Time	1 year
Depth to Bottom of Formation	3600 ft
Hydrostatic Gradient	0.433 psi/ft
Salt Mass Fraction	0.1
Temperature	90°F
Coordinate System	2 dimensional cylindrical
Radial Grid Spacing	67 nodes, variable spacing from 0.26 ft to 206 ft
Vertical Grid Spacing	100, uniform 1 ft spacing
Upper and Lower Boundary Conditions	no flow
Boundary Condition at Radius	0: Axis of symmetry
Boundary Condition at Radius	3342 ft
Hydrostatic Gradient	0.433 psi/ft
Pressure at Lower Boundary	1558.584 psi
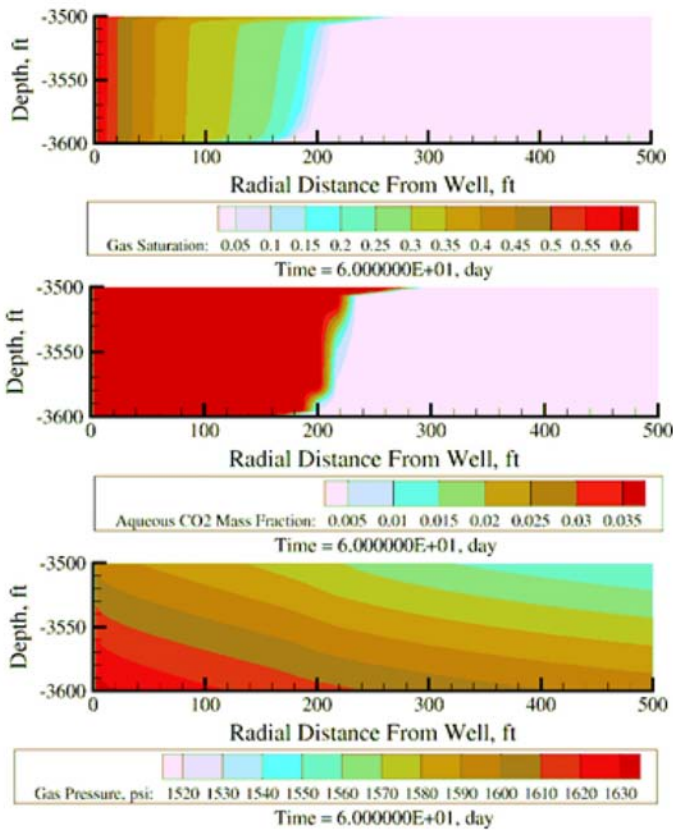
Figure 18: Distribution of Supercritical CO_2 Near the End of 60-Day Injection Predicted by Pre-Characterization Model

Simulations were executed on a 2-D radial Cartesian grid. The grid covered a vertical depth (in the Z-direction) of 512 ft, between the depths of 3514 to 3002 ft. The grid assumed horizontal radial symmetry around the well out to a distance of 1 mile. The grid had a resolution of 132 grid nodes in the horizontal X-direction and 124 nodes in the vertical Z-direction. Vertical grid spacing was 2 ft in the Bass Islands Dolomite and 5 ft in the Bois Blanc and Amherstburg. Horizontal grid spacing was 40 ft.

A downward pressure gradient of 0.45 psi/ft was used to initialize the brine pressure field. The pressure gradient was additionally assigned to vertical boundary surfaces located opposite from the vertical injection well. This assumption allows reservoir brine to be pushed outside of the computation domain as CO_2 is injected. An initial temperature gradient of 0.01 degrees/ft was assumed, with an initial formation temperature of 83.14 °F at a depth of 3514 ft. A brine density of 1159 kg/m^3 was assumed.

The simulation considered an injection period of 20 days, followed by an equilibration period, for a total simulation time of one year. A specified CO_2 injection rate of 500 metric tons/day was applied as a well model in STOMP-WCSE, using the same screened interval (72 ft) and wellbore diameter (8 5/8 inches) as the State Carlton #4-30 well. The injected CO_2 was assumed to be at the same temperature as the formation.
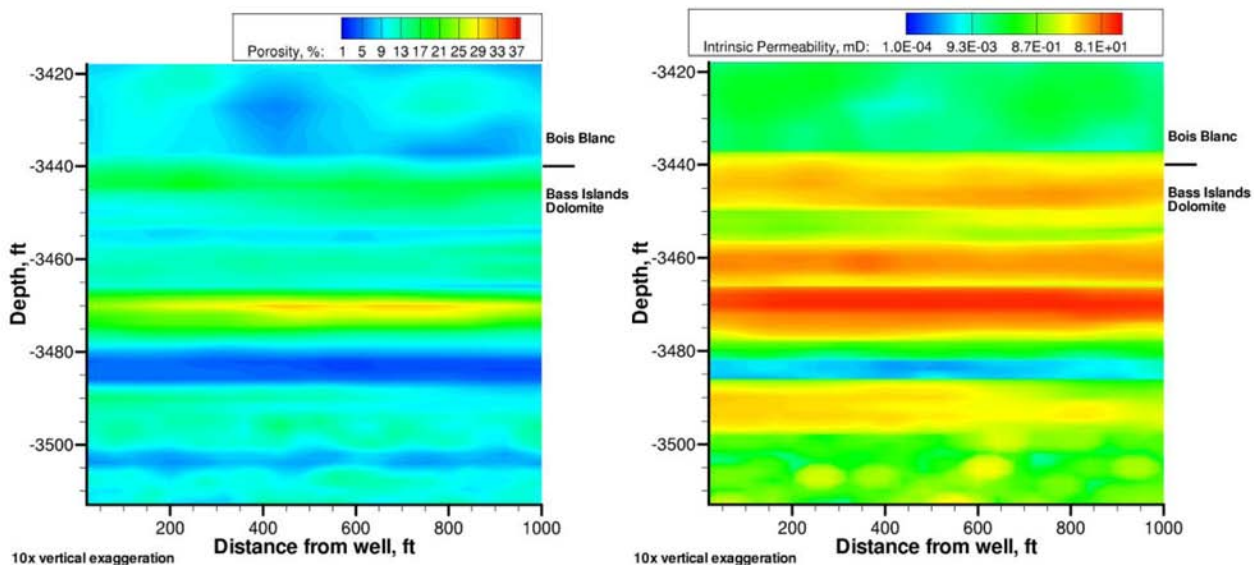
Figure 19: Geostatistical Realizations of Porosity and Permeability Based on Core Samples from the Bass Islands Dolomite and Lower Bois Blanc Formations
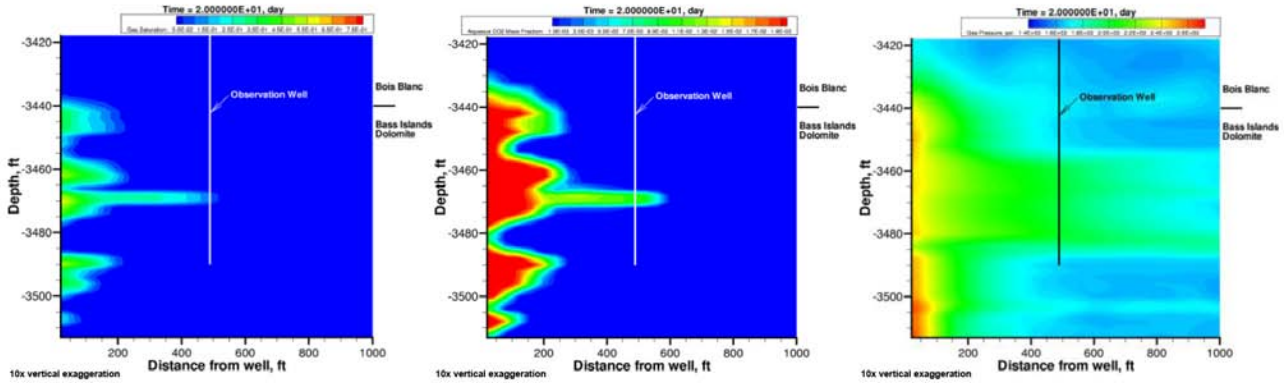
Figure 20: Distribution of Supercritical CO_2, Dissolved CO_2, and Gas Pressure Near the End of 20-Day Injection Predicted by Post-Characterization Model

The total amount injected was 10,000 metric tons; after 1 year 1,144 metric tons of CO_2 dissolved into the brine (Figure 20). After 100 days, the maximum radius of injected supercritical CO_2 is 600 ft, just beyond the monitoring well. At the end of the injection period, most of the injected supercritical CO_2 was within 200 ft of the injection well, with just a small finger reaching the observation well. The amount of dissolved CO_2 predicted to reach the monitoring well was small, and not likely high enough to be measureable. Measureable pressure changes of 500 psi were predicted to occur at the monitoring well. Pressures of up to 2800 psi are required in the injection well to inject supercritical CO_2 at a constant rate of 500 metric tons per day.

Model Calibration

After the CO_2 injection test, the model was calibrated to pressure observed in the injection well and monitoring well (Bacon et al., 2008). A step rate and pressure shut-in analysis was performed in the field as part of startup activities. Horner plot analysis of pressure decrease in the well appeared to indicate a complicated reservoir response with wellbore storage, skin effects, and dual porosity system with pseudo steady-state flow from the matrix to fractures (Sminchak et al., 2009). The formation permeability was estimated to be approximately 50 mD, 2.27 times greater than the average core permeability. The permeabilities used in the model were therefore scaled by a factor of 2.27x (Figure 21). The simulation considered an injection period of 17.9 days, followed by an equilibration period, for a total simulation time of 75 days. Numerical

dispersion was minimized by constraining the time steps to maintain the Courant condition (Press et al., 1992),

$$\Delta t \leq \frac{\Delta x}{v} \qquad (1)$$

where Δt is the simulation time step, Δx is the grid spacing, and v is the fluid velocity.
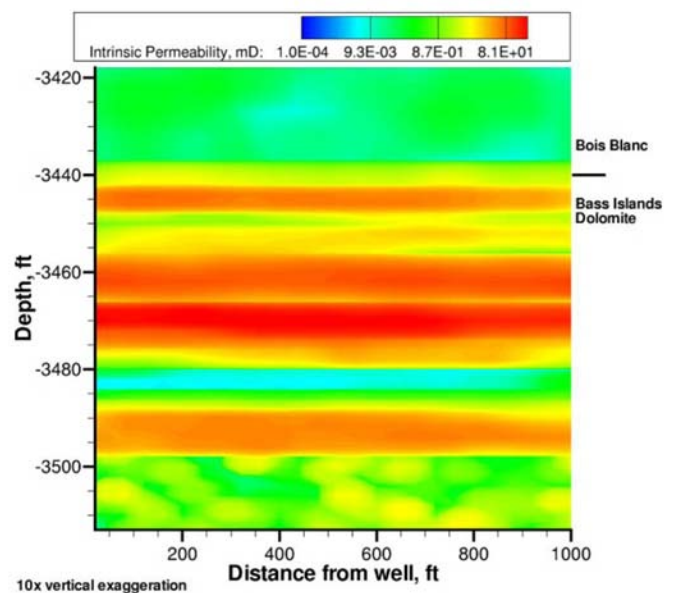
Figure 21: Geostatistical Realization of Permeability Based on Core Samples from the Bass Islands Dolomite and Lower Bois Blanc Formations, then Upscaled by a Factor of 2.27 to Match Average Permeability Predicted by Hydraulic Tests

Simulations were executed on a 2-D radial Cartesian grid. The grid covered a vertical depth (in the Z-direction) of 512 ft, between the depths of 3,002 to 3,514 ft. The grid assumed horizontal radial symmetry around the well out to a distance of 1 mile. The grid had a resolution of 132 grid nodes in the horizontal X-direction and 124 nodes in the vertical Z-direction. Vertical grid spacing was 2 ft in the Bass Islands Dolomite and 5 ft in the Bois Blanc and Amherstburg. Horizontal grid spacing was 40 ft.

A downward pressure gradient of 0.45 psi/ft was used to initialize the brine pressure field. The pressure gradient was additionally assigned to vertical boundary surfaces located opposite from the vertical injection well. This assumption allows reservoir brine to be pushed outside of the computation domain as CO_2 is injected. An initial temperature gradient of 0.01 degrees/ft was assumed, with an initial formation temperature of 89.51 °F at a depth of 3,514 ft. A brine density of 1,159 kg/m^3 was assumed.

The observed CO_2 injection rate and well-bottom temperature were applied as a well model in STOMP-WCSE, using the same screened interval (72 ft) and wellbore diameter (8 5/8 inches) as the State Carlton #4-30 well (Figure 22). The modeled injected supercritical CO_2 has a maximum radius of 440 ft after 17.9 days of injection, and 480 ft one year after the start of injection, which does not quite reach the observation well (Figure 23). This was consistent with a lack of CO_2 gas observed in the observation well during the test.

Figure 23: Modeled Supercritical CO_2 Saturation at 17.9 Days

The injected CO_2 was 18 to 29 degrees cooler than the formation brine, but lowered temperatures extend less than 165 ft from the injection well (Figure 24). This prediction was also consistent with a lack of temperature change in the observation well. Pressure changes were transmitted from the injection well to

Figure 22: Observed CO_2 Injection Rate and Well-Bottom Temperature, Applied as Source Term in Model
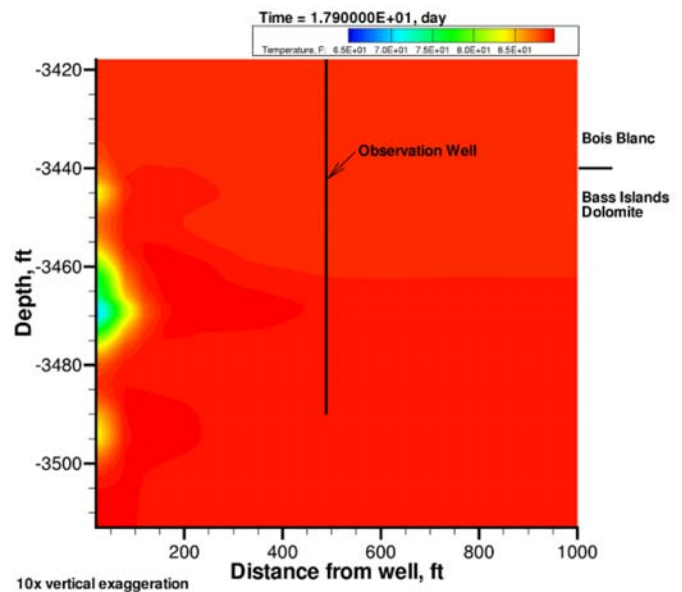
Figure 24: Modeled Temperatures at 17.9 Days

the observation well (Figure 25), and the pressure changes in the observation well are bracketed by predicted pressure changes at the top and bottom of the observation well (Figure 26). Modeled pressure responses at the injection and observation well are reasonably close to observed values, although the model somewhat over predicts injection well pressures at the higher injection rates. The model is sensitive to the permeabilities assumed in the Bass Islands dolomite, but using values consistent with hydraulic tests (scaled by 2.27x) gives the best results (Figure 27).
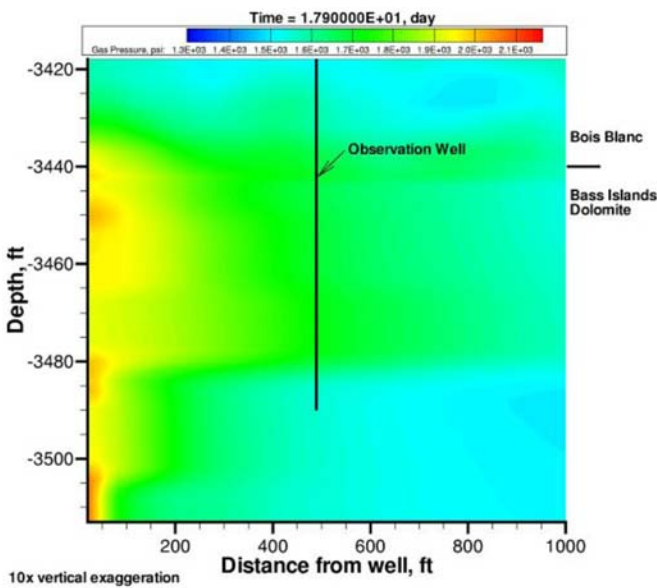
Figure 25: Modeled Pressures at 17.9 Days
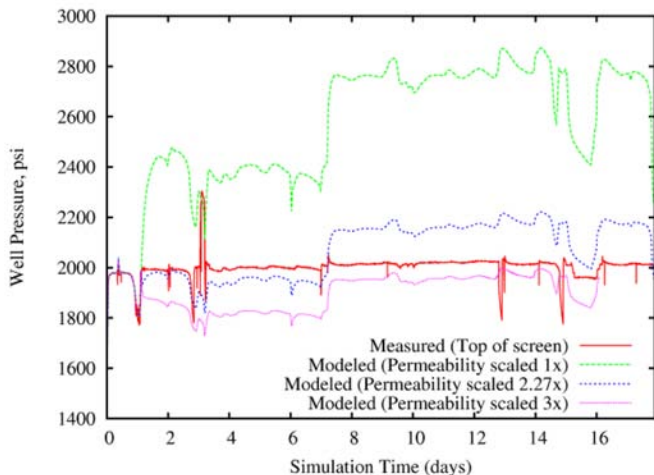
Figure 26: Comparison of Measured and Modeled Pressures at the Injection and Observation Wells
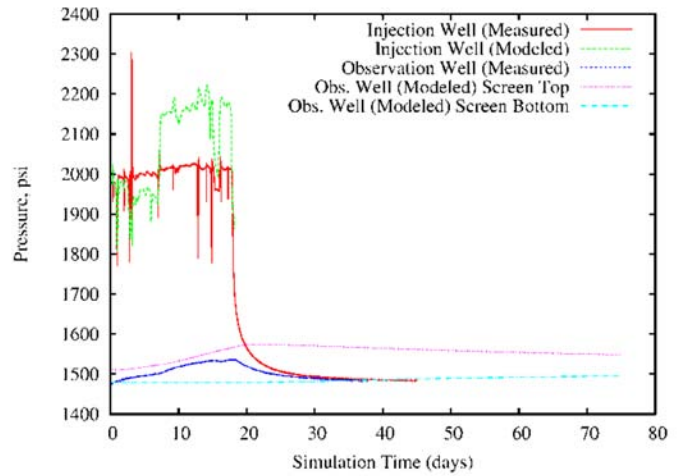
Figure 27: Sensitivity of Injection Well Pressure Response to Intrinsic Permeability

Post-Injection Model Validation

As described, the model was primarily calibrated to transient pressure and temperature readings measured in the injection well and monitoring well. However, several other monitoring techniques were applied at the Michigan Basin test site, including geophysical logging, microseismic monitoring, geochemical brine analysis, and cross-well seismic imaging (Gerst et al., 2008). Together, these monitoring methods provided a better depiction of the CO_2 distribution in the subsurface. In addition, approximately one year after the initial 10,000 metric ton injection test, an additional 50,000 metric tons of CO_2 were injected at the test site over a period of six months.

Consequently, the model was validated with the additional monitoring and injection information. This validation process is not discussed in this section, but the work required additional modifications to the model to match observed CO_2 distribution. In general, the complete suite of monitoring technologies from the Michigan site suggested that the CO_2 moved further upward in the storage zone than the model suggested. Therefore, it was necessary to adjust some of the hydraulic parameters in the CO_2 storage zone such as vertical permeability.

Overall, the MRCSP Phase II Michigan Basin test highlights the model development process for a previously uncharacterized deep saline formation. The storage formation was a carbonate rock, which presented complex reservoir conditions. As more information about the deep rock formation was obtained, the model was updated to determine a more accurate solution. In fact, significant changes were made to the base conceptual model as additional injection was completed and more meaningful monitoring results became available. The test also demonstrates the utility of reservoir simulations in integrating information on site characterization, injection operations, and monitoring to better understand a CO_2 storage reservoir.

References

Bacon, D, J. R. Sminchak, J. L. Gerst, and N. Gupta, 2008, Validation of CO_2 injection simulations with monitoring well data: Proceedings of GHGT-9, 9th International Conference on Greenhouse Gas Control Technologies, Pergamon Press, Washington, D.C., USA.

Gerst, J., P. Jagucki, J. Sminchak, and M. Bhargarva, 2008, Preliminary monitoring, mitigation, and verification results for the MRCSP Michigan field site: Seventh Annual Conference on Carbon Capture & Sequestration, Pittsburgh, PA, May 5-8, 2008.

Harrison, W.B., Grammar, G.M., and Barnes, D.A. , 2008, Reservoir characteristics of the Bass Islands Dolomite in Otsego County, Michigan: Results for a saline reservoir CO_2 sequestration test: Environmental Geosciences, v. 16, no. 3, p. 139-152.

Pruess, K., J. García, T. Kovscek, C. Oldenburg, J. Rutqvist, C. Steefel, and T. Xu, 2002, Intercomparison of numerical simulation codes for geologic disposal of CO_2, Berkeley, California, Lawrence Berkeley National Laboratory, p. 86.

Sminchak, J., J. Gerst, J. Herpst, and D. Bacon., 2008, An analysis of the relationship between CO_2 injectivity and hydraulic test data: Proceedings of the Seventh Annual Conference on Carbon Capture and Sequestration, Pittsburgh, PA.

Sminchak, J.R., Gupta, N., and Gerst, J., 2009, Well test results and reservoir performance for a carbon dioxide injection test in the Bass Islands Dolomite in the Michigan Basin: Environmental Geosciences, v. 16, no. 3, p. 153-162.

White MD and M Oostrom, 2006, STOMP: Subsurface Transport Over Multiple Phases, Version 4.0, User's Guide. PNNL-14286, Pacific Northwest National Laboratory, Richland, Washington.

Plain CO$_2$ Reduction Partnership

Northwest McGregor CO$_2$ Huff 'n' Puff Enhanced Oil Recovery Phase II Pilot Case Study

Charles D. Gorecki
Energy & Environmental Research Center
University of North Dakota

A carbon dioxide (CO$_2$) huff 'n' puff (HnP) enhanced oil recovery (EOR) project was conducted in the Northwest McGregor oil field of Williams County, North Dakota (Figure 28) as one of the Plains CO$_2$ Reduction Partnership (PCOR) Phase II pilot test projects. The test involved the injection of 440 tons of CO$_2$ over 2 days and subsequent production from the E. Goetz #1 well following a two-week soak period. The target of this EOR operation was the Mississippian Madison Formation, a fractured carbonate reservoir, and was arranged for the purpose of simultaneous EOR and CO$_2$ storage.

The HnP exercise conducted at Northwest McGregor represents one of the deepest operations of this type of EOR at 2454 m (over 8000 ft deep). The pressure (20.7 MPa, 3127 psi) and temperature (82 °C, 216 °F) are also among the highest worldwide for this type of operation. The reservoir is also unique because of the carbonate lithology with low matrix permeability and an extensive network of microfractures; whereas a majority of HnP projects have been conducted in clastic reservoirs.

Figure 28: Map of Northwestern North Dakota Depicting the Northwest McGregor Field (inset) and the Location of the E. Goetz Well (second inset) and the Monitoring Well Gudvangen #1

Assembly of Geologic Model

A geologic model consists of a complex combination of spatial data, rock properties, and interpretation formed for the purpose of visualizing and simulating subsurface situations. The approach taken for modeling a particular reservoir can vary greatly based on available information and often involves a complicated orchestration of well logs, core analysis, seismic surveys, literature, depositional analogs, and statistics. Schlumberger's Petrel geologic modeling software package was used by the Energy & Environmental Research Center (EERC) to produce the current Northwest McGregor geologic model, which was later utilized in numerical simulation of CO$_2$ movement in the reservoir, performed with Computer Modeling Group (CMG) GEM software. The geologic modeling and numerical simulations were performed for the evaluation of CO$_2$ movement within the reservoir, the estimation of the impact produced by the moving CO$_2$, the identification of trapping mechanisms, and the estimation of incremental oil recovery. Testing the effectiveness of cutting-edge monitoring techniques and the role of fractures in CO$_2$ migration were also studied.

Site Characterization

Site characterization activities included gathering and verifying formation tops from each well within a 100-mile study area. Well logs and existing core from all wells in the greater study area were examined for petrophysical properties (Table 5). Logs were normalized to account for tool and sensitivity advancements over 60 years of field operation. Literature including information on depositional environment, facies interpretation, and geological history was also collected.

All available well logs for the greater study area were digitized and examined. Petrophysical properties and lithology were determined from well logs, including mineral solver analysis using Senergy's Interactive

Table 5: Reservoir Properties

Property	Value
Matrix Porosity	15%
Matrix Permeability	0.35 mD
Fracture Porosity	>1%
Fracture Permeability	5-30 mD
Reservoir Temperature	82 °C
Reservoir Pressure	20.7 MPa
Pay Thickness	14 ft
Oil Gravity	41.7 API
Cumulative Oil Production	53,667 bbl
Cumulative Gas Production	574 mcf
Cumulative Water Production	381,830 bbl

Petrophysics software (Figure 29). Neural network algorithms were employed to produce complex rock properties, such as vertical permeability to gas, irreducible fluid saturations, and fracture intensity, as well as produce synthetic curves for missing zones or logs within the study area. Results of petrophysical properties were verified with laboratory analysis including QEMSCAN, x-ray diffraction (XRD), petrographic analysis, and core descriptions.

Additional well logs were run on the study well (E. Goetz #1) including a baseline reservoir saturation tool (RST) log and cement bond log, followed by two post injection RST runs. Pre-injection and post-injection vertical seismic profile (VSP) surveys were also performed. No major faults were present in the study area or observed on processed seismic data, and no evidence of faulting was uncovered in literature or well logs. The gathered data were used to generate a large-scale

Figure 29: A multimineral petrophysical analysis (MMPA) was completed after well log normalization and synthetic curve creation for missing curves using neural networks.
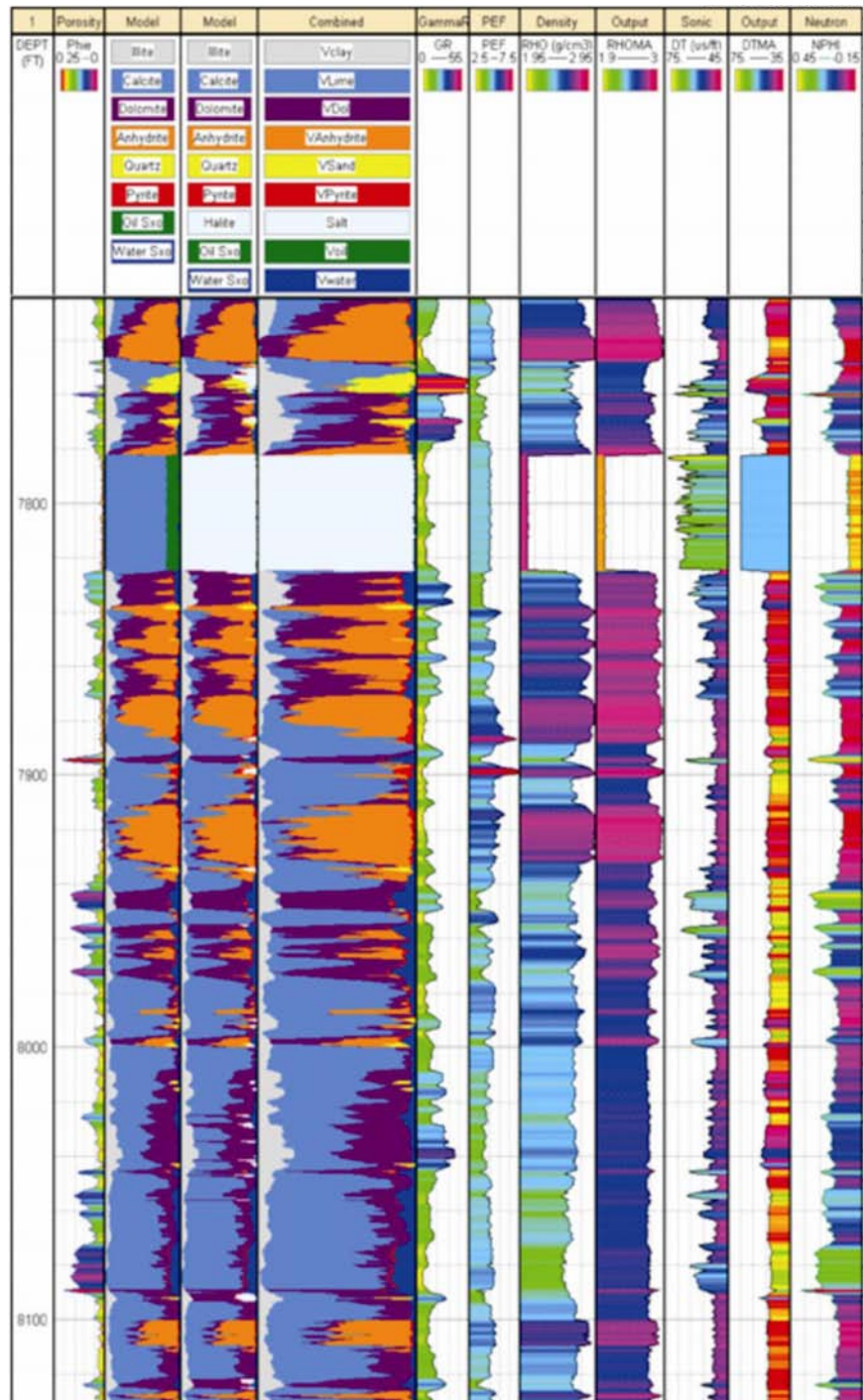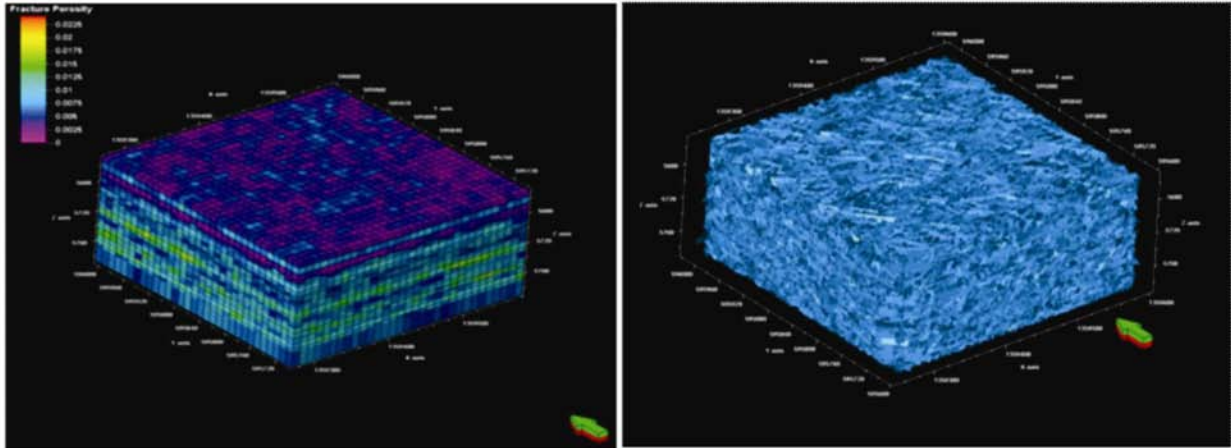
Figure 30: Model Showing the Fracture Intensity Property Used to Create the Discrete Fracture Network (left) and the Visualized DFN (right)

reconnaissance facies model. This type of model can be useful in defining structural and statistical trends as well as providing a framework for smaller, site-specific models suitable for simulation.

Fracture Modeling

Natural fractures were modeled using discrete fracture network (DFN) modeling processes and supported by fracture occurrence and orientation angle present in core samples. The presence of both fractures and intergranular

porosity resulted in the need to create a dual porosity–permeability model (Figure 30).

Grid Refinement

The larger-scale reconnaissance model produced for site characterization required refinement before it could be suitable for dynamic simulation. A smaller, downscaled injection model was produced using multiple-point statistics guided by seismic data generated from the baseline VSP (Figure 31).

Figure 31: Model images showing water saturation, irreducible water saturation, and residual oil. These properties were populated using VSP as a covariable for sequential Gaussian simulation. The smaller upscaled injection model is shown in the center of the larger geostatistical grid.
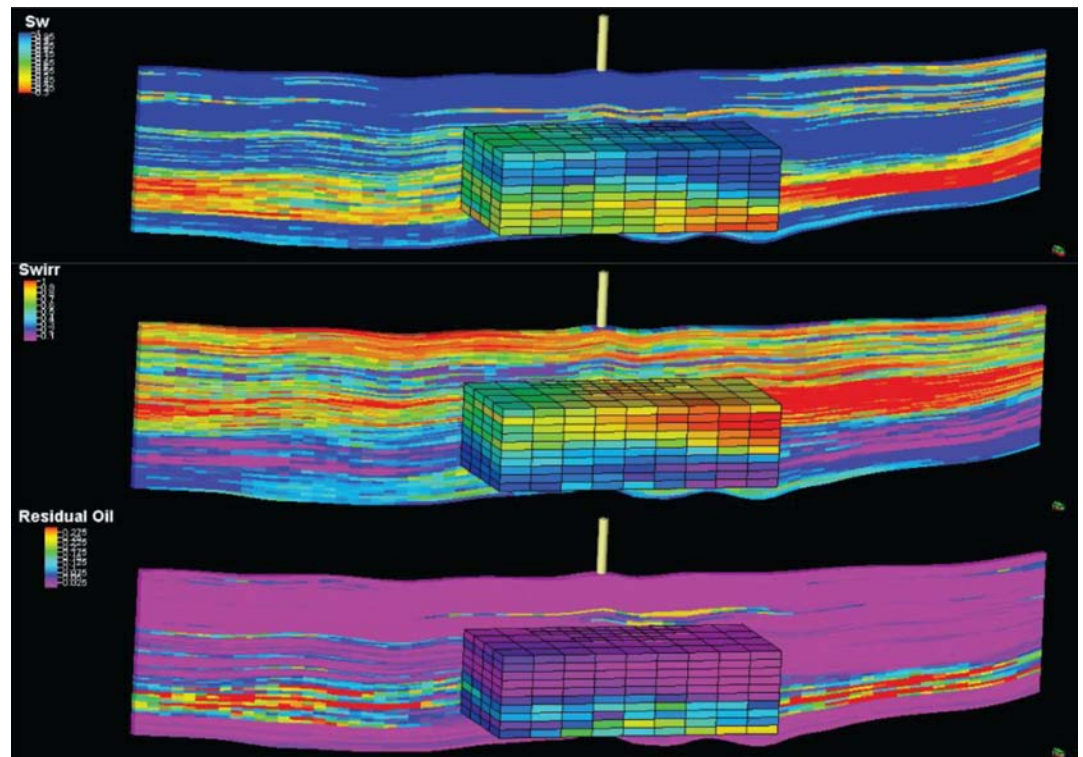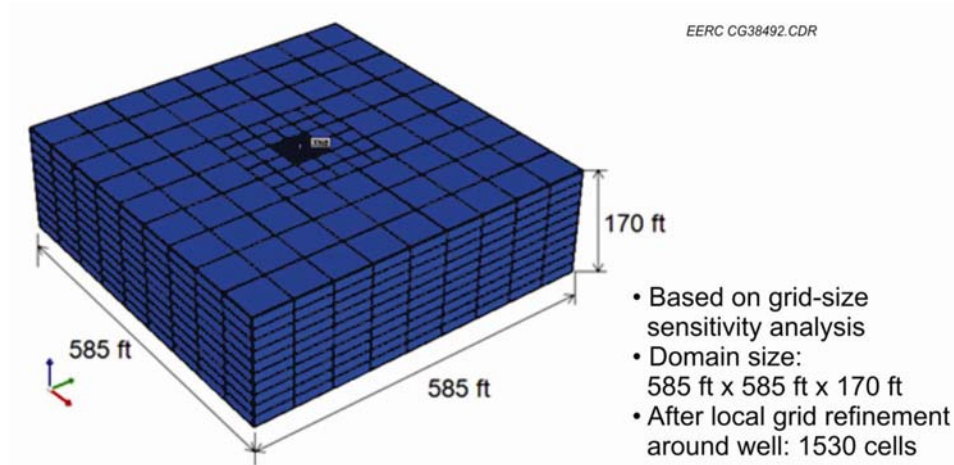
Figure 32: Image of the Simulation Domain with Fine Gridding; This Model Contains 1,530 Cells

The injection model was constructed with dimensions of 585 ft × 585 ft × 170 ft, simulating a depth from 7930 to 8100 feet (Figure 32). The model size was selected based on its ability to account for all of the injected CO_2 as well as illustrate the area directly influenced by production. Gridding was conducted following sensitivity analysis to identify optimal grid size, and local grid refinement was emplaced near the wellbore (Table 6). The grid was populated with dual porosity–permeability properties based on the Multiple Interacting Continua (MINC) method and discrete fracture network modeling.

Table 6: Model Settings

Settings	Values/Options
Gridding	Coarse: 810 cells
	Medium: 1,130 cells
	Fine: 1,530 cells
	Extremely fine: 2,090 cells

Properties were distributed throughout the model by upscaling using arithmetic mean methods, with the exception of vertical permeability, which utilized a harmonic mean. Initial reservoir conditions were also input, including pressure and temperature. Fluid saturations were distributed using the sequential Gaussian simulation algorithm. Boundaries were assigned with limited extents and zero leakage.

Dynamic Model Construction

The model was centered on the injection well, which was the only well within the simulation grid. An injection rate of 5,930 Mscf/day for 1.272 days was chosen to reflect the expected injectivity of the formation. The equation-of-state was built using CMG's Winprop software, and then imported into CMG's GEM software package for flow simulation. Geothermal and geomechanical phenomenon are integrated into the GEM code, and results from GEM can be coupled with CMG's CMOST for sensitivity analysis, history-matching, optimization, and uncertainty analysis. Time steps are automatically chosen to limit convergence errors within the simulation and increased from approximately 1 minute at the beginning of injection to around 7.3 days at the end of simulation, 6 months after the start of injection.

The boundary conditions and simulation criteria were calibrated with field observation and historic production and pressure data. Predictions were verified with field monitoring techniques (RST logs and VSP), pressure measurements, and production data. Many of the properties and parameters were adjusted from the initial values through the sensitivity analysis and history matching activities.

Summary

Site characterization and modeling activities were conducted on both a large fine-scale grid and then upscaled to a smaller grid for simulation. The model incorporated dual porosity–permeability properties to

represent the influence of the matrix and the fractures on EOR operation. Laboratory studies on core samples and petrophysical analysis were used to populate the remaining model properties, resulting, in part, in the generation of a discrete fracture network model. Finally, the simulation model was defined and grid refinement performed near the wellbore based on test simulations and history matching.

Dynamic Simulation and Analysis

Numerical simulations were performed using the previously mentioned grid. A history-matching exercise was performed, first using homogeneous models to reduce the ranges of each of the properties with a high level of uncertainty. History matching activities were then carried out on heterogeneous models using more refined ranges for each property and parameter until an acceptable match was achieved. Once the model validation was completed, predictions on future oil recovery and CO$_2$ movement were performed. The goal of simulations for the site was to examine the behavior of CO$_2$ in the unique scenario of this deep HnP, including the injectivity and trapping mechanics. The effectiveness of the EOR method and utility of VSP and RST monitoring techniques were also a task of the model and simulations.

Sensitivity Analysis

Sensitivity analysis was performed to determine the most influential variables for a given simulation by varying one variable over a realistic range while setting the remaining values to a constant and examining the net effect on the results. Once sensitivity analysis is completed for each variable in the simulation model, they are compared and analyzed to determine the most influential parameters. A total of 46 variables were tracked in the Northwest McGregor simulations, of which 33 had a significant effect on model output over a ±0.2% cutoff (Figure 33).
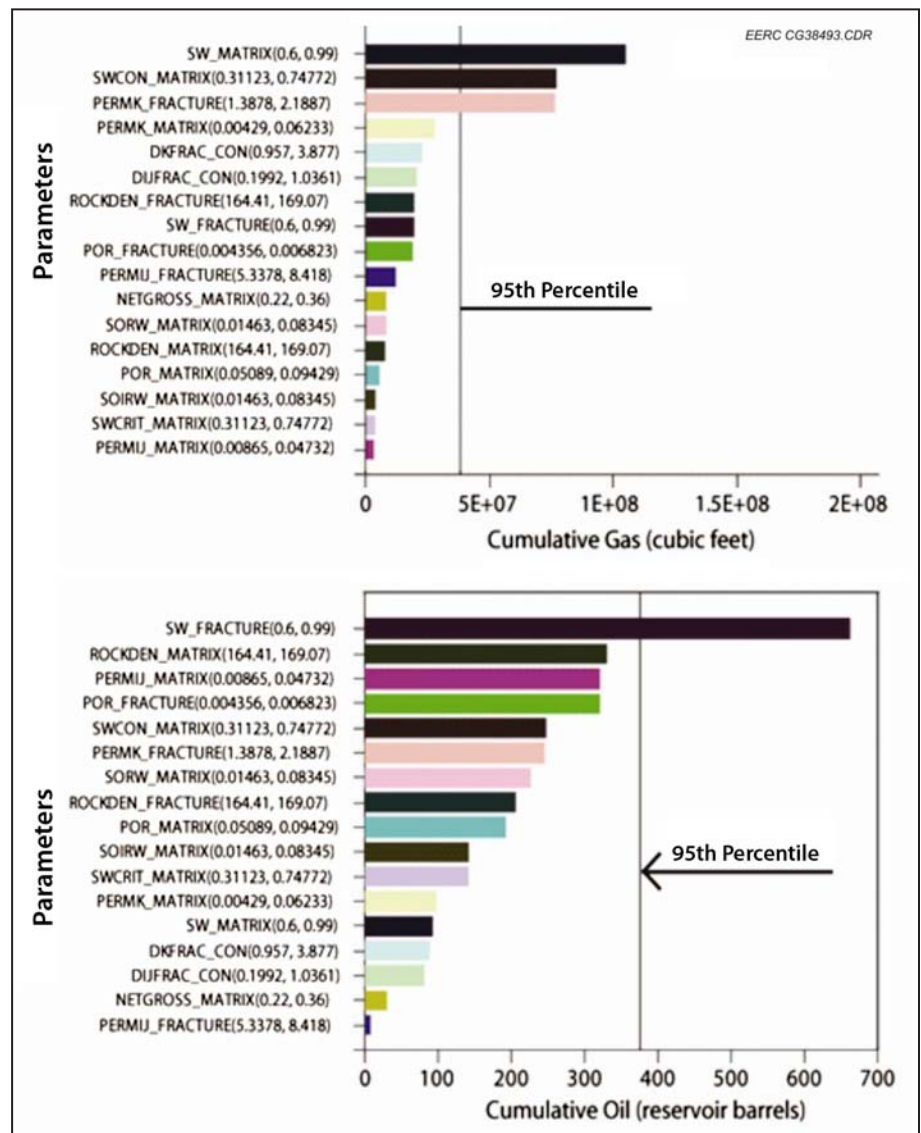
Figure 33: Tornado Chart Depicting the Influence of Selected Variables on the Simulation Output

Pre-injection Simulations

Pre-injection simulations were performed to aid in the estimation of injectivity, update original oil in place (OOIP), and estimate the impact of CO$_2$ EOR. The results of pre-injection simulation were used to delineate the area of review and aid in the selection of monitoring techniques. These simulations were also used to optimize future simulations. Injection and post injection phases focused on the movement of CO$_2$ within the reservoir and the changes that occur to the subsurface. The goal of these phases was not only to track and observe the plume, but to predict the future movement with regard to incremental oil production and the fate of the injected CO$_2$ within the reservoir (Figure 34). The additional data produced during actual injection were used in history matching, and no changes or updates were deemed necessary to the model.

Simulation Conditions

CMG's GEM software package was used for numerical simulations. Simulation parameters are listed at the conclusion of this section. Following history-matching and sensitivity analysis, the movements of CO$_2$, oil, water, and gas within the reservoir were assessed, as well as the saturations present within the matrix or fractures. It is expected that much of the remaining oil in place occupies the matrix, rather than the fractures, which were responsible for much of the primary and secondary production.

Figure 34: Simulation results showing the CO$_2$ saturation (left) and oil volume (right) within the injection model at baseline conditions (T1), at the end of injection (T2), and approximately 6 months after injection (T3).
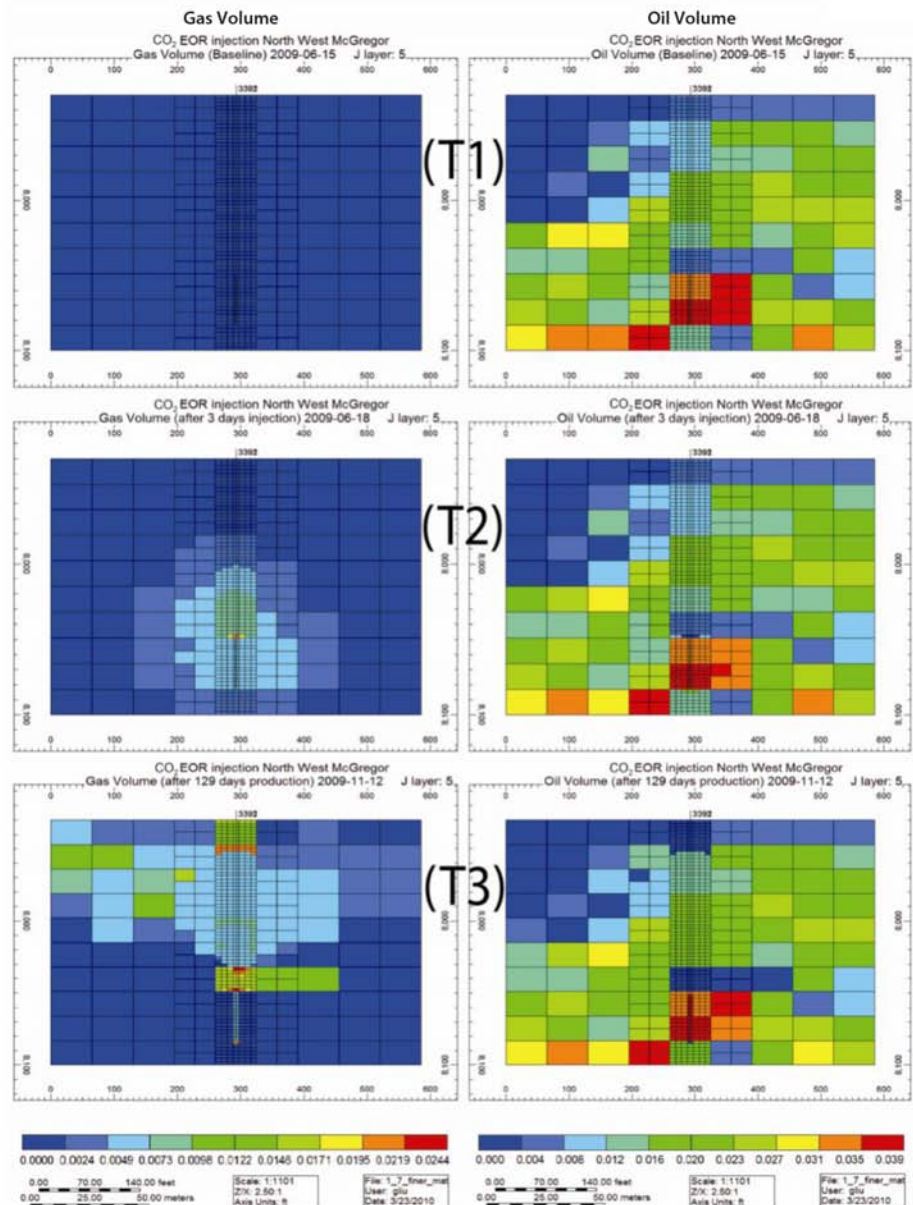
Results of Simulations

The simulation results show that injected CO$_2$ remained in the target reservoir and although it occupied portions of both the matrix and the fracture pore space, a majority of the CO$_2$ remained in the fractures and did not penetrate into the matrix blocks. It is expected that 31% of the CO$_2$ will be produced back, leaving 69% stored within the reservoir from this injection. This observation would not have been predicted without the use of a dual porosity–permeability model. The workflow and simulation were optimized, reducing run time and number of jobs by using a combination of numerical tuning, sensitivity analysis, and homogeneous model testing, all assisted by CMG's CMOST. Model and simulation results were validated by observed responses from the monitoring activities. Results from the model appear to agree with RST logs; however, it is still undetermined as to whether or not the injected CO$_2$ could be observed by the VSP.

Geochemical Modeling

In addition to the geologic and dynamic modeling, a geochemical modeling exercise was performed. The goal of the geochemical modeling was to evaluate the short-term risks for operations (e.g., porosity and permeability decrease) and long-term implications for CO$_2$ storage via mineralization. The formation mineralogy, mineral composition, and spatial variations at the Northwest McGregor site were determined using well logs and traditional core sample analysis with XRD, x-ray fluorescence (XRF), and QEMSCAN techniques. In addition, integrative mineralogical analysis was performed utilizing linear program normative analysis (LpNORM) for more accurate estimation of mineral phases. The results of these analyses determined the mineral phases selected for the initial model inputs, including anhydrite, calcite, dolomite, illite, quartz, and traces of pyrite.

Data Collection

A pressurized bottom-hole fluid sample was also collected, and the ionic, organic, and gas compositions of the sample was determined (Table 7, Figures 35 and 36). The results of this fluid sample were also used as input parameters for the numerical modeling exercises. In addition, the reservoir fluid-sampling program from the E.L. Gudvangen #1 observation well was organized in order to monitor the reservoir mineralogy and fluid interactions with the injected CO$_2$. Collected field data parameters included conductivity, pH, temperature, total dissolved solids (TDS), salinity, gas concentrations, oil parameters, etc. The data from this observation well were utilized for history-matching purposes.

Table 7: Comparison of Pre- and Post-Injection Reservoir Fluid Collected Using Schlumberger's E-line from a Depth of 8,087 ft from the E. Goetz #1 Well and Analyzed with Oilphase-DBR Technology

	pH	Density, g/cm³	Resistivity at 77°F	Salinity	TDS, mg/kg
Before Injection	5.55 (at 106 °F) 4.50 (at 216 °F – live ph) 4.23 (modeled)	1200	4.02	283,855	273,353
After Injection	5.4 (at 106°F) 3.1 (modeled)	1208	4.17	282,925	276,477
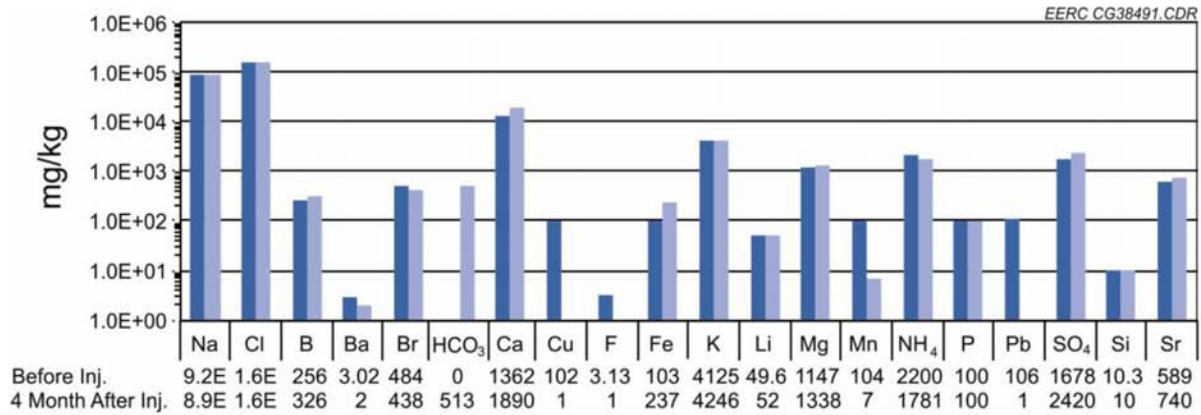
Figure 35: Extended comparison of pre- and post-injection reservoir fluid collected using Schlumberger's E-line from a depth of 8,087 ft at the E. Goetz #1 well and analyzed with Oilphase-DBR technology and adjusted with the geochemical modeling software.
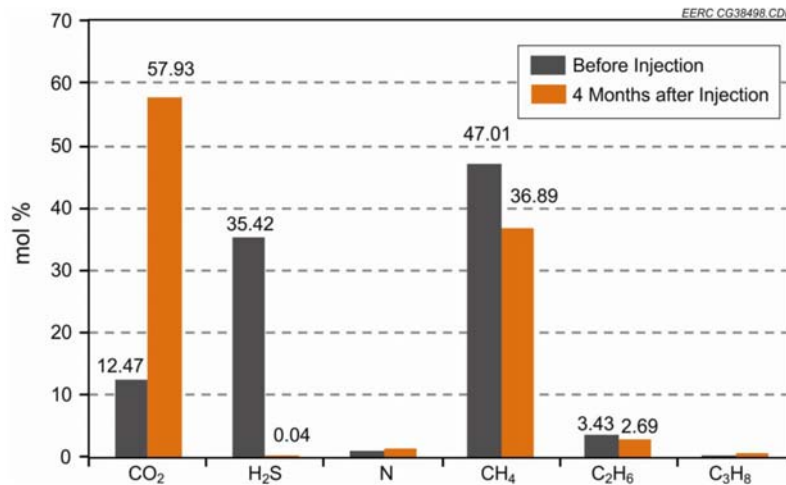
Figure 36: Comparison of pre- and post-injection reservoir gas compositions from zero-flash and subjected to chromatography from a depth of 8,087 ft at the E. Goetz #1 well.
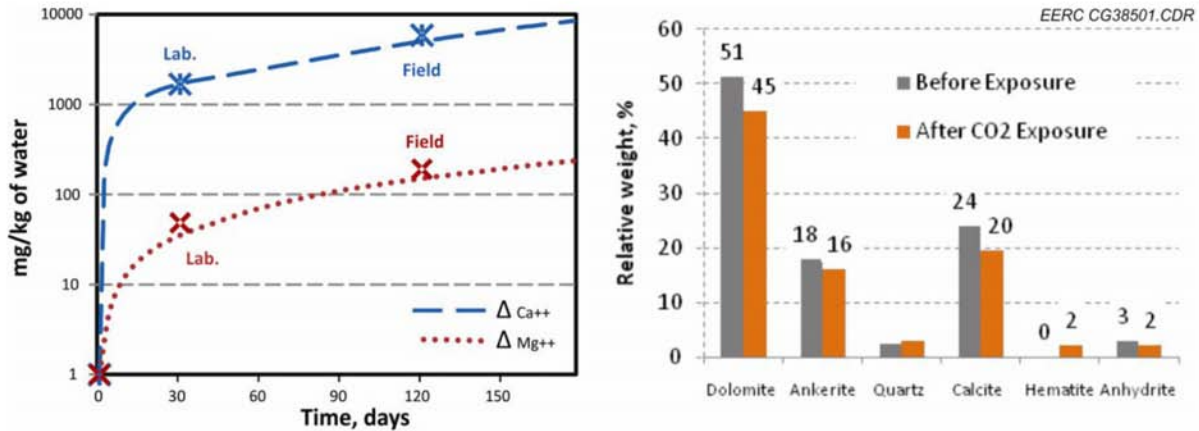
Figure 37: Mississippian Frobisher–Alida samples were saturated with synthetic NaCl brine and exposed to supercritical CO_2 at reservoir conditions. Changes in concentration of Ca^{2+} and Mg^{2+} are modeled and correlated with field and laboratory observations (left). Mineralogical changes are shown at right.

A series of laboratory experiments and numerical modeling of geochemical reactions was also conducted. Core samples collected from the target horizon, the Frobisher–Alida interval of the Madison Formation, were exposed for a period of 4 weeks to pure supercritical CO$_2$ at 2250 psi (155 bar) and 158 °F (70 °C) in 10 wt% NaCl synthetic brine conditions. Observations made during the laboratory experiments were in good correlation with field observations and illustrated the dissolution of the carbonate rocks. In addition, insignificant hematite precipitation due to iron mobilization was observed (Figure 37).

Simulation Conditions

Modeling was performed using PHREEQC and Geochemist Workbench software in order to determine the most favorable geochemical interactions and evaluate in situ fluid properties, etc. The CMG GEM simulator was utilized for the creation of a 2-D cross-sectional reservoir model for reactive transport evaluation (Figure 38). It was determined that the already acidic and highly saline environment of the Northwest McGregor oil field should not experience any significant changes in mineralogy, especially with the short-term, low-volume injection scenario. The dissolution of carbonate minerals, specifically calcite, was predicted by modeling and later was supported by field observations and laboratory experimentation. Also, according to the analysis of laboratory experiments, the possibility of iron mobilization and later re-precipitation of hematite and magnetite exists.

Results of Geochemical Simulations

The integrated investigation of field and laboratory data and numerical modeling exercises revealed that no significant changes in reservoir geochemistry have occurred. The slight porosity increase might have contributed to the improved oil production from the E. Goetz #1 well. Laboratory studies and numerical modeling suggest that the mineralogical storage factor will be minimal for the Northwest McGregor oil field EOR case. The factors that contribute to the minimal response of the reservoir to the stimulation could be accounted for by the high-concentration of dissolved solids in the formation fluid and low pH environment of the oil field.

Summary

The primary goals of this PCOR Partnership pilot project included determining the short- and long-term fate of a small volume of injected CO$_2$ (440 tons) and determining if a CO$_2$ HnP in this type of reservoir could be effective. The static and dynamic reservoir modeling proved to be an essential tool for decision-making purposes during the operations, conceptual understanding of the developed reservoir system, and excellent utility for monitoring, verification, and accounting activities.

In order to determine the fate of the injected CO$_2$ and the potential incremental oil production, time-lapse RST and VSP were used along with detailed static and numerical modeling. The VSP was an excellent tool for acquiring modeling parameters such as property
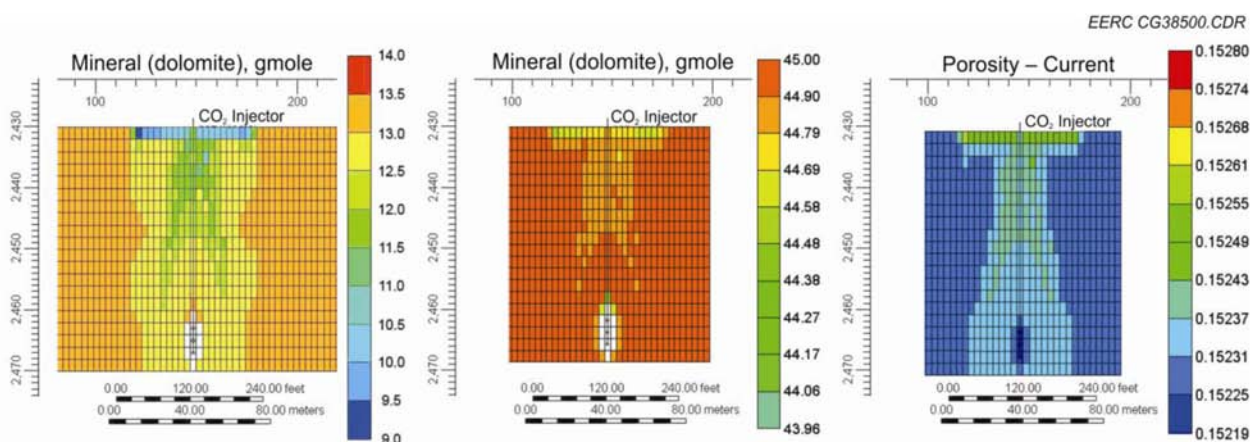
Figure 38: Spatial 2-D distribution of the calcite and dolomite dissolution and insignificant porosity increase modeled 10 years after the injection.

semivariograms, near-wellbore horizons, vertical deviations, and production of covariables for petrophysical simulation. However, because of the highly fractured nature of the reservoir and the extremely low pore volume of the fractures, which contained most of the CO$_2$, the repeat surveys were unable to accurately detect the location of the CO$_2$. The baseline and repeat RST logs were found to be an excellent tool for determining the vertical extent of the injected CO$_2$ near the wellbore, and the modeling and history-matching activities give good support for the overall extent of the injected CO$_2$ and will lead to better predictions of future incremental oil recovery. The geochemical modeling in conjunction with laboratory experiments and field observations provided better insight on the processes that occur in the reservoir after CO$_2$ injection. The additional clues for the CO$_2$ movement, reservoir performance, and trapping mechanisms found with the geochemical modeling need further integration with full-scale reservoir modeling.

Simulation Parameters

Settings		Values/Options
Grids		Coarse: 810 cells
		Medium: 1130 cells
		Fine: 1530 cells
		Extremely fine: 2090 cells
Depth		7930–8100 ft
Components		Three
Temperature		220°F
Equation of State		Peng-Robinson 1978
Aqueous Density Correlation		Rowe-Chou
Aqueous Viscosity Correlation		Kestin
Rock Compressibility, fracture		5.5E-05 1/psi
Rock Compressibility, matrix		5.6E-06 1/psi
Rock Compressibility, reference pressure		3550.0 psi
Rock Compressibility, reference temperature		77°F
Method for Matrix and Fracture Communications		MINC with Gilman and Kazemi formulation for the shape factor
Boundary Conditions		Carter-Tracy (limited extent) without leakage
Simulation Period		06/15/2009–12/15/2009
Well Radius		0.25 ft
Well Skin		0.1
Well 3392: CO$_2$ Injection Maximum Pressure		5207.11 psi
Well 3392: CO$_2$ Injection	Start from 2009/06/15	440 tons injected in the first 1.27 days
	End by 2009/06/16	
Well 3391: Production Minimum Pressure		2800 psi
Well 3391: Production	Start from 2009/07/06	Variable
	End by 2009/12/15	

Southeast Regional Carbon Sequestration Partnership

Numerical Modeling Activities at SECARB's Phase II and Phase III Field Projects

Kimberly Sams
Southern States Energy Board

Numerical modeling activities conducted at the Southeast Regional Carbon Sequestration Partnership's (SECARB) Phase II and Phase III field projects at the Cranfield, Mississippi oil and gas field were performed using CMG-GEM, a commercial compositional flow simulator. A large-scale CO_2 injection has been conducted at this site since July 2008. The subset of actual site operations of interest to SECARB consists of: (1) an early phase, object of this write-up, in which CO_2 is injected into the oil-bearing reservoir (Phase II); and (2) a second phase, started on April 1, 2009, in which CO_2 is injected at a high rate (10^6 ton/year) in the saline aquifer down dip of the reservoir and neighboring wells (Phase III). The oil field with a large gas cap and strong water drive was discovered in 1943 and was abandoned in 1965. After a shut-in of forty years, reservoir pressure prior to CO_2 injection had recovered to near original pressure levels. For this reason, the start of this EOR flood project provides an unique opportunity to monitor large-scale CO_2 injection into a reservoir without immediately preceding pressure perturbations typical of EOR. The objectives of the Phase II modeling were: (1) to gain insights on how to approach CO_2 injection modeling at the site and to transfer this knowledge to the Phase III modeling at Cranfield and other SECARB field projects; (2) to match pressure response to injection at several wells, including a dedicated observation well; and (3) to validate the importance of monitoring and prediction of reservoir pressure in a CO_2 storage project.

The reservoir is a near circular four-way anticline with a diameter of four miles and is hosted in the Cretaceous lower Tuscaloosa Formation at depths greater than 10,000 ft below the surface. The structure is created by a deep-seated salt dome. The reservoir dip averages 2° in an approximate radial fashion towards the apex of the anticline structure. A NW-SE trending, sealing crestal graben margin fault divides the center and west side of the reservoir from the east side. The normally-pressured reservoir temperature is 125 °C, and the reservoir

pressure was 32 MPa before historical production begun. The injection unit consists of heterogeneous fluvial deposits ranging from gravels to fine sandstones with multiple discontinuous mudstone interbeds. The thickness of the reservoir is variable and up to 80 ft. Complex primary porosity distribution has been further complicated by diagenesis, including variable amounts of authigenic chlorite, calcite, and quartz cements, variable grain dissolution, and grain fracturing, creating a broad range of relationships between porosity and permeability.

The area modeled for the Phase II project covers only the northwest part of the field. The static model was prepared with the Petrel software suite and integrates 3-D seismic and historic and modern well log information. Not all new data incorporated into updates on the east side of the field are included in the Phase II model. The dimensions of the model are 20,000 ft × 14,000 ft × 300 ft for a total of 18,368 (= 41×28×16) cells. The reservoir proper consists of layers 4 to 15. The model is isothermal and does not include chemical reactions with minerals of the reservoir rock matrix or geomechanical effects. Porosity data were calculated from well logs, core plugs, and historic full core measurements. The permeability-porosity transform is derived from selected wells. Both porosity and permeability fields are upscaled within Petrel. Permeability of the model ranges from a few mD to over 1 D. Water/oil and liquid/gas relative permeability sets used in the model assume a Brooks-Corey formalism. The SECARB team's investigation determined that the oil composition has not varied since the historical production period (1945–1965). The model used a Peng-Robinson EOS. The PVT data of C_2 + oil components was that internally available within CMG whereas PVT data for CO_2 and CH_4 were independently tuned to reservoir conditions. Chemical analyses measured formation water with a TDS >150,000 mg/L and a density of ~1.1. Boundary conditions are closed for the top, bottom, and

southern sides of the model, whereas that for the three other sides, where a good communication with the saline aquifer is evidenced by the strong water drive, are modeled by imaginary wells of variable rates.

Modeling was implemented in five stages:
  (1) initial equilibration stage in which the input parameters, such as pressure and saturations, are allowed to equilibrate to mimic undeveloped pristine steady state conditions through a long transient. This initial phase was iterated in order to obtain the proper oil/water and oil/gas contact elevations as well as the correct amount of oil and gas in place. At the onset of injection, the imaginary boundary wells were opened to maintain hydrostatic conditions at the boundaries;

  (2) oil production stage in which cumulative production from known historical production wells is allocated to historical wells (25 years);

  (3) gas production stage in which the gas-cap gas is blown down (10 years);

  (4) reservoir pressure recovery stage in which the reservoir pressure recovers from the gas blow down (as observed in the field). The recovery was modeled by injecting water to mimic a strong water drive (27 years); and

  (5) CO_2 injection stage– (initial 2 years).

Cranfield logs are poorly sensitive to fluid saturations, so the oil/water/gas saturation data needed to establish the model's initial conditions just prior to the CO_2 flood were not available. Therefore, the team decided to obtain such figures by including a generalized model of historical production into the modeling. Basic parameters such as original oil in place, production histories from the entire field, and original gas-oil and oil-water contact depths are known. By numerically producing hydrocarbon according to the production histories, the team obtained the assumed saturation distribution just prior to the CO_2 injection period. Although the early production histories (before 1954) for cumulative oil production and water cut show difference between field data and model results due to the lack of well by well production data, the cumulative oil production matches well at the end of the production (1964). These results suggest that the model simulates reasonably well the saturation distribution in the reservoir before CO_2 injection. To obtain this

relatively good match, the team needed to include both the produced gas reinjection program and the strong water drive.

Recent observations consisted mostly in continuous pressure measurements in a dedicated observation well that was centrally located relative to injection operations. The team also had periodic pressure measurements using pressure dip-in from four wells. The team conducted numerous repeat simulation runs to modify the boundary conditions, fluid properties, and reservoir properties to match observed fluid responses to production and to injection. A selective history match was designed, with tentative matching of the following features:
  (1) Correct amount of original oil and gas in place before production started

  (2) Approximate pressure history and water cut during historical period

  (3) Pressure build-up at selected wells during current EOR phase

  (4) Phase saturations at selected wells during current EOR phase

  (5) Water cut at selected wells during current EOR phase

  (6) CO_2 breakthrough time at selected wells during current EOR phase

In conclusion, a good understanding of subsurface heterogeneities and oil and gas composition of the reservoir was key to a good history matching. However, allocating the correct distribution of rock properties based on historic logs remained an area of uncertainty even as additional new data were obtained during characterization due to the complex interplay between the depositional environment and strong overprint of diagenesis. Parameters of utmost importance for a correct description of a flow field, in particular the relationship between porosity and permeability and the nature of permeability spatial variations, still remain uncertain. The uncertainty has been dealt with through sensitivity analyses. Ultimately, the constructed model shows a reasonable match with the data.

Southwest Regional Partnership on Carbon Sequestration

Evaluation of Trapping Mechanisms in Geologic CO_2 Sequestration: Case Study of SACROC Northern Platform, A 35-Year CO_2 Injection Site

Weon Shik Han
Energy and Geoscience Institute, University of Utah

Brian J. McPherson
Department of Civil and Environmental Engineering, University of Utah

Peter C. Lichtner
Los Alamos National Laboratory

Fred P. Wang
Texas Bureau of Economic Geology

CO_2 trapping mechanisms in geologic storage are the specific processes that hold CO_2 underground in porous formations after it is injected. The main trapping mechanisms of interest include (1) fundamental confinement of mobile CO_2 phase under low-permeability caprocks, or stratigraphic trapping, (2) conversion of CO_2 to mineral precipitates, or mineral trapping, (3) dissolution in *in situ* fluid, or solubility trapping, and (4) trapping by surface tension (capillary force) and, correspondingly, remaining in porous media as an immobile CO_2 phase, or residual CO_2 trapping. The purpose of this work is to evaluate and quantify the competing roles of these different trapping mechanisms, including the relative amounts of storage by each. For the sake of providing a realistic appraisal, we conducted our analyses on a case study site, the SACROC Unit in the Permian basin of western Texas. CO_2 has been injected in the subsurface at the SACROC Unit for more than 35 years for the purpose of enhanced oil recovery. Our analysis of the SACROC production and injection history data suggests that about 93 million metric tons of CO_2 were injected and about 38 million metric tons were produced from 1972 to 2005. As a result, a simple mass-balance suggests that the SACROC Unit has accumulated approximately 55 million metric tons of CO_2.

Our study specifically focuses on the northern platform area of the SACROC Unit where about 7 million metric tons of CO_2 is stored. In the model describing the SACROC northern platform, porosity distributions were defined from extensive analyses of both 3-D seismic surveys and calibrated well logging data from 368 locations. Permeability distributions were estimated from determined porosity fields using a rock-fabric classification approach. The developed 3-D geocellular model representing the SACROC northern platform consists of over 9.4 million elements that characterize detailed 3-D heterogeneous reservoir geology. To facilitate simulation using conventional personal computers, we upscaled the 9.4 million elements model using a "renormalization" technique to reduce it to 15,470 elements. Analysis of groundwater chemistry from both the oil production formations (Cisco and Canyon Groups) and the formation above the sealing caprock suggests that the Wolfcamp Shale Formation performs well as a caprock at the SACROC Unit. However, results of geochemical mixing models also suggest that a small amount of shallow groundwater may be contaminated by reservoir brine possibly due to: (1) downward recharge of recycled reservoir brine from brine pits at the surface, or (2) upward leakage of CO_2-saturated reservoir brine through the Wolfcamp Shale Formation.

Using the upscaled 3-D geocellular model with detailed fluid injection/production history data and a vast amount of field data, we developed two separate models to evaluate competing CO_2 trapping mechanisms at the SACROC northern platform. The first model simulated CO_2 trapping mechanisms in a reservoir saturated with brine only. The second model simulated CO_2 trapping mechanisms in a reservoir saturated with both brine and

oil. CO_2 trapping mechanisms in the brine-only model show distinctive stages accompanying injection and post-injection periods. In the 30-year injection period from 1972 to 2002, the amount of mobile CO_2 increased to 5.0 million metric tons without increasing immobile CO_2, and the mass of solubility-trapped CO_2 sharply rose to 1.7 million metric tons. After CO_2 injection ceased, the amount of mobile CO_2 dramatically decreased and the amount of immobile CO_2 increased. Relatively small amounts of mineral precipitation (less than 0.2 million metric tons of CO_2 equivalent) occurred after 200 years. In the brine-plus-oil model, dissolution of CO_2 in oil (oil-solubility trapping) and mobile CO_2 dominated during the entire simulation period. While supercritical-phase CO_2 is mobile near the injection wells due to the high CO_2 saturation, it behaves like residually trapped CO_2 because of the small density contrast between oil and CO_2. In summary, the brine-only model reflected dominance by residual CO_2 trapping over the long term, while CO_2 in the brine-plus-oil model was dominated by oil-solubility trapping.

Introduction

Over the past decade, the international scientific and engineering communities investigated the feasibility of long-term geologic storage of CO_2 in deep saline formations as a means of reducing atmospheric CO_2 levels (IEA, 2001; Gale, 2004; Orr, 2004; Thomas and Benson, 2005; Hollow, 2005; IPCC, 2005). Fundamental science questions considered and evaluated previously include:

(1) **The physico-chemical properties of CO_2, brine, and CO_2-brine for predicting multiphase transport and solubility trapping** (Bando and others, 2004; Portier and Rochelle, 2005; Spycher and others, 2003; Spycher and Pruess, 2005; Dubessy and others, 2005; Duan and Sun, 2003; Duan and others, 2006, 2008; Fuller and others, 2006; Hu and others, 2007; Fleury and Deschamps, 2008; McPherson and others, 2008).

(2) **Storage capacity estimation including appropriate storage site selection** (Bachu and Adams, 2003, NETL, 2005; Bradshaw and others, 2007; Bachu and others, 2007; Dilmore and others, 2008; Kopp and others, 2009; Litynski and others, 2008; Núñez-López and others, 2008).

(3) **Spatiotemporal trapping mechanisms including hydrodynamic, residual, solubility, and mineral trappings** (Ennis-King and Paterson, 2003, 2007; Doughty and Pruess, 2004; Hellevang and others, 2005; Knauss and others, 2005; White and others, 2005; van der Meer and van Wees, 2006; Zerai and others, 2006; Farajzadeh and others, 2007; Ide and others, 2007; Parry and others, 2007; Flett and others, 2007; Audigane and others, 2007; Suekane and others, 2008; Xu and others, 2004, 2005; Zhou and others, 2008; Qi and others, 2009; Zhang and others, 2009).

(4) **Caprock integrity** (Gaus and others, 2005; Chiquet and others, 2007; Gherardi and others, 2007; Plug and Bruining, 2007; Busch and others, 2008; Lu and others, 2009).

(5) **Monitoring and verification including plume migration and groundwater impact** (Klusman, 2003; Emberley and others, 2004; Lewicki and others, 2005; Winthaegen and others, 2005; Gasperikova and Hoversten, 2006; Saripalli and others, 2006; Wells and others, 2007; Newell and others, 2008).

(6) **Potential of CO_2 release from geologic storage sites** (Altevogt and Celia, 2004; Barlet-Gouêdard and others, 2006; Nordbotten and others, 2005; Oldenburg and Lewicki, 2006; Watson and Bachu, 2007; Pruess, 2005, 2008; Cortis and others, 2008).

While these studies have successfully addressed most aspects of these questions, effective prediction of spatiotemporal CO_2 trapping mechanisms (mobile CO_2, residual CO_2, dissolved CO_2, and mineral) is still a challenging problem because it is greatly affected by variability of subsurface conditions (pressure, temperature, and salinity), fluid properties (density, viscosity, solubility), and rock properties (porosity, permeability, and geochemical reactivity of minerals). Doughty and Pruess (2004) attempted to predict solubility trapping using a three-dimensional heterogeneous model of the fluvial/deltaic Frio Formation. They performed a numerical simulation to estimate CO_2 solubility trapping and storage capacity. Although their results showed strong interplay between geological heterogeneity and buoyancy-driven CO_2 flow, their model neglected both residual and mineral trapping. Kumar and others (2005) simulated the temporal variation of CO_2 trapping mechanisms in generalized three-dimensional, log-normally distributed permeability fields. They

concluded that the relative degree of residual CO_2 trapping could be significantly greater than both solubility and mineral trapping mechanisms. Since residual CO_2 trapping is regarded as a most-effective trapping mechanism during the short term (hundreds of years), several studies specifically focused on investigating various aspects (e.g., hysteresis, injection rate, water-alternating gas, and heterogeneity) to improve residual CO_2 trapping (Juanes and others, 2006; Ide and others, 2007; Flett and others, 2007; Doughty and others, 2007; Qi and others, 2009; Han and others, 2010a). Likewise, studies of mineral trapping include Xu and others (2004, 2005), Gaus and others (2005), White and others (2005), Zerai and others (2006), Audigane and others (2007), and Zhang and others (2009). Several different simulators were used in these studies, including TOUGHREACT, EQ3/6, CMG's GEM-GHG, ChemTOUGH2, PHREEQC, and Geochemist's Workbench (Wolery and Daveler, 1992; White, 1995; Bethke, 1996; Parkhurst and Appelo, 1999; Nghiem and others, 2004; Xu and others, 2006).

Despite the great deal of research on CO_2 trapping mechanisms, previous attempts to predict CO_2 trapping mechanisms appear to be hampered by several limitations:

(1) Most previous models did not explicitly couple all CO_2 trapping mechanisms simultaneously. Rather, model simulations were focused on predicting one or two specific mechanisms.

(2) Most previous models simplified their dimensions into either one or two, and neglected effects of heterogeneity.

(3) Although some of the models used a three-dimensional grid, either spatial heterogeneity or the CO_2 injection data measured from the field were disregarded or not available.

A primary purpose of this research was to provide a detailed analysis of spatiotemporal CO_2 trapping mechanisms. We focused our analysis on a case study of the Scurry Area Canyon Reef Operations Committee (SACROC) Unit, a site with an abundance of actual CO_2 injection and production data; over 93 million metric tons of CO_2 were injected for the purpose of enhanced oil recovery since 1972 (Raines and others, 2001). We selected this site because vast amounts of data are available including (1) fluid injection/production history data since 1948, (2) water chemistry data of both reservoir brine and shallow groundwater, and (3) a 3-D high-resolution

geocellular model that includes detailed characterization of reservoir structure and heterogeneity. The 3-D geocellular model employed in this study was developed using high-resolution geologic data (core data, well-logging data, sedimentologic and stratigraphic interpretation) and geophysical data (seismic attributes and rock physics data).

CO_2 Injection Site: SACROC Unit, Texas

Geologic Descriptions

The SACROC Unit is located in the southeastern segment of the Horseshoe Atoll within the Midland basin, western Texas (Figure 39A and B). Within the Horseshoe Atoll, the SACROC Unit comprises an area of 356 km^2 with an approximate north-south length of 40 km and an east-west length of 3–15 km (Vest, 1970). Geologically, the SACROC Unit is composed of massive amounts of bedded bioclastic limestone and thin shale beds representing the Strawn, Canyon, and Cisco Groups of the Pennsylvanian (Vest, 1970; Raines and others, 2001). The Wolfcamp Shale Formation of the lower Permian provides a low permeability caprock above the Pennsylvanian Cisco and Canyon Groups in the SACROC Unit. In detail, the Cisco and Canyon Groups are mostly composed of limestone with minor amounts of anhydrite. Sand, chert, and shale are present locally. Recently, Carey and others (2007) analyzed core samples from wells 49-5 and 49-6 in the SACROC Unit and indicated that the limestone was mostly calcite with minor ankerite, quartz, and thin clay lenses.

Previously, many petroleum geologists studied the SACROC Unit with respect to facies, depositional environment, and petrography (BergenBack and Terriere, 1953; Stafford, 1954; Myers and others, 1956; Stewart, 1957; Burnside, 1959; Vest, 1970; Schatzinger, 1988; Reid and Reid, 1991; Walker and others, 1991; Raines and others, 2001). Several investigators have attempted to identify the depositional environments from the present distribution of carbonate lithofacies in this area. Their goal was to deduce the spatial locations of the high porosity zones to improve oil production by understating the depositional environment. Initially, Bergenback and Terriere (1953) inferred depositional environments from the distribution of carbonate lithofacies such as calcilutite (calcite mud) and oolitic limestone, which were respectively deposited in environments with calm water and strong currents. Myers and others (1956) discussed the possible theories of Atoll growth and concluded that the "winds and
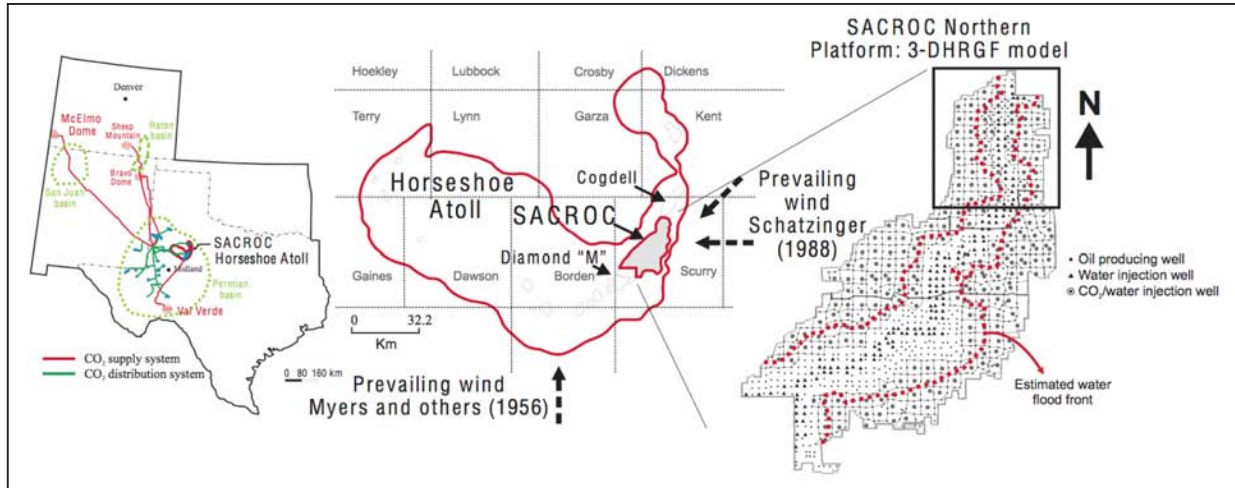
Figure 39: (A) SACROC Unit at the Horseshoe Atoll in western Texas and CO_2 supply system from natural CO_2 reservoirs, (B) Magnified map of the SACROC Unit within the Horseshow Atoll with indication of paleo-wind direction, (C) Well locations of SACROC Unit with the estimated water-flooding fronts at the end of water-flooding period in 1973 (Kane, 1979).

currents" theory by Fairbridge (1950) accounted for the shape of the Horseshoe Atoll. Their research deduces conclusions that the direction of prevailing wind and currents was from south to north (Figure 39B). Later, Schatzinger (1988) recognized the spatial variation of oolites, which evidently decrease from north (Cogdell field) to south (Diamond M field), in the eastern portions of the Horseshoe Atoll and inferred that sedimentation was influenced by east-northeast prevailing winds (Figure 39B). Walker and others (1991) tried to identify the distribution of carbonate species and accretion of the Horseshoe Atoll by placing it in its paleolatitude and paleogeographic orientation (Figure 40). According to their research, the carbonate platform was on the equator in the early Strawn (312 Ma). From early Strawn (312 Ma) to middle Canyon (306 Ma), the relative motion of the carbonate platform was northeast 63 degrees and the platform accumulated at 2 degrees north latitude. From early Cisco (298 Ma) to Wolfcampian (280 Ma), the direction of movement changed to northeast 24 degrees. As a result, the platform moved from 2 to 4 degrees North Latitude. Finally, carbonate accumulation stopped during the Wolfcampian at 6 degrees North Latitude due to the influx of fine-grained siliciclastics and dark shales (Walker and others, 1991). During its

accumulation, prevailing winds from the northeast had a major impact on the distribution of carbonate facies, resulting in the percentage of oolitic carbonate being highest on the northeast-facing edges of the platform.
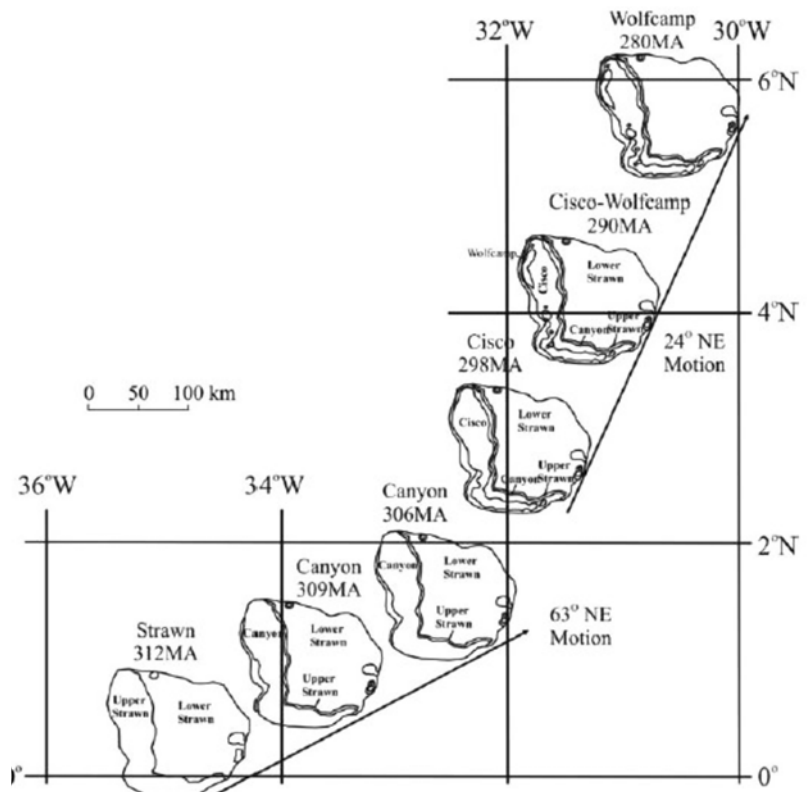
Figure 40: The Paleolatitude and Paleogeographic Location of the Horseshoe Atoll (Walker and others, 1991)

Along with an attempt to understand the spatial (aerial) distribution of carbonates in the SACROC Unit, previous researchers also investigated the variation of carbonates with depth and subsequently divided this Unit into Lower Canyon, Middle Canyon, Upper Canyon, and Cisco Groups through detailed analyses of cores, logging data, and biostratigraphy (fusulinid age) (Figure 41). Their analyses suggested that the Cisco Group, which was characterized as a highly heterogeneous group representing the dramatic changes in depositional environments, unconformably overlies the Canyon Group. The Upper Canyon is a highly porous zone, which includes erosional remnants resulting from a prolonged low sea level. The Middle/Lower Canyon Groups consist of high porosity layers separated by low porosity carbonate muds. More detailed classification of the stratigraphy in the Cisco and Canyon Groups can be found in Reid and Reid (1991) and Hawkins and others (1996).

Changes in depositional environments show a wide variability of both porosity (0 to 30 %) and permeability (0 to 1,000 mD) in the Cisco and Canyon Groups (Figure 41). Bergenback and Terriere (1953) megascopically observed porosity distribution and

reported their values that ranged between approximately 0 to 20 %. Similarly, Myers and others (1956) reported porosity values from 0 to 30 % after core analysis. Both found that most porosity is developed during secondary diagenetic processes such as calcitization, dolomitization, and silicification. Burnside (1959) indicated that open fractures markedly influenced the permeability field. Other studies such as Vest (1970), Kane (1979), Langston and others (1988), Raines (2005), and Brnak and others (2006) provided average porosity and permeability, and the reader is referred to these studies for more detailed discussion.

Schatzinger (1988) estimated porosity from analysis of the depositional environment. In this study, the eastern part of the Horseshoe Atoll was spatially divided into three zones. The first zone included the Cogdell field and northern SACROC Unit (Figure 39B), both reflecting turbulent environments with the deposition of basin-facing ooid shoals. The central and southern SACROC Unit shows intermediate turbulence conditions with the deposition of sponge-algal-bryozoan buildups. Finally, the Diamond M field and southern SACROC Unit reflect a low turbulence environment (Figure 39B). Research by Reid and Reid (1991) was more focused
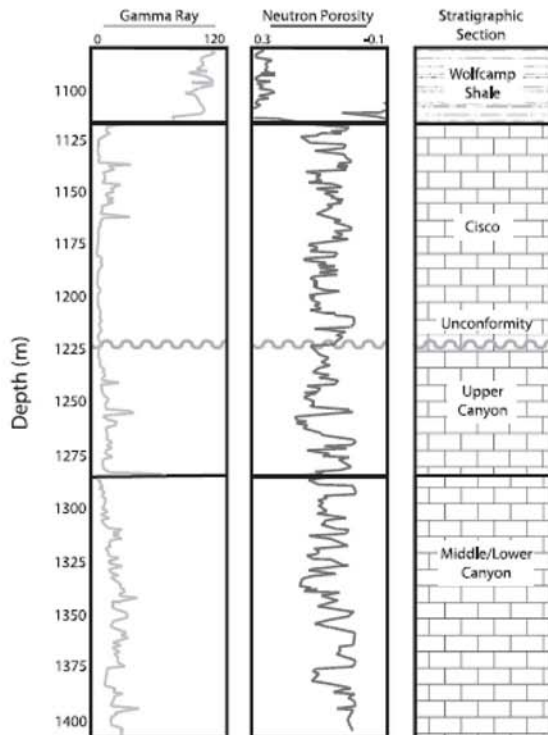
Summary of Previous Studies Estimating Carbonate Rock Properties in Cisco and Canyon Formations		
Porosity (%)	Permeability (mD)	References
(0-20)		Bergenback and Terriere (1953)
6 (0-30)	4.5 (0-85), cracks, fractures 2,500	Myers and others (1956)
6	(0-85)	Burnside (1959)
10.3	30.6	Vest, (1970)
3.93	19.4	Kane, (1979)
9.41	3.03	Langston and others (1988)
9.8 (0-22.5)	19 (0.1-1760)	Raines, (2005)
7.6	19.4	Brnak and others (2006)
Sponge mound facies (15-20)		Schatzinger, (1988)
Phylloid mound facies (<15)		
Oolitic grainstone facies (20-30)		
Peritida mud facies (locally 5)		
Breccia facies (locally 10)		
Oolitic grainstone facies (25-30)	Oolitic grainstone facies (>100)	Reid and Reid, (1991)
Bioclastic grainstone facies (25-30)	Bioclastic grainstone facies (10-50)	Codgell Field
Algal wackestone facies (15-20)	Algal wackestone facies (<10)	

Figure 41: Well Logs Representing the SACROC Northern Platform and Summary of Previous Studies Estimating Carbonate Rock Properties in Cisco and Canyon Groups

on the Cogdell field. In their work, the carbonate reef limestone was divided into nine zones after fusulinid age-dating and well logging correlations. Recently, there has been a similar effort to build stratigraphic frameworks and porosity distributions from the correlations of fusulinid biostratigraphy in the SACROC Unit (Hawkins and others 1996). After examination of core and correlation with well logging, Hawkins and others (1996) found that porosity patterns were closely related to changes in depositional facies and suggested that the biostratigraphic distinction was significant in this field.

Injection and Production History

The SACROC Unit was discovered in 1948. The estimated original oil in place (OOIP) was approximated at 2.73 billion Stock Tank Barrels (STB) (Dicharry and others, 1973). From 1948 to 1951, over 1200 production wells were drilled in this Unit (Bayat and others, 1996). During this period, oil was produced by the solution gas drive mechanism resulting in reduction of the original reservoir pressure (3122 psi = 21.53 MPa) by over 50% (1560 psi = 11.38 MPa) for only 5% of OOIP production (Dicharry and others, 1973; Brummett and others, 1976).

To improve oil production and prevent crippling pressure loss, one of the largest pressure maintenance projects in the United States was started in 1954 (Figure 42). Fifty three water wells initiated water injection at a rate of approximately 21,000 m³ per day along the crest of the SACROC Unit (Allen and LaRue, 1957; Allen and Thomas, 1959; Dixon and Newton, 1965; Dicharry and others, 1973; Brummett and others, 1976; Bayat and others, 1996). The locations of water injection wells are shown in Figure 39C. Before water injection began, only 1% of the reservoir was above the bubblepoint pressure (12.45 MPa). After 17 years (until 1971) of water injection, 77% of this Unit became above the bubblepoint pressure. The estimated waterflooding front at the end of waterflooding period in 1973 is shown in Figure 39C. However, despite the high sweep efficiency of the water injection, approximately 1.2 billion STB of oil still remained in this Unit at the end of the water injection period. In addition, the repressurization

plan eventually resulted in high reservoir pressure in the center of the SACROC Unit and low pressure towards the eastern and western margins. Because of the tremendous volume of oil still left in the reservoir after water injection, other enhanced oil recovery techniques were considered to improve oil recovery.

The SACROC field started with primary recovery, or the solution gas drive, then followed this with secondary recovery operations consisting of water-flooding. Based on engineering calculations, in 1972 the SACROC Unit operating committee decided that CO_2 injection would be the best tertiary oil recovery mechanism. The next major task was to find a CO_2 source near the SACROC Unit. The closest CO_2 sources were the
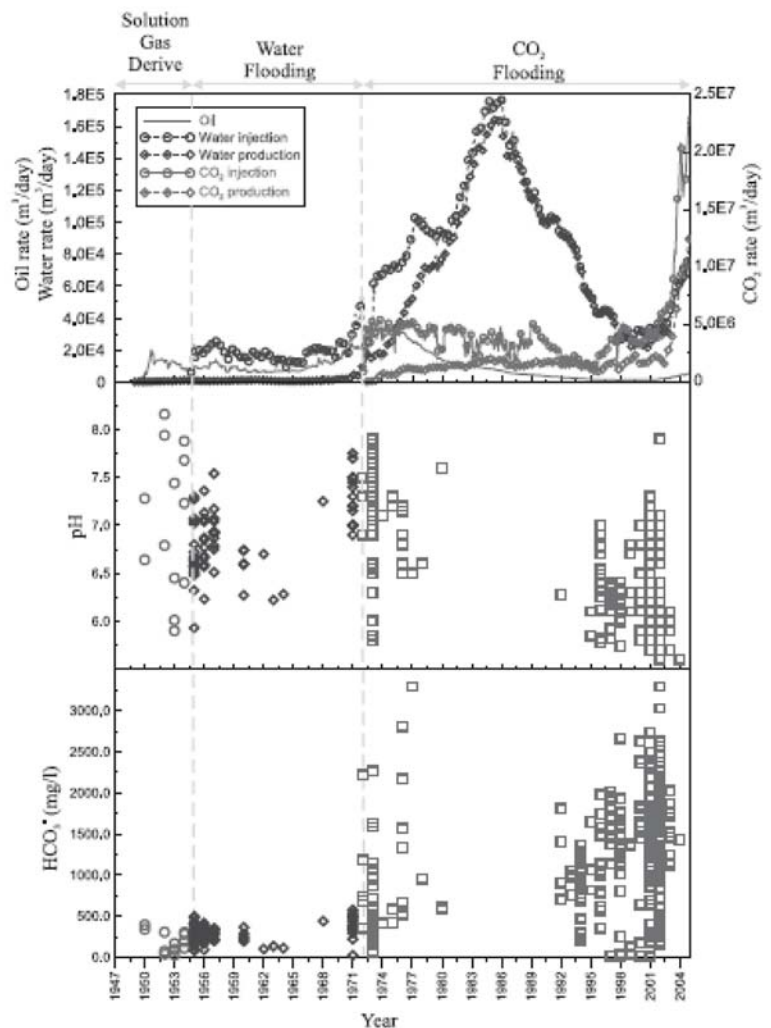
Figure 42: Injection and Production History of Oil, Water, and CO_2 (Raines and others, 2005) and Corresponding Evolution of pH and HCO_3^- in Produced Water from Cisco and Canyon Groups

Ellenburger hydrocarbon gas power plants in the Val Verde basin, about 220 miles (354 km) south of the SACROC Unit (Figure 39A). However, CO_2 from gas power plants were not ideal sources due to the lack of a consistent supply (gas power plants are subject to potential shutdowns due to their internal problems). Therefore, the SACROC operators switched CO_2 supply from gas power plants to McElmo Dome, a natural CO_2 reservoir in Colorado, in 1996 (Weeter and Halstead, 1982). The detailed characteristics including CO_2 accumulation in the CO_2 natural reservoir of McElmo Dome are discussed in Gerling (1983) and Allis and others (2001). By changing the source of CO_2 from the gas power plants to a natural CO_2 reservoir, operations became more stable because of the continuous CO_2 supply. In summary, about 93 million metric tons of CO_2 were injected and about 38 million metric tons were produced from 1972 to 2005 in this Unit. As a result, a simple mass-balance suggests that the site has accumulated about 55 million metric tons of CO_2 (Raines, 2005).

Effect of CO_2 Injection on Reservoir Brine Chemistry

Changes in reservoir brine chemistry due to injection of a massive amount of CO_2 have been observed in field-scale operations (Bowker and Shuler, 1991; Klusman, 2003; Emberley, 2004; Kharaka and others, 2006; Mito and others, 2008). These authors found that CO_2 dissolution typically results in the reservoir brine having a lower pH and higher HCO_3^- concentration. Subsequently, these reactions induce changes in reservoir rock properties. For this SACROC case study, we gathered and analyzed the brine chemistry data from the Cisco and Canyon Groups to investigate whether the similar alteration of reservoir brine chemistry, due to 35 years of CO_2 injection, occurred in the SACROC Unit. The brine chemistry data is a compilation of various analyses and reports from the Martin Water Laboratory, Unichem, the Texas Water Board, Permian Production Chemical, and the United States Geological Survey (Bowden, Kinder Morgan CO_2, personal communication, 2006). The statistical classification of these data sets, calculated for each period of differing oil-production mechanisms, is shown in Table 8.

Table 8: Statistics of Water Chemistry Analyses and Chemical Modeling of Reservoir Fluids in Cisco and Canyon Groups during Each Oil Production Mechanism

Oil Production Mechanisms		Solution Gas	Water Flooding	CO_2 Flooding
Period (Year)		1948-1952	1953-1971	1972-2004
Number of samples		13	69	758
Reservoir pressure (MPa)		21.50	11.38	16.55
Reservoir temperature (°C)		54.50	54.50	54.50
pH	Mean	7.06	6.88	6.43
	Std.	0.75	0.37	0.60
Na^+ (mg/L)	Mean	27,292.00	24,750.72	24,248.52
	Std.	11,011.07	11,026.97	9,192.98
Ca^{2+} (mg/L)	Mean	4,238.15	3,613.78	2,675.24
	Std.	2,256.80	2,065.09	1,644.09
Mg^{2+} (mg/L)	Mean	959.92	917.90	1,305.01
	Std.	444.99	464.05	833.68
Cl^- (mg/L)	Mean	51,496.46	46,263.46	44,587.90
	Std.	21,838.31	21,068.02	16,665.64
HCO_3^- (mg/L)	Mean	185.15	306.90	1313.69
	Std.	125.06	112.78	675.52
SO_4^{2-} (mg/L)	Mean	1,675.31	1,050.61	782.80
	Std.	755.17	697.64	679.30
CO_2 fugacity (MPa)	Mean	3.64* (0.0169)	3.35** (0.0294)	67.68*** (0.4089)
	Std.	3.77*	1.72**	54.36***
SI of calcite ($CaCO_3$)	Mean	0.68	0.80	0.62
	Std.	0.92	0.47	0.78
SI of dolomite ($CaMg[CO_3]_2$)	Mean	2.28	2.55	2.44
	Std.	1.81	0.95	1.51
SI of Magnesite ($Mg[CO_3]$)	Mean	0.13	0.28	0.35
	Std.	0.89	0.49	0.80
SI of anhydrite ($CaSO_4$)	Mean	-0.43	-0.69	-1.00
	Std.	0.26	0.26	0.46
SI of gypsum ($CaSO_4 \cdot H_2O$)	Mean	-0.57	-0.83	-1.14
	Std.	0.27	0.26	0.46

*, **, and *** is respectively calculated with reservoir pressure 21.5, 11.38, and 16.55 MPa because reservoir pressure varies historically (Dicharry and others, 1973; Brummett and others, 1976). Parentheses indicate the normalized CO_2 fugacity at 0.1 MPa. Reservoir temperature is from Langston and others (1988). SI represents the saturation index of mineral.

Statistics of the SACROC reservoir brine chemistry (Table 8) show that mean concentration of Na^+ and Cl^- were respectively 27,292 mg/L and 51,496 mg/L during the solution gas period (1948-1952) and their concentration decreased throughout the waterflooding (1953-1971) period (Na^+: 24,750 mg/L and Cl^-: 46,263 mg/L). This dilution of reservoir brine is the result of relatively fresh water being injected and recycled during the waterflooding period. Similarly, the dilution of reservoir brine during the waterflooding period has been observed in another oilfield, the Rangely Field, Colorado. Brine salinity before waterflooding was approximately 100,000 ppm in Rangely Field but it decreased to 33,000 ppm at the end of waterflooding (Bowker and Shuler, 1991). After the initiation of CO_2 flooding in the SACROC Unit (1972-2004), it was expected that increases of Na^+, Cl^-, and other species' concentrations would occur, similar to the observations in Rangely Field, Colorado by Klusman (2003). However, mean values of Na^+, Ca^{2+}, Cl^-, and SO_4^{2-} concentrations kept decreasing during the CO_2 flooding period in the SACROC Unit (Table 8). We presume that this difference occurred because the SACROC operators performed waterflooding prior to CO_2 injection even during the CO_2 flooding period to increase reservoir pressure up to minimum miscibility pressure and also employed Water-Alternating-Gas (WAG) processes. Therefore, huge amounts of water were injected and recycled even in the CO_2 flooding period (Figure 42), and caused the continued dilution of reservoir brine. In addition, the CO_2 injection formation in Rangely Field, Colorado, was sandstone but it is limestone in the SACROC Unit. Therefore, the potential chemistry changes between these two reservoirs due to CO_2 injection are expected to be different.

Evolving patterns of both pH and HCO_3^- concentrations shown in Figure 42 are similar to the observations from other field-scale operations (Klusman, 2003; Emberley, 2004; Kharaka and others, 2006; Mito and others, 2008). The pH becomes lower and the HCO_3^- concentration increases from the waterflooding period until the CO_2 flooding period. Especially, in the SACROC Unit, where the decrease in pH during CO_2 flooding was small (6.88 to 6.43 shown in Table 8) compared with the pH decrease in the Rangely field (6.69 to 5.50; Kluseman, 2003) and Frio field (6.7 to 5.5; Kharaka and others, 2006) where the formation rocks are sandstone. This result suggests that carbonate rock, which is the major rock in the SACROC Unit, buffered the drop in pH. The dramatic increase of HCO_3^- (306.90 to 1313.69 mg/L) is possibly caused by both the injected CO_2 being dissolved in the brine solution and the dissolution of calcite ($CaCO_3$) and dolomite ($CaMg(CO_3)_2$). Notably, the concentration of Mg^{2+} in the reservoir brine increased (464.05 to 833.68 mg/l) during the CO_2 flooding period, suggesting that CO_2 injection possibly caused the dissolution of dolomite ($CaMg(CO_3)_2$) and Magnesite ($MgCO_3$).

CO_2 fugacity can be an indicator as to whether injected CO_2 was dissolved in the reservoir brine, and the Saturation Indexes (SI) of minerals can provide key information associated with the degree of mineral saturation in the reservoir brine. Therefore, CO_2 fugacity and SI of representative carbonate and sulfate minerals are calculated with the B-dot activity coefficient model (Helgeson, 1969) using Geochemist's Workbench (GWB™) version 7.0 (Bethke, 1996). The statistics for the modeled CO_2 fugacity in Table 8 show that the mean of modeled CO_2 fugacity is similar throughout the solution gas (3.64 MPa) and waterflooding (3.35 MPa) periods. However, the mean value of the modeled CO_2 fugacity significantly increased to 67.68 MPa during the CO_2 flooding period showing the evidence of CO_2 dissolution in reservoir brine. The modeled SI values suggested that the reservoir brine in the Cisco and Canyon Groups was oversaturated with carbonate minerals but it was undersaturated with anhydrite and gypsum during the entire oil production period (1948-2004). Although the chemistry of the dissolved species in the reservoir brine evolves during oil production periods (Figure 42 and Table 8), the saturation states of minerals did not significantly vary, suggesting that chemical reactions between dissolved species are relatively faster than water-rock interaction. In addition, this analysis also suggests that 35 years is not enough time to predict definite changes of mineral saturation states.

Description of 3-D, High-Resolution Geocellular Model in SACROC Northern Platform and Upscaling

The 3-D geocellular model representing the Cisco and Canyon Groups in the SACROC northern platform is illustrated in Figure 43. The approximate size of the model is 4,000 m wide and 10,000 m long. The top of the geocellular model describes the top configuration of the Cisco Group, which is approximately 1200 m below sea level, and the bottom of the model describes the

bottom configuration of the Canyon Group, which is a depth of approximately 1400 m below.
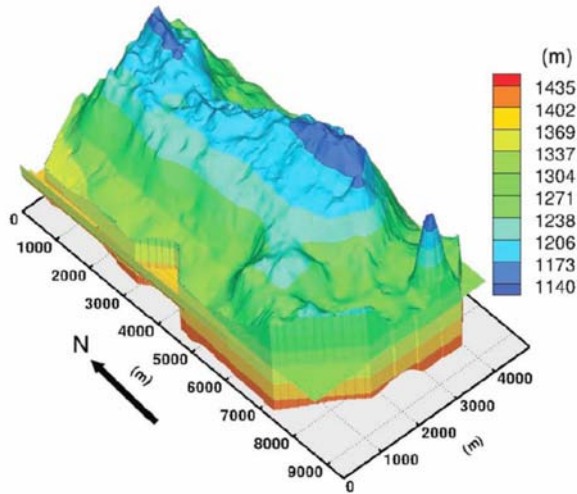
Figure 43: Structure of 3-D geocellular model representing Cisco and Canyon Groups in the SACROC northern platform. Label (m) indicates the formation depth from the sea level.

Figure 44A-D show the external and internal distributions of both porosity and permeability. In this model, porosity distributions were defined from both 3-dimensional seismic surveys and 368 well logging analyses. Subsequently, permeability distributions were calculated from seismically calibrated porosity distributions using empirical equations derived from rock fabric classification (Lucia and Kerans, 2004). The global transforming equation has been derived for carbonate rock as (Lucia, 1995, 1999; Jennings and Lucia, 2003):

$$\log(k) = (9.792 - 12.0838\log(\lambda)) + (8.6711 - 8.2965\log(\lambda))\log(\phi) \quad (2)$$

where, λ, k, and ϕ are, respectively, rock-fabric number, permeability, and interparticle porosity. Specifically, λ represents the specific class of carbonate rock based on petrophyiscal properties such as inter-particle porosity in tandem with geological descriptions of particle size and sorting. Lucia and Kerans (2004) applied this equation to estimate the permeability distribution in the
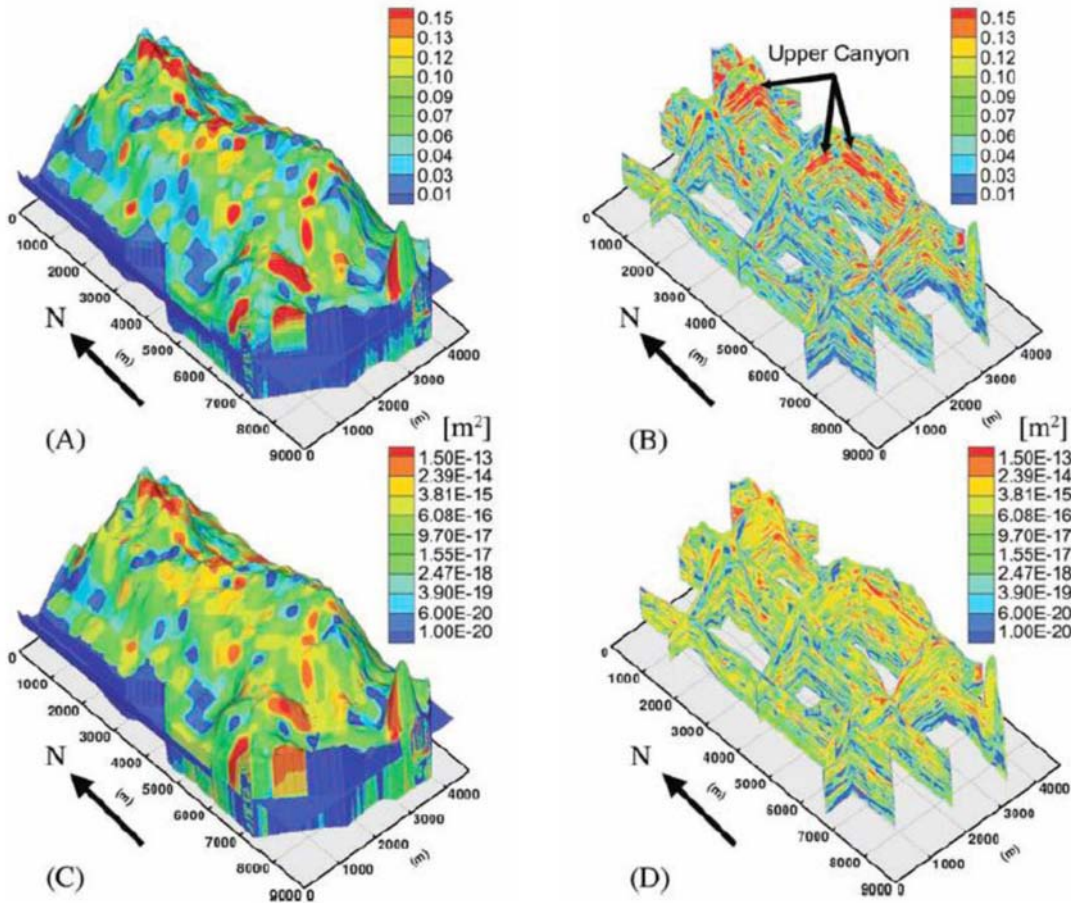
Figure 44: Internal and external distributions of porosity and permeability in the 3-D geocellular model: (A) external distribution of porosity, (B) internal distribution of porosity, (C) external distribution of permeability (m²), and (D) internal distribution of permeability (m²).

Table 9: Permeability Estimation Using Porosity and Rock-Fabric Number (Lucia and Kerans, 2004)

Formation	Sequence	Rock-Fabric Number (λ)	Transforming Equations	
Cisco	1	Reduced major axis transformation	$k = 2.1625 \times 10^6 \times \phi^{3.8844}$	Highest portion of Cisco (Implication of karsting)
	2	1.7	$k = 1.031 \times 10^7 \times \phi^{6.7592}$	Late Cisco (wide variety of rock fabrics)
	3	1.9	$k = 2.69 \times 10^6 \times \phi^{6.3584}$	Early Cisco (Characterized by fusulinid/crinoidal/peloid grain dominated packstones, grainstones, and wackestones
Canyon	1	2.5	$k = 97628 \times \phi^{5.3696}$	Early Canyon: (Characterized by moldic ooid grainstone, grain-dominated packstone, and mud-dominated fabrics)
	2	1.75	$k = 38520 \times \phi^{5.0923}$	Late Canyon: (Characterized by crinoidal/fusulinid/peloid, grain-dominated packstones, and mud-dominated fabrics having vuggy porosity)

SACROC northern platform. The detailed parameters of rock-fabric numbers in this model are described in Table 9.

This 3-D geocellular model preserves the detailed heterogeneity variation of both porosity and permeability (Figures 44A-D). The model reveals that the Cisco and Canyon Groups typically lie within a "stacked system" of alternating high and low porosity layers (Figure 44B). The thick and high porous zone shown in Figure 44B represents the Upper Canyon Group. The Cisco Group is located above the Upper Canyon Group, and the Middle/Lower Canyon Groups are below this Upper Canyon Group. Specifically, the Middle/Lower Canyon Groups consist of several layered high porosity zones separated by low-porosity carbonate mud.

The 3-D geocellular model describing the Cisco and Canyon Groups includes 9,450,623 (149 × 287 × 221) elements (Figures 43 and 44). Although the model provides a quantified characterization of the natural heterogeneity of both porosity and permeability distributions in the SACROC northern platform, the utilization of this model in describing CO_2 trapping

mechanisms was hampered due to the large number of elements; only supercomputers capable of massively parallel computation were capable of accommodating simulations with this model. For this reason, we elected to upscale the model to fewer elements. Such upscaling invariably results in a loss of heterogeneity resolution, but we tried to preserve as much of this heterogeneity as possible. The purpose of upscaling was two-fold: (1) about 9.4 million elements exceeded the memory capacity of our model simulators on a personal computer and (2) the original porosity and permeability data as estimated from geophysical data varied extremely from cell-to-cell, sometimes as much as several orders of magnitude in permeability. Upscaling smoothes these data through the averaging process and facilitates a more stable numerical solution, albeit with the loss of heterogeneity resolution.

In this study, porosity is upscaled by the volumetric averaging technique, and k permeability is upscaled with an algorithm developed through an equivalent resistor network model (King, 1989). The upscaling equation and conceptual diagram used in this work is shown in eq 3 and Figure 45, respectively.

$$k_{eff} = \frac{4(k_1 + k_3)(k_2 + k_4)[k_2 k_4(k_1 + k_3) + k_1 k_3(k_2 + k_4)]}{[k_2 k_4(k_1 + k_3) + k_1 k_3(k_2 + k_4)][k_1 + k_2 + k_3 + k_4] + 3(k_1 + k_2)(k_3 + k_4)(k_1 + k_3)(k_2 + k_4)]} \quad (3)$$
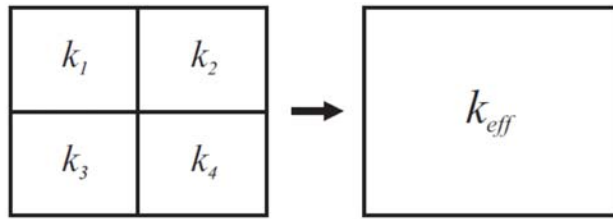
Figure 45: Upscaled permeability using renormalization and the equivalent equation is shown in eq 3.

This technique is generally called "renormalization" because it successively upscales the symmetric grid-blocks using self-repetitive geometry until the final grid-block size is reached. Using this approach is fast and computationally cheap because it does not require solutions to the differential equations. In addition, it is not constrained by the number of grid-blocks. Because of these practical advantages, many researchers have studied and updated renormalization techniques (Hinrichsen and others, 1993; King, 1996; Gautier and Noetinger, 1997, Renard and others, 2000). Despite its many advantages, renormalization has several drawbacks. If there is a high contrast between neighboring permeability values, using this approach will underestimate the upscaled permeability value (King, 1989; Renard and de Marsily, 1997). In addition, this method has some limitations with respect to applicable boundary conditions (Malick, 1995). Finally, renormalization is specially designed for

orthogonal grids. Although our model satisfies several conditions to apply this renormalization technique, the grid is not completely orthogonal. The grid is orthogonal in both the x- and y-direction; however, the z-direction is irregular, which could induce some error in the resulting upscaled permeability. It is extremely difficult to quantify the error due to this non-orthogonality, although we estimate the accrued error to be less than the uncertainty associated with seismic and well logging data used to calibrate the model.

Sequential results of permeability distributions by renormalization are shown in Figure 46. In addition, the detailed statistics of permeability values, the number of grid-blocks, and their sizes are shown in Table 10. As the grid is upscaled, the size of grid-block becomes greater, and both the means (arithmetic, harmonic, and geometric) and standard deviation of the permeability
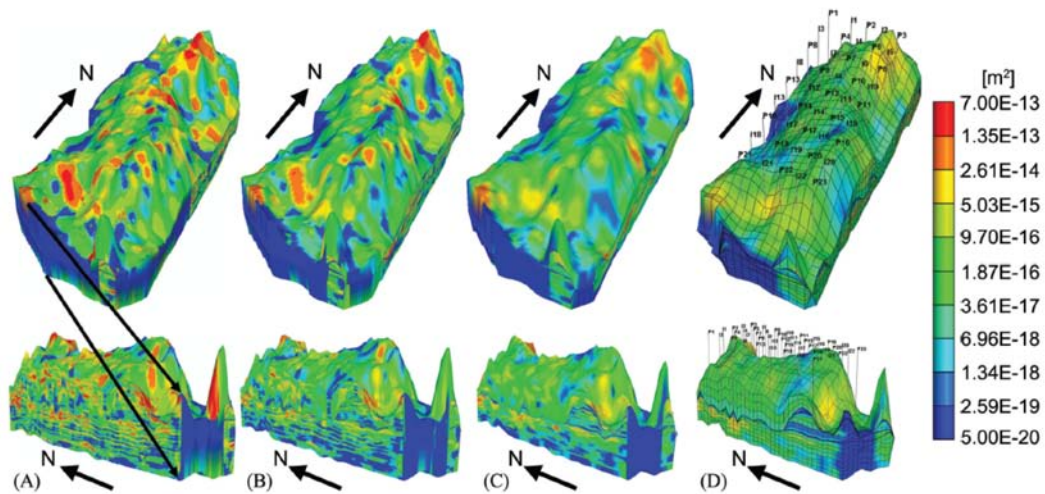
Figure 46: Internal and external permeability distributions during each renormalization procedure. The detailed grid statistics are shown in Table 9: (A) 149x287x221=9,450,623 elements, (B) 74x143x110=1,164,020 elements, (C) 36x71x54=139,968 elements, and (D) 17x35x26=15,470 elements.

Table 10: Detailed Statistics of Permeability, Grid Dimensions,
and Size of Grids During the Renormalization Process

	Number of Grid			Total Number of Grids	Grid Size (m)			Permeability (m²)			
	X	Y	Z		X	Y	Z	Mean Arithmetic	Harmonic	Geometric	Std. Dev.
1	149	287	221	9,450,623	30.54	30.46	vary	5.62E-15	8.75E-20	2.13E-18	4.20E-14
2	74	143	110	1,164,020	61.08	60.91	vary	3.58E-15	8.46E-20	1.58E-18	2.40E-14
3	36	71	54	139,968	122.16	121.83	vary	1.93E-15	8.21E-20	1.12E-18	1.38E-14
4	17	35	26	15,470	244.32	243.66	vary	5.10E-16	7.45E-20	5.76E-19	3.26E-15

become smaller. Decrease of the means of upscaled permeability suggests that low permeability values have a greater influence on the calculation of upscaled permeability values. Similarly, decrease of standard deviation of upscaled permeability suggested that permeability distribution from cell-to-cell becomes smoother. Finally, for the model development utilized for the simulation of CO_2 trapping mechanisms in the SACROC northern platform, we obtained the upscaled grid with 15,470 elements shown in Figure 46D.

Determination of Boundary Conditions: Evaluation of Wolfcamp Shale Formation as a Suitable Seal

To evaluate the seal integrity of the Wolfcamp Shale Formation, we gathered and analyzed the available water chemistry data to determine the potential sealing effect of this formation. These chemical analyses do not provide definitive proof to whether or not CO_2 leaks through the Wolfcamp Shale Formation because the SACROC Unit comprises a huge area, 356 km² (Figure 39). Therefore, even the most detailed datasets will not cover the entire SACROC Unit. As such, the ultimate goal of these analyses is to evaluate the overall performance of the Wolfcamp Shale Formation and evaluate the likelihood that the Wolfcamp Shale Formation currently acts as a suitable seal in this area.

During the geologic time period, the Wolfcamp Shale Formation about 150 m thick was the caprock overlying the hydrocarbon in the Cisco and Canyon Groups (Vest, 1970; Raines, 2001). Although CO_2 has been injected during the last 35 years, previous researchers have not reported any indication of CO_2 leakage such as travertine deposits at the surface, changes of shallow groundwater chemistry, anomalous CO_2 gas concentration at the surface, or changes in surface vegetation over time. In addition, several scientific investigations supported the premise that the Wolfcamp Shale Formation might be a suitable seal within the SACROC Unit. For example, Carey and others (2007) measured vertical permeability of the Wolfcamp Shale Formation and suggested that it was low enough (<0.05 mD) to build a capillary barrier that hampers buoyancy-driven migration of CO_2. In addition, their mineralogical and isotopic (oxygen and carbon) analyses suggested that the carbonates in the Wolfcamp Shale Formation appear to be derived from primarily diagenetic processes, supporting that CO_2 is effectively trapped in the Cisco and Canyon Groups.

For this study, we gathered and analyzed the available water chemistry data to determine the potential sealing efficacy of the Wolfcamp Shale Formation. Detailed statistics of brine samples (840) gathered from the Cisco and Canyon Groups are shown in Table 8, and those for shallow groundwater samples (170) gathered from the Dockum formation above the Wolfcamp Shale Formation are summarized in Table 11. A Piper diagram analysis in Han (2008) illustrated that the chemistry of the shallow groundwater is distributed from Na-HCO_3 to Ca-HCO_3 while most of the brine is the Na-Cl type.

With a similar approach to analyzing reservoir brine as described in the previous section, "*Effect of CO$_2$ Injection on Reservoir Brine Chemistry*" we calculated the CO$_2$ fugacity and saturation indexes (SI) of minerals from shallow groundwater. Interestingly, mean values of CO$_2$ fugacity from the shallow groundwater did not change from water flooding to CO$_2$ injection period (Table 11), suggesting that CO$_2$ injection into the Cisco and Canyon Groups did not significantly impact the chemistry of the shallow groundwater above the Wolfcamp Shale formation. In addition, SI analysis suggests that shallow groundwater is oversaturated with respect to calcite and dolomite, but the degree of oversaturation in the shallow groundwater is smaller than that in the reservoir brine of Cisco and Canyon Groups.

We hypothesized that the concentrations of reservoir brine in the Cisco and Canyon Groups and shallow groundwater above the Wolfcamp Shale Formation would show the evidence of a mixing effect if CO$_2$-saturated reservoir brine leaked through highly permeable conduits such as faults or fractures in the Wolfcamp Shale Formation. The flow systems in the Cisco and Canyon Groups are advection-dominant due to a significant alteration of pressure by injection and production activities. Such conditions may accelerate the migration of reservoir brine through highly permeable conduits with the result that CO$_2$-saturated reservoir brine may make its way to the above shallow groundwater zone.

To evaluate the potential chemical signatures of such mixing effects, we simulated equilibrium mixing with mean values of dissolved species from both reservoir brine and shallow groundwater collected during CO$_2$ flooding periods (Tables 8 and 11), using PHREEQC version 2.15.0 with thermodynamic data known as phreeqc.dat (Parkhurst and Appelo, 1999). Three sets of mixing models were simulated after varying the volume of reservoir brine (10, 30, and 50%). The simulation results are plotted in the Box-Whisker plot between concentrations of individual species in the reservoir brine and

Table 11: Statistics of water chemistry analyses and chemical modeling of shallow groundwater above Wolfcamp shale formation (Dockum formation) during each oil production mechanism.

Oil Production Mechanisms		Solution Gas	Water Flooding	CO$_2$ Flooding
Period (Year)		1948-1952	1953-1971	1972-2004
Number of Samples		No Sample	48	122
Temperature (°C)	*Mean*		20.85	21.03
	Std.		0.67	1.15
pH	*Mean*		7.48	7.63
	Std.		0.47	0.68
Na$^+$ (mg/L)	*Mean*		278.98	349.26
	Std.		383.12	1009.94
Ca^{2+} (mg/L)	*Mean*		104.18	125.67
	Std.		130.81	126.47
Mg^{2+} (mg/L)	*Mean*		46.03	40.92
	Std.		65.08	41.86
Cl$^-$ (mg/L)	*Mean*		336.13	484.66
	Std.		631.31	1552.49
HCO$_3^-$ (mg/L)	*Mean*		323.27	304.09
	Std.		105.38	81.21
SO$_4^{2-}$ (mg/L)	*Mean*		292.16	284.57
	Std.		461.91	421.18
SiO$_2$(aq) (mg/L)	*Mean*		22.15	25.17
	Std.		11.26	10.53
CO$_2$ Fugacity* (MPa)	*Mean*		0.009	0.009
	Std.		0.007	0.010
SI of Calcite (CaCO$_3$)	*Mean*		0.08	0.45
	Std.		0.44	0.49
SI of Dolomite (CaMg(CO$_3$)$_2$)	*Mean*		0.91	1.53
	Std.		0.87	1.00
SI of Magnesite (Mg(CO$_3$))	*Mean*		-0.83	-0.58
	Std.		0.46	0.53
SI of Anhydrite (CaSO$_4$)	*Mean*		-2.24	-2.03
	Std.		0.81	0.71
SI of Gypsum (CaSO$_4$·H$_2$O)	*Mean*		-2.01	-1.80
	Std.		0.81	0.71

* CO$_2$ fugacity is calculated with a pressure of 0.1 MPa. SI represents the saturation index of mineral.

shallow groundwater (Figure 47). The plot shows that concentrations of dissolved species between reservoir brine and shallow groundwater are typically different and generally provide no distinct indication of communication. However, results of the equilibrium mixing model show that a few shallow groundwater samples potentially show the mixing effect with reservoir brine. Results of 10%-brine mixing simulations (circle in Figure 47) are plotted within the range of both brine and shallow groundwater. In detail, less than 5% of shallow groundwater samples have the concentration greater than the modeled concentration of the 10%-brine mixing model. This analysis suggests that a few shallow groundwater samples might be locally contaminated with reservoir brine. However, it is difficult to conclude that the contamination of shallow groundwater is mainly due to the leakage of CO_2-saturated reservoir brine through the Wolfcamp Shale Formation. In the SACROC Unit, there exist many brine pits on the surface used to store recycled reservoir brine. Therefore, it is possible that this stored reservoir brine on the surface could recharge downward into the shallow groundwater zones and induce the contamination of shallow groundwater.

Based on the analysis of brine and shallow groundwater chemistry, we concluded that the Wolfcamp Shale Formation generally acts as a suitable seal in the SACROC Unit. Previous results of CO_2 fugacity calculation showed that there was no significant increase of modeled CO_2 fugacity in shallow groundwater (Table 11) although the modeled CO_2 fugacity of reservoir brine in the Cisco and Canyon Groups significantly increases during the CO_2 flooding period. In addition, the equilibrium mixing model shows that only less than 5% of shallow groundwater samples displays the evidence of mixing effects with reservoir brine. Even then, it is also possible that this mixing is due to the downward recharge of recycled brine from brine pits at the surface during enhanced oil recovery.

Sources and Sinks: Actual CO_2 Injection and Production Histories

We analyzed CO_2 injection and production histories provided by Kinder Morgan CO_2 Inc. in the SACROC northern platform. According to these records, 97 wells were used as CO_2 injectors at the SACROC northern platform from 1972 to 2002. Among them, 51 wells were actively used to inject about 13 million metric tons of CO_2 (13,048,845,748 kg) into Cisco and Canyon Groups. Another 219 wells were used as CO_2 producers during the same period. Among them, 124 wells were used to produce about 6 million metric tons of CO_2 (6,104,258,074 kg). A simple mass-balance suggests a net of about 7 million tones of CO_2 (6,944,587,674 kg) are stored in the SACROC northern platform.
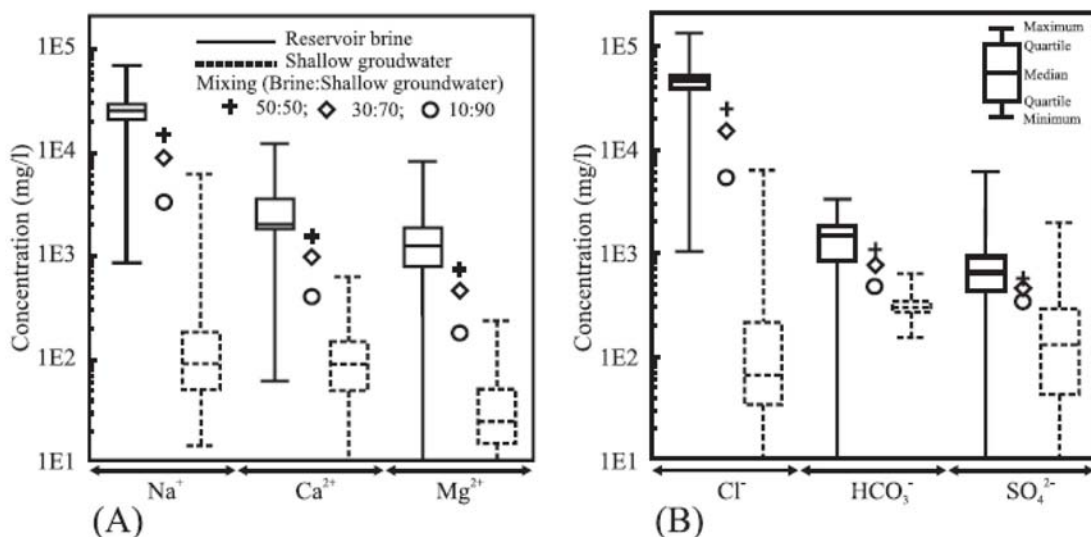
Figure 47: Box-and-whisker diagram showing the range of brine and shallow groundwater, and results of equilibrium mixing model simulated after varying the volume of reservoir brine (10, 30, and 50%).

Analysis of Competing CO_2 Trapping Mechanism at SACROC Northern Platform

We developed two different models representing CO_2 trapping mechanisms at the SACROC northern platform, both utilizing the hydrogeologic framework, boundary conditions, and sources/sinks described above. The objective of these two simulations was to predict and compare the major trapping mechanisms, including hydrostratigraphic, residual, brine-solubility, oil-solubility, and mineralization.

The first model was designed for simulating CO_2 trapping mechanisms in a reservoir saturated with brine only. The other model was designed for simulating CO_2 trapping mechanisms in a reservoir saturated with both brine and oil. The latter model provides a relatively realistic representation of CO_2 trapping mechanisms in the SACROC field because this field is a petroleum reservoir subjected to a long history of CO_2 injection for enhanced oil recovery. We conducted all simulations during a 200-year time period from 1972 to 2172. All simulations were performed with the CMG's GEM simulator, a multi-dimensional, finite-difference, isothermal compositional simulator (Computer Modeling Group, 2008).

SACROC CO_2 Trapping Model – Brine Only

Initial Conditions

From 1954 to 1971, water was injected in a centerline pattern to increase the reservoir pressure above bubblepoint pressure (12.45 MPa) as illustrated in Dicharry and others (1973) and Langston and others (1988). As a result, when CO_2 injection began in 1972, reservoir pressure had risen above 16.55 MPa. This pressure condition is assigned as the initial average reservoir pressure (16.55 MPa) in the upscaled geocellular model with 15,470 (=17x35x26) elements shown in Figure 46D. To achieve this average pressure, reservoir pressure was assigned as hydrostatic pressure from the formation top equal to 15.73 MPa to the bottom pressure equal to 17.90 MPa in the upscaled model. Langston and others (1988) reported the reservoir temperature as 54.5 °C, and we used this value as an average reservoir temperature. In the model, the initial reservoir temperature was assigned using a conductive gradient with temperature at the top equal to 54.35 °C and bottom equal to 59.8 3°C. The assigned temperatures in the model remain constant during the simulation period although there could be

the occurrence of a non-isothermal effect caused by CO_2 injection and migration. We refer readers to other studies about the detailed non-isothermal effect related to CO_2 storage processes (Bielinski and others, 2008; Lu and Connell, 2008; André and others, 2010; Han and others, 2010b).

Boundary Conditions

Through rigorous analysis of water chemistry data, we were able to predict a possibility of local contamination of shallow groundwater caused by either surface recharge of recycled brine or leakage of CO_2-saturated brine through the Wolfcamp Shale Formation. Local brine-contamination notwithstanding, we assume that the Wolfcamp Shale Formation is a sufficient sealing unit. Some observations that justify this assumption include

(1) The Wolfcamp Shale Formation, as thick as 150 m, was a seal for hydrocarbon in the Cisco and Canyon Groups during vast periods of geologic time (Vest, 1970; Raines, 2001).

(2) Measured vertical permeability (k_z) in the Wolfcamp Shale Formation is low (<0.05 mD) enough to prevent vertical CO_2 migration, according to Carey and others (2007).

(3) X-ray diffraction analysis suggests that carbonate minerals in the Wolfcamp Shale formation appear to derive from primarily diagenetic processes and their isotope compositions show typical marine-originated $\delta^{13}C$ values (Carey and others, 2007).

(4) CO_2 fugacity in reservoir fluids of Cisco and Canyon Groups significantly increases during the CO_2 injection period (Table 8) but CO_2 fugacity does not vary in shallow groundwater above the Wolfcamp Shale Formation (Table 11).

As such, we assigned a no-flow condition at the upper boundary in the 3-D upscaled geocellular model. Although both Kaszuba and others (2005), Xu and others (2005), and Busch and others (2008) indicate that the caprock can also act as a reactive component and contribute to mineralization, we think that the role of the caprock as a reactive component is not significant since the flow mechanism in the caprock is dominantly diffusion-driven. Gaus and others (2005) concluded that the mineralization due to diffusion in typical seals occurs in the lower 2 m after 3000 years. Similarly, Lu and others (2009) measured carbon isotopes from

mudrock seal immediately above a natural CO_2-rich reservoir in the North Sea Miller oil field suggested that CO_2 migrated only 12 m through mudrock seal during 70-80 million years. Consequently, the mineralization within such caprocks will be much smaller than that in the targeted reservoir formations. Therefore, treating the seals as no-flow boundaries will not significantly affect the prediction of CO_2 trapping mechanisms and capacity estimation.

Due to these reasons, the eastern, western, and northern boundaries are treated as no-flow boundaries because the Wolfcamp Shale Formation meets these boundaries; the carbonate reef complex of the Cisco and Canyon Groups is prism-shaped (Vest, 1970). The bottom boundary is also designated as a no-flow boundary because the Strawn Formation below the Cisco and Canyon Groups is also a low permeable unit (Raines, Kinder Morgan CO_2 Inc., personal communication, 2006). Finally, a hydrostatically constant pressure condition known as the "Dirichlet" condition is assumed at the southern boundary of the model because this boundary is connected to the middle part of the SACROC Unit (Figure 39C).

Transport and Chemistry Input Data

Relative permeability curves of supercritical-phase CO_2($k_r^{CO_2}$) and brine (k_r^{br}) in the 3-D geocellular model were developed by extrapolating ($k_r^{CO_2}$) data measured by Bennion and Bachu (2005). They measured ($k_r^{CO_2}$) and (k_r^{br}) in a 0.16 m core of low-permeability carbonate rock collected from Wabamun Lake, with experimental conditions of 41 °C and 22.4 MPa. Hysteretic effects were included in the ($k_r^{CO_2}$) curve using a modified Land equation (Land, 1968; Kumar and others, 2005; Han and others, 2010a).

$$k_r^{CO_2}(S_{CO_2}) = (S_{CO_2}) \text{ during drainage} \qquad (4)$$

$$k_r^{CO_2}(S_{CO_2}) = k_r^{CO_2}(S_{CO_2}{}^{(shifted)}) \text{ during imbibition} \qquad (5)$$

Where

$$S_{CO_2}{}^{(shifted)} = \frac{S_{CO_2} - S_{grh}}{S_{gh} - S_{grh}} S_{gh} \qquad (6)$$

and

$$\frac{1}{S_{gr}^{max}} = \frac{1}{S_{grh}} - \frac{1}{S_{gh}} + 1 \qquad (7)$$

S_{gh} is the value of S_{CO_2} when the shift to imbibition occurs. S_{grh} is the value of S_{gr} corresponding to S_{gh}.

Adopting the Land equation requires the determination of maximum residual saturation (S_{gr}^{max}). An empirical formulation ($S_{gr}^{max} = 0.5437 - 0.969\phi$) determining S_{gr}^{max} from porosity (ϕ) was proposed by Holtz (2002). Using this empirical formulation, S_{gr}^{max} was calculated as 0.4 in this model. Capillary pressure curve for brine and supercritical-phase CO_2 was also developed by extrapolating data measured by Bennion and Bachu (2006). Here, for simplification, the same capillary pressure curve is used for both drainage and imbibition conditions, and the scaling of capillary pressure curve dependent on heterogeneous permeability field (Leverett, 1941; Durmore and Schols, 1974) is not implemented. We refer readers to Plug and Bruining (2007) and Saadatpoor and others (2010) for this specific topic in relation to geologic CO_2 storage. Both CO_2 density and viscosity were respectively calculated from the Peng-Robinson equation of state (Peng and Robinson, 1976) and Jossi and others (1962). CO_2 solubility was calculated using Henry's law (Li and Nghiem, 1986) adjusted for the effects of temperature (Harvey, 1996), salinity, and salting out (Bakker, 2003). Drying out effects due to brine evaporation at the vicinity of injection wells was not considered in this work since our primary objective was to identify CO_2 trapping mechanisms at a reservoir scale. We refer readers to other studies for discussion of salt precipitation effects near CO_2 injection wellbores due to drying out processes (André and others, 2007; Giorgis and others, 2007; Pruess and Müller, 2009) and studies of mutual solubility (Duan and Sun, 2003; Spycher and others, 2003). Finally, density and viscosity of the CO_2-H_2O aqueous mixtures with the effects of brine concentration were estimated using data and relationships discussed by Rowe and Chou (1970) and Kestin and others (1981), respectively.

We assigned mineralogy in the 3-D upscaled geocellular model based on X-ray diffraction analyses results (Table 12) measured by Carey and others (2007) who analyzed core samples collected from Cisco and Canyon Groups. In their analyses, dolomite and anhydrite were not detected. However, previous geological studies described in Section "*Geologic Descriptions*" indicated that the Cisco and Canyon Groups were highly altered by calcitization and dolomitization processes and included minor amounts of anhydrite, dolomite, sand, and shale (Bergenback and Terriere, 1953; Myers and others, 1956; Raines and others, 2001). Therefore, we modified mineralogy to include dolomite and anhydrite (Table 12).

Table 12: Volume Fractions, Surface Areas, and Kinetic Rates Assigned in the Upscaled Geocellular Model

Mineral	Weight Percent (Carey, 2007)	Modified Weight Percent	Volume Fraction	Surface Area (m²/m³)	Activation Energy (J/mol)	Logk₂₅ (mol/m²s)	Model Kinetic Rate
Calcite	0.82	0.62	0.6063	586.72	41870	-8.80	Svensson and Dreybrodt, (1992)
Dolomite	0	0.1	0.0933	559.86	41870	-9.22	White, (2005)
Kaolinite	0.01	0.01	0.0110	6115.38	62760	-13.00	Nagy, (1995)
Anhydrite	0	0.1	0.0892	535.35	41870	-8.80	Same as calcite
Quartz	0.03	0.03	0.0303	606.87	87500	-13.90	Tester and others, (1994)
Illite	0.02	0.02	0.0193	5781.82	58620	-14.00	Knauss and Wolery, (1989)
Ankerite	0.12	0.12	0.1043	521.31	41870	-10.22	Estimated from Dolomite
Dawsonite	0	0	0	657.02	62760	-9.09	Hellevang, (2005)
Siderite	0	0	0	401.52	41870	-10.22	Estimated from Dolomite

Geologic studies suggest that dawsonite specifically is considered to be a late-stage mineral deposited in natural CO_2 reservoirs (Baker and others, 1995; Moore and others, 2005). Due to this reason, the possibility of dawsonite precipitation during CO_2 storage processes has been studied with various experiments (Kaszuba and others, 2005; Hellevang and others, 2005; Bénézeth and others, 2007). In the SACROC Unit, Carey and others (2007) previously found a single X-ray diffraction peak of dawsonite in the SACROC core and indicated the possibility of dawsonite precipitation. Therefore, in the 3-D upscaled geocellular model, dawsonite was chosen for the secondary minerals with siderite.

Since no direct measurements of BET-surface areas are available, the specific surface area ($A_m = (A \times v \times \rho_m)/(V \times M_w)$) proposed by Knauss and others (2005) was calculated using grain volume (V:[m^3]), grain surface area (A:[m^2]), molar volume (v:[m^3/mol]), molecular weight (M_w:[g/mol]), and mineral density (ρ_m:[g/m^3]), as detailed in Table 12. To calculate V and A, the mineral grains are assumed to be spherical. An average grain radius of 0.00125 m is assumed for all minerals except clay minerals (0.000125 m) such as kaolinite and illite.

The kinetic rate law for the dissolution and precipitation of minerals is from Lasaga (1984) with a temperature-dependent rate constant derived by Arrhenius' law:

$$r_m = \text{sgn}\left(A_m k_{25} \exp\left[-\frac{E_a}{R}\left(\frac{1}{T} - \frac{1}{298.15}\right)\right]\left(1 - \frac{Q_m}{R_m}\right)\right) \quad (8)$$

Where, m is the mineral index, r is the dissolution/precipitation rate [$mol/m^3 s$] (positive value indicates precipitation and negative value indicates dissolution), A_m is the reactive surface area [m^2/m^3], k_{25} is the kinetic rate coefficient at 25 °C [$mol/m^2 s$], E_a is the activation energy [J/mol], R is the gas constant [$8.314\ J/mol\ K$], K_m is the equilibrium constant for mineral reaction, and finally, Q_m is the activity product. As shown in eq 8, the kinetic rate law is limited to describe the growth of secondary minerals in relation to nucleation, preferential growth, and Ostwald ripening, with which only a few studies have been previously concerned (Steefel and van Cappellen, 1990; Ozkan and Ortoleva, 2000). In addition, the kinetic rate constant is often expressed as the sum of three mechanisms such as neutral, acid, and base mechanisms (Lasaga and others, 1994; Palandri and Kharaka, 2004). Among these three mechanisms, only neutral mechanism is considered here for simplicity. The kinetic rate coefficients and activation energies of different minerals assigned in the 3-D upscaled geocellular model are summarized in Table 12. Some kinetic data are taken directly from the scientific literature and others are set to minerals with known kinetic properties.

Thermodynamic parameters, including equilibrium constants, were chosen from the SOLMINEQ.88 and PHREEQC databases (Kharaka and others, 1989; Parkhurst and Appelo, 1999). Particularly, the equilibrium constant of ankerite, which is a solid-solution between siderite and dolomite, varies

with its composition. In a natural system, a binary soild-solution, $Ca(Fe_xMg_{1-x})(CO_3)_2$, where $Mg^{2+}>>Fe^{2+}$ has been observed (Mozley and Hoernle, 1990), but the end-member ankerite, $CaFe(CO_3)_2$, has not (Chai and Navrotsky, 1996). Therefore, the composition of ankerite is assumed to be $CaFe_{0.25}Mg_{0.75}(CO_3)_2$ and its equilibrium constant is calculated from a regular solid-solution approach (Appelo and Postma, 1993) using free energy data from Wood and Garrels (1992). The detailed calculation of ankerite equilibrium constant is described in Han (2008).

For the activity coefficient calculation, the B-dot model (Helgeson, 1969) was implemented in this study because this model is relatively easy to incorporate new species and estimate activity coefficients under high temperature conditions. However, the Pitzer model (Pitzer, 1987) can accurately describe the behavior of electrolyte solutions especially at high ionic strength fluid (Monnin, 1989; Lichtner and Felmy, 2003; Zhang and others, 2006), and furthermore, the Pitzer's ion interaction parameters for various aqueous species are becoming more available (Harvie and others, 1984; Azaroual and others, 1997; Felmy and others, 1994; Accornero and Marini, 2009). In CO_2 storage processes, the reservoir fluids into which supercritical-phase CO_2 is injected typically have high ionic strengths. Therefore, the application of the Pitzer model can improve the prediction of activity coefficients compared to the B-dot model implemented in this work. Recently, Gaus (2010) discussed the essentials of the Pitzer model in a CO_2 storage problem. From the discussion in Gaus (2010), the application of the Pitzer model coupling into reactive transport simulator, TOUGHREACT, is currently ongoing (Zhang and others, 2006), and the development of the complete database for the Pitzer ion interaction parameters is going to be an essential task. Finally, we acquired the initial concentration of brine chemistry (Table 13) in the upscaled geocellular model by batch geochemical modeling with the input of average values of brine water chemistry data (Table 8) and mineralogy (Table 12).

Assignment of CO_2 Injection and Production Wells

More than 300 wells have been used for CO_2 injection and production over the last 35 years in the SACROC northern platform. Because the sizes of grid elements in the upscaled geocellular model are larger than the distance between individual wells in the actual

field, we were forced to lump groups of wells within each grid element. Each was assigned as an inverted 5-spot pattern, and as such we could not assign the actual number of injection and production wells. Consequently, we implemented 23 pumping (P) wells and 22 injection (I) wells in the 3-D upscaled model (Figure 46D). In addition, both injection and production wells are partially penetrated with the intervals of 10 to 20 m, approximately 40 m above from the bottom of the model.

We simulated CO_2 injection and production in the field for a 30-year period, from 1972-2002. During this field-operation period, a net of about 6.9 million metric tons of CO_2 (6,944,587,674 kg) has been stored in the SACROC northern platform (see the discussion in "Sources and Sinks: Actual CO_2 Injection and Production Histories"). Nevertheless, in the 3-D upscaled geocellular model, the exact field injection

Table 13: Description of Primary and Secondary Species and their Initial Concentrations

Primary Species	Concentration (mol/l)		Secondary Species
H^+	3.981E-7 (pH=6.4)		CO_3^{2-}
K^+	3.981E-7	Estimated	$NaCl(aq)$
Na^+	1.094E0		$NaCO_3^-$
Ca^{2+}	1.314E-1		$NaHCO_3(aq)$
Mg^{2+}	5.700E-2		$CaCO_3(aq)$
$SiO_2(aq)$	2.345E-3	Estimated	$CaHCO_3^+$
Al^{3+}	2.318E-11	Estimated	$MgCO_3(aq)$
Fe^{2+}	8.850E-4		$MgHCO_3^+$
Cl^-	1.391E0		$Al(OH)_4^-$
HCO_3^-	5.300E-2		$Al(OH)_3(aq)$
SO_4^{2-}	4.050E-2		$Al(OH)_2^+$
			$Al(OH)^{2+}$
			$FeCl_4^{2-}$
			$FeCl^+$
			$Fe(OH)_2$
			$Fe(OH)^+$
			$H_4SiO_4(aq)$

and production history do not match because of issues associated with the scale of the upscaled grid. Rather, net storage at the end of injection period was matched only. In the upscaled model, the CO_2 net storage was about 6.7 million metric tons (6,745,407,000 kg). Consequently, the relative error of CO_2 net storage between the actual field and the model is 2.9%.

Results: Spatial distribution of hydrostratigraphic (mobile)- and residual-trapped CO_2.— Figures 48A and 48B respectively show the spatial distribution of supercritical-phase CO_2 and the associated $k_r^{CO_2}$ values, 100 years after CO_2 injection starts (year 2072). Due to the difficulty of showing three-dimensional distributions, two-dimensional cross-sectional views/slices are presented instead. By comparing the spatial distribution between CO_2 saturation (Figure 48A) and associated $k_r^{CO_2}$ values (Figures 48B), it is possible to distinguish the location of free (mobile) CO_2 and residual (immobile) CO_2. By definition, supercritical-phase CO_2 becomes mobile when the $k_r^{CO_2}$ value is greater than zero. In reverse, the supercritical-phase CO_2 becomes immobile, and its $k_r^{CO_2}$ value is equal to zero. In Figures 48A, CO_2 saturation is greater than zero within the CO_2 plumes. However, Figures 48B shows that although certain grid-blocks have CO_2 saturations greater than zero, they have a zero value for $k_r^{CO_2}$. These grid-blocks indicate where CO_2 is trapped as a residual form.

According to Juanes and others (2006), mobile CO_2 is located at the front of the CO_2 plume, while residual-trapped CO_2 is located at the tail of the CO_2 plume. Similarly, in this simulation, values were greater than zero at the front of the CO_2 plume, indicating the presence of mobile CO_2. However, values were zero at the tail of the CO_2 plume although values of CO_2 saturations were not zero, indicating that supercritical-phase CO_2 was stored in a residual form at the tail of the CO_2 plume. Finally, the distribution of aqueous-phase CO_2 imitates the distribution patterns of supercritical-phase CO_2, but with a wider extent (Figures 48C).

Results: Spatial and temporal distribution of aqueous species and minerals.—For most minerals (especially silicate minerals), two hundred years is an insufficient time to reach equilibrium with reservoir fluids. Even, after 200 years, all minerals are still dissolving or precipitating. Generally, mineral changes initiate as the dissolution of CO_2 lowers the pH of reservoir brine, which has also been observed in previous laboratory and field experiments (Bowker and Shuler, 1991; Klusman, 2003; Kaszuba and others, 2005; Kharaka and others, 2006). Decreasing pH subsequently induces changes in aqueous concentrations and minerals. In this simulation, initial pH of the reservoir fluid was 6.4 at year 1972 and decreases to approximately 4.5 at year 2072 after 100 years (Figures 49A). The pH does not decrease below 4.5 because the carbonate rock acts as a
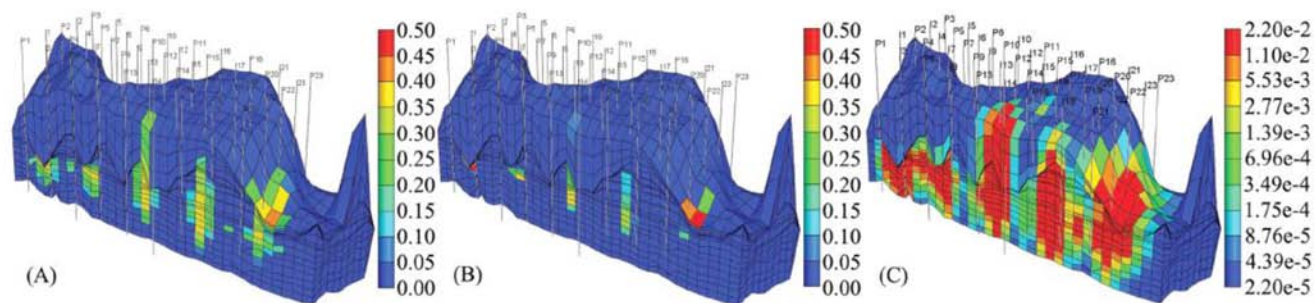
Figure 48: Two-dimensional cross-section view at year 2072 (100 years after CO_2 injection starts): (A) saturation of supercritical-phase CO_2 with the linear scale, (B) relative permeability ($k_r^{CO_2}$) of supercritical-phase CO_2 with the linear scale, and (C) mole fraction of aqueous-phase CO_2 with the logarithmic scale.
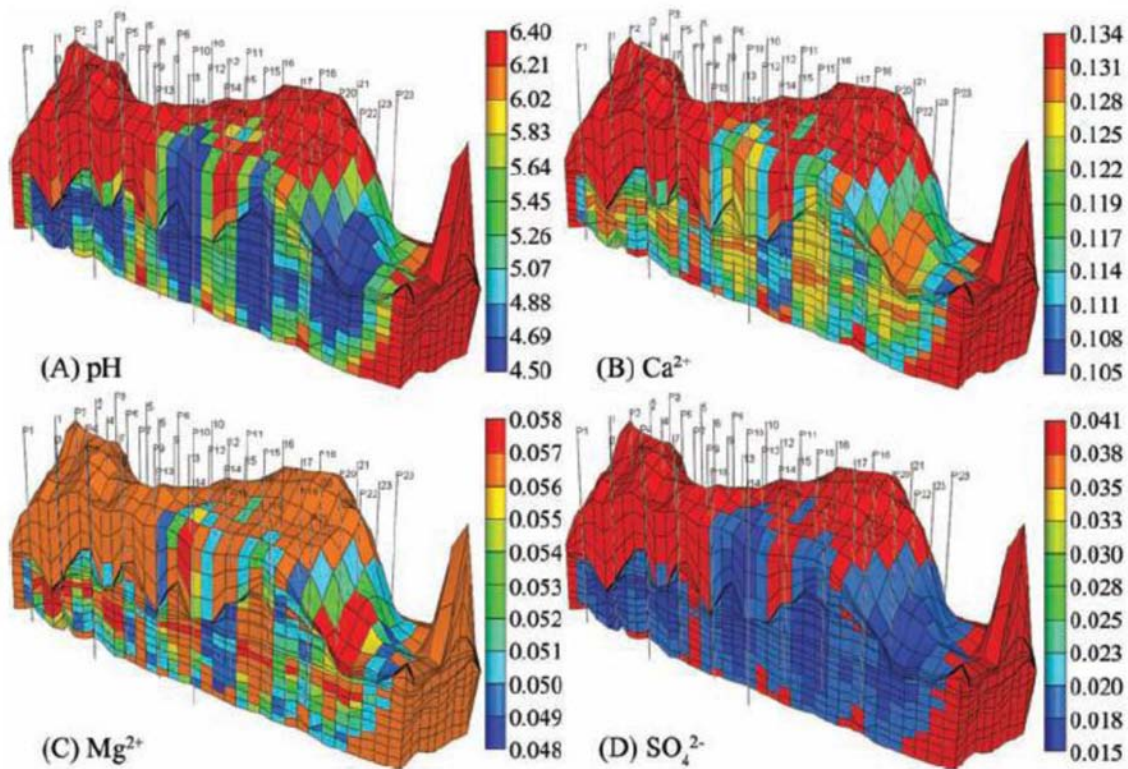
Figure 49: Two-dimensional cross-section view at year 2072 (100 years after CO_2 injection starts): (A) pH, molalities of (B) Ca^{2+}, (C) Mg^{2+}, and (D) SO_4^{2-}.

buffer. Specifically, the predicted pH (Figures 49A) in the brine-only model was decreased more than pH observed in the actual SACROC oil field (Table 8). Although various processes and uncertainties among model parameters could result in the discrepancy of model predicted pH, we presume that the one of the main causes would be the presence of oil in the field.

Calcite, the major mineral in the SACROC Unit, predominantly dissolves during a 200-year simulation. Both anhydrite and dolomite are the major minerals precipitated in this same period. Dawsonite and ankerite are also precipitated but in minor amounts, respectively. In addition to the carbonate minerals, kaolinite and illite respectively precipitated and dissolved. The associated mineral reactions in this model are:

$$CaSO_4(Anhydrite) = Ca^{2+} + SO_4^{2-} \tag{9}$$

$$CaCO_3(Calcite) + H^+ = Ca^{2+} + HCO_3^- \tag{10}$$

$$CaMg(CO_3)_2(Dolomite) + 2H^+ = Ca^{2+} + Mg^{2+} + 2HCO_3^- \tag{11}$$

$$CaFe_{0.25}Mg_{0.75}CO_3(Ankerite)\ 2H^+ = Ca^{2+} + 0.25Fe^{2+} + 0.75Mg^{2+} + 2HCO_3 \tag{12}$$

$$FeCO_3(Siderite) + H^+ = Fe^{2+} + HCO_3^- \tag{13}$$

$$NaAl(CO_3)(OH)_2(Dawsonite) + 3H^+ = Na^+ + Al^{3+} + HCO_3^- + 2H_2O \tag{14}$$

$$Al_2Si_2O_5(OH)_4(Kaolinite) + 6H^+ = 5H_2O + 2SiO_2(aq) + 2Al^{3+} \tag{15}$$

$$K_{0.6}(Mg_{0.25}Al_{1.8})(Al_{0.5}Si_{3.5})O_{10}(OH)_2(Illite) + 8H^+ = 0.25Mg^{2+} + 0.6K^+ + 2.3Al^{3+} + 3.5SiO_2 + 5H_2O \tag{16}$$
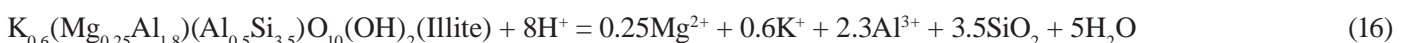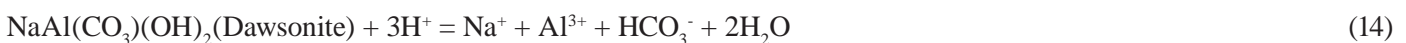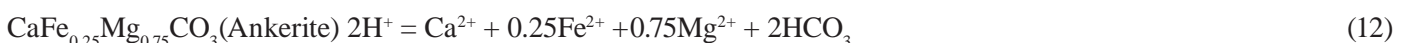
Mineral precipitation and dissolution patterns are closely related to spatially varying aqueous species. Figure 49B shows the spatial distribution of Ca^{2+} ions. Calcite dissolution (eq 10 and Figure 50A) supplies Ca^{2+} ions to the reservoir brine and triggers the precipitation of dolomite (eq 11 and Figure 50B), anhydrite (eq 9 and Figure 50C), and ankerite (eq 12 and Figure 50D). Especially, CO_2 injection induces dolomitization process with concurrent calcite dissolution. Previous laboratory studies suggested that elevated temperature, exceeding 60 °C, initiates precipitation of dolomite (Usdowski, 1994) although dolomite generally does not precipitate at surface temperature. Similarly, the model predicts that subsurface reservoir temperature is close to 60 °C in the SACROC Unit and a high Mg^{2+} concentration in brine fluid initiates dolomite precipitation.
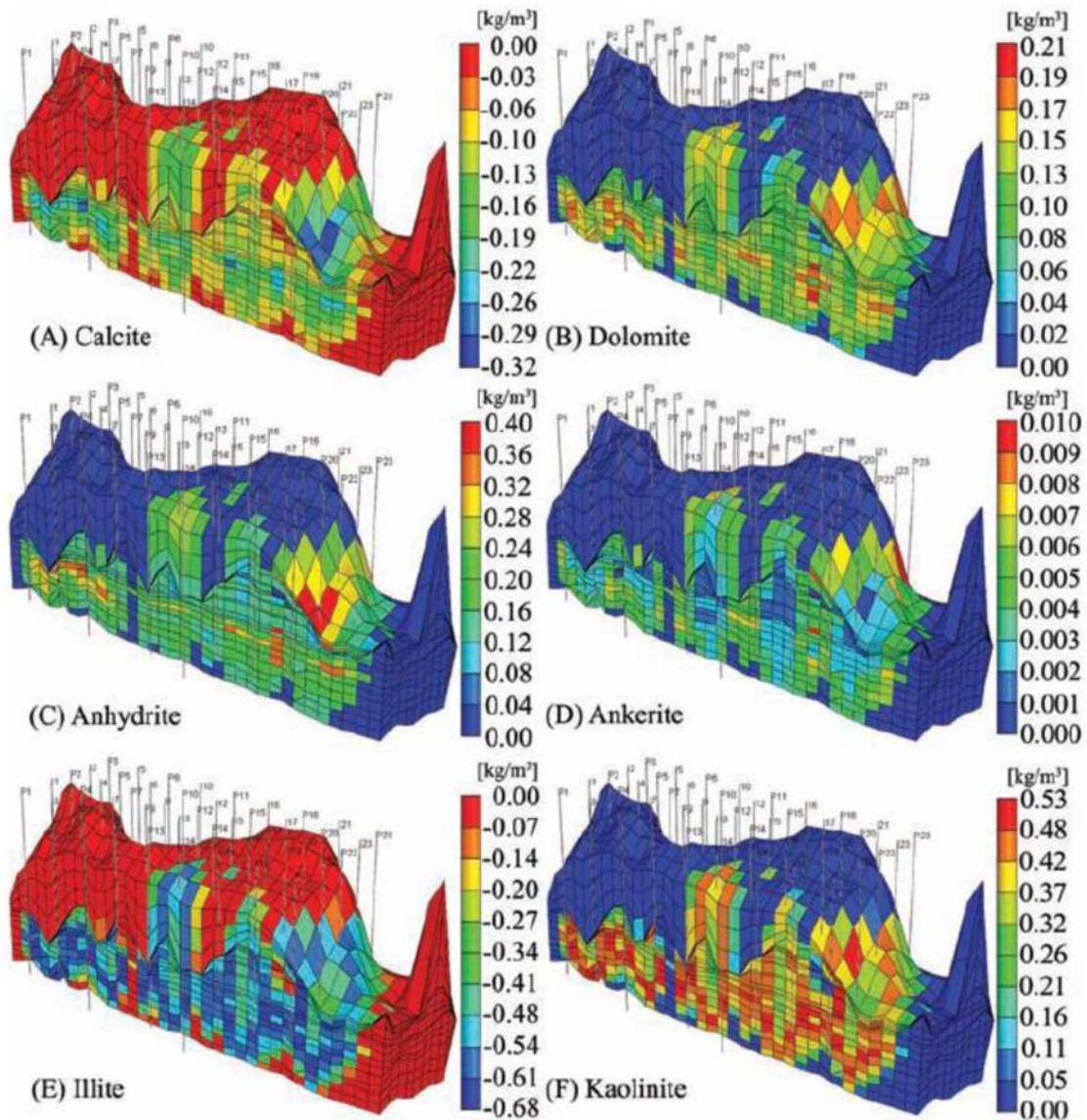
Figure 50: Two-dimensional cross-section view of minerals (kg/m³) at year 2072 (100 years after CO_2 injection starts): (A) calcite, (B) dolomite, (C) anhydrite, (D) ankerite, (E) illite, and (F) kaolinite.

Figure 49C shows the spatial distribution of Mg^{2+} ions, which are consumed during the precipitation of dolomite (Figure 50B) and ankerite (Figure 50D), and concurrently, supplied from the dissolution of illite (Figure 50E). Mg^{2+} concentration in brine fluid was initially 0.057 molality and was depleted to approximately 0.050 molality (Figure 49C) after 100 years (year 2072), suggesting that the Mg^{2+} ion consumption for dolomite and ankerite precipitations is greater than Mg^{2+} ions supply from illite dissolution. In addition to illite, other Mg-bearing aluminosilicates such as montmorillonite and saponite occur naturally. Although these two minerals were not implemented in this simulation, the presence of these minerals in a natural system could affect both Mg^{2+} and Al^{3+} concentration. Finally, calcite dissolution and high SO_4^{2-} concentration in reservoir brine induces anhydrite precipitation (Figure 50C). Due to anhydrite precipitation, SO_4^{2-} concentration in the brine fluid decreased from an initial 0.04 molality to 0.018 molality after 100 years (Figure 49D).

Reactions involving aluminosilicate minerals have been observed experimentally by Bertier and others (2006). In this SACROC simulation, illite and kaolinite respectively dissolved and precipitated (Figure 50E and 50F). Although kinetic rates of aluminosilicate minerals are slow, the chemical reactions of such aluminosilicate minerals can change the concentration of Al^{3+} ions in brine and cause dawsonite to precipitate (Xu and others, 2004; Hellevang and others, 2005; Audigane and others, 2007). In this simulation, Al^{3+} is supplied from illite dissolution and consumed for the precipitation of kaolinte and dawsonite. Through the simulation period, Al^{3+} ions increase from 10^{-11} to 10^{-7} molality due to the dissolution of illite minerals. Consequently, the change in Al^{3+} ion concentration causes precipitation of a small amount of dawsonite after 100 years. Again, the presence of other aluminosilicate minerals in a natural system could affect this process.

In addition to the spatial distribution of minerals, the temporal evolutions of net changes of minerals per the total model volume (kg per m^3) are predicted during the 200-year of simulation period and plotted in Figure 51A and 51B. Over 200 years, approximately 0.12 kg per m^3 of dolomite, 0.11 kg per m^3 of anhydrite, 0.003 kg per m^3 of ankerite, 0.003 kg per m^3 of dawsonite are precipitated, and about 0.076 kg per m^3 of calcite is dissolved (Figure 51A). In addition to carbonate minerals, 0.43 kg per m^3 of kaolinite, 0.11 kg per m^3 of quartz are precipitated, and about 0.56 kg per m^3 of illite is dissolved (Figure 51B).
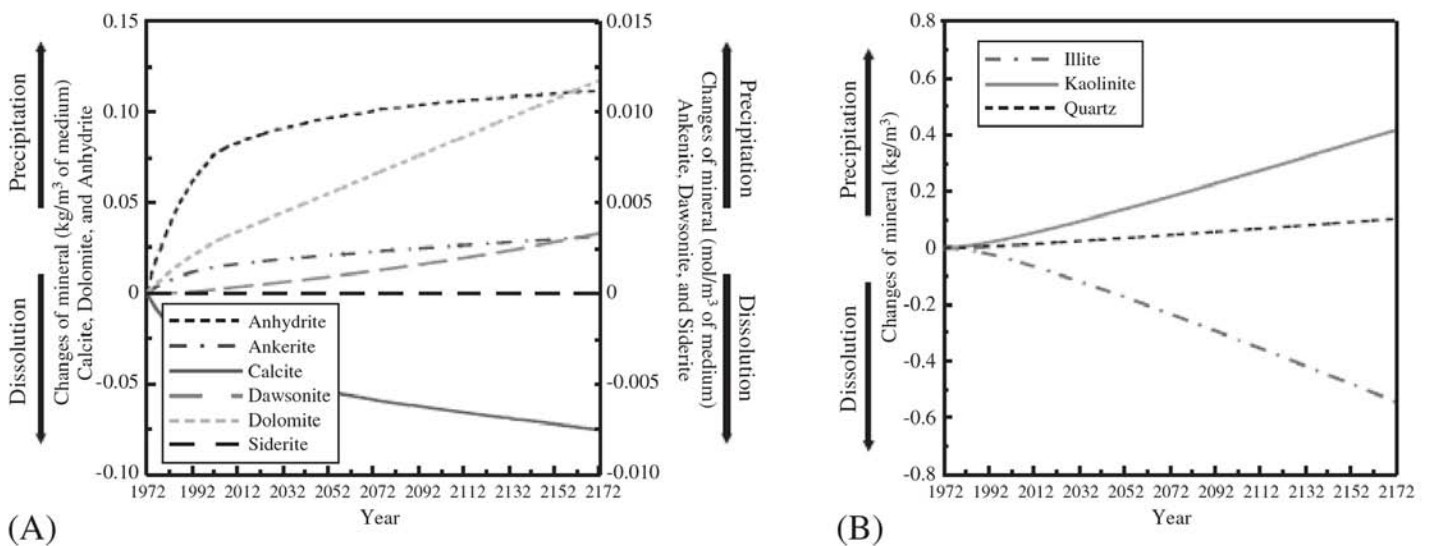
Figure 51: Temporal evolution of net changes of minerals per the total model volume (kg per m^3): (A) carbonate minerals and (B) silicate and clay minerals.

The mineral changes of simulated dissolution and precipitation cause changes in porosity. The altered porosity field is shown in Figure 52A, indicating the net reduction $(\Delta\phi = \phi_{initial} - \phi_{current})$ of porosity due to CO_2 injection. After 100 years, mineral precipitation due to CO_2 storage causes the reduction of porosity by approximately 7.5e-5. The corresponding changes of permeability are calculated from the Kozeny-Carman model:

$$\frac{k_{current}}{k_{initial}} = \left(\frac{\phi_{current}}{\phi_{initial}}\right)^3 \left(\frac{1 - \phi_{initial}}{1 - \phi_{current}}\right)^2 \qquad (17)$$

where ϕ is the porosity, k is the permeability (m²). The altered permeability field ($k_{current}/k_{initial}$) is shown in Figure 52B. The corresponding permeability reduction ($k_{current}/k_0$) was about 0.993.

Results: Quantification of CO_2 trapping mechanisms.— Figure 53A summarizes the CO_2 mass stored in different forms, with CO_2 trapping mechanisms detailed in injection and post-injection periods. During the injection period (1972–2002), 6.7 million metric tons of CO_2 are stored into the Cisco and Canyon Groups of the 3-D upscaled geocellular model. In this period, the CO_2 saturation gradually increases near the injection wells. At the same time, the CO_2 plume migrates either vertically or horizontally through preferential flow paths due to the injection-induced pressure. Specifically, the amount of mobile CO_2 increases up to 5.0 million metric tons without increasing immobile CO_2 until the end of injection period, suggesting that a drainage process [CO_2 (=the non-wetting phase) displaces brine (=the wetting phase)] occurs. In addition, CO_2 injection increases reservoir pressure,
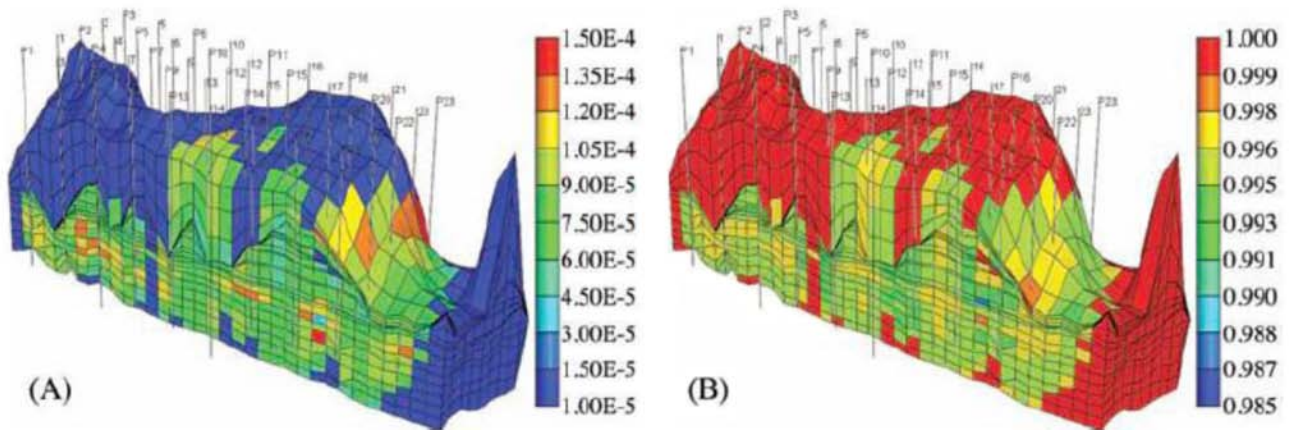
Figure 52: Changes of porosity ($\Delta\phi=\phi_{initial}-\phi_{current}$) and permeability ($k_{current}/k_{initial}$) at year 2072 (100 years after CO_2 injection starts): (A) porosity and (B) permeability.
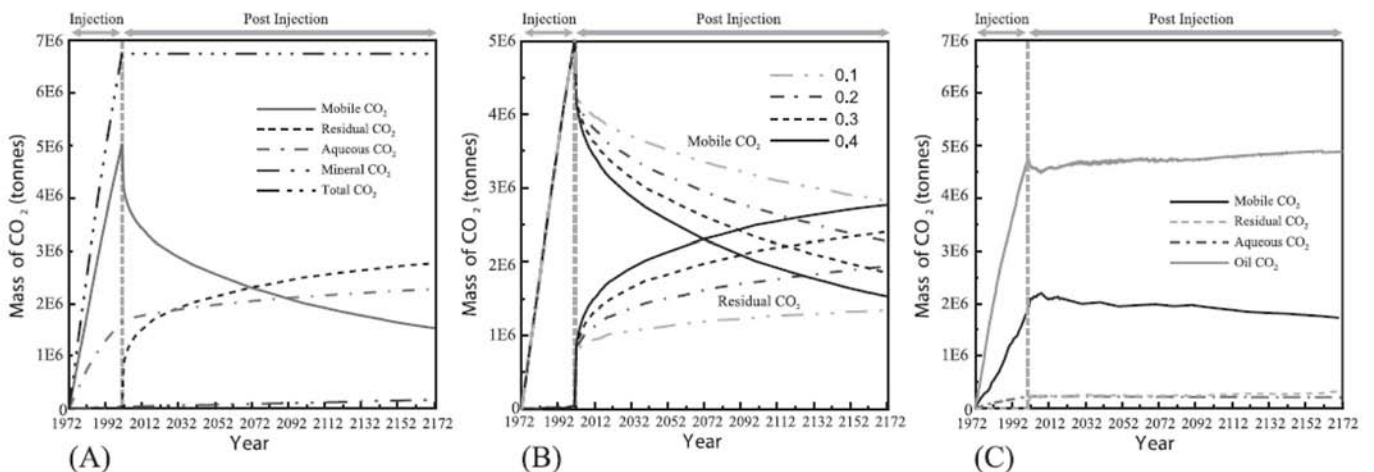
Figure 53: (A) CO_2 trapping mechanisms in brine-only model as a function of time, (B) sensitivity studies of mobile and residual-trapped CO_2 with S_{gr}^{max} in brine-only model, and (C) CO_2 trapping mechanisms in brine+oil model as a function of time.

leading to the increased CO_2 dissolution in brine. In result, the mass of solubility-trapped CO_2 sharply increases up to 1.7 million metric tons at the end of the injection period.

After CO_2 injection ends (2002-2172; post injection period), the CO_2 plume starts to migrate upward due to the buoyant force associated with the density contrast between reservoir brine and CO_2. While the CO_2 plume migrates vertically, some CO_2 becomes trapped as a residual form at the tail of the CO_2 plume where imbibition (brine displaces CO_2) occurs. Due to this process, the amount of residual-trapped CO_2 increases dramatically immediately after CO_2 injection stops, and consequently, the amount of mobile CO_2 decreases (Figure 53A). Simulation results suggest that the vertical CO_2 migration after injection stops is the critical factor governing the residual CO_2 trapping mechanisms. After 200 years of CO_2 injection, the mass of mobile CO_2 and immobile CO_2 respectively becomes 1.5 million and 2.8 million metric tons. Finally, the mass of solubility-trapped CO_2 continues to increase up to 2.3 million metric tons, but at a slower rate because injection-induced CO_2 partial pressure decreases almost immediately after CO_2 injection ceases. Relatively small amounts (0.17 million metric tons of CO_2) of minerals precipitate after 200 years.

As shown, previous researchers concurred that the most effective short-term storage mechanism is residual CO_2 trapping, and its sensitivity is strongly dependent on S_{gr}^{max} in the Land hysteresis equation shown as eq 7 (Kumar and others, 2005; Juanes and others, 2006; Doughty, 2007). However, until now, only one laboratory dataset (Suekane and others, 2008) predicting S_{gr}^{max} in the supercritical CO_2/brine system has been available. Due to this reason, many researchers rely on one fitting equation developed with data from gas reservoirs (Holtz, 2002). Therefore, we performed sensitivity studies of CO_2 trapping mechanisms with S_{gr}^{max}. Simulation results predicted that the amount of residual-trapped CO_2 increases with larger (Figure 53B). For example, residually trapped CO_2 with 0.1 S_{gr}^{max} was 1.35 million metric tons after 200 years and that with 0.4 S_{gr}^{max} was 2.78 million metric tons. Results suggest that the predicted amount of residually trapped CO_2 can be doubled with the choice of S_{gr}^{max}.

SACROC CO_2 Trapping Model – Oil and Brine

Initial and Boundary Conditions

The initial conditions for pressure and temperature distribution and boundary conditions are the same as those described in the previous section "*SACROC CO_2 Trapping Model – Brine Only*". However, the initial condition for fluid saturation is different from that of the brine-only model. The reservoir is assumed to be saturated with both water (0.28) and oil (0.72), following reservoir characterization details provided by Vest (1970). The oil phase is regarded as a mixture of 11 different gas components. The initial oil composition used is from Dicharry and others, (1973), summarized in Table 14.

Table 14: Initial Oil Composition (Dicharry and others, 1973) in the Upscaled Geocellular Model

Oil Composition	Mol	Molecular Weight
CO_2	0.0032	44.01
N_2	0.0083	28.01
C1(Methane)	0.2865	16.04
C2(Ethane)	0.1129	30.07
C3(Propane)	0.1239	44.10
I-C4(I-Butane)	0.0136	58.12
N-C4(N-Butane)	0.0646	58.12
I-C5(I-Pentane)	0.0198	72.15
N-C5(N-Pentane)	0.0251	72.15
FC6(Hexane)	0.0406	86.00
C7+(Heptanes plus)	0.3015	275.00

Transport Input Data and Well Assignment

Oil densities are calculated from the Peng-Robinson equation of state (Peng and Robinson, 1976) and Oil viscosity is estimated from Jossi and others (1962). Finally, CO_2 solubility in oil is predicted from flash calculations, which are decoupled from the transport equation and solved using the Quasi Newton Successive Substitution (Nghiem, 1983). The $k_r^{CO_2}$ curve and its hysteretic effect is the same as those in brine-only model. The k_r^{oil} curve is developed after extrapolating data from the SACROC core measured at 50 °C and

1.4 MPa (Rohan and Haggerty, 1996). Finally, the feature of well assignments and performance period were the same as those described in the previous section "*Assignment of CO_2 injection and production wells*".

Results: Quantification of CO_2 trapping mechanisms. Figure 53C shows simulation results describing the temporal evolution of the CO_2 mass stored in the SACROC model saturated with both brine and oil. Specifically, the slope of oil-CO_2 curve is steep during the period between 1972 to 2002. Significant amounts of CO_2 (about 4.5 million metric tons) dissolved into oil during this period. Compared to CO_2 dissolved in oil, only a small amount of CO_2 (about 0.2 million metric tons) dissolves in the brine in the same period. The difference of CO_2 dissolution in both oil and brine is caused by the difference of CO_2 solubility in both fluids and initial fluid saturation. The model predictions show that the approximate CO_2 solubility was respectively 0.010~0.018 mole fraction in brine and 0.3~0.6 mole fraction in oil at this reservoir condition. That is to say, CO_2 solubility in oil was about 30~40 times greater than that in brine. Moreover, oil saturation (0.72) was greater than brine saturation (0.28) in this model indicating that more oil volume is available for CO_2 dissolution. Therefore, the oil-solubility trapping is significantly greater than the brine-solubility trapping

in this model. The amount of mobile CO_2 increased up to about 2.1 million metric tons at the end of the injection year (Figure 53C). Similar to the brine-only model, no CO_2 is trapped as a residual form during the injection period (1972–2002). Overall, the dominant CO_2 trapping mechanism is oil trapping, with about 4.5 million metric tons of CO_2 dissolved in the oil during the full 200-year simulation periods. In addition, about 2.1 million metric tons of CO_2 is stored as a mobile form.

In the previous brine-only model, the amount of mobile CO_2 is dramatically decreased and the amount of residual CO_2 is suddenly increased after CO_2 injection stops (Figure 53A). However, in the brine + oil model, the relative amounts of both mobile and residual CO_2 do not change over time (Figure 53C). Further, compared to the amount of residual-trapped CO_2 in the brine-only model, residual-trapped CO_2 in the brine + oil model is significantly less (Figure 53C). To investigate the difference of the amount of residual-trapped CO_2 in both simulations, the saturations of supercritical-phase CO_2 at year 2072 were plotted and compared (Figures 48A and 54). The comparison of CO_2 plume saturation shows that CO_2 migration behavior is distinctively different in both simulations. After 100 years, supercritical-phase CO_2 in the brine-only
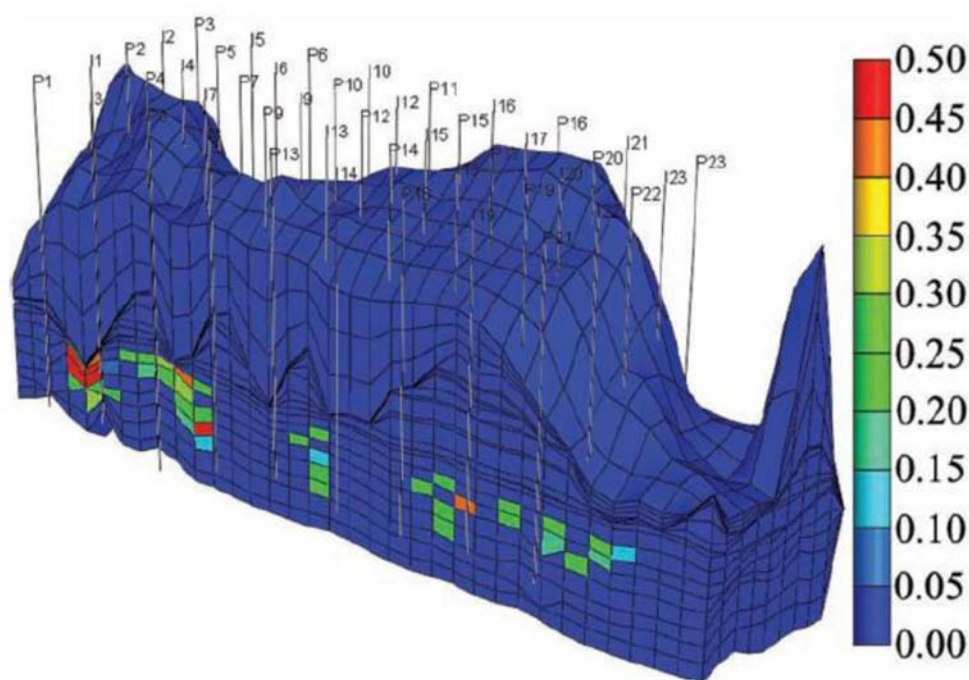
Figure 54: Two-dimensional cross-section view of saturation of supercritical-phase CO_2 in brine + oil model at year 2072 (100 years after CO_2 injection starts).

model migrated vertically and several CO_2 plumes were able to reach the top of the Cisco and Canyon Groups (Figure 48A). The amount of residual-trapped CO_2 increased at the tail of the CO_2 plumes while supercritical-phase CO_2 plumes migrated vertically. However, in the brine + oil model, supercritical-phase CO_2 did not migrate vertically but stayed near the injection wells with a high CO_2 saturation (Figure 54). In general, supercritical-phase CO_2 in the brine + oil model is stored as a mobile form due to its high CO_2 saturation but does not migrate vertically due to smaller density contrast between oil and supercritical-phase CO_2 and larger CO_2 solubility in oil. Therefore, mobile CO_2 in the brine + oil model behaves like residual-trapped CO_2.

To evaluate the difference of CO_2 vertical migration behavior between brine-only and brine + oil models (Figures 48A and 54), the density of gas, brine, and oil phases in this model were compared. Model prediction in brine + oil model shows that the densities of CO_2, oil, and brine are, respectively, about 700~800 kg/m³, 800 kg/m³, and 1100 kg/m³ at these reservoir conditions. Since oil is a dominant fluid (72 % saturation), the density contrast between supercritical-phase CO_2 and oil is smaller than about 100 kg/m³, which is 3~4 times smaller than that between supercritical-phase CO_2 and brine. Since the density contrast between oil and supercritical-phase CO_2 is small, the vertical CO_2 migration is small (In the simulations of brine+oil model, no CO_2 plume reaches the top of the Cisco and Canyon Groups after 200 years). Consequently, the amount of residual-trapped CO_2 is not significant (less than 0.3 million metric tons) in this model (Figure 53C). In addition to the contrast of fluid densities, CO_2 mobility is reduced when three phases coexist, e.g., injecting CO_2 in a brine + oil reservoir, as opposed to injecting into a reservoir with brine only. In the brine + oil model representing a three-phase environment, the vertical movement of supercritical-phase CO_2 will be relatively retarded. Furthermore, significant CO_2 solubility in the oil phase reduces the volume of supercritical-phase CO_2 in brine + oil model and reduces buoyant force. In summary, the buoyancy-driven force was lower in the brine + oil reservoir model due to less contrast in fluid densities, smaller mobility, and larger CO_2 solubility in the oil phase. Consequently, supercritical-phase CO_2 did not migrate vertically but tended to stay closer to the injection wells.

Summary and Conclusions

The main purpose of this research was to predict CO_2 trapping mechanisms in the SACROC northern platform where about 7 million metric tons of CO_2 have been injected for the purpose of enhanced oil recovery from 1972 to 2002. This model was carefully developed with a dataset that includes injection/production history data since 1948 and water chemistry data from both reservoir brine and shallow groundwater. First, a 3-D, high-resolution, geocellular model describing the detailed reservoir structure and heterogeneity was constructed. After the renormalization process for reducing the number of model elements to manageable levels to fit on a single workstation, two models evaluating CO_2 trapping mechanisms in the SACROC northern platform were developed. Initial/boundary conditions, and other parameters in this model were carefully chosen based on the results of data analyses such as groundwater chemistry and CO_2 injection/production history. The first model was designed for simulating CO_2 trapping mechanisms in a reservoir only saturated with brine. The second model was designed for simulating CO_2 trapping mechanisms in a reservoir saturated with both brine and oil. As far as we know, this is the first attempt to compare the fate and distribution of supercritical-phase CO_2 in a reservoir containing both oil and brine versus a reservoir containing brine only. Major conclusions in this work are as follows:

1. Incorporating geologic knowledge, geophysical logs, and seismic surveys provided a foundation for interpreting 3-dimensional subsurface structures. The geocellular model reveals that the Upper Canyon Group is represented as a thick, highly porous zone (Figure 44B) and the Middle/Lower Canyon Group consists of several layered porosity zones separated by low porous carbonate mud.

2. Direct application of the subsurface structure model to develop the flow and transport models is hindered due to the lack of currently available computer resources. The renormalization technique successfully upscaled the model from 9,450,623 to 15,470 elements with a preservation of the variation of heterogeneity (Figures 46A-D).

3. Modeled CO_2 fugacity of reservoir fluids in the Cisco and Canyon Groups was significantly increased during the CO_2 injection period (Table 8) but it did not vary in shallow groundwater above the Wolfcamp

Shale Formation (Table 11) suggesting that the Wolfcamp Shale Formation typically acts as a suitable seal in the SACROC Unit. However, analysis of water chemistry also revealed that a few shallow groundwater samples underwent local contamination with reservoir brine possibly due to the downward recharge of recycled reservoir brine from the surface during enhanced oil recovery or upward leakage of CO_2-saturated brine through the Wolfcamp Shale Formation.

4. CO_2 trapping mechanisms in the brine-only model showed two distinctive periods (Figure 53A). During injection period (1972~2002), most supercritical-phase CO_2 is stored as mobile phase. After CO_2 injection ceases, the amount of mobile CO_2 dramatically decreases and residual-trapped CO_2 consequently increases. Therefore, during post injection period (2002~2172), both the residual trapping and solubility trapping mechanisms become dominant. In addition, the amount of residually trapped CO_2 is strongly dependent on the S_{gr}^{max} in Land Equation (Figure 53B).

5. In the reservoir model with oil (72%) and brine (28%) phases, CO_2 trapping mechanisms do not vary distinctly over time (Figure 53C). The dominant trapping mechanism is oil trapping. Most supercritical-phase CO_2 is stored as a mobile phase near the injection wells and does not migrate: behaving much like residually trapped CO_2. This occurs because of a lower contrast in fluid densities, smaller mobility, and larger CO_2 solubility in oil phase.

6. Mobile CO_2 is located at the front of the CO_2 plume where drainage is dominant (CO_2 displaces water), while residually trapped CO_2 is located at the tail of the CO_2 plume where imbibition is dominant (water displaces CO_2).

7. Injected CO_2 is stored as several different forms of minerals in the brine-only model. Calcite (0.076 kg per m³), the major mineral in the SACROC Unit, predominantly dissolves after a 200-year simulation. Both anhydrite (0.11 kg per m³) and dolomite (0.12 kg per m³) are the major minerals precipitated in the same period. Dawsonite (0.003 kg per m³) and ankerite (0.003 kg per m³) are also precipitated but in minimal amounts. In addition to the carbonate minerals, kaolinite (0.43 kg per m³) and illite (0.56 kg per m³) are precipitated and dissolved, respectively.

8. The induced porosity changes due to mineralization are minor during 100 years. Mineral precipitation due to CO_2 storage causes the reduction of porosity by approximately 7.5e-5 after 100 years. The corresponding permeability reduction was 0.993.

The results of CO_2 trapping mechanisms presented here possess some limitations associated with upscaling, including effects of grid-coarsening and averaged ("smoothed") values of porosity and permeability. In the geocellular model, renormalization decreases the number of elements from 9,450,623 to 15,470 as shown in Table 10 and, correspondingly, increases the grid size. Through the upscaling procedure, it is clear that the contrast in permeability between adjacent elements becomes smaller (Figure 46A-D), and thus, standard deviation of effective permeability decreases (Table 10). Previously, only a few studies evaluated the grid coarsening effects on CO_2 trapping mechanisms and these previous studies only considered grid effects within homogeneous models (Solubility trapping by Doughty and Pruess, 2004; Residual CO_2 trapping by Juanes and others, 2006; mineral trapping by Audigane and others, 2007; Yamamoto and Doughty, 2009). All these studies have suggested that the grid coarsening would generate certain errors in predicting CO_2 trapping mechanisms. Although we did not include the study associated with the grid effect here, we investigated the renormalization effect on various 2-dimensional heterogeneous permeability fields and found that the sequential renormalization underestimated residual CO_2 trapping by increasing grid scale and averaging permeability. Therefore, we expected that the residual CO_2 trapping in the presented SACROC model could be underestimated. In future work, we will employ massively parallel computing using the code, PFLOTRAN (Lu and Lichtner, 2007), to predict CO_2 trapping mechanisms in the 3-D geocellular model without the need for upscaling.

Finally, the prediction of spatiotemporal CO_2 trapping mechanisms (mobile CO_2, residual CO_2, dissolved CO_2, and mineral) is one of the daunting problems because (1) the nature of CO_2 trapping is dependent on time, (2) individual trapping mechanism is strongly coupled with each other, and (3) subsurface conditions and properties are altered significantly with CO_2 injection. More importantly, it is difficult to acquire field data from the targeted formations typically below 800 m and monitor their in-situ variations. Therefore, previous

models predicting CO_2 trapping mechanisms always included certain limitations. In this study, we utilized a specific site with the detailed 3-D geologic frame model, relevant laboratory, and field data to overcome the limitation of previous studies. In result, this study is to provide the first successful quantification of all significant CO_2 trapping mechanisms concurrently based on the detailed geologic model. We expect that the processes of model development are intended to serve as an exemplary or template procedure for evaluating the relative roles of different CO_2 trapping mechanisms at other geological storage sites.

Acknowledgements:

References

Accornero, M., and Marini, L., 2009, Empirical prediction of the Pitzer's interaction parameters for cationic Al species with both $SiO_{2(aq)}$ and $CO_{2(aq)}$: Implications for the geochemical modeling of very saline solutions: Applied Geochemistry, v. 24, p. 747-759.

Allen, H. H., and LaRue, C. R., 1957, SACROC Unit operations: Journal of Petroleum Technology, v. 9, p. 21-25.

Allen, H. H., and Thomas, J. B., 1959, Pressure maintenance in SACROC Unit operations January 1, 1959: Journal of Petroleum Technology, v. 11, p. 42-48.

Allis, R., White, S., Chidsey, T., Gwynn, W., Morgan, C., Adams, M., and Moore, J., 2001, Natural CO_2 reservoirs on the Colorado plateau and southern Rocky Mountains: Candidate for CO_2 sequestration: Proceedings of the First National Conference on Carbon Sequestration, Washington DC, May 2001.

Altevogt, A. S., and Celia, M. A., 2004, Numerical modeling of carbon dioxide in unsaturated soils due to deep subsurface leakage: Water Resources Research, W03509, doi:10.1029/2003WR002848.

André, L., Audigane P., Azaroual M., and Menjoz, A., 2007, Numerical modeling of fluid-rock chemical interactions at the supercritical CO_2-liquid interface during CO_2 injection into a carbonate reservoir, the Dogger aquifer (Paris basin, France): Energy Conversion and Management, v. 48, p. 1782-1797.

André, L., Azaroual, M., and Menjoz, A., 2010, Numerical simulations of the thermal impact of supercritical CO_2 injection on chemical reactivity in a carbonate saline reservoir: Transport in Porous Media, v. 82, p. 247-274.

Appelo, C.A.J., and Postma, D., 1993, Geochemistry, Groundwater and Pollution: Balkema A.A. Publishers, Rotterdam, Netherlands, 536 p.

Audigane, P., Gaus, I., Czernichowski-Lauriol, I., Pruess, K., and Xu, T., 2007, Two-dimensional reactive transport modeling of CO_2 injection in a saline aquifer at the Sleipner site, North Sea: American Journal of Science, v. 307, p. 974-1008.

Azaroual, M., Fouillac, C., and Matray J. M., 1997, Solubility of silica polymorphs in electrolyte solutions, I. Activity coefficient of aqueous silica from 25° to 250°C, Pitzer's parameterisation: Chemical Geology v. 140, p. 155-165.

Bachu, S., and Adams, J. J., 2003, Sequestration of CO_2 in geological media in response to climate change: capacity of deep saline aquifers to sequester CO_2 in solution: Energy Conversion and Management, v. 44, p. 3151-3175.

Bachu, S., Bonijoly, D. Bradshaw, J., Burruss, R., Holloway, S., Christensen, N. P., and Mathiassen, O. M., 2007, CO_2 storage capacity estimation: Methodology and gaps: International Journal of Greenhouse Gas Control v. 1, p. 430-443.

Baker, J. C., Bai, G. P., Hamilton, P. J., Golding, S. D., and Keene, J. B. 1995, Continental-scale magmatic carbon dioxide seepage recorded by dawsonite in the Bowen-Gunnedah-Sydney basin system, eastern Australia: Journal of Sedimentary Research, v. 65, p. 522-530.

Bakker, R. J. 2003, Package FLUIDS 1. Computer programs for analysis of fluid inclusion data and for modeling bulk fluid properties: Chemical Geology, v. 194, p. 3-23.

Bando, S., Takemura, F., Nishio, M., Hihara, E., and Akai, M., 2004, Viscosity of aqueous NaCl solutions with dissolved CO_2 at (30 to 60)°C and (10 to 20) MPa: Journal of Chemical and Engineering Data, v. 49, p. 1328-1332.

Barlet-Gouêdard, V., Rimmelé, G., Goffé, B., and Porcherie, O., 2006, Mitigation strategies for the risk of CO_2 migration through wellbores: IADC/SPE Drilling Conference, 21-23 February 2006, Miami, Florida, USA.

Bayat, M. G., Pickard, C. D., Benvegnu, A. J., Wingate, T. P., and Larkin, R., 1996, Linking reservoir characteristics and recovery processes at SACROC-controlling wasteful cycling of fluids at SACROC while maximizing reserves: Second Annual Subsurface Fluid Control Symposium and Conference.

Bénézeth, P., Palmer, D. A., Anovitz, L. M., and Horita, J., 2007, Dawsonite synthesis and reevaluation of its thermodynamic properties from solubility measurements: Implications for mineral trapping of CO_2: Geochimica et Cosmochimica Acta, v. 71, p. 4438-4455.

Bennion, B., and Bachu, S., 2005, Relative permeability characteristics for supercritical CO_2 displacing water in a variety of potential sequestration zones in the western Canada sedimentary basin: SPE Annual Technical Conference and Exhibition, 9-12 October 2005, Dallas, Texas, USA.

Bennion, B., and Bachu, S., 2006, The impact of interfacial tension and pore size distribution/capillary pressure character on CO_2 relative permeability at reservoir conditions in CO_2-brine system: SPE/DOE symposium on Improved Oil Recovery, 22-26 April 2006, Tulsa Oklahoma, USA.

Bergenback, R. E., and Terriere, R. T., 1953, Petrography and petrology of Scurry reef, Scurry County, Texas: AAPG Bulletin, v. 37, p. 1014-1029.

Bertier, P., Swennen, R., Laenen, B., Lagrou, D., and Dreesen, R., 2006, Experimental identification of CO_2-water-rock interactions caused by sequestration of CO_2 in Westphalian and Buntsandstein sandstones of the Campine basin (NE-Belgium): Journal of Geochemical Exploration, v. 89, p. 10-14.

Bethke, C. M., 1996, Geochemical Reaction Modeling: University Press, New York. 397 p.

Bielinski, A., Kopp, A., Schütt, H., and Class, H., 2008, Monitoring of CO_2 plumes during storage in geological formations using temperature signals: Numerical investigation, v. 2, p. 319-328.

Bowker, K. A., and Shuler, P. J., 1991, Carbon dioxide injection and resultant alteration of the Weber sandstone, Rangely Field, Colorado: AAPG Bulletin, v. 75, p. 1489-1499.

Bradshaw, J., Bachu, S., Bonijoly, D., Burruss, R., Holloway, S., Christensen, N. P., and Mathiassen, O. M., 2007, CO_2 storage capacity estimation: Issues and development of standards: International Journal of Greenhouse Gas Control, v. 1, p. 62-68.

Brnak, J., Petrich, B., and Konopczynski, M. R., 2006, Application of smartwell technology to the SACROC CO_2 EOR project: A case study: SPE/DOE Symposium on Improved Oil Recovery, 22-26 April 2006, Tulsa, Oklahoma, USA.

Brummett, Jr. W. M., Emanuel, A. S., and Ronquille, J. D., 1976, Reservoir description by simulation at SACROC-a case history: Journal of Petroleum Technology, v. 28, p. 1241-1255.

Burnside, R. J., 1959, Geology of part of Horseshoe Atoll in Borden and Howard Counties, Texas: Geological Survey Professional Paper 315-B, 34 p.

Busch, A., Alles, S., Gensterblum, Y., Prinz, D., Dewhurst, D. N., Raven, M. D., Stanjek, H., Krooss, B. M., 2008, Carbon dioxide storage potential of shales: International of Journal of Greenhouse Gas Control v. 2, p. 297-308.

Carey, J. W., Wigand, M., Chipera, S. J., WoldeGabriel, G., Pawar, R., Lichtner, P. C., Wehner, S. C., Raines, M. A., and Guthrie, Jr. G. D., 2007, Analysis and performance of oil well cement with 30 years of CO_2 exposure from the SACROC unit, west Texas, USA: International Journal of Greenhouse Gas Control, v. 1, p. 75-85.

Chai, L., and Navrotsky, A., 1996, Synthesis, characterization, and energetics of solid solution along the dolomite-ankerite join, and implications for the stability of ordered $CaFe(CO_3)_2$: American Mineralogists, v. 81, p. 1141-1147.

Chiquet, P., Daridon, J. -L., Broseta, D., and Thibeau, S., 2007, CO_2/water interfacial tensions under pressure and temperature conditions of CO_2 geological storage: Energy Conversion and Management, v. 48, p. 736-744.

Computer Modeling Group, 2008. User's guide GEM, Advanced compositional reservoir simulator (version 2008). Computer Modeling Group Ltd. 954 p.

Cortis, A., Oldenburg, C. M., and Benson, S. M., 2008, The role of optimality in characterizing CO_2 seepage from geologic carbon sequestration sites: International Journal of Greenhouse Gas Control, v. 2, p. 640-652.

Dicharry, R. M., Perryman, T. L., and Ronquille, J. D., 1973, Evaluation and design of a CO_2 miscible flood project-SACROC Unit, Kelly-Snyder field: Journal of Petroleum Technology, v. 25, p. 1309-1318.

Dilmore, R. M., Allen, D. E., Jones, J. R. M., Hedges, S. W., and Soong, Y., 2008, Sequestration of dissolved CO_2 in the Oriskany Formation: Environmental Science and Technology, v. 42, p. 2760-2766.

Dixon, B. P., and Newton, Jr. L. E., 1965, Reinjection of large volumes of produced water in secondary operations: Journal of Petroleum Technology, v. 17, p. 781-789.

Doughty, C., 2007, Modeling geologic storage of carbon dioxide: Comparison of non-hystereric and hysteretic characteristic curves: Energy Conversion and Management, v. 48, p. 1768-1781.

Doughty, C., and Pruess, K., 2004, Modeling supercritical carbon dioxide injection in heterogeneous porous media: Vadose Zone Journal, v. 3, p. 837-847.

Duan, Z., and Sun, R., 2003, An improved model calculating CO_2 solubility in pure water and aqueous NaCl solutions from 273 to 533 K and from 0 to 2000 bar: Chemical Geology, v. 193, p. 257-271.

Duan, Z., Hu, J., Li, D., and Mao, S., 2008, Densities of the CO_2-H_2O and CO_2-H_2O-NaCl systems up to 647 K and 100 MPa: Energy and Fuels, v. 22, p. 1666-1674.

Duan, Z., Sun, R., Zhu, C., and Chou, I. -M., 2006, An improved model for the calculation of CO_2 solubility in aqueous solutions containing Na^+, K^+, Ca^{2+}, Mg^{2+}, Cl^-, and SO_4^{2-}: Marine Chemistry, v. 98, p. 131-139.

Dubessy, J., Tarantola, A., and Sterpenich, J., 2005, Modeling of liquid-vapor equilibria in the H_2O-CO_2-NaCl and H_2O-H_2S-NaCl systems to 270°C: Oil and Gas Science and Technology, v. 60, p. 339-355.

Dumore, J. M., and Schols, R. S., 1974, Drainage capillary-pressure functions and the influence of connate water: Society of Petroleum Engineers Journal, v. 14, p. 437-444.

Emberley, S., Hutcheon, I., Shevalier, M., Durocher, K., Gunter, W. D., and Perkins, E. H., 2004, Geochemical monitoring of fluid-rock interaction and CO_2 storage at the Weyburn CO_2-injection enhanced oil recovery site, Saskatchewan, Canada: Energy, v. 29, p. 1393-1401.

Ennis-King, J., and Paterson, L., 2003, Role of convective mixing in the long-term storage of carbon dioxide in deep saline formations: Society of Petroleum Engineers Journal, v.10, p. 349-356.

Ennis-King, J., and Paterson, L., 2007, Coupling of geochemical reactions and convective mixing in the long-term geological storage of carbon dioxide: International Journal of Greenhouse Gas Control, v. 1, p. 86-93.

Fairbridge, R. W., 1950. Recent and Pleistocene coral reefs of Australia: Geology, v. 58, n. 4, p. 330-401.

Farajzadeh, R., Salimi, H., Zitha, P. L. J., and Bruining, H., 2007, Numerical simulation of density-driven natural convection in porous media with application for CO_2 injection projects: International Journal of Heat and Mass Transfer, v. 50, p. 5054-5064.

Felmy, A. R., Rustad, J. R., Mason, M. J., and de la Bretonne, R., 1994, A chemical model for the major electrolyte components of the Hanford waste tanks: the binary electrolytes in the systems: Na-NO_3-NO_2-SO_4-CO_3-F-PO_4-OH-Al(OH)$_4$-H_2O: PNNL Technical Report TWRS-PP-94-090, Pacific Northwest National Laboratory, Richland, Washington.

Flett, M., Gurton, R., and Weir, G., 2007, Heterogeneous saline formations for carbon dioxide disposal: Impact of varying heterogeneity on containment and trapping: Journal of Petroleum Science and Engineering, v. 57, p. 106-118.

Fleury, M., and Deschamps, H., 2008, Electrical conductivity and viscosity of aqueous NaCl solutions with dissolved CO_2: Journal of Chemical and Engineering Data, v. 53, p. 2505-2509.

Fuller, R. C., Prevost, J. H., and Piri, M., 2006, Three-phase equilibrium and partitioning calculations for CO_2 sequestration in saline aquifers: Journal of Geophysical Research, v. 111, B06207, doi:10.1029/2005JB003618.

Gale, J., 2004, Geological storage of CO_2: What do we know, where are the gaps and what more needs to be done?: Energy, v. 29, p. 1329-1338.

Gasperikova, E., and Hoversten, G. M., 2006, A feasibility study of nonseismic geophysical methods for monitoring geologic CO_2 sequestration: The Leading Edge, v. 25, p. 1282-1288.

Gaus, I., 2010, Role and impact of CO_2-rock interactions during CO_2 storage in sedimentary rocks: International Journal of Greenhouse Gas Control, v. 4, p. 73-89.

Gaus, I., Azaroual, M., and Czernichowski-Lauriol, I., 2005, Reactive transport modeling of the impact of CO_2 injection on the clayey cap rock at Sleipner (North Sea): Chemical Geology, v. 217, p. 319-337.

Gautier, Y., Noetinger, B., 1997, Preferential flow-paths detection for heterogeneous reservoirs using a new renormalization technique: Transport in Porous Media, v. 26, p. 1-23.

Gerling, C. R., 1983. McElmo dine Leadville carbon dioxide field, Colorado, *in* Fassett J. E. editor, Oil and gas fields of the four corners area: Four Corners Geological Survey, v. 3, p. 735-739.

Gherardi, F., Xu, T., and Pruess, K., 2007, Numerical modeling of self-limiting and self-enhancing caprock alteration induced by CO_2 storage in a depleted gas reservoir: Chemical Geology, v. 244, p. 103-129.

Giorgis, T., Carpita, M., and Battistelli, A., 2007, 2D modeling of salt precipitation during the injection of dry CO_2 in a depleted gas reservoir: Energy Conversion and Management, v. 48, p. 1816-1826.

Han, W. S., 2008, Evaluation of CO_2 Trapping Mechanisms at the SACROC Northern Platform: Site of 35 Years of CO_2 Injection: Ph.D. thesis, New Mexico Institute of Mining and Technology, Socorro. 465 p.

Han, W. S., Lee, S. –Y., Lu, C., and McPherson, B. J., 2010a, Effects of permeability on CO_2 trapping mechanisms and buoyancy-driven CO_2 migration in saline formations: Water Resources Research, doi:10.1029/2009WR007850.

Han, W. S., Stillman, G. A., Lu, M., Lu, C., McPherson, B. J., and Park, E., 2010b, Evaluation of potential non-isothermal processes and heat transport during CO_2 sequestration: Journal of Geophysical Research, doi:10.1029/2009JB006745.

Harvey, A. H., 1996, Semiempirical correlation for Henry's constants over large temperature ranges: AIChE Journal v. 42, p. 1491-1494.

Harvie, C. E., MØller, N., and Weare, J. H., 1984, The prediction of mineral solubilities in natural waters: The Na-K-Mg-Ca-H-Cl-SO_4-OH-HCO_3-CO_3-CO_2-H_2O system to high ionic strengths at 0 to 25° C: Geochimica et Cosmochimica Acta, v. 48, p. 723-751.

Hawkins, J. T., Benvegnu, A. J., Wingate, T. P., McKamie, J. D., Pickard, C. D., and Altum, J. T., 1996, SACROC Unit CO_2 flood: Multidisciplinary team improves reservoir management and decreases operating costs: SPE Reservoir Engineering v. 11, p. 141-148.

Helgeson, H. C., 1969, Thermodynamics of hydrothermal systems at elevated temperatures and pressures: American Journal of Science, v. 267, p. 729-804.

Hellevang, H., Aagaard, P., Oelkers, E. H., and Kvamme, B., 2005, Can Dawsonite permanently trap CO_2?: Environmental Science and Technology, v. 39, p. 8281-8287.

Hinrichsen, E. L., Aharony, A., Fedar, J., Hansen, A., JØssang, T., and Hardy, H. H., 1993, A fast algorithm for estimating large-scale permeabilities of correlated anisotropic media: Transport in Porous Media, v. 12, p. 55-72.

Holloway, S., 2005, Underground sequestration of carbon dioxide—a viable greenhouse gas mitigation option: Energy, v. 30, p. 2318-2333.

Holtz, M. H., 2002, Residual gas saturation to aquifer flux: A calculation method for 3-D computer reservoir model construction: SPE Gas Technology Symposium, 30 April-2 May 2002, Calgary, Alberta, Canada.

Hu, J., Duan, Z., Zhu, C., and Chou, I. –M., 2007, PVTx properties of the CO_2-H_2O and CO_2-H_2O-NaCl systems below 647 K: Assessment of experimental data and thermodynamic models: Chemical Geology, v. 238, p. 249-267.

Ide, S. T., Jessen, K., and Orr, Jr. F. M., 2007, Storage of CO_2 in saline aquifer: Effects of gravity, viscous, capillary forces on amount and timing of trapping: International Journal of Greenhouse Gas Control, v. 1, p. 481-491.

IEA Greenhouse Gas R&D Programme, 2001, Putting Carbon Back into the Ground: IEA Greenhouse Gas R&D Programme, 28 p.

Intergovernmental Panel on Climate Change, 2005, Carbon Dioxide Capture and Storage: Cambridge University Press, UK, 431p.

Jennings, Jr., J. W., and Lucia, F. J., 2003, Predicting permeability from well logs in carbonates with a link to geology for interwell permeability mapping: SPE Reservoir Evalution and Engineering, v. 6, p. 215-225.

Jossi, J. A., Stiel, L. I., and Thodos, G., 1962, The viscosity of pure substances in the dense gaseous and liquid phase: AIChe Journal, v. 8, p. 59-63.

Juanes, R., Spiteri, E. J., Orr, Jr. F. M., and Blunt, M. J., 2006. Impact of relative permeability hystersis on geologic CO_2 storage: Water Resources Research, v. 42, W12418, doi:10.1029/2005WR004806.

Kane, A. V., 1979, Performance review of a large-scale CO_2-WAG enhanced recovery project, SACROC Unit Kelly-Snyder field: Journal of Petroleum Technology, v. 31, p. 217-231.

Kaszuba, J. P., Janecky, D. R., and Snow, M. G., 2005, Experimental evaluation of mixed fluid reactions between supercritical carbon dioxide and NaCl brine: Relevance to the integrity of a geologic carbon repository: Chemical Geology, v. 217, p. 277-293.

Kestin, J., Khalifa, H. E., and Correia, R. J., 1981, Tables of the dynamic and kinematic viscosity of aqueous NaCl solutions in the temperature range 20-150°C and the pressure range 0.1-35 MPa: Journal of Physical and Chemical Reference Data, v. 10, p. 71-87.

Kharaka, Y. K., Cole, D. R., Thordsen, J. J., Kakouros, E., and Nance, H. S., 2006, Gas-water-rock interactions in sedimentary basins: CO_2 sequestration in the Frio Formation, Texas, USA: Journal of Geochemical Exploration, v. 89, p. 183-186.

Kharaka, Y. K., Gunter, W. D., Aggarwal, P. K., Perkins, E., and Debraal, J. D., 1989, SOLMINEQ.88: A computer program for geochemical modeling of water-rock reactions: USGS Water-Resources Investigations Report 88-4227.

King, P. R., 1989, The use of renormalization for calculating effective permeability: Transport in Porous Media, v. 4, p. 37-58.

King, P. R., 1996, Upscaling permeability: Error analysis for renormalization: Transport in Porous Media, v. 23, p. 337-354.

Klusman, R. W., 2003, A geochemical perspective and assessment of leakage potential for a mature carbon dioxide-enhanced oil recovery project and as a prototype for carbon dioxide sequestration; Rangely field, Colorado: AAPG Bulletin, v. 87, p. 1485-1507.

Knauss, K. G., Johnson, J. W., and Steefel, C. I., 2005, Evaluation of the impact of CO_2, co-contaminant gas, aqueous fluid and reservoir rock interactions on the geologic sequestration of CO_2: Chemical. Geology, v. 217, p. 339-350.

Kopp, A., Class, H. and Helmig, R., 2009, Investigations on CO_2 storage capacity in saline aquifers—Part 2: Estimation of storage capacity coefficients: International Journal of Greenhouse Gas Control, v. 3, p. 277-287.

Kumar, A., Noh, M. H., Ozah, R. C., Pope, G. A., Bryant, S. L., Sepehrnoori, K., and Lake, L. W., 2005, Reservoir simulation of CO_2 storage in deep saline aquifers: Society of Petroleum Engineers Journal, v. 10, p. 336-348.

Land, C. S., 1968, Calculation of imbibition relative permeability for two- and three-phase flow from rock properties: Society of Petroleum Engineers Journal, v. 8, p. 149-156.

Langston, M. V., Hoadley, S. F., and Young, D. N., 1988, Definitive CO_2 flooding response in the SACROC Unit: SPE Enhanced Oil Recovery Symposium, 16-21 April, Tulsa, Oklahoma, USA.

Lasaga, A. C., 1984, Chemical kinetics of water-rock interactions: Journal of Geophysical Research, v. 89, p. 4009-4025.

Lasaga, A. C., Soler, J. M., Ganor, J., Burch, T. E., and Nagy, K. L., 1994, Chemical weathering rate laws and global geochemical cycles: Geochimica et Cosmochimica Acta, v. 58, p. 2361-2386.

Leverett, M. C., 1941, Capillary behavior in porous solids: Transactions of the American Institute of Mining, Metallurgical, and Petroleum Engineers, v. 142, p. 152-169.

Lewicki, J. L., Hilley, G. E., and Oldenburg, C. M., 2005, An improved strategy to detect CO_2 leakage for verification of geologic carbon sequestration: Geophysical Research Letters, v. 32, L19403, doi:10.1029/2005GL024281.

Li, Y. -K., and Nghiem, L. X., 1986, Phase equilibria of oil, gas, and water/brine mixtures from a cubic equation of states and Henry's law: Canadian Journal of Chemical Engineering, v. 64, p. 486-496.

Lichtner, P. C., and Felmy, A. R., 2003, Estimation of Hanford SX tank waste compositions from historically derived inventories: Computers and Geosciences, v. 29, p. 371-383.

Litynski, J. T., Plasynski, S., McIlvried, H. G., Mahoney, C., and Srivastava, R. D., 2008, The United States Department of Energy's Regional Carbon Sequestration Partnerships Program validation phase: Environment International, v. 34, p. 127-138.

Lu, C., and Lichtner, P. C., 2007, High resolution numerical investigation on the effect of convective instability on long term CO_2 storage in saline aquifers: Journal of Physics, Conference Series 78, doi:10.1088/1742-6596/78/1/012042.

Lu, J., Wilkinson, M., Haszeldine, R. S., and Fallick, A. E., 2009, Long-term performance of a mudrock seal in natural CO_2 storage: Geology, v. 37, p. 35-38.

Lu, M., and Connell, L. D., 2008, Non-isothermal flow of carbon dioxide in injection wells during geologic storage: International Journal of Greenhouse Gas Control, v. 2, p. 248-258.

Lucia, F. J., 1995, Rock-fabric/petrophysical classification of carbonate pore space for reservoir characterization: AAPG Bulletin, v. 79, p. 1275-1300.

Lucia, F. J., 1999, Carbonate Reservoir Characterization: Springer-Verlag, Berlin, 226 p.

Lucia, F. J., and Kerans, C., 2004, Permeability estimation using porosity logs and rock fabric stratigraphy: an example from the SACROC (Pennsylvanian) field, Scurry County, Texas, *in* Trentham R., editor, Banking on the Permian Basin: Plays, Field Studies, and Techniques: West Texas Geological Society Publication 04-112, p. 271-274.

Malick, K. M., 1995, Boundary effects in the successive upscaling of absolute permeabilities: M.S. thesis, Stanford University, San Francisco.

McPherson, B. J. O. L., Han, W. S., and Cole, B. S., 2008, Two equations of state assembled for basin analysis of multiphase CO_2 flow and in deep sedimentary basin conditions: Computers and Geoscience, v. 34, p. 427-444.

Mito, S., Xue, Z., and Ohsumi, T., 2008, Case study of geochemical reactions at the Nagaoka CO_2 injection site, Japan: International Journal of Greenhouse Gas Control, v. 2, p. 309-318.

Monnin, C., 1989, An ion-interaction model for the volumetric properties of natural waters: Density of the solution and partial molal volumes of electrolytes to high concentrations at 25° C: Geochimica et Cosmochimica Acta, v. 53, p. 1177-1188.

Moore, J., Adams, M., Allis, R., Lutz, S., and Rauzi, S., 2005, Mineralogical and geochemical consequences of the long-term presence of CO_2 in natural reservoirs: An example from the Springerville-St. Johns field, Arizona, and New Mexico, U.S.A: Chemical Geology, v. 217, p. 365-385.

Mozley, P. S., and Hoernle, K., 1990, Geochemistry of carbonate cements in the Sag River and Shublik Formations (Triassic/Jurassic), North Slope, Alaska: implications for the geochemical evolution of formation waters: Sedimentology, v. 37, p. 817-836.

Myers, D. A., Stafford, P. T., and Burnside, R. J., 1956, Geology of the late Paleozoic Horseshoe Atoll in west Texas: Bureau of Economic Geology Publication 5607, 113 p.

Nagy, K. L. (1995), Dissolution and precipitation kinetics of sheet silicates, *in* White A.F. and Brantley S.L., editors, Chemical Weathering Rates of Silicate Minerals: Reviews in Mineralogy, v. 31, p. 173-233.

National Energy Technology Laboratory, 2005, Regional Carbon Sequestration Partnerships Phase I accomplishments: United States Department of Energy, Office of Fossil Energy, National Energy Technology Laboratory, 15 p.

Newell, D. L., Kaszuba, J. P., Viswanathan, H. S., Pawar, R. J., and Carpenter, T., 2008, Significance of carbonate buffers in natural waters reacting with supercritical CO_2: Implications for monitoring, measuring, and verification (MMV) of geologic carbon sequestration: Geophysical Research Letters, v. 35, L23403, doi:10.1029/2008GL035615.

Nghiem, L. X., 1983, A new approach to quasi-Newton methods with application to compositional modeling: SPE Reservoir Simulation Symposium, 15-18 November, San Francisco, California, USA.

Nghiem, L. X., Sammon, P., Grabenstetter, J., and Ohkuma, H., 2004, Modeling CO_2 storage in aquifers with a fully-coupled geochemical EOS compositional simulator: SPE/DOE Symposium on Improved Oil Recovery, 17-21 April 2004, Tulsa, Oklahoma, USA.

Nordbotten, J. M., Celia, M. A., Bachu, S., and Dahle, H. K., 2005, Semianalytical solution for CO_2 leakage through an abandoned well: Environmental Science and Technology, v. 39, p. 602-611.

Núñez-López, V., Holtz, M. H., Wood, D. J., Ambrose, W. A., and Hovorka, S. D., 2008, Quick-look assessments to identify optimal CO_2 EOR storage sites: Environmental Geology, v. 54, p. 1695-1706.

Oldenburg, C. M., and Lewicki, J. L., 2006, On leakage and seepage of CO_2 from geologic storage sites into surface water: Environmental Geology, v. 50, p. 691-705.

Orr, Jr. F. M., 2004, Storage of carbon dioxide in geologic formations: Journal of Petroleum Technology, vol. 56, p. 90-97.

Ozkan, G., and Ortoleva, P., 2000, A mesoscopic model of nucleation and Ostwald ripening/stepping: Application to the silica polymorph system: Journal of Chemical Physics, v. 112, p. 10510-10525.

Palandri, J., and Kharaka, Y. K., 2004, A compilation of rate parameters of water-mineral interaction kinetics for application to geochemical modeling: US Geological Survey Open File Report 2004-1068, 64 p.

Parkhurst, D. L., and Appelo, C. A. J., 1999, User's guide to PHREEQC (version 2)—A computer program for speciation, batch-reaction, one-dimensional transport, and inverse geochemical calculation: U.S. Geological Survey Water-Resources Investigations Report 99-4259, 312 p.

Parry, W. T., Forster, C. B., Evans, J. P., Bowen, B. B., and Chan, M. A., 2007, Geochemistry of CO_2 sequestration in the Jurassic Navajo sandstone, Colorado Plateau, Utah: Environmental Geosciences, v. 14, p. 91-109.

Peng, D. Y., and Robinson, D. B., 1976, A new two-constant equation of state: Industrial and Engineering Chemistry Fundamentals, v. 15, p. 59-64.

Pitzer, K. S., 1987, A thermodynamic model for aqueous solutions of liquid-like density, *in* Carmichael I. S. E. and Eugster H. P., editors, Thermodynamic Modeling of Geological Materials: Minerals Fluids and Melts: Reviews in Mineralogy, v. 17, p. 97-142.

Plug, W. -J., and Bruining, J., 2007, Capillary pressure for the sand-CO_2-water system under various pressure conditions. Application to CO_2 sequestration: Advances in Water Resources, v. 30, p. 2339-2353.

Portier, S., and Rochelle, C., 2005, Modeling CO_2 solubility in pure water and NaCl-type waters from 0 to 300 °C and from 1 to 300 bar application to the Utsira formation at Sleipner: Chemical Geology, v. 217, p. 187-199.

Pruess, K., 2005, Numerical studies of fluid leakage from a geologic disposal reservoir for CO_2 show self-limiting feedback between fluid flow and heat transfer: Geophysical Research Letters, v. 32, L14404, doi:10.1029/2005GL023250.

Pruess, K., 2008, Leakage of CO_2 from geologic storage: Role of secondary accumulation at shallow depth: International Journal of Greenhouse Gas control, v. 2, p. 37-46.

Pruess, K., and Müller, N., 2009, Formation dry-out from CO_2 injection into saline aquifers: 1. Effects of solids precipitation and their mitigation: Water Resources Research, v. 45, W03402, doi:10.1029/2008WR007101.

Qi, R., LaForce, T. C., and Blunt, M. J., 2009, Design of carbon dioxide storage in aquifers: International Journal of Greenhouse Gas control, v. 3, p. 195-205.

Raines, M., 2005, Kelly-Snyder (Cisco-Canyon) Fields/SACROC unit: Oil and Gas fields in West Texas VIII: West Texas Geological Society Publication 05-114, p. 69-78.

Ranies, M. A., Dobitz, J. K., and Wehner, S. C., 2001, A review of the Pennsylvanian SACROC Unit, *in* Viveros J. J. and Ingram S. M., editors, The Permian Basin: Microns to Satellites, Looking for Oil and Gas at All Scales: West Texas Geological Society Publication 01-110, p. 67 - 74.

Reid, A. M., and Reid, S. A. T., 1991, The Cogdell field study, Kent and Scurry counties, Texas: A post-mortem, *in* Candelaria M., editor, The Permian Basin Plays: Tomorrow's Technology Today: West Texas Geological Society Publication 91-89, p. 39-66.

Renard, P., and de Marsily, G., 1997, Calculating equivalent permeability: a review: Advances Water Resources, v. 20, p. 253-278.

Renard, P., Le Loc'h, G., Ledoux, E., de Marsily, G., and Mackay, G., 2000, A fast algorithm for the estimation of the equivalent hydraulic conductivity of heterogeneous media: Water Resources Research, v. 36, p. 3576-3580.

Rohan, J. A., and Haggerty, D., 1996, Carbonate species core analysis study for Pennzoil exploration and production company: Elevated temperature centrifuge study: Technical Report, Westport Technology Center, IIT Research Institute.

Rowe, Jr. A. M., and Chou, J. C. S., 1970, Pressure-volume-temperature-concentration relation of aqueous sodium chloride solutions: Journal of Chemical and Engineering Data, v. 15, p. 61-66.

Saadatpoor, E. Bryant, S. L., and Sepehrnoori, K., 2010, New trapping mechanism in carbon sequestration: Transport in Porous Media, v. 82, p. 3-17.

Saripalli, P., Amonette, J., Rutz, F., and Gupta, N., 2006, Design of sensor networks for long term monitoring of geological sequestration: Energy Conversion and Management, v. 47, p. 1968-1974.

Schatzinger, R. A., 1988, Changes in facies and depositional environments along and across the trend of Horseshoe Atoll, Scurry and Kent Counties, Texas, *in* Cunningham B. K., editors, Permian and Pennsylvanian Stratigraphy Midland Basin, West Texas: Studies to Aid Hydrocarbon Exploration: Permian Basin Section, Society for Economic Paleontologists and Mineralogists Publication 88-28, p. 79-95.

Spycher, N., and Pruess, K., 2005, CO_2-H_2O mixtures in the geological sequestration of CO_2. II. Partitioning in chloride brines at 12-100°C and up to 600 bars: Geochimica et Cosmochimica Acta, v. 69, p. 3309-3320.

Spycher, N., and Pruess, K., and Ennis-King, J., 2003, CO_2-H_2O mixtures in the geological sequestration of CO_2. I. Assessment and calculation of mutual solubilities from 12 to 100°C and up to 600 bar: Geochimica et Cosmochimica Acta, v. 67, p. 3015-3031.

Stafford, P. T., 1954, Scurry field: Scurry, Kent and Border Counties, Texas, *in* Herald F. A., editor, Occurrence of Oil and Gas in West Texas: Bureau of Economic Geology, Austin, Texas, v. 5716, p. 295-302.

Steefel, C. I., and van Cappellen, P., 1990, A new kinetic approach to modeling water-rock interaction: The role of nucleation, precursors, and Ostwald ripening: Geochimica et Cosmochimica Acta, v. 54, p. 2657-2677.

Stewart, R. W., 1957, Reef limestones of the north Snyder oil field Scurry County, Texas: Ph.D thesis. Department of Geology. Massachusetts Institute of Technology, Cambridge.

Suekane, T., Nobuso, T., Hirai, S., and Kiyota, M., 2008, Geological storage of carbon dioxide by residual gas and solubility trapping: International Journal of Greenhouse Gas Control, v. 2, p. 58-64.

Svensson, U., and Dreybrodt, W., 1992, Dissolution kinetics of natural calcite minerals in CO_2-water systems approaching calcite equilibrium: Chemical Geology, v. 100, p. 129-145.

Tester, J. W., Worley, W. G., Robinson, B. A., Grigsby, C. O., and Feerer, J. L., 1994, Correlating quartz dissolution kinetics in pure water from 25 to 625ºC, Geochimica et Cosmochimica Acta, v. 58, p. 2407-2420.

Thomas, D., and Benson, S., 2005, Carbon dioxide capture for storage in deep geologic formations: results from the CO_2 capture project-Volume 2: Amsterdam, Elsevier, 1328 p.

Usdowski, E., 1994, Synthesis of dolomite and geochemical implications, *in* Purser, B., Tucker M., and Zenger D., editors, Dolomites: A volume in honor of Dolomieu: International Association of Sedimentologists, Special Publication n. 21, Blackwell Scientific Publication, Oxford, p. 345-360.

van der Meer, L. G. H., and van Wees, J. D., 2006, Limitations to storage pressure in finite saline aquifers and the effect of CO_2 solubility on storage pressure: SPE Annual Technical Conference and Exhibition, 24-27 September 2006, San Antonio, Texas, USA.

Vest, Jr. E. L., 1970, Oil Fields of Pennsylvanian-Permian Horseshoe Atoll, West Texas, *in* Halbouty, M. T., editor, Geology of Giant Petroleum Fields: AAPG Memoir 14, p. 185-203.

Walker, D. A., Golonka, J., and Reid, A. M., 1991, The effects of late Paleozoic paleolatitude and paleogeography on carbonate sediment in the Midland basin, Texas, *in* Candelaria M., editor, Permian Basin Plays, Tomorrow's Technology Today: West Texas Geological Society Publication 91-89, p. 141-162.

Watson, T. L., and Bachu, S., 2007, Evaluation of the potential for gas and CO_2 leakage along wellbores: E&P Environmental and Safety Conference, 5-7 March 2007, Galveston, Texas.

Weeter, R. F., and Halstead, L. N., 1982, Production of CO_2 from a reservoir—A new concept: Journal of Petroleum Technology, v. 34, p. 2144-2148.

Wells, A. W., Diehl, J. R., Bromhal, G., Strazisar, B. R., Wilson, T. H., and White, C. M., 2007, The use of tracers to assess leakage from the sequestration of CO_2 in a depleted oil reservoir, New Mexico, USA: Applied Geochemistry, v. 22, p. 996-1016.

White, S. P., 1995, Multiphase nonisothermal transport of systems of reacting chemicals: Water Resources Research, v. 31, p. 1761-1772.

White, S. P., Allis, R. G., Moore, J., Chidsey, T., Morgan, C., Gwynn, W., and Adams, M., 2005, Simulation of reactive transport of injected CO_2 on the Colorado Plateau, Utah, USA: Chemical Geology, v. 217, p. 387-405.

Winthaegen, P., Arts, R., and Schroot, B., 2005, Monitoring subsurface CO_2 storage: Oil and Gas Science and Technology, v. 60, p. 573-582.

Wolery, T. J., and Daveler, S. A., 1992, EQ6, A computer program for reaction path modeling of aqueous geochemical systems: Theoretical manual, user's guide and related documentation (version 7.0): Report UCRL-MA-110662 PT IV. Lawrence Livermore National Laboratory.

Wood, T. L., and Garrels, R. M., 1992, Calculated aqueous-solution-solid-solution reactions in the low-temperature system $CaO-MgO-FeO-CO_2-H_2O$: Geochimica et Cosmochimica Acta, v. 56, p. 3031-3043.

Xu, T., Apps, J. A., and Pruess, K., 2004, Numerical simulation of CO_2 disposal by mineral trapping in deep aquifers: Applied Geochemistry, v. 19, p. 917-936.

Xu, T., Apps, J. A., and Pruess, K., 2005, Mineral sequestration of carbon dioxide in a sandstone-shale system: Chemical Geology, v. 217, p. 295-318.

Xu, T., Sonnenthal, E., Spycher, N., and Pruess, K., 2006, TOUGHREACT-A simulation program for non-isothermal multiphase reactive geochemical transport in variably saturated geologic media: Applications to geothermal injectivity and CO_2 geologic sequestration: Computers and Geoscience, v. 32, 145-165.

Yamamoto, H., and Doughty, C., 2009, Investigation of gridding effects for numerical simulation of CO_2 geologic sequestration: Proceedings of TOUGH Symposium, Lawrence Berkeley National Laboratory, Berkeley, California, September 14-16, 2009.

Zerai, B., Saylor, B. Z., and Matisoff, G., 2006, Computer simulation of CO_2 trapped through mineral precipitation in the Rose Run sandstone, Ohio: Applied Geochemistry, v. 21, p. 223-240.

Zhang, G., Spycher, N., Sonnenthal, E., and Steefel C., 2006, Implementation of a Pitzer activity model into TOUGHREACT for modeling concentrated solutions: Proceedings of TOUGH Symposium, Lawrence Berkeley National Laboratory, Berkeley, California, May 15-17, 2006.

Zhang, W., Li, Y., Xu, T., Cheng, H., Zheng, Y., and Xiong, P., 2009, Long-term variations of CO_2 trapped in different mechanisms in deep saline formations: A case study of the Songliao Basin, China: International Journal of Greenhouse Gas Control, v. 3, p. 161-180.

Zhou, Q., Birkholzer, J. T., Tsang, C. –F., and Rutqvist, J., 2008, A method for quick assessment of CO_2 storage capacity in closed and semi-closed saline formation: International Journal of Greenhouse Gas Control, v. 2, p. 626-639.

West Coast Regional Carbon Sequestration Partnership

Pre-Injection Modeling in a Saline Formation in the Southern San Joaquin Valley, California

Christine Doughty
Lawrence Berkeley **National Laboratory**

The hydrodynamic behavior of carbon dioxide (CO_2) injected into a deep saline formation is investigated, focusing on trapping mechanisms that lead to CO_2 plume stabilization. A numerical model of the subsurface is developed to model injection of 1,000,000 metric tons of CO_2 over a four-year period, and the subsequent evolution of the CO_2 plume for hundreds of years. Key measures are plume migration distance and the time evolution of the partitioning of CO_2 between dissolved, immobile free-phase, and mobile free-phase forms. Model results indicate that the injected CO_2 plume is effectively immobilized at 25 years. At that time, 38% of the CO_2 is in dissolved form, 59% is immobile free phase, and 3% is mobile free phase. The plume footprint is roughly elliptical, and extends much farther up-dip of the injection well than down-dip. The pressure increase extends far beyond the plume footprint, but the pressure response decreases rapidly with distance from the injection well, and decays rapidly in time once injection ceases. Sensitivity studies that were carried out to investigate the effect of poorly constrained model parameters permeability, permeability anisotropy, and residual CO_2 saturation indicate that small changes in properties can have a large impact on plume evolution, causing significant trade-offs between different trapping mechanisms.

Introduction

Understanding the hydrodynamic behavior of large-volume CO_2 plumes is critical for advancing the technology of geologic carbon storage in deep saline formations. This behavior is examined by developing a numerical model of the subsurface at a promising site for CO_2 storage in the southern San Joaquin Valley, California (Figure 55), known as the Kimberlina site. As shown in Figure 1, the sedimentary basin that forms

California's Central Valley, which is divided into the Sacramento Valley in the north and the San Joaquin Valley in the south, provides a huge potential capacity for geologic carbon storage, thus lessons learned from the Kimberlina site should be widely applicable.
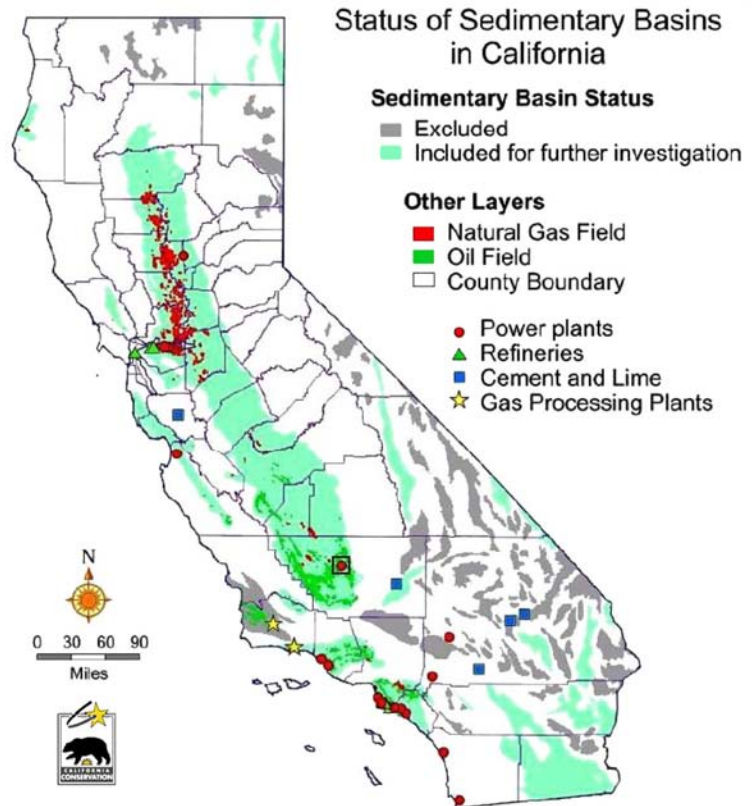

Figure 55: Map of California showing potential geologic carbon storage sites in sedimentary basins (light green shading), courtesy of the California Energy Commission. The Kimberlina site is located in the Southern San Joaquin Valley (boxed red dot).

The target storage formation is a high-permeability sand layer located at a depth of 2 km, which is over- and underlain by low-permeability shales. Within the formation itself, sands and shales are interleaved in a lenticular fashion. This geological setting provides an ideal situation for examining the interplay of buoyancy flow, capillary forces, CO_2 dissolution, and geologic heterogeneity in controlling the behavior of the injected CO_2 plume. The model simulates a pilot test with a four-year injection period, in which a total of one million metric tons of CO_2 are injected, and the subsequent evolution of the CO_2 plume for hundreds of years. Because specific geologic information at the site of the proposed injection well is lacking (the nearest well penetrating the storage formation is 2.5 km away), the simulation results should not be taken as precise predictions, but rather general indications of the key features of CO_2 plume behavior.

In the subsurface, CO_2 exists as an immiscible free phase and as a solute in the aqueous phase. For typical hydrostatic pressure gradients and geothermal temperature gradients, free-phase CO_2 is supercritical at depths greater than about 800 m. The present study does not consider pressure/temperature conditions below the critical point of CO_2 (73.8 bars, 31 °C), so CO_2 never exists as a free phase in liquid or gaseous form. Supercritical CO_2 is lighter and much less viscous than the native brine, so in a two-phase flow context it is referred to as gas, whereas the aqueous phase is referred to as liquid.

Trapping CO_2 is a significant challenge because the low density of free-phase CO_2 compared to native brine makes it strongly buoyant. Immobilizing CO_2 in the subsurface for long-term geologic storage can be accomplished by four primary mechanisms: (1) Stratigraphic or structural trapping: buoyant free-phase CO_2 is trapped beneath low-permeability layers or faults or in anticline structures. (2) Residual CO_2 trapping (also known as capillary trapping, mobility trapping, or phase trapping): multi-phase flow processes immobilize free-phase CO_2. In the petroleum literature (e.g., Land, 1968; Holtz, 2002) it is commonly assumed that residual gas saturation (the saturation below which CO_2 is immobile) is history-dependent, with a zero or small value during the drainage process (CO_2 displacing brine), and a potentially large value during imbibition (brine displacing CO_2), which increases as the maximum historical gas saturation increases.

(3) Dissolution trapping (also known as solubility trapping): the CO_2 that dissolves in brine is no longer buoyant so there is no driving force toward the surface. In fact, CO_2-saturated brine is denser than native brine. As CO_2-laden brine sinks deeper into the formation it can set up circulation patterns that enable more free-phase CO_2 to come into contact with native brine, enabling more dissolution to occur (Ennis-King and Paterson, 2005; Pruess and Zhang, 2008). (4) Mineral trapping: CO_2 reacts with rock minerals to form carbonate compounds, typically over long time scales (Pruess et al., 2003; Xu et al., 2003, 2005; Gherardi et al., 2007). The first three mechanisms, collectively referred to as hydrodynamic trapping by Bachu et al. (1994), dominate plume behavior over the hundred-year time scale and are the focus of the present paper. Because trapping mechanisms are scale-dependent, understanding large-volume pilots is a necessary step between existing studies involving small-scale CO_2 injection tests and actual commercial CO_2 storage operations. Additionally, predicting the spatial and temporal evolution of the CO_2 plume and the attendant pressure increase can help optimize design of the monitoring methods used for the pilot.

Model Development

Numerical Simulator

Numerical modeling is conducted using TOUGH2 (Pruess et al., 1999), a general-purpose numerical simulator for multi-phase, multi-component fluid and heat flow in porous and fractured media. TOUGH2 incorporates accurate phase-partitioning and thermophysical properties of all fluid phases and components and uses a multi-phase extension of Darcy's law that includes relative permeability and capillary-pressure effects. The present studies utilize an equation of state package called ECO2N (Pruess and Spycher, 2007; Spycher and Pruess, 2005), designed to treat a two-phase (liquid, gas), three-component (water, salt (NaCl), CO_2) system in pressure/temperature regimes above the critical point of CO_2 ($P = 73.8$ bars, $T = 31$ °C), and a hysteretic formulation for capillary pressure and relative permeability (Doughty, 2007). Chemical reactions between CO_2, brine, and rock minerals are not considered in TOUGH2, but a companion code, TOUGHREACT (Xu et al., 2006), is available for such studies. Likewise, possible hydromechanical responses to CO_2 injection, such as expansion of pore space, fault

reactivation, or breaching of sealing layers, are not included, but can be examined with TOUGH-FLAC, a coupled code that integrates TOUGH2 with the mechanical code FLAC3D (Rutqvist et al., 2002).

In TOUGH2, dissolution of both CO_2 and NaCl in the aqueous phase is modeled as an equilibrium process. That is, in any grid block where one or both of these components exists, there is instantaneous partitioning between the aqueous phase (dissolution) and the free phase (supercritical for CO_2 and solid for NaCl). Partitioning is controlled by the solubility of each component in the aqueous phase. NaCl solubility depends only on temperature, whereas CO_2 solubility depends on temperature, pressure, and salinity, as illustrated in Figure 56 for typical CO_2 storage conditions. CO_2 solubility increases with increasing pressure and decreases with increasing temperature and salinity. Because pressure and temperature are usually correlated, both increasing with depth, their effect on CO_2 solubility tends to cancel out, leaving salinity as the primary controlling factor.

If the amounts of CO_2 and NaCl in a given grid block are each below their respective solubility, then no free phase exists. If the amount of NaCl exceeds its solubility (e.g., as the grid block dries out), then solid salt precipitates. If the amount of CO_2 exceeds its solubility (e.g., as CO_2 is injected), then a supercritical phase develops. An important distinction between these two free phases is that solid salt is always immobile, whereas supercritical CO_2 may be mobile or immobile. Additionally, a small amount of liquid water evaporates into the supercritical phase, whereas the solid phase is pure NaCl. The fraction of pore space occupied by each phase is the saturation S, with S_g denoting the supercritical phase (primarily CO_2, with a small amount of water vapour), S_l denoting the aqueous phase (primarily water, with dissolved CO_2 and NaCl), and S_s denoting the solid salt precipitate. For each grid block, $S_g + S_l + S_s = 1$.

Together, capillary pressure P_c, liquid relative permeability k_{rl}, and gas relative permeability k_{rg} variation as a function of saturation are known as characteristic curves; they control the way the brine (the wetting phase, also called the liquid phase) and supercritical CO_2 (the non-wetting phase, also called the gas phase) interact. In a hysteretic formulation, P_c, k_{rl}, and k_{rg} depend not only on the saturation of the grid block, but also on the history of the saturation of the grid block. When gas saturation S_g increases because
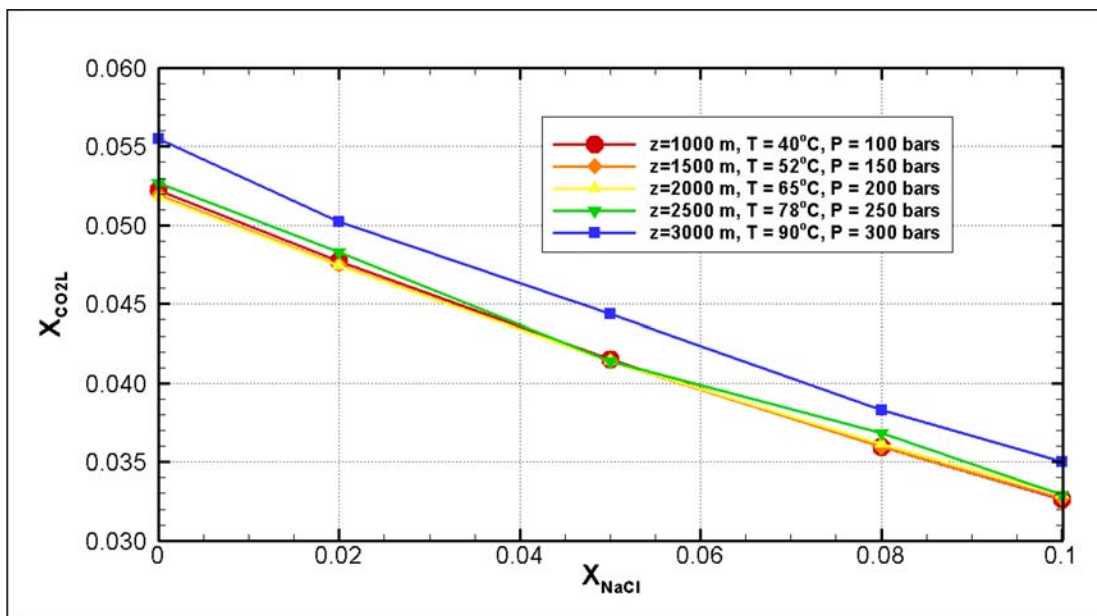

Figure 56: CO_2 solubility (plotted as mass fraction of CO_2 in the aqueous phase) as a function of salinity (plotted as mass fraction of NaCl in the aqueous phase) for various depths, assuming a hydrostatic pressure gradient $P(z) = 1 + 0.1\,z$ and a geothermal temperature gradient $T(z) = 15 + 0.025\,z$. (z in meters)

more CO_2 enters a grid block than leaves it, the process is known as drainage. Alternatively, when liquid saturation S_l increases because more brine enters a grid block than leaves it, the process is known as imbibition. With regard to CO_2 storage, the most critical parameter of the characteristic curves is the residual gas saturation, denoted $S_{gr}{}^\Delta$, which is the saturation below which gas is immobile (i.e., the saturation below which immiscible CO_2 is trapped). TOUGH2 uses the conceptualization common in the petroleum literature (Land, 1968) in which it is assumed that under drainage conditions, $S_{gr}{}^\Delta = 0$, but for imbibition, $S_{gr}{}^\Delta$ increases as maximum historical gas saturation increases. Thus, grid blocks that once contained the most CO_2 are those which trap the most CO_2. The maximum value of $S_{gr}{}^\Delta$, known as S_{grmax}, is a material property dependent on rock porosity (Holtz, 2002). Figure 57 shows the capillary pressure and relative permeability curves under primary drainage conditions and for imbibition when $S_{gr}{}^\Delta = S_{grmax}$. Smaller values of $S_{gr}{}^\Delta$ would produce curves within the envelope formed by these two curves. Figure 57 illustrates that CO_2 mobility can be much smaller under imbibition than under drainage.

During a CO_2 injection period, drainage is the dominant process because the CO_2 plume is growing in all directions, hence $S_{gr}{}^\Delta = 0$ and no CO_2 is trapped as residual gas. After injection ends, the leading edge of the CO_2 plume may still undergo drainage as the plume moves upward and up dip by buoyancy forces, but at the trailing edge of the plume imbibition occurs, $S_{gr}{}^\Delta >> 0$, and a significant fraction of the CO_2 plume may be trapped as residual gas.

Although TOUGH2 has the capability to solve fully coupled fluid and heat flow problems, temperature is assumed to remain constant for the present simulations, to increase computational efficiency. Previous studies (Doughty and Myer, 2009) have shown that thermal effects of CO_2 injection are minor if the injected CO_2 is pre-heated to near in situ temperature. Additionally, the slow flow process of aqueous-phase diffusion of dissolved species is not included in these simulations. For a typical CO_2 diffusivity of $D = 2 \cdot 10^{-9}$ m^2/s (Pruess and Zhang, 2008), the characteristic diffusion length $(Dt)^{1/2}$ is only 0. 5 m for 4 years, 2.5 m for 100 years, and 8 m for 1,000 years, all small compared to CO_2 plume dimensions. Finally, TOUGH2 has the capability to decrease intrinsic permeability due to salt precipitation, but it is not invoked for the present simulations because the amount of salt that precipitates is small.
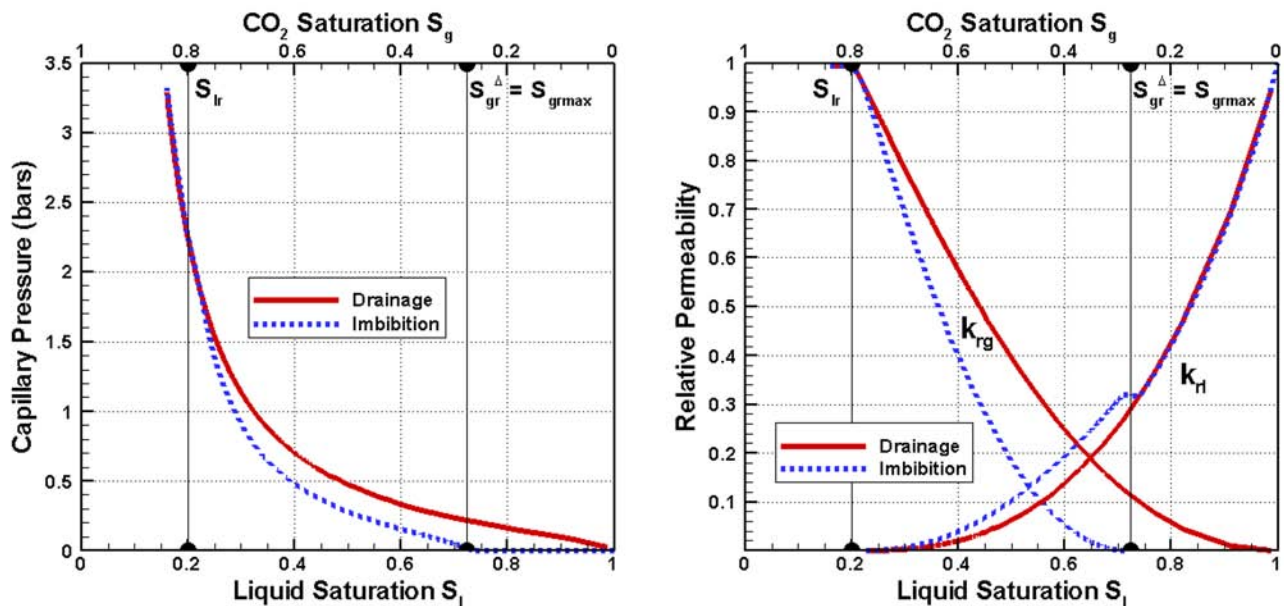
Figure 57: Capillary pressure and relative permeabilities as a function of saturation for primary drainage and for imbibition when $S_{gr}{}^\Delta = S_{grmax}$. Smaller values of $S_{gr}{}^\Delta$ would produce curves within the envelope formed by these two curves. The curve labeled k_{rg} shows relative permeability for supercritical CO_2 and the curve labeled k_{rl} shows relative permeability for brine.

Geologic and Facies Models

A geologic model of the Southern San Joaquin Valley surrounding the Kimberlina site (Wagoner, 2009) is shown in Figure 58. The target CO_2 storage formation is the Vedder Formation, a lower Miocene, fine- to coarse-grained massive marine sandstone with subordinate siltstone and shale. At the Kimberlina site, the Vedder Formation depth is 2 km and its thickness is about 160 m. The overlying Freeman-Jewett Formation, a 100-m thick lower Miocene marine shale and siltstone, provides the upper seal.

A facies model of the Vedder Formation surrounding the Kimberlina site (J. Wagoner, personal communication, 2007) provides the basis for the TOUGH2 model. The facies model (Figure 59) is centered at the proposed Kimberlina power plant site and covers an area of 125 km². Over the entire model area, Vedder Formation thickness ranges from 110 m to 187 m, but within the 2 km surrounding the power plant site, thickness only ranges from 150 m to 164 m. The Vedder Formation dips 7° to the WSW.

The facies model uses 180 layers, of equal thickness, to represent the Vedder Formation. Each layer contains 2500 cells: 50 cells each 250 m wide in the E-W (x) direction by 50 cells each 200 m long in the N-S (y) direction. A facies (either sand or shale) is assigned to each cell, by interpolating sand/shale picks obtained from eight well logs. Because of the limited information available from such a small number of wells, no attempt is made to represent heterogeneity within the individual facies. Overall, the facies model contains about 50% sand and 50% shale, interleaved in a lenticular fashion, with typical lens size 15 m thick and several kilometers in lateral extent. At the location of the proposed injection well, the Vedder Formation is 158 m thick and consists of five sand layers with total thickness 79 m, separated by four shale lenses with total thickness 79 m.
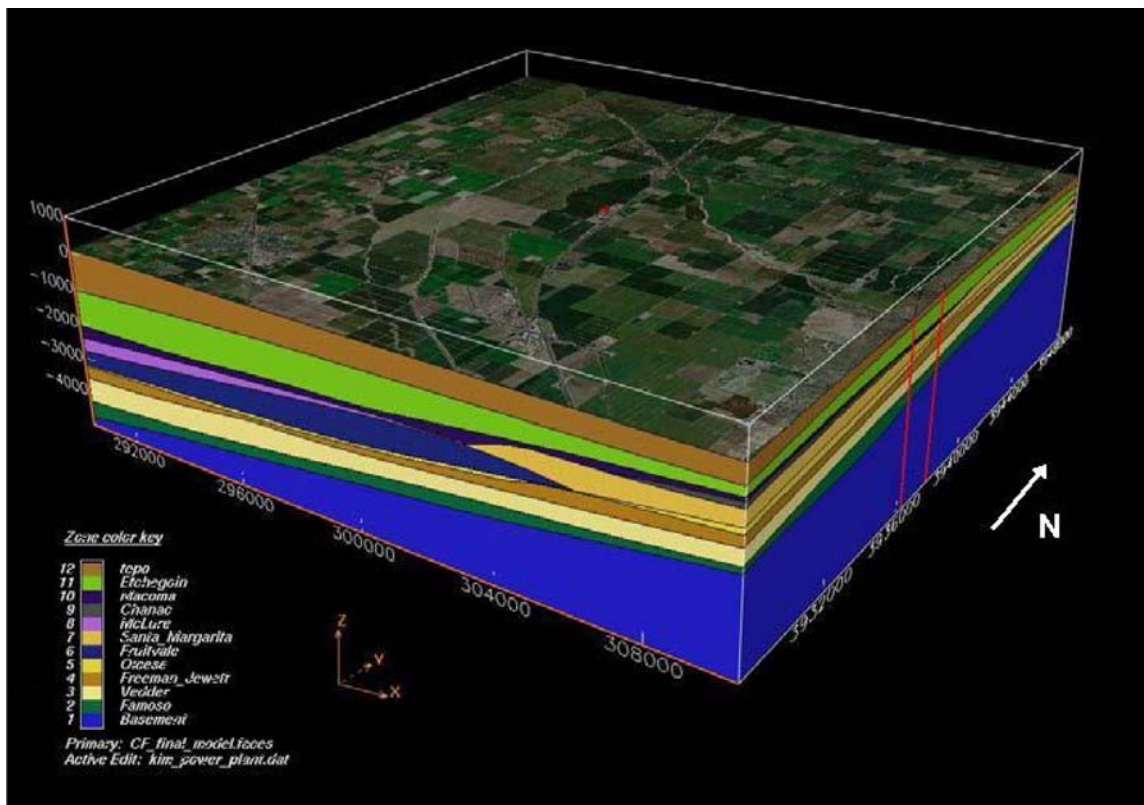
Figure 58: Geologic model of the southern San Joaquin Valley (adapted from Wagoner, 2009). The location of the Kimberlina site is shown by the red dot near the center.
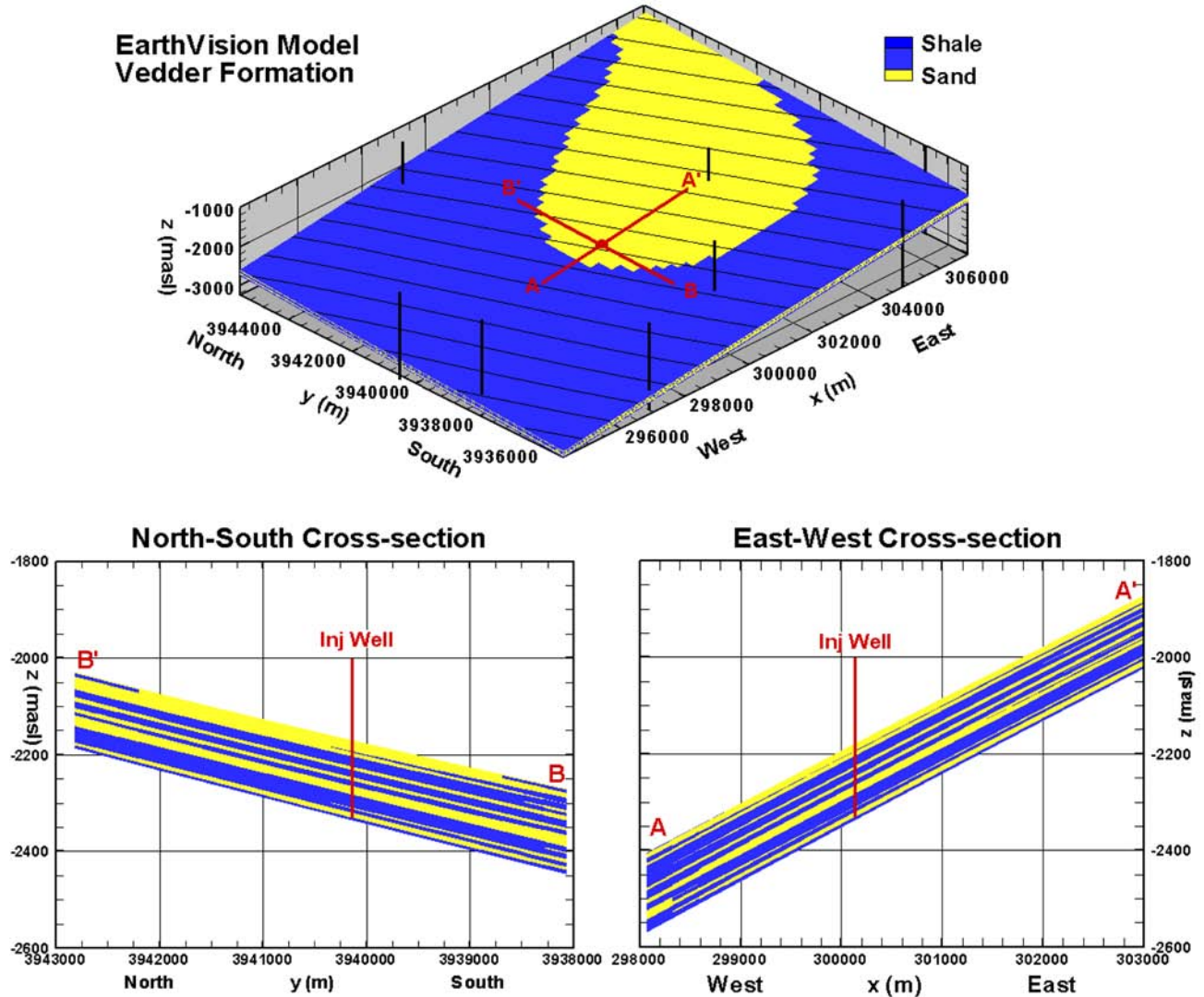
Figure 59: Three views of the facies model of the Vedder Formation. The perspective view (top) has no vertical exaggeration, whereas the two cross-sections (bottom) have five times vertical exaggeration, to enable sand/shale layering to be seen. In the perspective view, the thick black line segments show the locations of the eight wells used to develop the facies model, the thin black lines are depth contours, and the intersection of the two cross-sections marks the location of the injection well in the TOUGH2 simulations.

Numerical Model

The TOUGH2 model (Figure 60) covers roughly the same spatial extent as the facies model. Because the formation dip and thickness are nearly uniform in the vicinity of the Kimberlina site (note that depth contour lines in the perspective view of Figure 59 are essentially equidistant and linear), the TOUGH2 model is constructed as a tilted plane, with just a single value of thickness (157.5 m) and dip (7°). The up-dip direction is 30° counter-clockwise from the $+x$-axis

(ENE), corresponding to the WSW down-dip direction. Each TOUGH2-model layer is formed by combining six facies-model layers, resulting in 30 layers, each 5.25 m thick. At the (x,y) location of each facies-model cell, the facies of the TOUGH2-model layer is taken to be the facies that occurs the most times among the six facies-model layers that are combined to form it. As can be seen by comparing Figure 59 and Figure 60, this combining scheme captures the essential features of the lenticular sand/shale structure of the facies model.
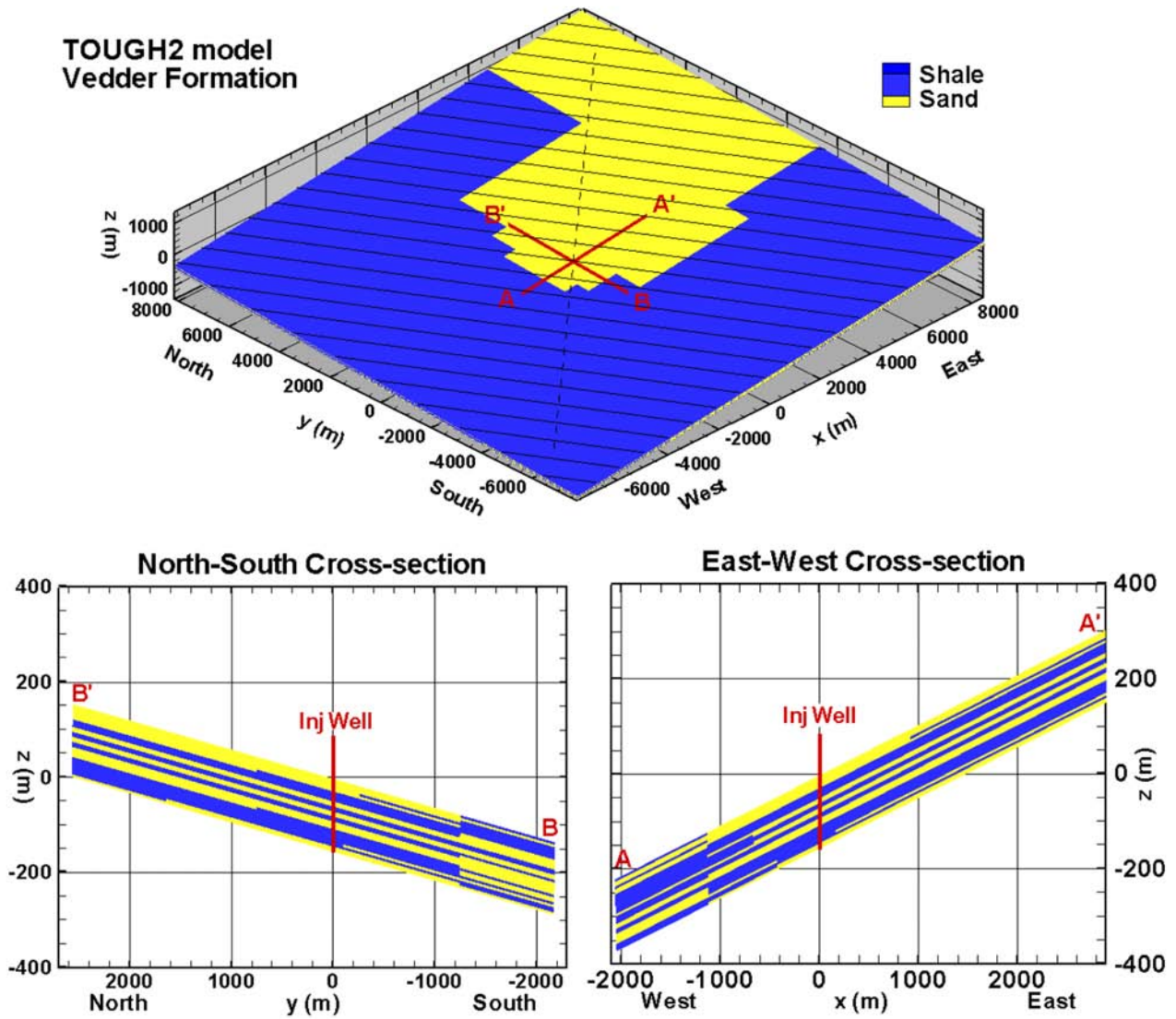
Figure 60: Three views of the TOUGH2 model of the Vedder Formation. The perspective view (top) has no vertical exaggeration, whereas the two cross-sections (bottom) have five times vertical exaggeration, to enable sand/shale layering to be seen. In the perspective view, the thin black lines are depth contours, and the intersection of the two cross-sections marks the location of the injection well in the TOUGH2 simulations. Note that the coordinate system has been translated so that the origin is where the injection well intersects the top of the Vedder Formation. The dashed line shows the along-dip profile through the injection well for which simulation results are shown in Figure 70.

The computational grid for the TOUGH2 model is shown in Figure 61. Laterally, the TOUGH2 model grid-block size varies, with finest grid blocks in the vicinity of the injection well (5 m by 5 m), increasing to 55 m by 55 m in the region where the CO_2 plume is expected to go (roughly an ellipse with a major axis less than 2 km), and gradually increasing further beyond that region.

The lateral extent of the active portion of the TOUGH2 model is 11 km by 11 km, beyond which additional grid blocks are added to represent lateral boundary conditions. The vertical discretization of the TOUGH2 model into 30 layers results in at least two model layers per sand layer, to enable vertical flow arising from buoyancy forces to be resolved.
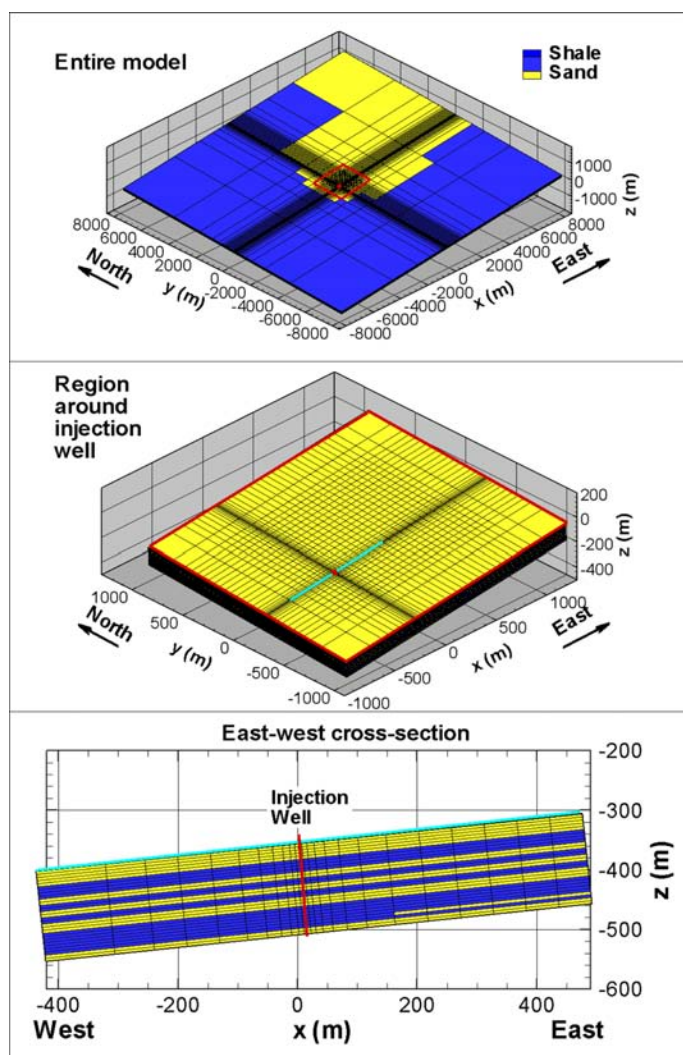
Figure 61: Three views of the TOUGH2 model of the Vedder Formation showing the computational grid.

The 5-m width of the grid-block used for the injection well is much greater than an actual well diameter, so the simulation is not expected to accurately reproduce all near-wellbore effects arising during CO_2 injection. For example, the modeled pressure increase will not be the actual pressure increase in the wellbore, but an average over five meters of formation surrounding the well. However, the focus of the present paper is on plume-scale effects, and using a grid fine enough to represent an actual wellbore would greatly slow down the simulations. Two features that are not included in the present simulations, thermal effects and intrinsic permeability decrease due to salt precipitation, have their main effect within or close to the wellbore, so neglecting them is consistent with the use of the present grid.

The top and bottom boundary of the TOUGH2 model are no-flow boundaries, to represent regionally extensive, continuous shale layers over- and underlying the Vedder Formation. In the x-direction the lateral boundaries are constant pressure boundaries and in the y-direction the lateral boundaries are no-flow boundaries. These boundary conditions are chosen for numerical convenience rather than geological accuracy. The actual extent of the Vedder Formation is estimated to be 55 km in the east-west direction and 90 km in the north-south direction, far beyond the lateral extent of the TOUGH2 model. As shown in the "simulation results" section below, the lateral boundaries are so far away from the injection well and the region the CO_2 plume occupies that they have little impact on the evolution of the CO_2 plume. Table 15 summarizes the geometric properties and boundary conditions of the TOUGH2 model.

Table 15: Geometric properties and boundary conditions of the TOUGH2 model for the Vedder Formation at the Kimberlina site.

Parameter	Value	Comment
Depth at injection well (m)	2200	Same as facies model
Thickness (m)	157.5	Facies model thickness ranges from 110 m to 187 m
Percent sand/shale	50/50	Sand occurs in five distinct layers, with interleaving shales
Number of model layers	30	Each model layer 5.25 m thick, combines 6 facies-model layers
Lateral extent (km)	11 by 11	Comparable to facies model
Lateral grid spacing	Varies	5 m by 5 m at injection well; maximum 55 m by 55 m within CO_2 plume footprint
Formation dip	7°	Up-dip direction is ENE, 30° counter-clockwise from +x-axis
Boundary Conditions		
Top and bottom	No flow	Represent continuous, extensive shale layers
Lateral, x-direction	Constant pressure	
Lateral, y-direction	No flow	

The initial conditions for the CO_2 injection are a brine-saturated formation with a hydrostatic pressure distribution, and a pressure of 220 bars at the injection well location. Initial temperature and salinity are uniform at 81°C and 50,000 TDS, respectively. This temperature is calculated assuming a surface temperature of 15°C and a geothermal gradient of 30°C per km, both of which are rough estimates considered reasonable for Southern California. In the absence of specific information on salinity for the Vedder Formation, a moderate value of 50,000 TDS is chosen. The primary impact of the initial pressure and temperature are to define the density and viscosity of the CO_2 plume in the subsurface. Density controls not only the volume of the plume, but the strength of the buoyancy force, which is proportional to the density difference between injected CO_2 and native brine. In conjunction with permeability, viscosity controls how mobile the CO_2 is. The effects of initial pressure and temperature on plume migration are examined elsewhere (Jordan and Doughty, 2008). According to Figure 56, salinity is inversely related to CO_2 solubility. If actual salinity turns out to be lower than 50,000 TDS (values as low as 20,000 TDS have been proposed), a greater fraction of the injected CO_2 will dissolve and the free-phase plume will be correspondingly smaller. Additionally, lower salinity means smaller brine density, which decreases the driving force for buoyant flow of free-phase CO_2. Thus the present simulation results may be considered to be conservative in terms of predicting plume extent and migration. Table 16 summarizes the

initial conditions used for the Kimberlina simulations, and the resulting density and viscosity of the injected CO_2 and the native brine. It shows that the injected plume will be strongly buoyant in the subsurface.

The material properties used in the base-case TOUGH2 model are summarized in Table 17. Porosity and permeability values are consistent with the geologic model, but relative permeability and capillary pressure parameters are not known for the Kimberlina site, so parameter values are adapted from other studies of CO_2 geologic storage in saline formations (Doughty, 2007; Doughty et al., 2008). Sensitivity studies then examine the impact of varying permeability, permeability anisotropy (both vertical and lateral), and maximum residual gas saturation. Table 17 shows that the permeability contrast between the sand and shale facies is large; thus CO_2, which is injected only into sand layers, is expected to remain in the sand layers. The functional forms of the hysteretic characteristic curves (Doughty, 2007) are based on the van Genuchten (1980) formulation.

Table 16: Initial Conditions and Flow Properties of CO_2 and Brine

Initial Condition	Value	
Initial pressure	Hydrostatic pressure distribution; average 220 bars at injection well	
Initial temperature	81°C	
Initial salinity	50,000 mg/L	
CO_2 Solubility in Brine	43,000 mg/L	
Flow Property	CO_2	Brine
Density (kg/m³)	632	1014
Viscosity (Pa-sec)	$5 \cdot 10^{-5}$	$4 \cdot 10^{-4}$

Table 17: Material Properties of the Base-Case TOUGH2 Model

Property	Sand	Shale
Porosity	28%	15%
Horizontal* Permeability, k_x, k_y	200 mD	0.1 mD
Vertical* Permeability k_z	20 mD	0.01 mD
Relative Permeability Parameters		
Residual Liquid Saturation S_{lr}	0.2	0.3
Maximum Residual Gas Saturation S_{grmax} **	0.27	0.29
van Genuchten parameter m	0.917	0.917
Capillary Pressure Parameters (same for drainage and imbibition branches)		
Capillary pressure strength P_{c0}	$1.88 \cdot 10^4$ Pa	$8.41 \cdot 10^5$ Pa
van Genuchten parameter m	0.412	0.412

* "Horizontal" means parallel to layering; "vertical" means perpendicular to layering

** Residual gas saturation S_{gr}^A is zero during drainage and non-zero during imbibition, where it depends on saturation history and has a maximum value of S_{grmax}.

The CO_2 injection well is located at the center of the model and penetrates the entire Vedder Formation thickness. Because the TOUGH2 model does not include an actual wellbore model (recall that lateral grid spacing at the injection well location is 5 m by 5 m), injection is modeled as a mass source distributed among the sand layers, with source strength proportional to layer thickness. Altogether, 250,000 T/year are injected for a period of four years, resulting in 1,000,000 metric tons of CO_2 injected.

Simulation Results

The TOUGH2 simulations cover the four-year injection period and at least 100 years thereafter, when CO_2 is subject only to gravity and capillary forces. All simulations use the computational grid shown in Figure 61 and the properties shown in Tables 15 and 16. Base-case simulations use the properties shown in Table 17, while sensitivity studies consider alternative values whose ranges reflect the uncertainty of our knowledge of actual properties.

Base Case

Supercritical CO_2

Figure 62 and Figure 63 show snapshots of the supercritical CO_2 plume at various times. Figure 62 shows a plan view of the uppermost layer of the model, which is the layer in which the greatest lateral extent of CO_2 occurs. Figure 63 shows x-z cross-sections through the model, and illustrates the formation of five sub-plumes in the five sand layers within the Vedder formation. Note from Figure 62 that the x-z plane does not show the maximum lateral extent of CO_2, which occurs in the up-dip direction. Together, Figure 62 and Figure 63 illustrate the strong buoyancy flow that moves CO_2 to the top of each sand layer, and from there moves the plume up dip. Figure 62 also shows that during injection, the rectilinear grid produces numerical artifacts in the plume distribution by enabling enhanced flow along the grid axis directions. Recent work (Yamamoto and Doughty, 2009) has shown that using hexagonal grids or unstructured grids created with Voronoi tessellation can eliminate this problem with little increase in computational effort, supplanting rectangular grids as the discretization method of choice.

Figure 62: Top view of the base-case supercritical CO_2 plume at a series of times, shown by plotting S_g, saturation of supercritical CO_2, in the uppermost model layer.

Key measures of the CO_2 plume are its up-dip extent at stabilization and the time evolution of the partitioning of CO_2 between dissolved, immobile-gas, and mobile-gas forms. For the present paper, plume stabilization is defined as occurring when two successive snapshots show no advance of the leading edge of the plume. Figure 62 shows that the base-case plume has stabilized by 25 years, at which time it is about 1500 m long, 900 m wide, and extends 1300 m up-dip of the injection well.

Quantification of the trapping and stabilization process is presented in Figure 64, which shows the time evolution of the CO_2 mass distribution for the entire model. The total amount of CO_2 injected is divided into two parts: a gas-like supercritical phase and a dissolved phase. The supercritical phase is further divided into mobile and immobile portions, with CO_2 immobile when its saturation is below residual gas saturation S_{gr}^A. Throughout the injection period,

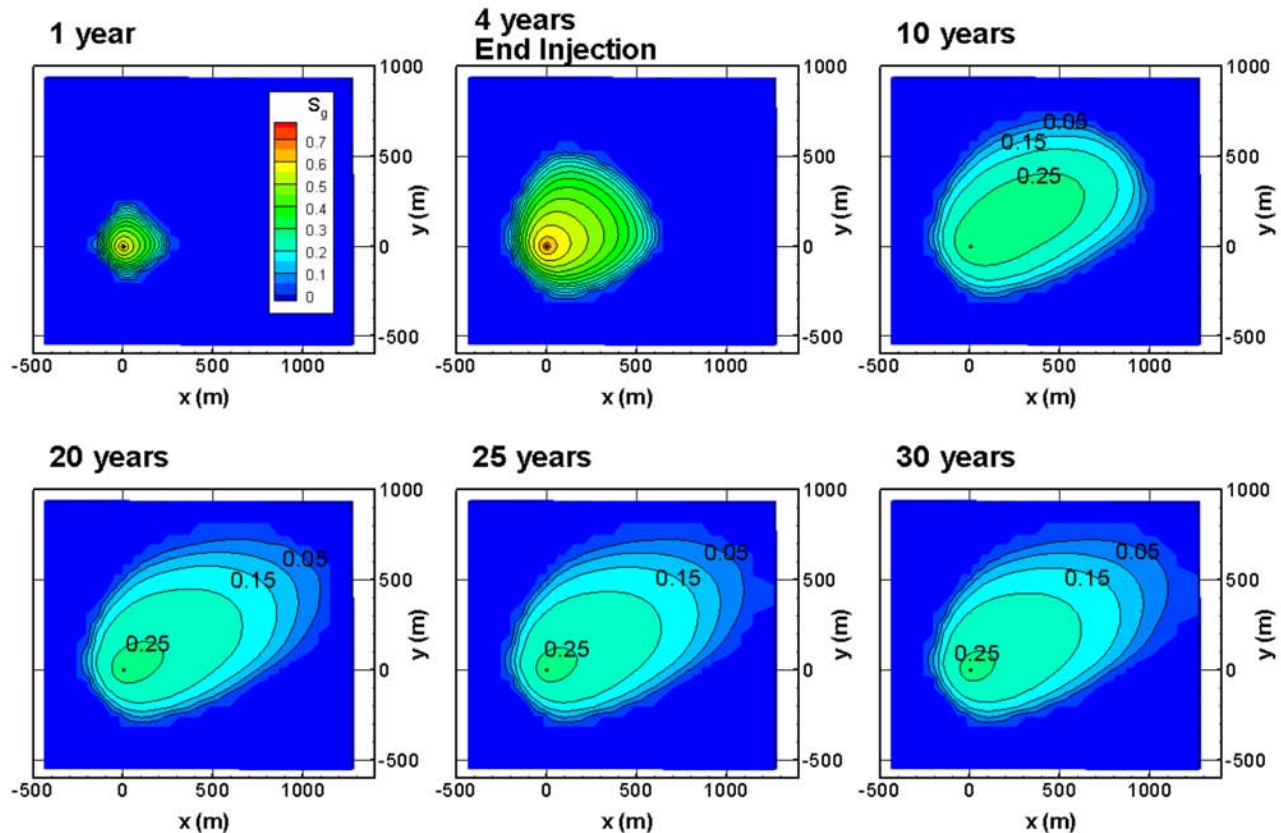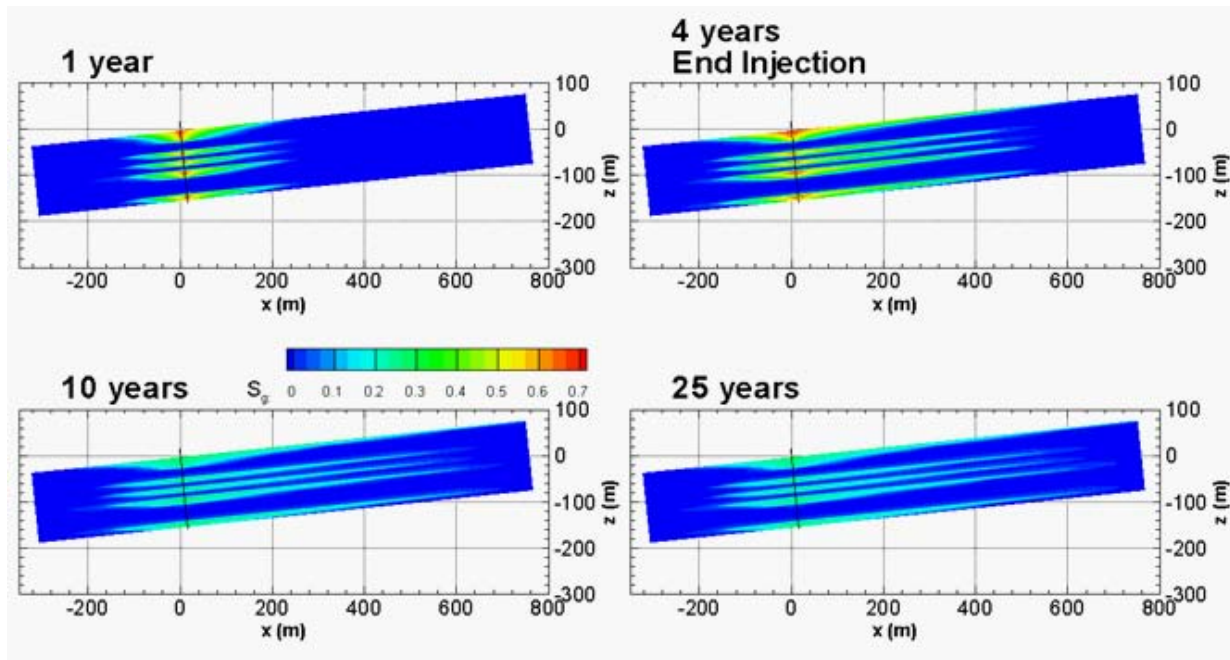Figure 63: East-west cross-section of the base-case supercritical CO_2 plume at a series of times, shown by plotting S_g, saturation of supercritical CO_2, in the plane $y = 0$.
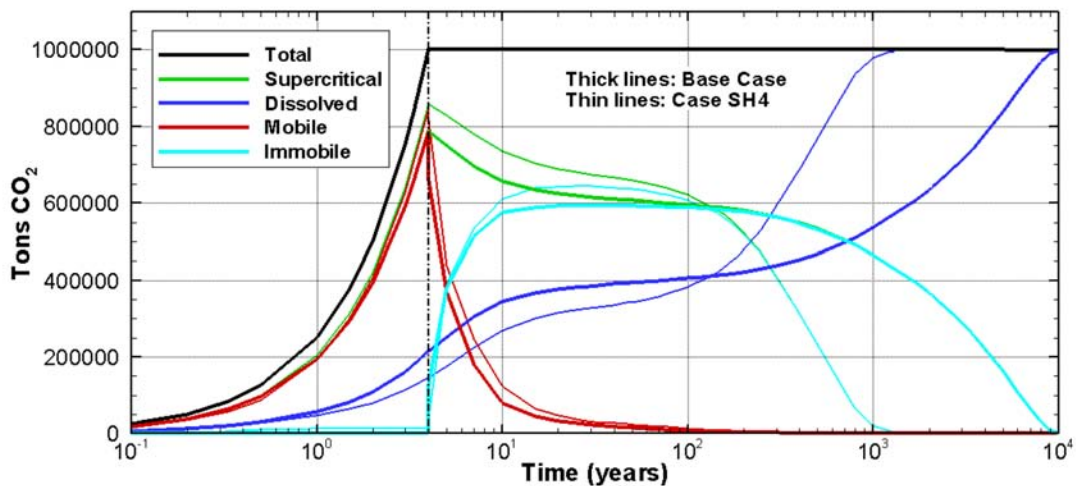
Figure 64: Time evolution of the CO_2 mass distribution for the entire model for the base case (thick lines) and sensitivity-study case SH4, which models the Vedder Formation as a homogeneous, isotropic sand (thin lines).

about 20% of the CO_2 dissolves, and essentially all the supercritical-phase CO_2 is mobile. After injection ends, the dissolved fraction increases gradually to 38% as the plume moves up dip and encounters new under-saturated brine. This up-dip movement is accompanied by residual CO_2 trapping, and Figure 64 shows how the mobile fraction of supercritical CO_2 decreases concurrent with the increase of the immobile fraction. By 25 years the supercritical CO_2 is largely immobile, coinciding with the stabilization of the plume shown in Figure 62. Thereafter, the plume does not move as a whole, but subtle redistributions of the immiscible phase further decrease the mobile fraction and dissolution of supercritical CO_2 continues, slowly increasing the dissolved fraction. The supercritical plume has nearly completely dissolved by 10,000 years.

Insight into residual CO_2 trapping can be obtained by examining the spatial distribution of drainage and imbibition at a series of times during and after injection. Figure 65 displays ICURV, the variable identifying which branch of the capillary pressure curve is being followed, for each grid block in the uppermost model layer. Recall that residual CO_2 trapping requires a non-zero value of residual gas saturation, which only occurs during imbibition. Nearly the entire plume is undergoing drainage just after the injection period ends, except for a narrow imbibition zone at the trailing (down-dip) edge of the plume. The imbibition zone grows steadily until 25 years, when drainage is limited to a few grid blocks at the leading (up-dip) edge of the plume, at which time the plume has stabilized. Thereafter, the zone of drainage gradually shrinks further, until it has disappeared by 100 years.
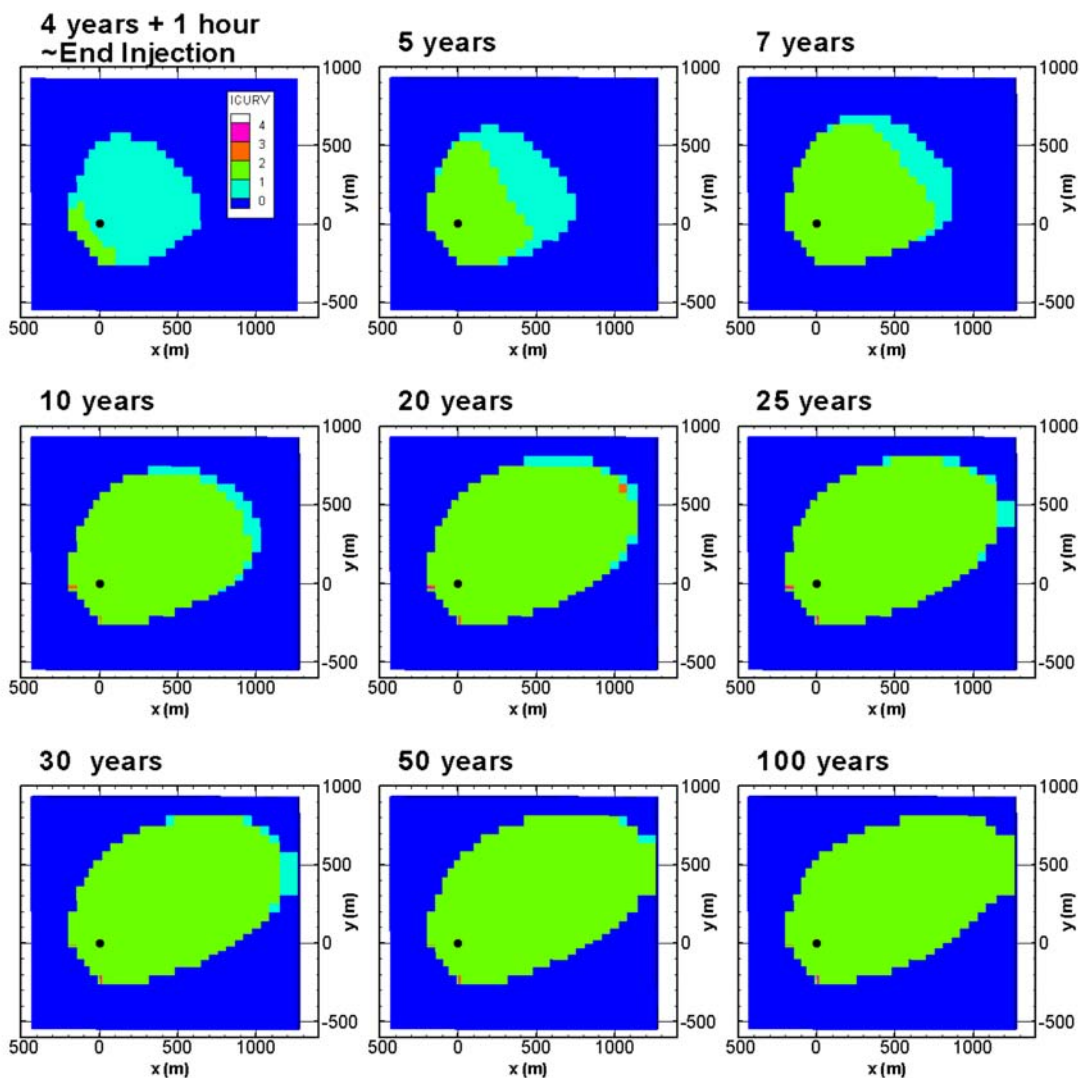
Figure 65: Top view of base-case distribution of drainage and imbibition at a series of times: ICURV = 0 - single-phase liquid, 1 – primary drainage, 2 – first-order imbibition, 3 – second-order drainage, 4 – third-order imbibition.
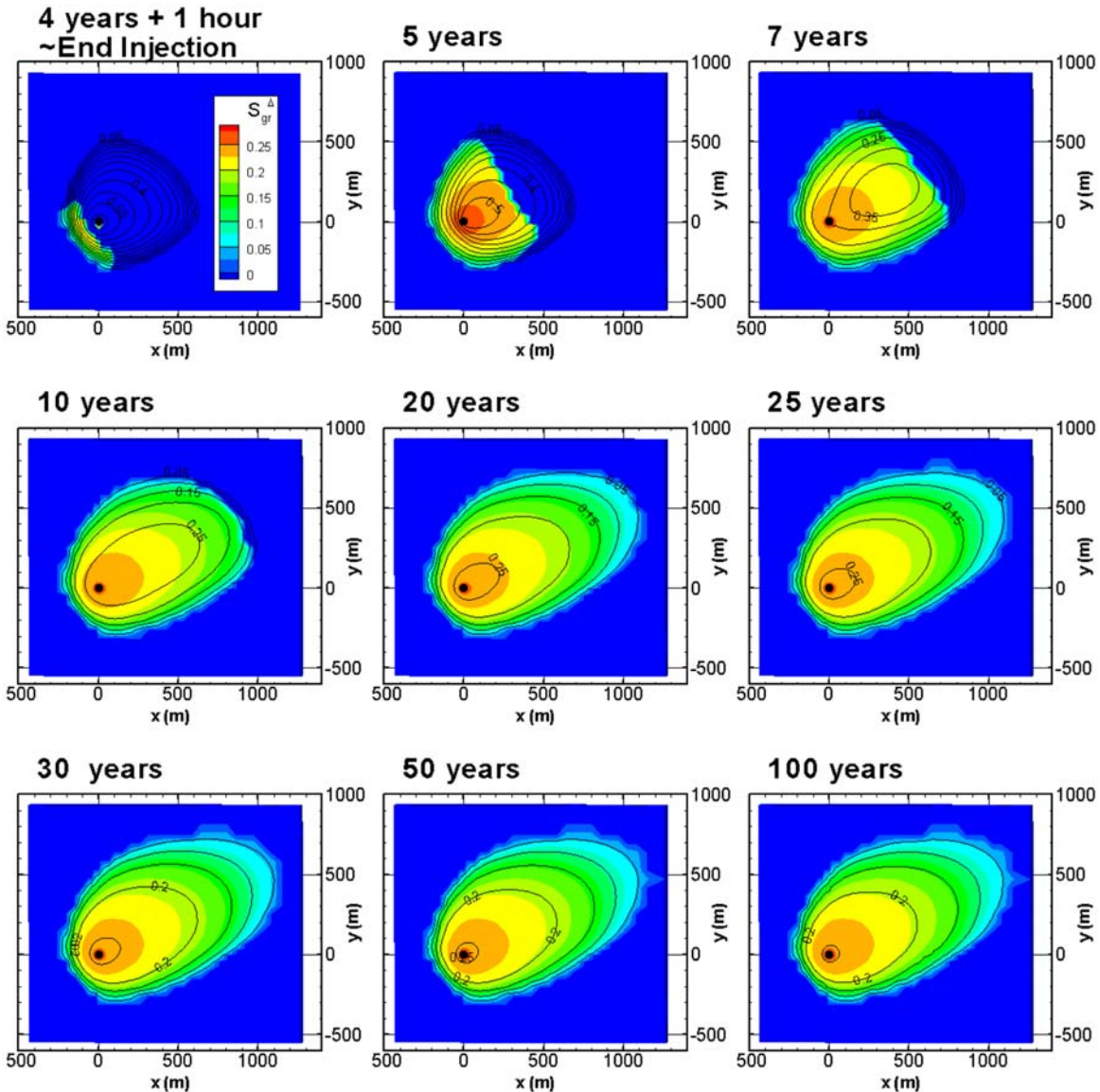
Figure 66: Top view of base-case distribution of residual gas saturation S_{gr}^{Δ} at a series of times (colors). Contour lines show supercritical CO_2 saturation S_g, illustrating the spatial distribution of the plume itself.

Because imbibition dominates the plume for most of the post-injection period, the residual gas saturation S_{gr}^{Δ} is non-zero over much of the plume (Figure 66), enabling significant residual CO_2 trapping. The S_{gr}^{Δ} distribution does not change after the plume stabilizes at 25 years.

Figure 67 shows the spatial distribution of $(S_g - S_{gr}^{\Delta})$, the difference between gas saturation and residual gas saturation. The larger the value of $(S_g - S_{gr}^{\Delta})$, the more mobile the plume is (Figure 57). There is a sharp decrease in mobility at the transition from drainage $(S_{gr}^{\Delta} = 0)$ to imbibition $(S_{gr}^{\Delta} > 0)$ at 4, 5, and 7 years (compare to Figure 65 and Figure 66). From 10 years

on, $(S_g - S_{gr}^{\Delta})$ is small throughout the plume. Beginning at 20 years, negative values of $(S_g - S_{gr}^{\Delta})$ develop, which can only happen by if immobile free-phase CO_2 is dissolving. Continued dissolution of immobile CO_2 implies that the brine must be moving, because quiescent brine adjacent to immobile free-phase CO_2 would quickly saturate, precluding further dissolution. The present simulations do not include regional groundwater flow, so the only driving force for brine movement is natural convection, arising from the small brine density increase that occurs when CO_2 dissolves. The banded character of the negative $(S_g - S_{gr}^{\Delta})$ values evident at 500 and 1,000 years suggests the formation of

convection cells in the brine underlying the free-phase CO_2, with the top of each cell (where lighter CO_2-free native brine up-wells) coincident with a band of enhanced dissolution.

Figure 67: Top view of base-case distribution of $(S_g - S_{gr}^A)$ at a series of times (colors). Contour lines show S_{gr} saturation of supercritical CO_2, illustrating the spatial distribution of the plume itself. Note that different color maps are used for the first four frames and for the final eight frames, where all negative values of $(S_g - S_{gr}^A)$ are shown in dark blue.

Dissolved CO_2
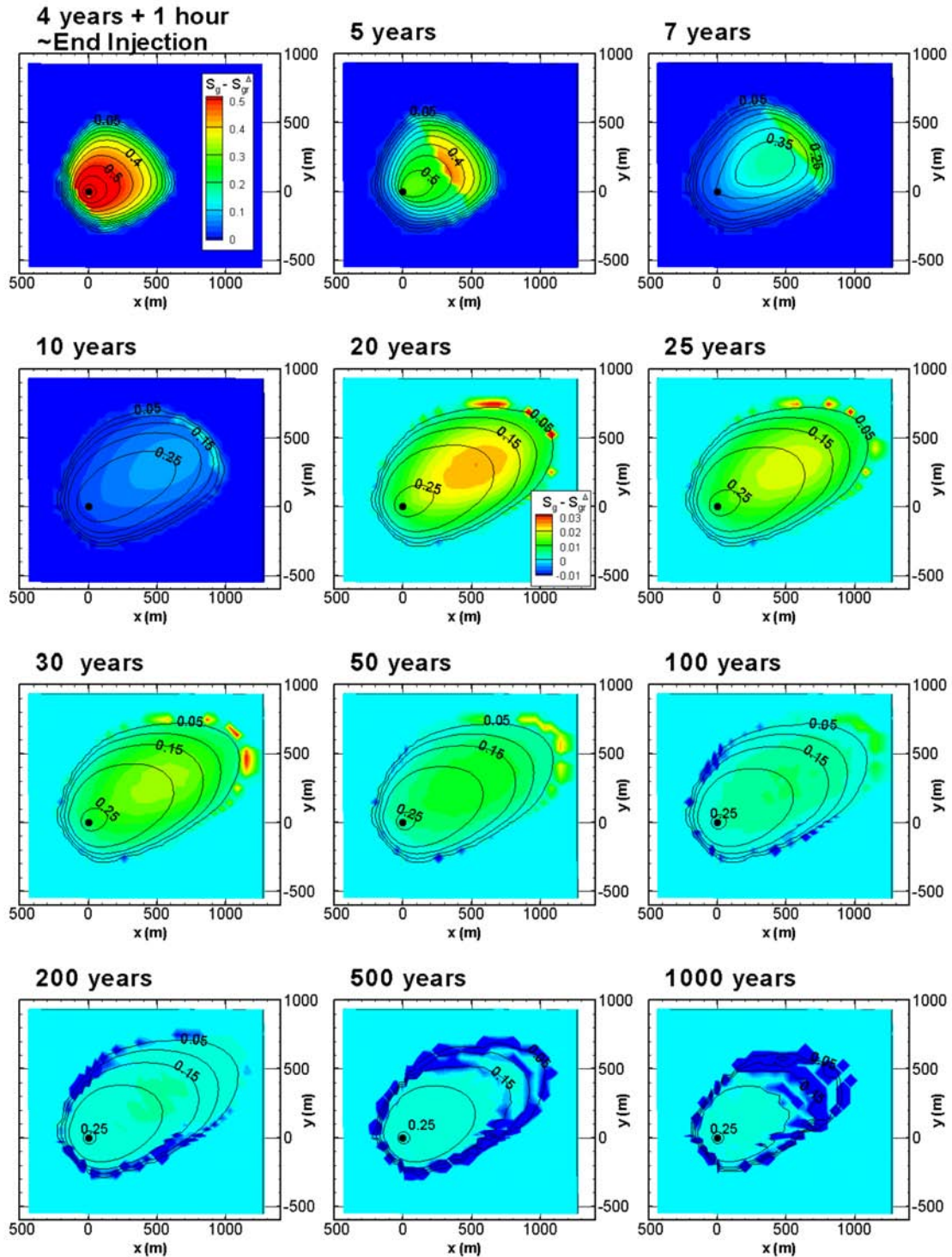
Before investigating the natural convection of CO_2-laden brine, it is worthwhile to examine further how the free-phase CO_2 and dissolved CO_2 interact. Figure 68 shows a vertical cross-section of the storage formation in the vicinity of the injection well at four years, the end of the injection period. The top frame shows free-phase CO_2, the second frame shows CO_2 dissolved in the brine, the third frame shows the NaCl dissolved in the brine, and the bottom frame shows precipitated NaCl. Dissolved species are shown as mass fractions in the aqueous phase, whereas precipitated NaCl is shown as solid saturation S_s (i.e., the pore volume fraction of precipitated NaCl).

For the most part, the spatial distribution of dissolved CO_2 coincides with that of free-phase CO_2. The one exception is close to the injection intervals where S_g is large. In these locations, strong capillary forces arising from large values of S_g draw brine toward the well. Near the well, some of the water evaporates into the supercritical CO_2 phase, increasing dissolved NaCl content in the remaining brine. There is an inverse correlation between NaCl content and CO_2 solubility (Figure 56), resulting in the regions of low dissolved CO_2 near the injection intervals. Otherwise, the close correspondence between the spatial extents of free-phase and dissolved CO_2 indicates that natural convection of brine is negligible at this time. Recall that aqueous-phase diffusion is not included in these simulations. The slight extension of the dissolved-CO_2 plume beyond the free-phase plume visible in Figure 68 is likely due to numerical dispersion.

Figure 69 shows dissolved CO_2 distributions at 25, 100, and 500 years. With time, spatial distributions of dissolved and free-phase CO_2 increasingly differ, confirming that natural convection of CO_2-laden brine is significant, and the convection cells themselves are illustrated by the irregular distribution of dissolved CO_2 in the up-dip region of the top sand layer at 100 and 500 years. The low-permeability shales separating each of the five sub-plumes, constrain the bulk of the brine flow to the sand layers. Flow is greater down-dip, but up-dip flow into the deeper parts of each sand layer is also evident. At times beyond 500 years (not shown), down-dip migration of dissolved CO_2 continues, but its up-dip extent does not change appreciably. At the final simulation time (10,000 years) the dissolved CO_2 plume extends about 4 km down-dip from the injection well.
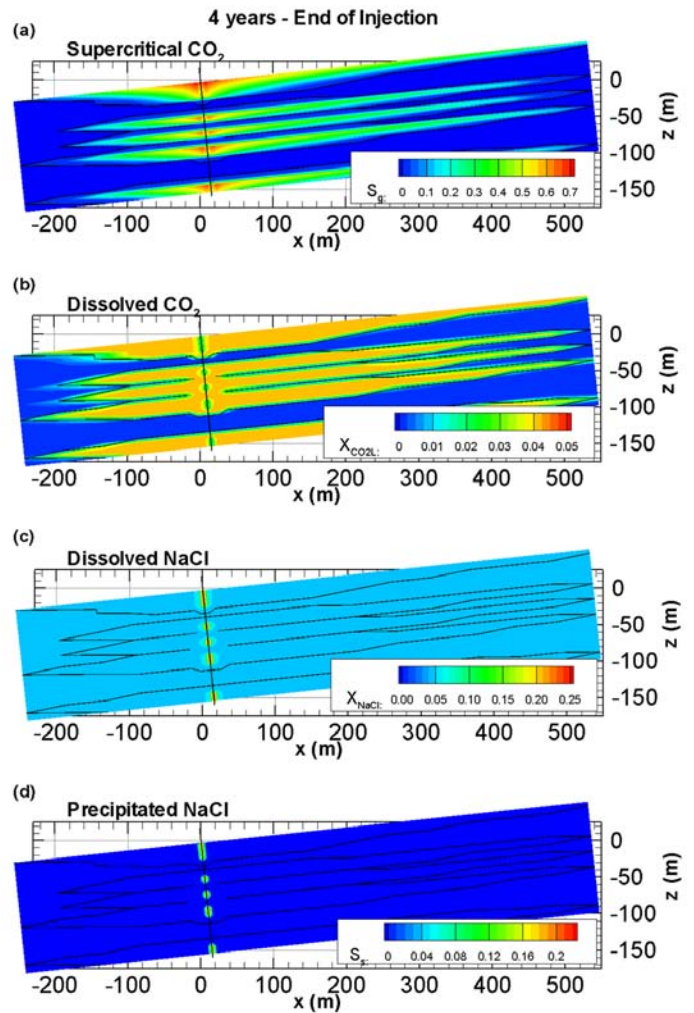
Figure 68: East-west cross-section of the base-case plume in the plane $y = 0$ at four years: (a) S_g shows saturation of supercritical CO_2; (b) X_{CO2L} shows the mass fraction of CO_2 dissolved in the aqueous phase; (c) X_{NaCl} shows the mass fraction of NaCl dissolved in the aqueous phase; (d) S_s shows saturation of precipitated NaCl. The black contour lines show $S_g = 0$, illustrating the maximum extent of the supercritical plume.
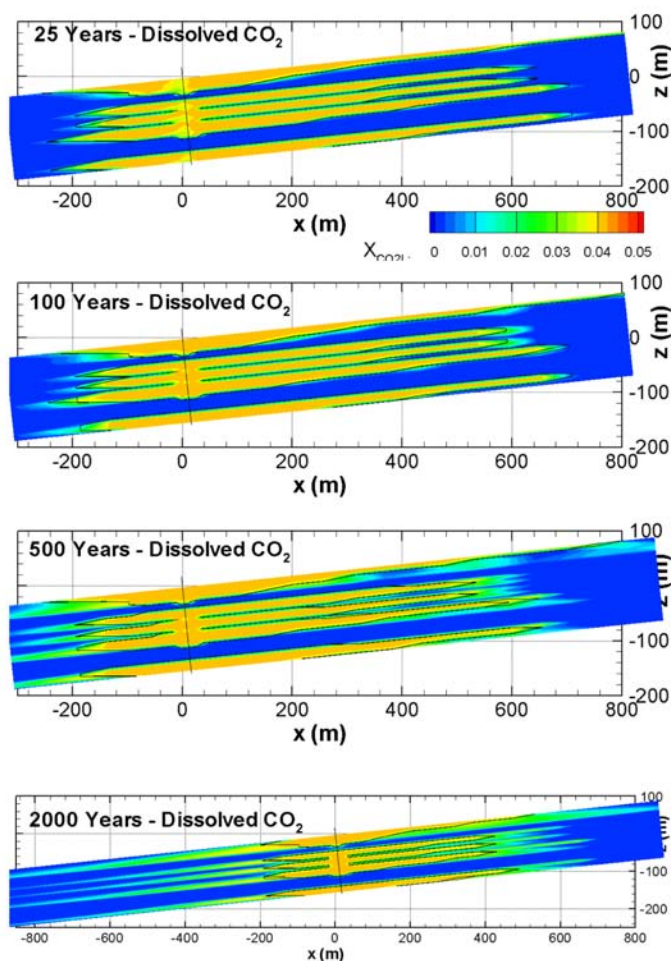
Figure 69: Late-time (i.e., post-stabilization) distributions of base-case dissolved CO_2, shown by plotting X_{CO2L}, the mass fraction of CO_2 dissolved in the aqueous phase, in the plane $y = 0$. The black contour lines show $S_g = 0$, illustrating the maximum extent of the supercritical plume.

Pressure Response

Figure 70 compares the lateral extent of the pressure response to CO_2 injection with the lateral extent of the CO_2 plume itself. The profiles show pressure change and gas saturation in the uppermost layer in the model, along a transect through at the injection well and extending in the dip direction, as shown in Figure 60. During the injection period, pressure close to the injection well does not increase monotonically with time. This occurs because the viscosity of injected CO_2 is much lower than that of the native brine (Table 16),

and as the CO_2 plume grows there is less resistance to flow, so less pressure increase in response to the constant CO_2 injection rate. After injection ends, CO_2 saturation decreases as the plume stretches out, with the leading edge of the CO_2 plume moving up dip and the maximum pressure increase moving along with it. Although the pressure response extends far beyond the CO_2 plume, the pressure response beyond the CO_2 footprint is small (less than 1.5 bars). Moreover, pressure response decreases as distance from the injection well increases, and quickly dissipates after injection ceases (less than 1 bar everywhere one year after injection ends).

Part of the asymmetry in the pressure profile between up-dip and down-dip directions arises from the presence of a shale lens about 1.5 km down-dip from the injection well (see Figure 60). In the low-permeability shale, pressure builds up more during the injection period and does not dissipate as rapidly once injection ends, compared to the pressure response in the high-permeability sand. This effect combines with the post-injection up-dip movement of the CO_2 plume to create a pressure minimum at the down-dip edge of the plume, where pressure actually drops slightly below the initial hydrostatic pressure.

Recall that the base-case model assumes partially-open (constant-P), partially-closed (no flow) boundary conditions. Two additional simulations, assuming either all-open or all-closed lateral boundary conditions, produce identical CO_2 plumes, and only slightly different pressure responses. During the injection period, pressure responses are similar for all cases. Only near the lateral boundary does the all-closed case differ significantly, with a pressure increase of just over 0.2 bars (the pressure response at the open boundaries is guaranteed to be zero). After injection ceases, the pressure change at all distances decreases to near zero for the base case (Figure 70) and the all-open case (not shown) within 20 years. For the closed case, the pressure change becomes uniform in space at a value just below 0.3 bars.
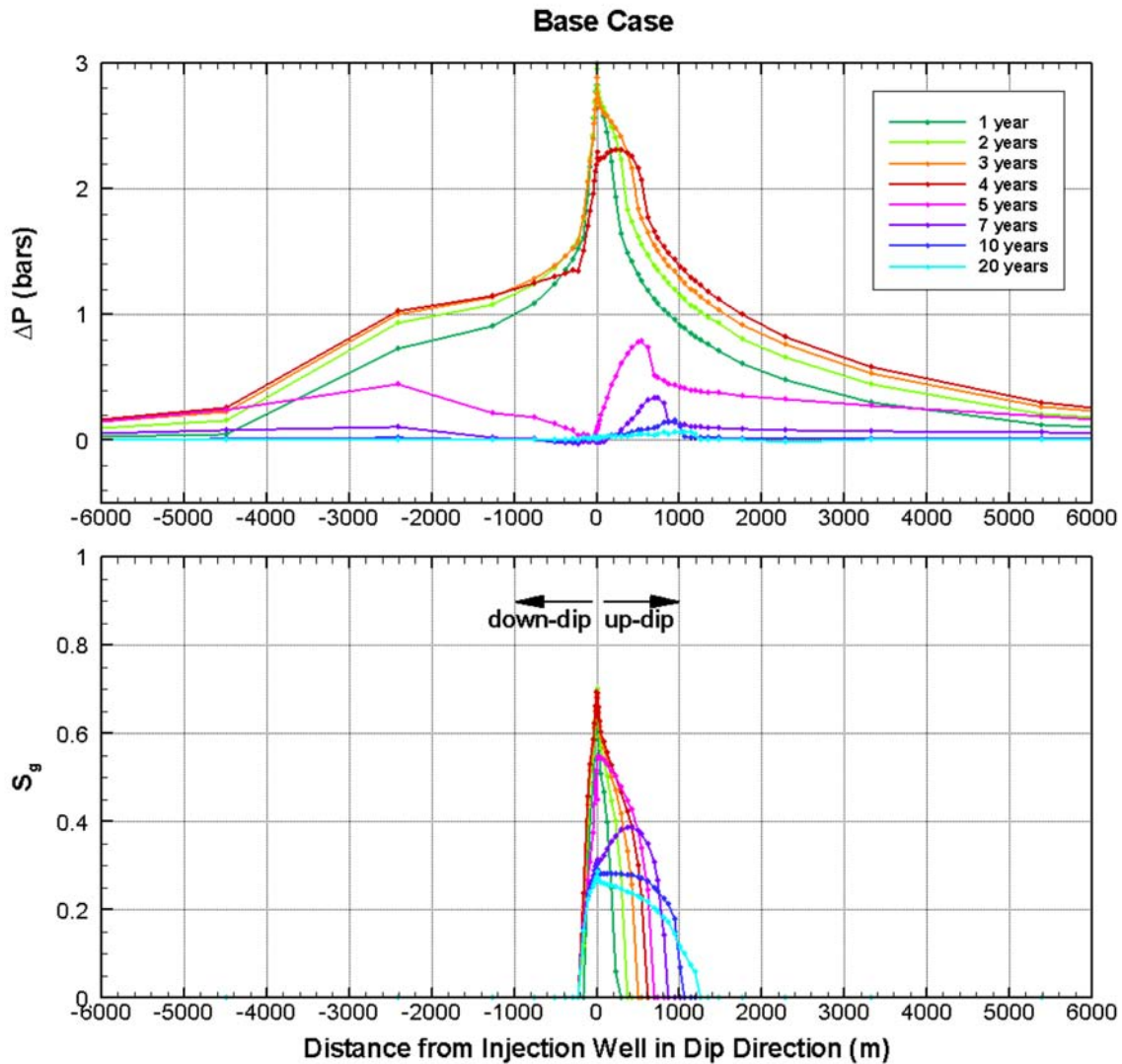
Figure 70: Pressure change and supercritical CO_2 saturation S_g versus distance from the injection well in the dip direction for the base case.

Sensitivity Studies

Values for most of the material properties used as input to the base-case numerical simulation are not well known. To assess the impact of parameter uncertainty on plume evolution and trapping mechanisms, sensitivity studies are carried out using alternative parameter choices for poorly-known parameters. Table 18 summarizes the cases and the key performance measures. Figure 71 shows a plan view of the top of the stabilized plume for each case.

The time-variation of the mass of mobile CO_2 (Figure 64) shows an initial rapid decrease after injection ends followed by a slow approach to zero, which does not provide a convenient means for determining when a plume has stabilized. It is clear from the time series of CO_2 distributions (Figure 62) that the plume does not move perceptibly after 25 years, even though mobile CO_2 remains. Rather than trying to find a threshold mass of mobile CO_2 that defines stabilization, the CO_2 distributions are used directly, and stabilization is defined

Table 18: Summary of Sensitivity Studies

Case	Key Features	Time to 3% Mobile CO_2 (years)	Time of Plume Stabilization (years)	Up-dip Migration Distance at Stabilization (km)	Percent Dissolved at Stabilization
Base Case	$k_x = k_y = 200$ mD, $k_z = 20$ mD, $S_{grmax} = 0.27$	23	25	1.30	38
Sand Anisotropy Studies					
AN1	Isotropic permeability $k_x = k_y = k_z = 200$ mD	22	25	1.35	39
AN2	Lateral permeability anisotropy $k_x = k_y/3$, $<k_x k_y>_g = 200$ mD, $k_z = 20$ mD	23	25	1.50	39
AN3	Lateral permeability anisotropy $k_x = k_y/10$, $<k_x k_y>_g = 200$ mD, $k_z = 20$ mD	21	20	2.50	41
Sand Permeability Studies*					
SA1	Very low permeability $k_x = k_y = 20$ mD, $k_z = 2$ mD	94	85	0.70	32
SA2	Low permeability $k_x = k_y = 66$ mD, $k_z = 6.6$ mD	37	50	1.00	34
SA3	High permeability $k_x = k_y = 500$ mD, $k_z = 250$ mD	16	20	2.00	45
SA4	Very high permeability $k_x = k_y = k_z = 1000$ mD	12	15	2.50	52
Shale Permeability Studies*					
SH1	Medium-permeability shale $k_x = k_y = 2$ mD, $k_z = 0.2$ mD	29	25	1.30	39
SH2	High-permeability shale $k_x = k_y = 20$ mD, $k_z = 2$ mD	20	40	1.50	38
SH3	No shale $k_x = k_y = 200$ mD, $k_z = 20$ mD	27	25	1.80	33
SH4	No shale $k_x = k_y = k_z = 200$ mD	32	40	2.20	33
Residual Gas Saturation Studies**					
SG1	High residual gas saturation $S_{grmax} = 0.40$	10	15	1.05	32
SG2	Medium-high residual gas saturation $S_{grmax} = 0.30$	19	25	1.20	37
SG3	Medium-low residual gas saturation $S_{grmax} = 0.20$	45	25	1.45	43
SG4	Low residual gas saturation $S_{grmax} = 0.10$	114	30	1.80	53

* When permeability decreases, capillary pressure strength P_{c0} and S_{grmax} increase

** Here only S_{grmax} is varied

as occurring when two successive distributions are indistinguishable. However, it is also useful to compare among cases how long it takes to reach a given amount of mobile CO_2.   The "time to 3% mobile CO_2" entry in Table 18 serves this purpose. The value of 3% is used because all cases reach it within the simulation

period (typically 100 years). Table 18 indicates that there is generally a good correlation between the "time to 3% mobile CO_2" and "time of plume stabilization" entries, so they are often referred to collectively as time measures for plume mobility.
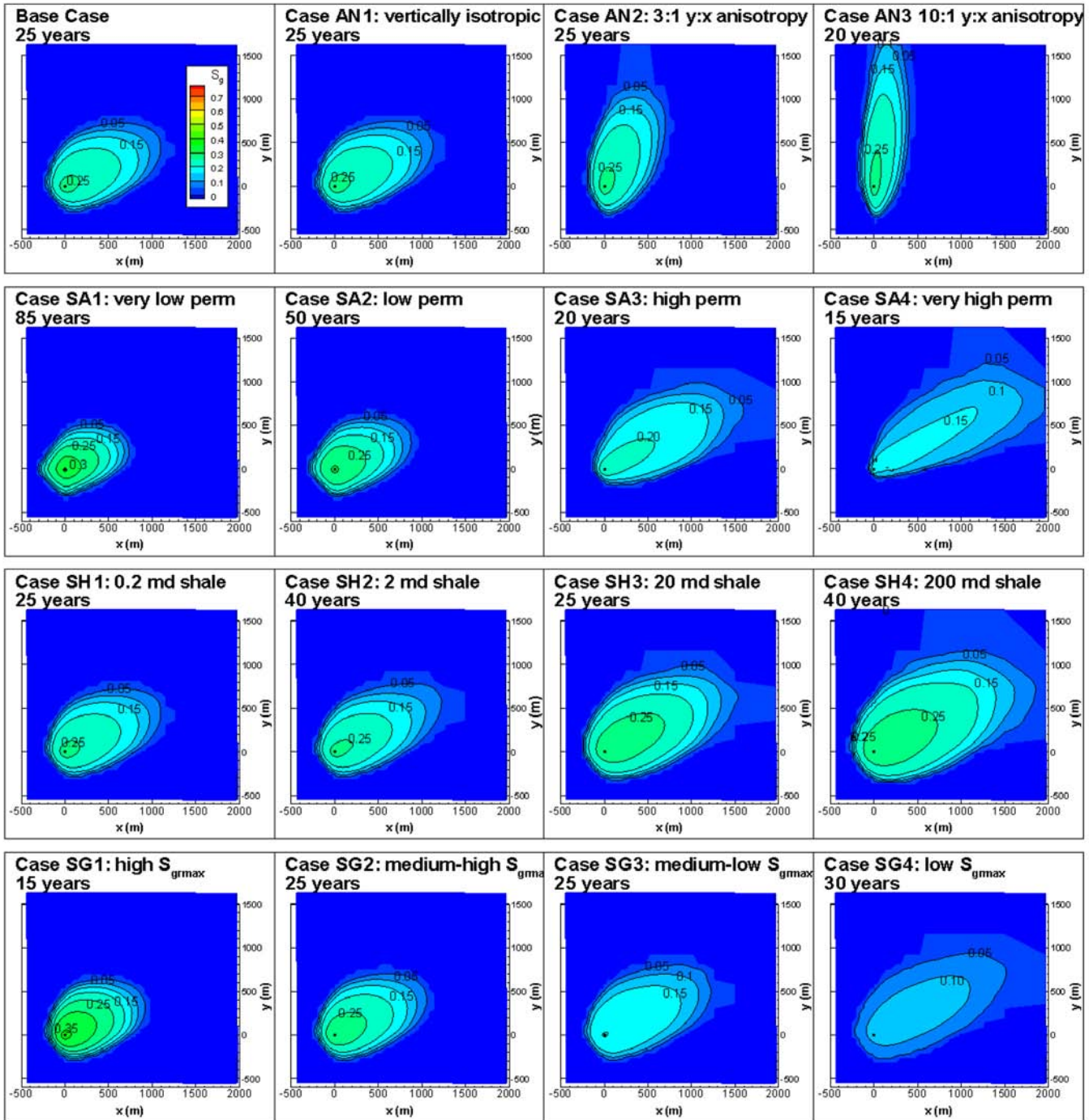

Figure 71: Top view of stabilized supercritical CO_2 plumes for all cases, shown by plotting S_g, saturation of supercritical CO_2, in the uppermost model layer. The time to stabilization is shown for each case.

Sand Anisotropy Studies

The base-case model assumes vertical permeability is 1/10th of horizontal permeability, a common assumption for sands with permeability in the hundred millidarcy range. Assuming an isotropic medium (Case AN1), produces only subtly different plume evolution: comparable time measures for plume mobility, only 50 m more up-dip migration, and similar percent dissolved CO_2. This insensitivity largely arises from the sand/shale layering, which creates five sub-plumes in the sand layers, and thereby limits the amount of buoyancy flow that can occur. A factor of ten change in permeability anisotropy has a much greater effect for a homogeneous sand formation (see Cases SH3 and SH4, below).

The region surrounding the Kimberlina site contains numerous small faults trending generally north-south. Whether these faults act as conduits or barriers to flow, their net effect is likely to be a lateral (x:y) anisotropy in sand permeability with a greater permeability in the north-south (y) direction. Cases AN2 and AN3, with a 3:1 and 10:1 y:x anisotropy ratio, respectively, show that the direction of plume migration shifts dramatically from the up-dip direction (30° north of due east) toward the north. For the 10:1 anisotropy ratio, the time measures for plume mobility are shorter and up-dip plume extent and percent dissolved CO_2 are greater, features common to the high sand permeability cases described below.

Sand Permeability Studies

Sand horizontal permeability values ranging from 20 mD to 1,000 mD are considered here (Cases SA1, SA2, SA3, and SA4). In our conceptual model, when sand permeability k increases, vertical to horizontal permeability ratio k_z/k_x increases, capillary pressure strength P_{c0} decreases as $P_{c0} \sim k^{-1/2}$, and maximum residual gas saturation S_{grmax} decreases as $S_{grmax} = 0.48 - 0.04 \ln(k)$, with k in mD, which is adapted from correlations developed by Holtz (2002; personal communication, 2003) based on Gulf Coast sandstone literature.

Increasing sand permeability has a strong effect on the plume performance measures shown in Table 18, with up-dip plume extent and percent dissolved CO_2

increasing, whereas time measures for plume stability and maximum CO_2 saturation decrease. All these effects are a consequence of the greater buoyancy flow enabled by larger permeability. Larger up-dip plume extent means more brine is encountered by the plume, so more dissolution occurs. Because the trailing (down-dip) edge of the plume is trapped, larger up-dip extent means the plume is stretched out more and hence CO_2 saturation is lower, leading to greater residual CO_2 trapping, less mobile CO_2, and earlier stabilization. It should be noted that while well logs from the Kimberlina region do show sand permeabilities even higher than 1,000 mD and even lower than 20 mD, it is not known how regionally extensive such extreme features are.

Shale Vertical Permeability Studies

Shale vertical permeability largely controls the vertical distribution of CO_2 within the storage formation, as shown in Figure 72. In the base case (Figure 63), shale permeability is so low and capillary pressure strength so high that supercritical CO_2 is effectively excluded from shale lenses. Cases SH1 SH2, SH3, and SH4 consider larger shale permeabilities, which are intended to represent sub-grid-scale heterogeneity in which sand and shale interfinger at scales that are less than the 55-m grid size. P_{c0} and S_{grmax} values are correlated to permeability using the same relations given for sand above. In the limiting case (Cases SH3 and SH4), shale lenses are assigned pure sand properties, so shale is actually absent, and the Vedder Formation is modeled as a homogeneous sand layer. In these cases, buoyancy flow is much stronger, resulting in much greater upward migration of CO_2. This is especially true for Case SH4, in which vertical permeability equals horizontal permeability. For Case SH2, with shale permeability ten times smaller than sand permeability, supercritical CO_2 preferentially flows into sand layers, but does move into shale lenses as well. The Case SH2 plume shows more buoyancy flow than the base case, but not nearly as much as when the shale lenses are absent. For Case SH1, with a shale permeability 100 times smaller than sand permeability, the CO_2 distribution is indistinguishable from that of the base case, which has a shale permeability 2000 times smaller than sand permeability.
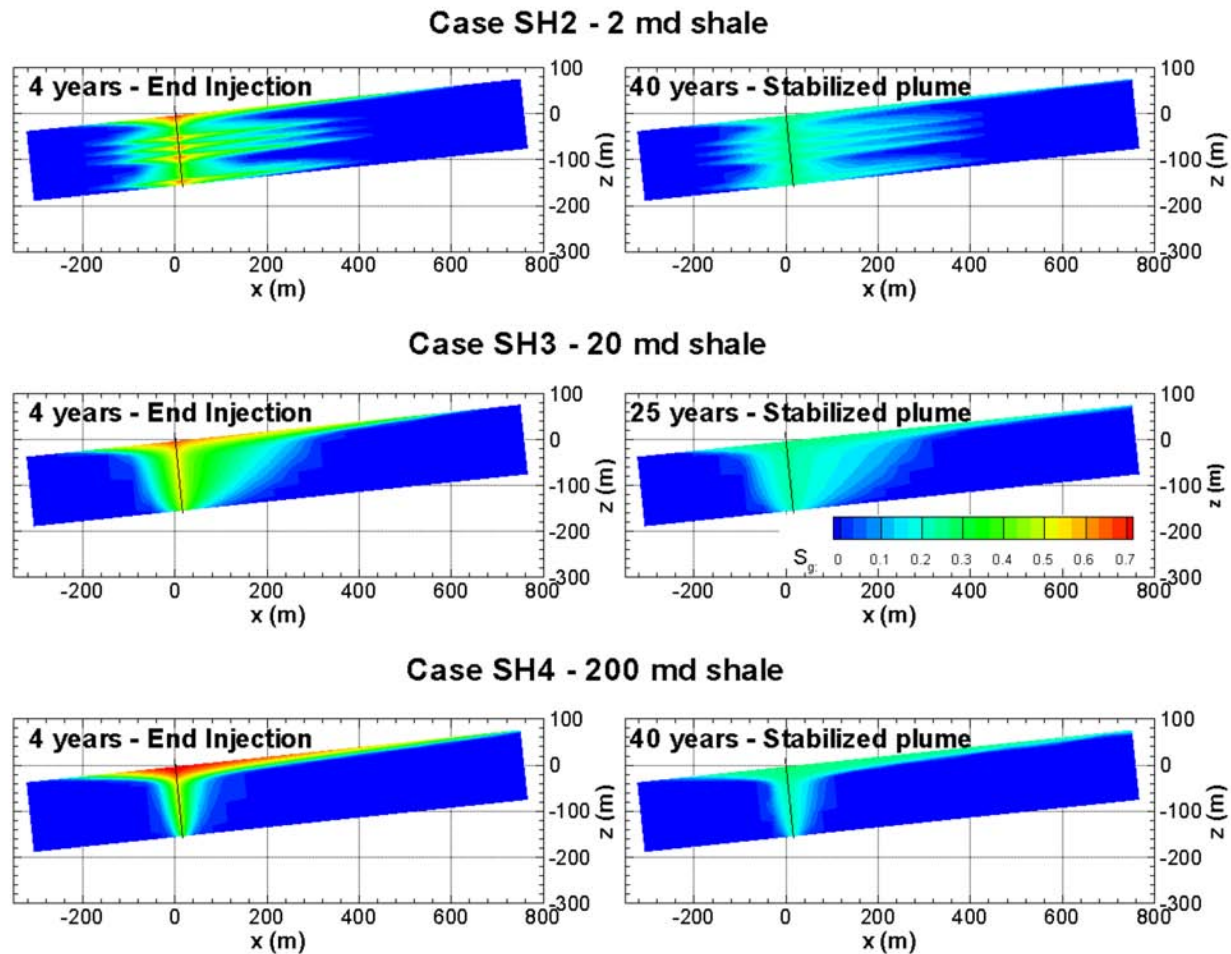
Figure 72: East-west cross-section of the supercritical CO_2 plume at two times for sensitivity-study cases with different values of shale vertical permeability, shown by plotting S_g, saturation of supercritical CO_2, in the plane $y = 0$. Compare to base-case cross-sections in Figure 63.

Increasing shale permeability has a strong effect on the plume performance measures shown in Table 18, with up-dip plume extent increasing and percent dissolved CO_2 decreasing. Both these effects are a consequence of the more localized flow that occurs when the shale lenses do not divide the CO_2 into multiple plumes. CO_2 saturation in the single plume is higher than in the five individual plumes, so residual CO_2 trapping is diminished and up-dip migration is enhanced. Dissolution trapping also decreases, a consequence of the smaller CO_2/brine contact area.

Since the presence or absence of shale lenses so strongly impacts the evolution of the supercritical CO_2 plume, it is useful to examine the behavior of dissolved CO_2, in the no-shale case as well. Figure 73 shows dissolved CO_2 distributions for Case SH4, in which the Vedder

Formation is modeled as a homogeneous isotropic sand layer. As for the base case (Figure 68), at the end of the injection period, the dissolved CO_2 distribution correlates closely with the supercritical CO_2 distribution. Thereafter, the two distributions differ significantly as natural convection of brine begins. Comparing Figure 73 with Figure 69 shows that the absence of shale lenses greatly enhances natural convection compared to the base case, which in turn enhances late-time dissolution. The integrated mass-distribution in Figure 64 illustrates how the Case-SH4 dissolved fraction, which is less than the base-case dissolved fraction when the plumes stabilize, later becomes significantly greater than it. The supercritical plume has nearly completely dissolved by 1,300 years, far sooner than the base-case dissolution time of 10,000 years.

Case SH4 - 200 md shale

4 Years - Dissolved CO$_2$

X_{CO2L}: 0   0.01   0.02   0.03   0.04   0.05

25 Years - Dissolved CO$_2$

100 Years - Dissolved CO$_2$
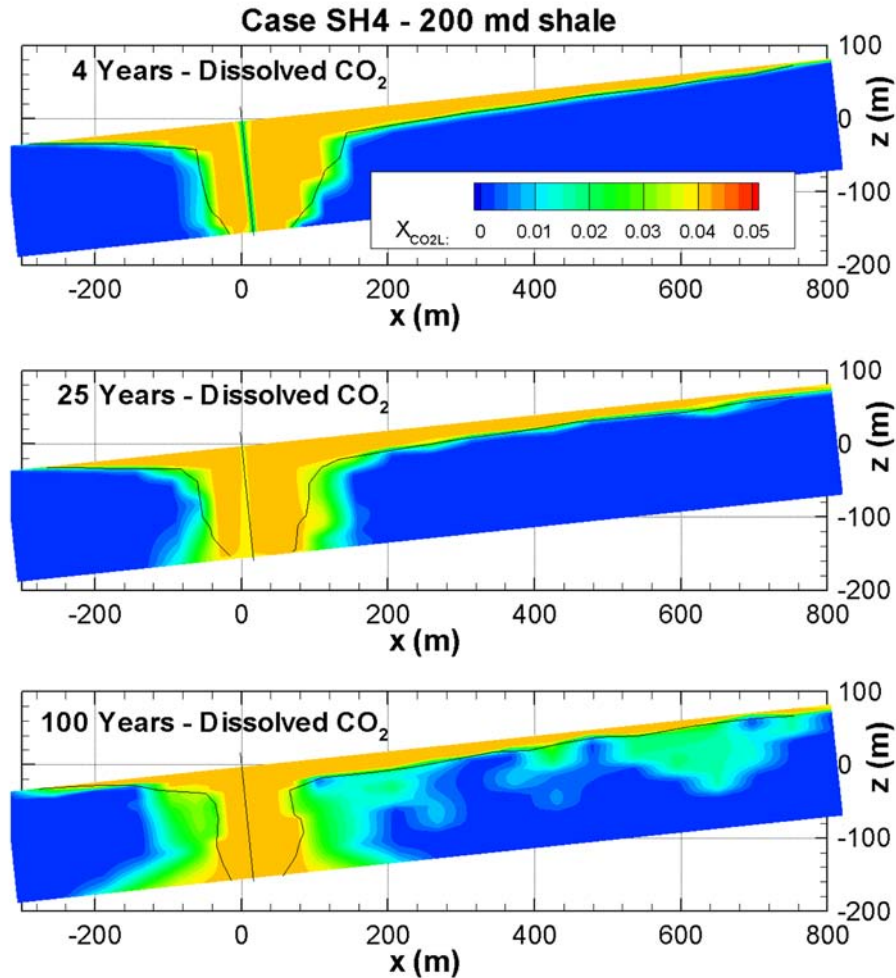
Figure 73: East-west cross-section of the dissolved CO$_2$ plume at a series of times for sensitivity-study Case SH4, shown by plotting X_{CO2L}, mass fraction of CO$_2$ in the aqueous phase, in the plane $y = 0$. Case SH4 models the storage formation as a homogeneous isotropic sand layer. The black contour lines show $S_g = 0$, illustrating the maximum extent of the supercritical plume.

Numerical studies of brine convection (Pruess and Zhang, 2008) using much finer grid resolution than the present study indicate that the details of convection (e.g., how many convection cells, individual cell locations) are quite sensitive to grid spacing, but integrated measures such as how much CO$_2$ crosses a given horizontal interface, are not. Because the lateral grid resolution (55 m over most of the plume) is so coarse, the results shown in Figure 73 should not be considered precise predictions of dissolved CO$_2$ movement, but rather provide an indication of the overall magnitude of convective transport.

Residual Gas Saturation Studies

Unlike permeability sensitivity studies, in which a range of property values are used because of limited knowledge of subsurface property distributions, for residual gas saturation, there is even significant uncertainty in our conceptual model. To a large extent, we rely on experience with other multiphase systems, primarily from the petroleum literature, in which maximum residual gas saturation S_{grmax} is significantly above zero. The relatively few studies of CO$_2$/brine systems (e.g., Bachu and Bennion, 2008; Benson et al., 2007; Doughty et al., 2008) support this approach, but

residual CO_2 trapping is such an important process for immobilizing plumes in the absence of structural traps that further study is needed. Therefore, S_{grmax} is treated as an independent parameter, and the effect of decreasing it from the base-case value is examined (Cases SG1, SG2, SG3, SG4). Decreasing S_{grmax} has a strong effect on the plume performance measures shown in Table 18, producing greater up-dip migration and increased time measures for plume mobility because of the diminished residual CO_2 trapping ability. In contrast, the additional up-dip migration enables more dissolution to occur.

Conclusions

The evolution of the CO_2 plume formed during a large-scale pilot test for geologic CO_2 storage in a moderately dipping saline aquifer has been modeled using the numerical simulator TOUGH2. Simulation results show that for the base case, about 20% of the 1,000,000 metric tons of injected CO_2 is in dissolved form at the end of the four-year injection period, and this percent increases to 38% by the time the CO_2 plume stabilizes at 25 years. At stabilization, of the 62% of the plume that exists as supercritical free phase, only 3% is mobile. From this time onward, plume evolution consists solely of slow dissolution, aided by natural convection of dissolved-CO_2-laden brine. The stabilized plume footprint is roughly elliptical, and is strongly asymmetric about the injection well, extending 1,300 m in the up-dip direction and 200 m in the down-dip direction. The pressure increase in response to CO_2 injection extends far beyond the plume footprint, reaching the model boundaries eight kilometers away from the injection well. However, the pressure response decreases rapidly with distance from the injection well, and decays rapidly in time once injection ceases.

Sensitivity studies show that uncertain model parameters permeability anisotropy, permeability itself, and maximum residual gas saturation strongly affect the direction and extent of CO_2 plume movement, demonstrating the importance of site characterization efforts to better constrain these parameters prior to CO_2 injection. Even a subtle sand lateral permeability anisotropy strongly affects plume migration direction. Sand vertical permeability anisotropy does not have much effect on plume shape when shale lenses are present, but the opposite is true for a storage formation composed solely of sand, where vertical anisotropy

plays a dominant role controlling buoyancy flow of both light free-phase CO_2 and heavy dissolved-CO_2-laden brine. Even the presence of a small amount of shale, as represented by shale lenses with permeability only ten times smaller than that of sand, greatly diminishes upward buoyancy flow of free-phase CO_2.

Figure 74 summarizes the results shown in Table 18 graphically, demonstrating the trade-offs in trapping mechanisms that occur as sand permeability, shale permeability, and residual gas saturation are varied. As sand permeability increases (Figure 74a), up-dip buoyancy flow is enhanced so up-dip plume migration increases. Dissolution trapping increases as more brine is exposed to free-phase CO_2. Residual CO_2 trapping ability decreases insofar as S_{grmax} decreases with increasing permeability, but the two time measures for plume mobility – time to 3% mobile CO_2 and time to plume stabilization – decrease significantly as sand permeability increases. This indicates that the lower CO_2 saturation resulting from greater spreading of the plume leads to more rapid residual CO_2 trapping, despite the lower S_{grmax} values.

As shale permeability increases (Figure 74b), enhanced upward flow enables the five individual plumes to coalesce into a single plume that rises to the top of the formation, and thereafter spreads up-dip (Figure 72). This more localized flow enables CO_2 saturation in the single plume to remain higher than in the five individual plumes, so residual CO_2 trapping is diminished and up-dip migration is enhanced. Dissolution trapping also decreases slightly in response to the coalescence into a single plume, as the higher CO_2 saturation results in a more compact plume and thus smaller CO_2/brine contact area. The time measures for plume mobility still roughly track together, and show only a slight increase with shale permeability.

Finally, if S_{grmax} values are typically smaller than the presently-accepted ones (Figure 74c), residual CO_2 trapping decreases, leading to greater up-dip migration, increased time measures for plume mobility, and more dissolution trapping. For small values of S_{grmax}, time to 3% mobile CO_2 becomes much longer than time to plume stabilization, because the threshold for absolute immobility (S_{grmax}) becomes much harder to reach even though the relative permeability of the plume as a whole is small enough for the plume to stabilize.

The sedimentary basin that forms California's Central Valley provides a huge potential capacity for geologic carbon storage, and the geologic stratigraphy suggests that the dipping planar structure of interleaved sands and shales that characterizes the Kimberlina model is likely common. For the longer injection periods and much greater CO_2 volumes associated with full-scale CO_2 storage, plume migration distance will be greater and time to stabilization will be longer. Scoping studies (Jordan and Doughty, 2009) suggest that as injection rate increases, buoyancy flow becomes relatively less important. Moreover, for larger plumes the residual trapping that occurs at the down-dip margin of the plume has less impact on the up-dip, leading edge of the plume. However, the conclusions about the interaction of trapping mechanisms drawn from the present study may still be widely useful for storage locations with limited knowledge of reservoir flow parameters.
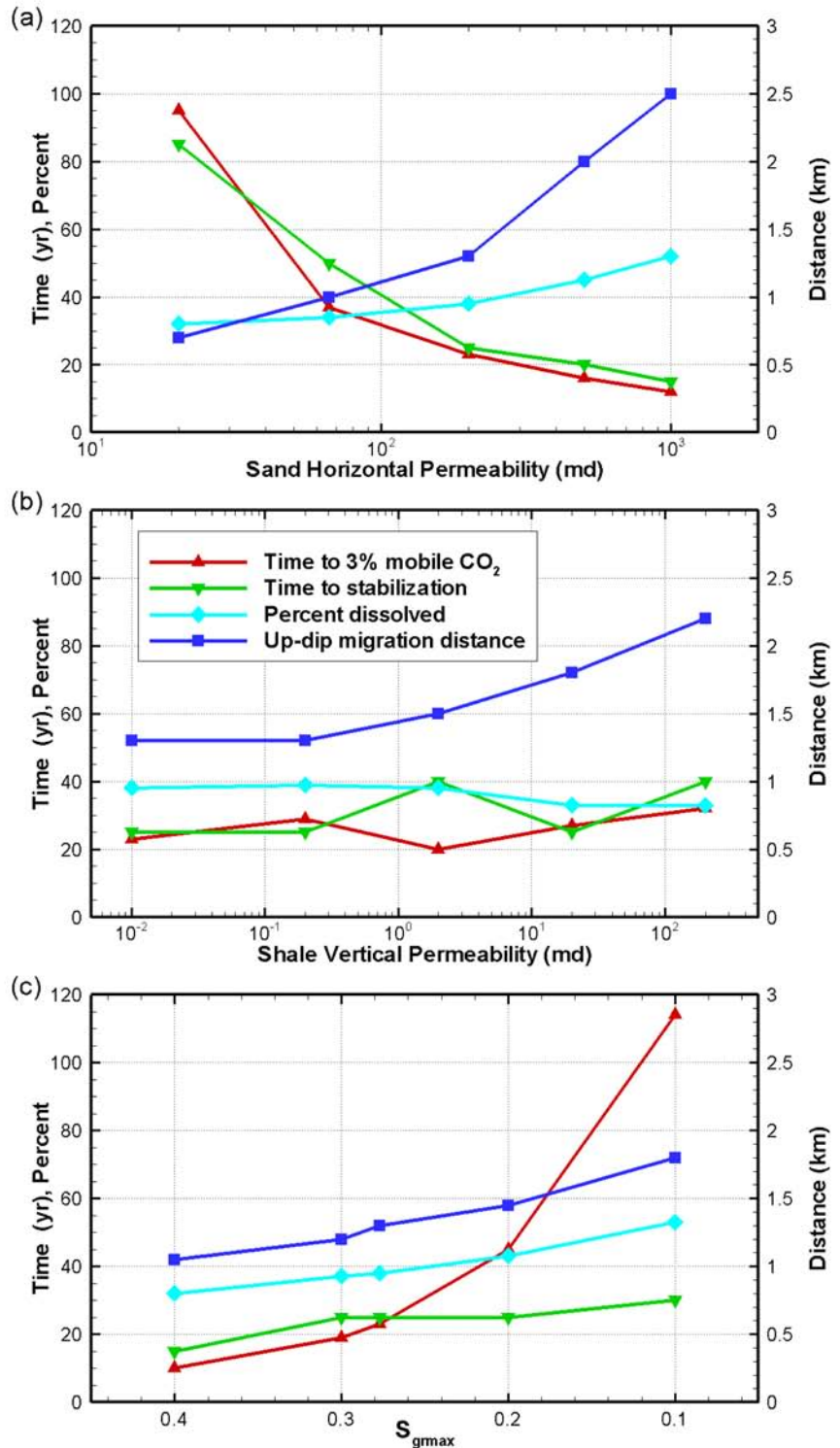

Figure 74: Summary of sensitivity study results for (a) sand horizontal permeability when low-permeability shale layers are present; (b) shale vertical permeability; and (c) residual gas saturation S_{grmax}.

References

Bachu, S. and Bennion, D.B., 2008, Effects of in-situ conditions on relative permeability characteristics of CO_2-brine systems: Environmental Geology, v. 54, no. 8, p. 1707-1722

Bachu, S, Gunter, W.D., and Perkins, E.H., 1994, Aquifer disposal of CO_2: hydrodynamic and mineral trapping: Energy Conversion and Management, v. 35, no. 4, p. 269-279

Benson, S.M., Miljkovic, L., Tomutsa, L., and Doughty, C., 2007, Relative permeability and capillary pressure controls on CO_2 migration and brine displacement—Elucidating fundamental mechanisms by laboratory experiments and simulation: Sixth National Conference on Carbon Capture and Sequestration, National Energy Technology Laboratory, Pittsburgh, PA, May 7-10 (2007)

Doughty, C., 2007, Modeling geologic storage of carbon dioxide: comparison of non-hysteretic and hysteretic characteristic curves: Energy Conversion and Management, v. 48, no. 6, p. 1768-1781

Doughty, C. and Myer, L.R., 2009, Scoping calculations on leakage of CO_2 in geologic storage: The impact of overburden permeability, phase trapping, and dissolution. In: Carbon Sequestration and its role in the global carbon cycle, Brian J. McPherson and Eric T. Sundquist, Editors, Geophysical Monograph Series, Volume 183, 350 pp., American Geophysical Union, Washington DC

Doughty, C., Freifeld, B.M., and Trautz, R.C., 2008, Site characterization for CO_2 geologic storage and vice versa – the Frio brine pilot, Texas, USA as a case study: Environmental Geology, v. 54, no. 8, p. 1635-1656

Ennis-King, J. and Paterson, L., 2005, Role of convective mixing in the long-term storage of carbon dioxide in deep saline formations (SPE 84344): Society of Petroleum Engineers Journal, v. 10, no. 3, p. 349-356

Gherardi, F., Xu, T., and Pruess, K., 2007, Numerical modeling of self-limiting and self-enhancing caprock alteration induced by CO_2 storage in a depleted gas reservoir: Chemical Geology, v.244, no. 1-2, p. 103-129

Holtz, M.H., 2002, Residual gas saturation to aquifer influx: A calculation method for 3-D computer reservoir model construction (SPE 75502): SPE Gas Technology Symposium, Calgary, Alberta, 30 April-2 May (2002)

Jordan, P. and Doughty, C, 2008, Sensitivity of CO_2 migration estimation on reservoir temperature and pressure uncertainty: GHGT-9 Conference, Washington DC, November 16-20 (2008)

Jordan, P. and Doughty, C., 2009, Considerations for scale-up between the Kimberlina Phase III Pilot and full deployment. Eighth National Conference on Carbon Capture and Sequestration, National Energy Technology Laboratory, Pittsburgh, PA, May 4-7 (2009)

Land, C.S., 1968, Calculation of imbibition relative permeability for two- and three-phase flow from rock properties (SPE 1942): Society of Petroleum Engineers Journal, v. 8, p. 149-156

Pruess, K. and Spycher, N., 2007, ECO2N – A fluid property module for the TOUGH2 code for studies of CO_2 storage in saline aquifers: Energy Conversion and Management, v.48, no. 6, p. 1761-1767

Pruess, K. and Zhang, K., 2008, Numerical modeling studies of the dissolution-diffusion-convection process during CO_2 storage in saline aquifers, Lawrence Berkeley National Laboratory, Berkeley, CA

Pruess, K, Oldenburg, C.M., and Moridis, G.J, 1999, TOUGH2 user's guide, version 2.0. Rep. LBNL-43134, Lawrence Berkeley National Laboratory, Berkeley, CA

Pruess K, Xu, T., Apps, J. and García, J., 2003, Numerical modeling of aquifer disposal of CO_2 (SPE 83695): Society of Petroleum Engineers Journal, v. 8, no. 1, p. 49-60

Rutqvist, J., Wu, Y.-S., Tsang, C.-F., and Bodvarsson, G.S., 2002, A modeling approach for analysis of coupled multiphase fluid flow, heat transfer, and deformation in fractured porous rock: International Journal of Rock Mechanics and Mining Sciences, v. 39, p. 429–442

Spycher, N and Pruess, K., 2005, CO_2-H_2O mixtures in the geological sequestration of CO_2: II Partitioning in chloride brines at 12-100°C and up to 600 bars: Geochimica et Cosmochimica Acta, v. 69, no. 13, p. 3309-3320

van Genuchten, M. Th., 1980, A closed-form equation for predicting the hydraulic conductivity of unsaturated soils: Soil Science Society of America Journal, v. 44, no. 5, p. 892-898

Wagoner, J., 2009, 3D geologic modeling of the southern San Joaquin Basin for the WESTCARB Kimberlina demonstration project- A status report, Rep. LLNL-TR-410813, Lawrence Livermore National Laboratory, Livermore, CA

Xu, T., Apps, J., and Pruess, K., 2003, Reactive geochemical transport simulation to study mineral trapping for CO_2 disposal in deep arenaceous formations: Journal of Geophysical Research, v.108, B2, p. 2071-284, doi:10.1029/2002JB001979

Xu, T., Apps, J., and Pruess, K., 2005, Mineral sequestration of carbon dioxide in a sandstone-shale system, Chemical Geology, v. 217, p. 295-318

Xu, T., Sonnenthal, E.L., Spycher, N., and Pruess, K., 2006, TOUGHREACT - A simulation program for non-isothermal multiphase reactive geochemical transport in variably saturated geologic media: Applications to geothermal injectivity and CO_2 geological sequestration: Computers & Geosciences, v. 32, p. 145-165

Yamamoto, H. and Doughty, C., 2009, Investigation of gridding effects for numerical simulation of CO_2 geologic sequestrations: In Proceedings, TOUGH Symposium 2009, Rep. LBNL-2790), Lawrence Berkeley National Lab., Berkeley CA, September 14-16 (2009)

West Coast Regional Carbon Sequestration Partnership

Application of the Certification Framework (CF) to the Kimberlina Site, Southern San Joaquin Valley

Curtis M. Oldenburg
Lawrence Berkeley National Laboratory

Steven L. Bryant
CPGE

Jean-Philippe Nicot
Bureau of Economic Geology, University of Texas

Mary Jane Coombs
California Air Resources Board

Christine Doughty
Lawrence Berkeley National Laboratory

Preston Jordan
Lawrence Berkeley National Laboratory

Navanit Kumar
CPGE

Jeff Wagoner
Lawrence Livermore National Laboratory

Introduction

The characterization and modeling of the Kimberlina site (see WESTCARB simulation case study) along with FEP analysis provides the needed information to carry out a preliminary assessment of the risks using the certification framework (CF) approach. We apply the CF approach as it has developed over the last two years. The CF to date only has only considered CO_2 leakage risk, but here we expand the CF to consider brine migration risk. The first step is to define the storage region, which we take as the Vedder formation within 10 km (6 mi) of the injection well. Migration out of the storage region is considered leakage. The fundamental components driving risk are (1) the CO_2 injection as a perturbation to the system, (2) the potential for leakage to occur through conduits (wells and faults), and (3) the potential for impacts to compartments. We assess the potential for negative impacts to the compartments associated by considering each of these components alone and together in the following sections. Because of the difficulty of assigning quantitative probabilities with limited data, we adopt here a likelihood terminology inspired by that of Hnottavange-Telleen (Schlumberger Carbon Services) but significantly modified.

CO_2 Injection

Free Phase CO_2

The CO_2 injection plume simulations show that CO_2 will spread from the injection well preferentially in the east-northeast direction in response to the upward 7° dip of the Vedder. The maximum simulated extent of the free-phase CO_2 plume in the up-dip direction after four years is 600 m (2,000 ft), and after 50 years is 1.5 km (0.9 mi). Note these simulations neglect any effects of faults or fault zones that may be present, which may tend to rotate the plume migration trend counterclockwise from the up dip direction predicted by the simulation results. Model results for CO_2 phase partitioning shows the rapid decline in mobile CO_2 after injection is stopped. In short, the million tons of CO_2 injected in the model is predicted to migrate as free-phase CO_2 no more than 1.5 – 2 km or so before becoming trapped. Figure 75 shows the predicted extent of the CO_2 plume, which is small relative to the Kimberlina submodel, but large relative to the property lines of the potential power plant site.
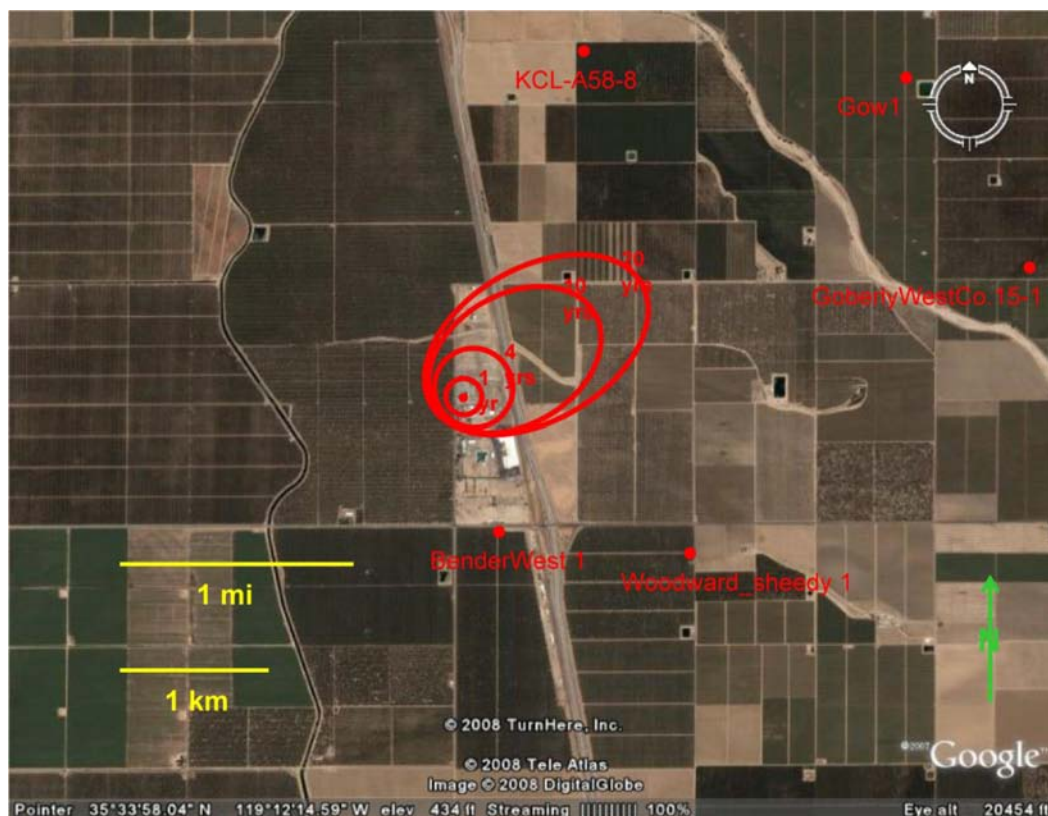
Figure 75: Prediction of footprint of the CO_2 plume from TOUGH2 numerical model.

Pressure Perturbation

The simulated extent of the pressure perturbation due to CO_2 injection is much larger than the extent of the CO_2 plume. This pressure perturbation at the edge of the 10 km (6 mi) area of consideration for the risk assessment is expected to be small, on the order of fractions of a bar. As such, we expect most of the driving force for brine migration to occur within an area around the injection well. Calculations (not included here for brevity) show that pressure changes greater than 0.3 bar are potentially capable of driving brine upwards to USDW. From modeling results we observe the 0.3 bar isobar is at a distance of approximately 4,500 m (15,000 ft) from the injection well, or around three times the maximum bulk phase CO_2 migration distance based upon the numerical simulation. We note that the pressure pulse is not significantly altered by the dip of the formation and is therefore more symmetric than the CO_2 plume around the injection well, extending both down dip and up dip. A few meters of lateral displacement of brine at the boundary of the 10 km (6 mi) radius storage region is all that is required to

accommodate the volume of CO_2 injected in the model (calculations not included for brevity). Although this is technically brine leakage, it has no measurable impact because the degree of displacement is small.

Potential CO_2 Leakage Conduits

Wells

There are no known wells that penetrate the Vedder within the footprint of the simulated CO_2 plume. The nearest wells are the BenderWest 1 (approx. 1 km (0.62 mi) away to the south) and Woodward_Sheedy 1 (approx. 2 km (1.2 mi) away to the southeast), but neither of these penetrates to the Vedder. The nearest wells that penetrate to the Vedder are more than 2.5 km (1.5 mi) away to the north and northeast (Figure 75). In the CF, we assign a probability of intersection of the CO_2 plume with potential conduits and in this case the probability would be near zero because the CO_2 plume is not predicted to migrate as far as the nearest well. Intersection could occur if there are wells that are not known, but we consider this improbable to unlikely.

Intersection could also occur if the simulation results underpredict plume extent by a factor of almost two causing the plume to reach known wells. Given the uncertainties in local geologic conditions around the proposed injection well, such underprediction is likely. Although not carried out for this study, a probability distribution of plume sizes could be developed through examination of uncertainties in key properties such as reservoir temperature, pressure, permeability, anisotropy, etc. Despite the known model uncertainty, we believe it is unlikely that the injected CO_2 plume will intersect a well that will be conductive to CO_2, i.e., allow significant CO_2 migration.

Further support for this conclusion comes from a study of surface well blowouts from 1991 to 2005 in the southern San Joaquin Valley (Jordan and Benson, 2008). This study found only one possible blowout from an unknown, or previously poorly located, abandoned well. This occurred in an oil field undergoing thermal recovery via steam injection. Steam, as a buoyant fluid, encountered, on average, 23,000 known abandoned wells in such oil fields. So the rate of blowouts from unknown or poorly located abandoned wells is one per 300,000 known abandoned wells per year in areas with steam injection. The rate over the maximum 20-year span for mobile CO_2 resulting from the modeled CO_2 injection would be approximately one unknown or poorly located abandoned well blowout per 15,000 known abandoned wells. The blowout rate for well-known and located abandoned wells was twice these. This indicates that even when wells are encountered by steam, flow up them to the surface is improbable. So for either unknown or known abandoned wells, the blowout rate for CO_2 injection would have to be several orders of magnitude higher for the blowout risk from an unknown or poorly located abandoned well to rise to the level of concern for the modeled CO_2 injection. A consideration of the differences in thermodynamic behavior of steam versus CO_2 does not suggest the CO_2 blowout rate will be this different from the steam blowout rate (Jordan and Benson, 2008).

Although the CF analysis normally models wellbore flow as a leakage process, we consider it unnecessary to carry out wellbore-flow modeling in this case to evaluate impacts because of the low-probability of occurrence of wells penetrating the Vedder, intersecting the CO_2 plume, and having properties sufficient to allow flow.

Faults

Fault-Plume Intersection Probability

Figure 76 shows CO_2 saturation and saturation above residual at several time steps in the numerical modeling. Saturation above residual is referred to as the mobile fraction. On Figure 76, 0 is no saturation, and 1 is full saturation above residual, respectively. Figure 77 shows the margin of the mobile CO_2 at the end of the four-year injection, as well as six years after injection has ceased. The margin shown is at approximately the 5% mobile saturation contour (100% mobile saturation is defined as 100% total saturation less residual gas saturation) on Figure 76. Figure 77 also shows an estimated outline of the total area swept by mobile CO_2 from the start of injection through time to full residual saturation and solution trapping. This area is termed the "plume area" for the purposes of analyzing the probability of mobile CO_2 encountering a fault. This definition of the plume area differs from other possible definitions, such as the area with dissolved CO_2.

Due to the small size of the plume area, the occurrence of a fault large enough to significantly offset the 180 m (600 ft) thick seal is not expected because (1) the density of these faults is low, as derived from structure maps of nearby oil and gas field, and (2) this magnitude of displacement would probably be apparent on the structure map developed from well log data. However, faults interpreted by EOG resources northeast of the Kimberlina site are not readily apparent from the structure contours, despite their 5 to 15 km (3 to 9 mi.) length. This suggests the need for another method to check the conclusion that there are probably no significant faults within the expected Kimberlina mobile-CO_2 plume area.

A method for approximating this probability has been developed (not included here for brevity). The inputs are the plume area, the throw truncation, the fault density equation, the aspect ratio of the plume (the length divided by the width), and the acute angle between the plume axis and the faults of interest. This method assumes only one fault crosses the plume and this fault crosses the entire plume. Therefore this method is only useful for plumes with fault-perpendicular dimensions considerably smaller than the average spacing between the faults of interest.
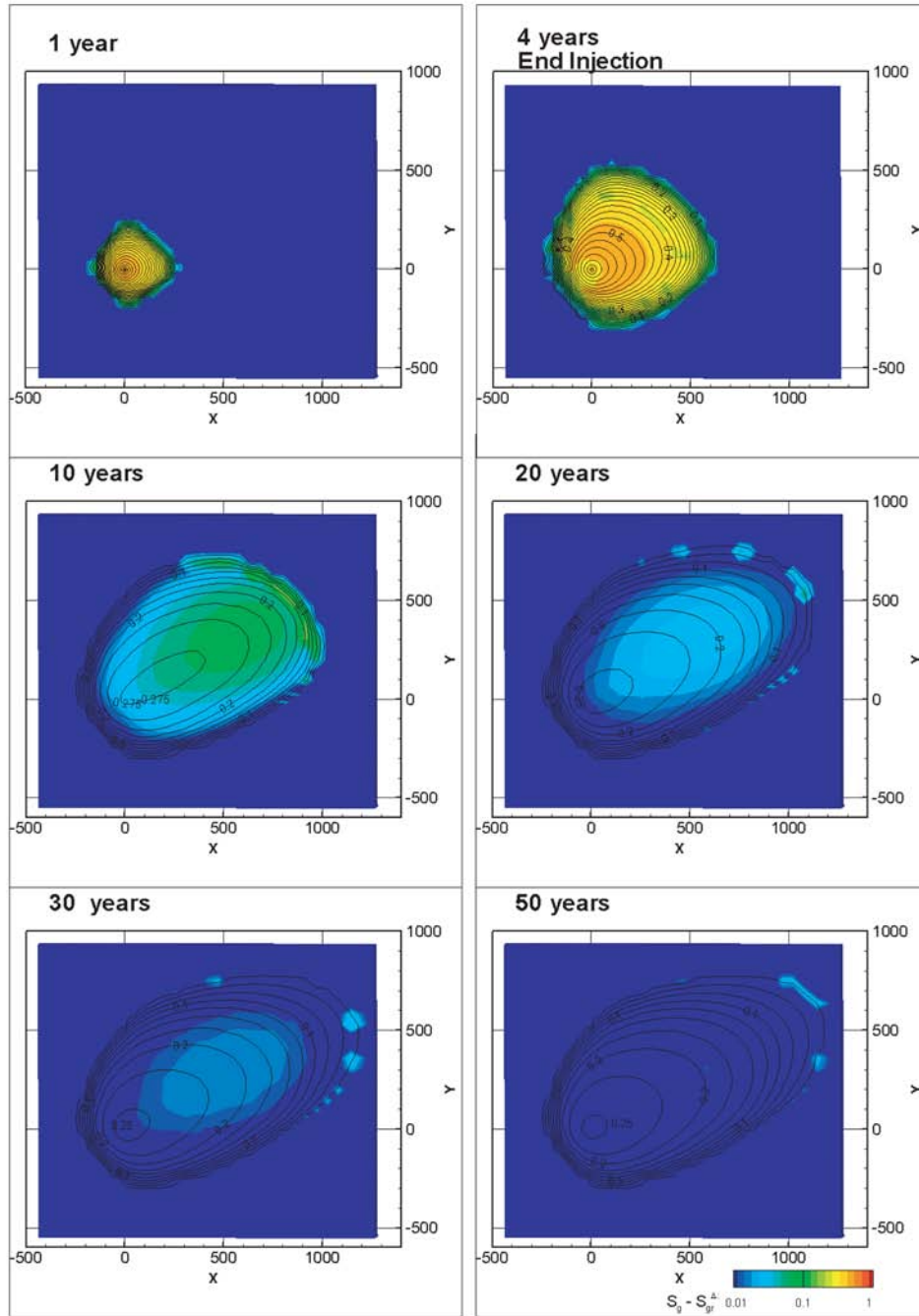
Figure 76: Total CO$_2$ saturation and saturation in excess of residual from the numerical simulation. Total saturation is shown by black contours. Saturation in excess of residual is shown by colors. Note the color bands for saturation in excess of residual are defined on a log scale. Coordinates are in meters. North is up.

For Kimberlina, the plume area, as measured from Figure 77 is 0.83 km² (0.32 mi²). The throw truncation is selected for relevance to potential leakage of CO_2. As a first approximation, throws that fully offset the sealing formations over the target reservoirs are of concern. As previously mentioned, the sealing formations over the two storage targets at the Kimberlina site have a vertical thickness of approximately 180 m (600 ft) each. The corrected fault density equation derived from structure maps of nearby oil and gas fields indicates the average fault density at this throw truncation is 0.028 km/km² (0.046 mi/mi²). This is a low density, so the condition that the fault-perpendicular plume dimension is much smaller than the spacing between faults is sufficiently met to use the probability estimation method.

The plume aspect ratio of the Kimberlina plume from Figure 76 is 1.32. The direction of the plume axis from Figure 76 is 60° (updip). The dominant fault strike near Kimberlina is taken as 170°. The acute angle between these two orientations is 70°. At these values, the method indicates the probability of the numerically simulated plume encountering a fully seal-offsetting fault is 3.3%, which would correspond to the unlikely category of Table 19. The probability of the plume encountering a length of fault greater than a particular value is shown on Figure 81. The average fault length encountered is 0.72 km (0.45 mi.).

Table 19: Expectation Terminology (modified from Hnottavange-Telleen, Schlumberger Carbon Services)

Occurrence Expectation Terminology	If there were 100 projects like the simulated CO_2 injection, …
Improbable	… less than once in the 100 projects
Unlikely	… in 1 to 5 of the 100 projects
Somewhat likely	… in 6 to 10 of the 100 projects
Likely	… in 11 to 50 of the 100 projects
Very likely	… more than 50 times within the 100 projects

The numerical model did not incorporate the effect on flow due to fault zones, however. As indicated by the corrected power-law distribution of faults derived from structure maps of nearby oil and gas fields, the density of smaller offset faults is probably quite high. For instance, at a throw cutoff of 3 m (10 ft), the density is approximately 3 km/km² (5 mi/mi²). Despite their small offset, the permeability in these fault zones will likely contrast with that of the host rock. Given their
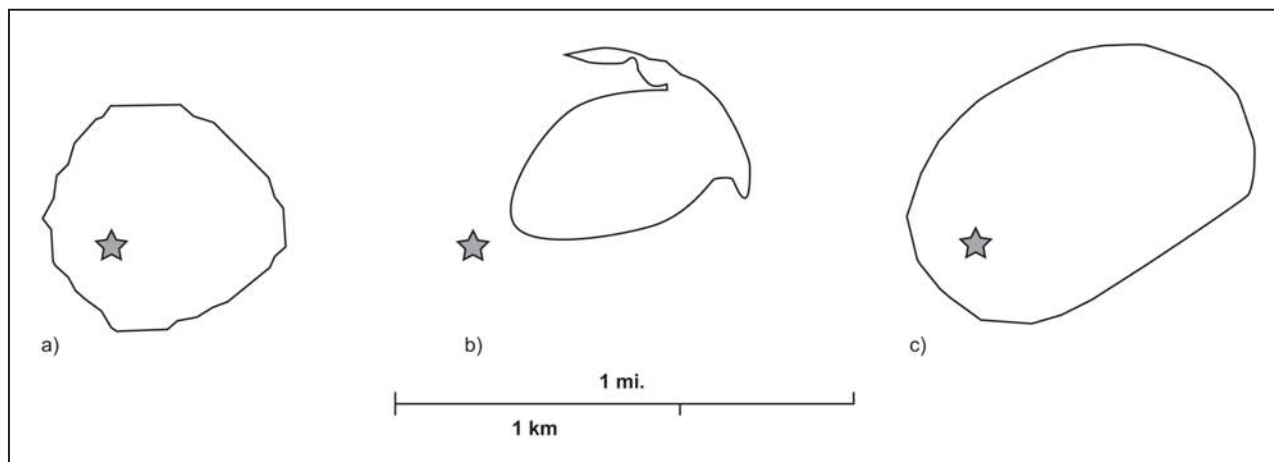

Figure 77: Limit of mobile CO_2 from the numerical simulation; (a) is at the end of injection (four years after start of injection), (b) is 10 years after the start of injection (six years after the end of injection), and (c) is approximately limit of area swept by CO_2. Star is injection site. North is up.

See text for definition of mobile CO_2.

Figure 78: Probability of encountered fault length exceeding various lengths for the Kimberlina plume with an aspect ratio of 1.32 and an angle between the plume axis and fault of 70°.
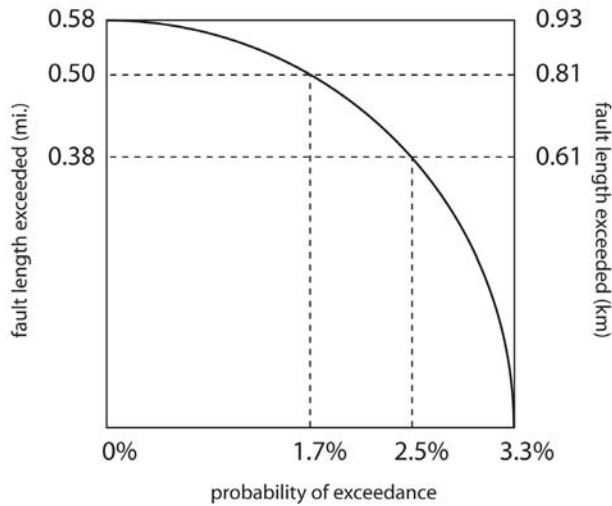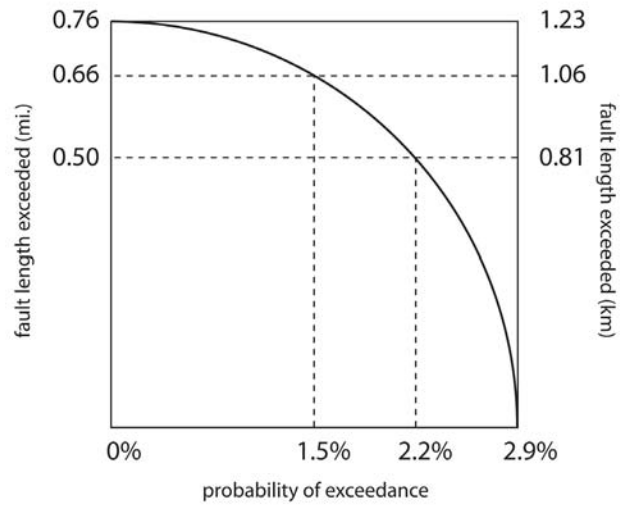

Figure 79: Probability of encountered fault length exceeding various lengths for the Kimberlina plume with an aspect ratio of two and an angle between the plume axis and fault of 35°.

high density, it is likely the plume will encounter these small faults and be deflected somewhat to the north. These faults are likely to cause greater elongation of the plume compared to the numerical model results as well.

Taking a plume aspect ratio of two and an acute angle between the plume axis and the faults as 35° as perhaps more typical due to faulting-induced anisotropy, the probability of the plume encountering a fully seal-offsetting fault is 2.9% (unlikely). The average fault length encountered is 0.50 mi (0.81 km), which is larger than the average of 0.72 km (0.45 mi) for an aspect ratio of 1.32 and an acute plume axis-to-fault angle of 70°. The derivation of the probability estimation method indicates that the probability of a fault encounter is inversely proportional to the average fault length encountered. The probability of a plume with an aspect ratio of two and a plume axis-to-fault angle of 35° encountering a length of fault greater than a particular value is shown on Figure 79.

The plume aspect ratio and the angle between the plume axis and the faults can be treated as variables in the probability estimation method. This affords an understanding of the sensitivity of the probability estimate to variation in these parameters. Table 20 and Figure 80 show the probability that the Kimberlina plume will encounter a fully seal-offsetting fault across a wide range of plume aspect ratios and the full range of plume axis to fault angles.

The probability of leakage through a fault that fully offsets the seal is considerably less than the probability of the plume encountering such a fault. One approach to understanding fault zone permeability is the shale gouge ratio (SGR). Roughly speaking, the SGR is the percentage of strata consisting of clay or shale beds (as identified from geophysical logs) displaced past a point on a fault surface. Various researchers have postulated that if the SGR is greater than 20%, the probability is close to one that the fault zone will contain a continuous clay seal (e.g., Yielding et al., 1997). By this theory,

Table 20: Probability of the Kimberlina mobile-CO_2 plume encountering a fully seal-offsetting fault for selected plume aspect ratios and plume axis to fault angles.

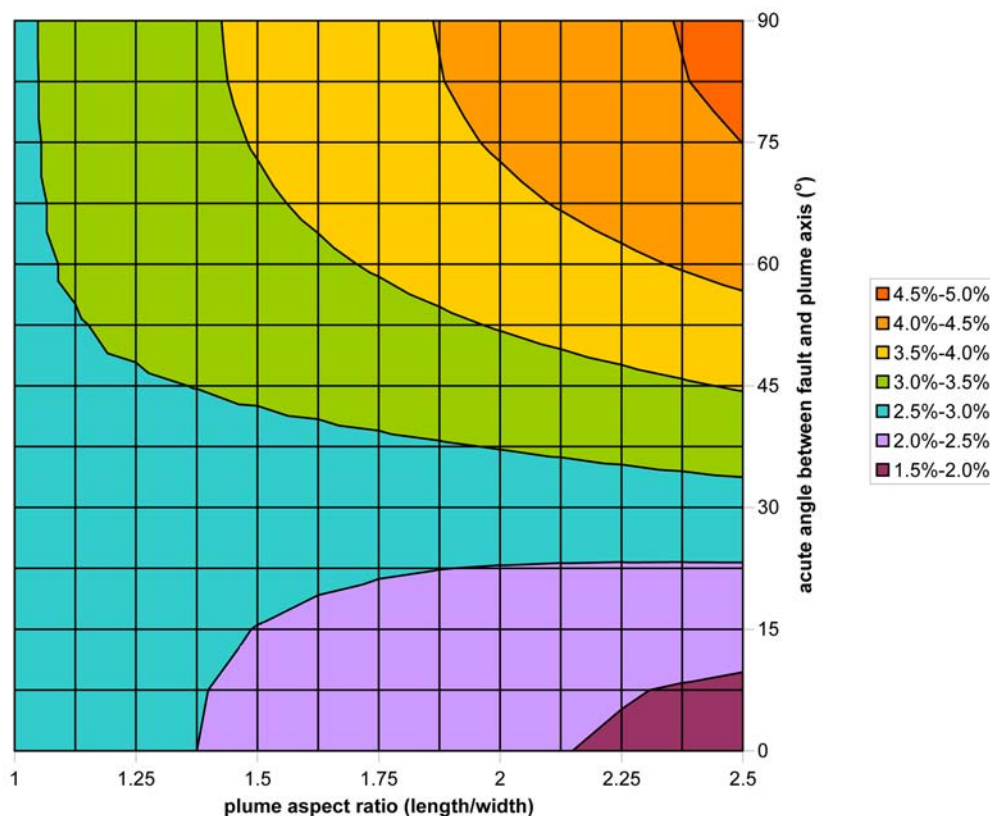|		Plume Aspect Ratio						
		1	1.25	1.5	1.75	2	2.25	2.5
Angle Between Plume Axis and Fault	0	2.9%	2.6%	2.4%	2.2%	2.1%	2.0%	1.9%
	15	2.9%	2.7%	2.5%	2.4%	2.3%	2.2%	2.2%
	30	2.9%	2.8%	2.7%	2.7%	2.7%	2.8%	2.8%
	45	2.9%	3.0%	3.1%	3.2%	3.3%	3.4%	3.5%
	60	2.9%	3.1%	3.3%	3.5%	3.7%	3.9%	4.1%
	75	2.9%	3.2%	3.5%	3.8%	4.0%	4.3%	4.5%
	90	2.9%	3.3%	3.6%	3.9%	4.1%	4.4%	4.6%

Figure 80: Probability that the Kimberlina plume will encounter a fault fully offsetting the seal.

a fault that just fully offsets a seal consisting of 100% shale with significant clay content will have a minimum SGR of 50% and therefore have near-shale (low permeability) rather than near-reservoir-rock permeability.

Table 21 and Figure 81 provide the probability of the CO_2 plume encountering a fault that offsets the seal at least halfway (90 m (300 ft)). This is provided not because these faults are particularly significant, but rather to provide some feel for the variation in probability with variation in throw truncation.

The detailed analysis carried out here to estimate fault occurrences and orientations suggests it is somewhat likely that the plume will encounter faults with smaller offsets (much less than the thickness of the overlying sealing formation). While it is improbable that these faults would be leakage pathways, they are likely to be less permeable than the reservoir rock. As such, they will have the tendency to deflect the plume (and displaced brine) toward their orientation, most likely to the north to north by northwest.

The fault orientation and occurrence analysis indicates that it is unlikely (a few percent chance) that the CO_2 plume will encounter a fault that fully offsets the overlying sealing formation. Most of these faults are expected to have sufficiently low permeability and high gas-entry pressure to preclude any CO_2 leakage due to the high proportion of shale in the offset lithologies.

Table 21: Probability of the Kimberlina mobile-CO_2 plume encountering a fault that offsets the seal by at least half for selected plume aspect ratios and plume axis to fault angles.

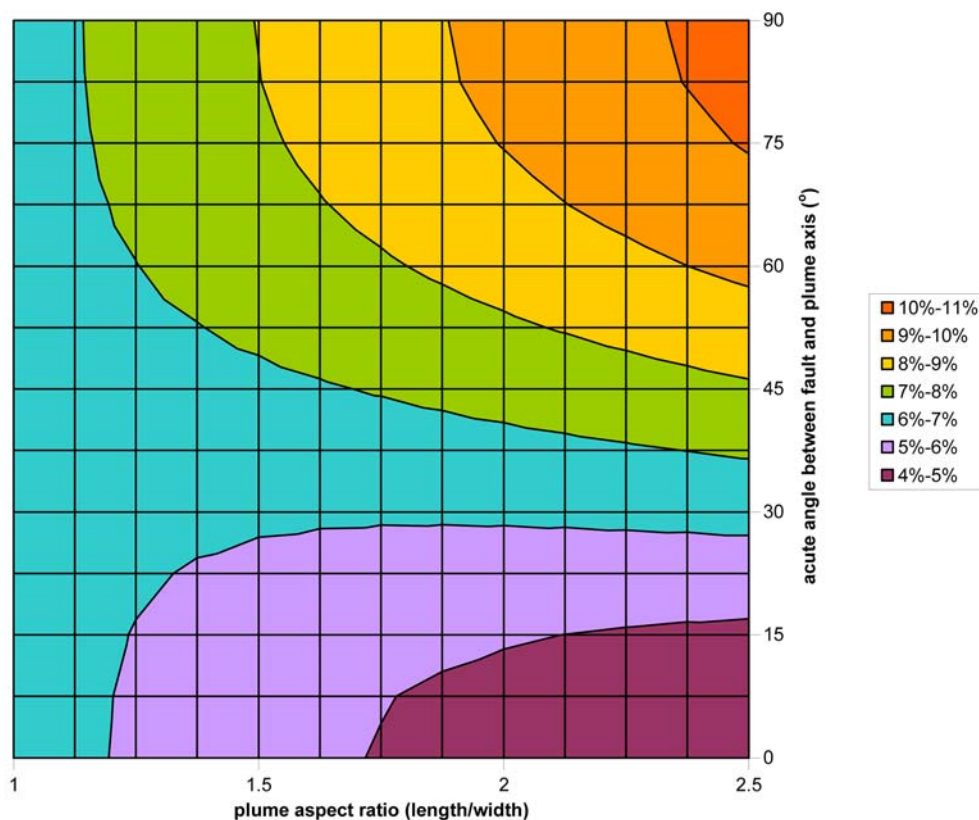|		Plume Aspect Ratio						
		1	1.25	1.5	1.75	2	2.25	2.5
Angle Between Plume Axis and Fault	0	7%	6%	5%	5%	5%	4%	4%
	15	7%	6%	6%	5%	5%	5%	5%
	30	7%	6%	6%	6%	6%	6%	6%
	45	7%	7%	7%	7%	7%	8%	8%
	60	7%	7%	7%	8%	8%	9%	9%
	75	7%	7%	8%	8%	9%	10%	10%
	90	7%	7%	8%	9%	9%	10%	10%

Figure 81: Probability that the Kimberlina plume will encounter a fault that offsets the seal at least halfway.

Combining the small probability of the CO_2 plume encountering a fully seal-offsetting fault with the low probability that such a fault will be conductive, our current understanding of the area suggests a small probability that faults will allow CO_2 to migrate upward out of the Vedder. In the context of the CF, we would say that it is improbable that CO_2 will migrate upward along faults out of the Vedder storage region.

Potential Brine Leakage Conduits

Wells

Because of the larger footprint of the pressure perturbation relative to the CO_2 plume, numerous wells that penetrate the Vedder will be intersected by the pressure pulse. However, elevated pressure alone will not cause brine migration. The properties of the well and the fluids within the wells control wellbore flow. We show in Figure 82 all of the oil and gas wells within the 20 km x 20 km (12 mi x 12 mi) Kimberlina submodel with color coding to indicate the reported well abandonment method. Red indicates cement plugs,

and yellow is either open-hole or wellbore filled with drilling mud. Calculations have been done to provide an analysis of wellbore flow for various fluids initially within the wellbore. There are many wells but our analysis suggests that upward brine flow will be minor if it happens at all. In most cases, well cement will be intact preventing flow, and/or dense drilling mud will absorb the pressure pulse by establishing a new hydrostatic equilibrium within the well. We conclude that, even though the probability of the pressure pulse intersecting boreholes is 100%, actual brine leakage up these boreholes and into USDW is unlikely due to the presence of well cement and/or drilling mud in the wells.

This conclusion is supported by the absence of any blowouts consisting only of brine between 1991 and 2005 in California Oil and Gas District 4 (Jordan and Benson, 2008), despite the presence of numerous injection activities and approximately 50,000 wells on an average annual basis. There was one blowout that involved a significant quantity of brine, which impacted the surrounding agricultural land, but this blowout occurred during a workover operation in a gas field.

Faults

As with wells, there is a near 100% chance that the region of elevated pressure will intersect faults in the Kimberlina area. Based on SGR theory (see Section 3.2.1), faults with throws large enough to offset the caprock—which would be evident if present on the structure map developed from well-log data as mentioned in Sec. 3.2.1--will have SGR values of 50% or more and therefore be low-permeability features. However, SGR theory is not 100% accurate in predicting fault properties especially in the fault plane as opposed to normal to it. Faults with large throws and sufficient permeability to allow leakage may exist. Additionally, the pressure increase will encounter a much larger number of smaller faults. These faults will have higher SGR values through the caprock, making flow along them less likely, but there are more of them and SGR theory is not 100% reliable. As with flow up a well, flow up faults is driven by pressure gradients as modified by density gradients, therefore calculations done to assess the risk of wellbore flow also apply here. In particular, calculations (not shown for brevity) suggest that upward brine flow will be minor. Therefore, because faults in the area are considered to have low-permeability and the driving forces are small, we consider measurable brine leakage up faults to be unlikely.

Impact to Compartments

The CF considers five compartments in which CO_2 fluxes or concentrations provide proxy impacts. Below we discuss potential impacts to these compartments.

Hydrocarbon and Mineral Resources (HMR)

Because there are no known oil or gas pools in the area, we consider the probability of impacting the HMR compartment to be zero.

Underground Sources of Drinking Water (USDW)

Fresh water for irrigation and drinking is a valuable commodity in the Kimberlina area. If either CO_2 or brine migrates into USDW, the project would be considered to have impacted USDW regardless of the actual changes in water quality that would occur. With USDW defined as water with less than 10,000 mg/L TDS, the vertical distance from the Vedder to the base of fresh water in the Kimberlina area is approximately 1 km (3,300 ft). Faults and wells are the only possible conduits for leakage of brine or CO_2, and we have already estimated their ability to transport CO_2 and brine as minimal. Therefore, we consider it improbable that the CO_2 injection will result in any impact to USDW.

Health, Safety, and the Environment (HSE)

In order for either CO_2 or brine to enter the HSE compartment (near-surface environment), there needs to be transport of these fluids upwards from the Vedder. Because well and fault conduits are considered unlikely to act as conduits, and there are few people living in the area, we consider HSE impact due to leaking CO_2 or brine to be improbable.

Although outside of the scope of the CF analysis, we point out that surface activities involving power generation, compression of CO_2, and injection into the well entail industrial processes with accident potential relevant to HSE that, when combined with certain aspects of the Kimberlina power plant site (e.g., lower than average winds, high summer temperatures, stagnant winter Tule Fog conditions, nearby presence of railroad and highway, and 100-year flood zone), suggest the project should carefully consider mitigation measures for operational risks.

Emissions Credit and Atmosphere (ECA)

As with the HSE compartment, we conclude it is improbable that CO_2 will migrate to the near surface and out of the ground over any project-relevant time scale.

Overall CO_2 Leakage Risk

CO_2 Leakage Risk (CLR) is the product of the probability of occurrence of some event or process leading to impact and the impact caused by that event or process. Based on the characterization of the site and numerical simulations as described here, our analysis suggests that the CLR is approximately zero. We cannot say that it is exactly zero because there is always uncertainty in the well record and in knowledge of faulting in the area, and unknown wells or faults could provide a conduit for upward migration of CO_2. However, we feel it is improbable that an unknown well or fault in the area will provide a flow conduit for CO_2 or brine to cause any impact to compartments.

References

Jordan, P. D. and S. M. Benson, 2008. Well blowout rates and consequences in California oil and gas district 4 from 1991 to 2005: implications for geological storage of carbon dioxide, Environmental Geology, *in review.*

Yielding G., T. Needham and H. Jones, 1996, Sampling of fault populations using sub-surface data: a review. Journal of Structural Geology 18:2-3, p. 135 – 146.

Contacts

If you have any questions, comments, or would like more information about DOE's Carbon Sequestration Program, please contact the following persons:

John Litynski
Technology Manager
Sequestration Division

Traci Rodosta
Division Director
Sequestration Division

William O'Dowd
General Engineer
Sequestration Division

William Fernald
Office of Fossil Energy
U.S. Department of Energy

NETL's "Risk Analysis and Simulation for Geologic Storage of CO_2" Best Practices Manual is available at: http://www.netl.doe.gov/technologies/carbon_seq/refshelf/BPM_RiskAnalysisSimulation.pdf.
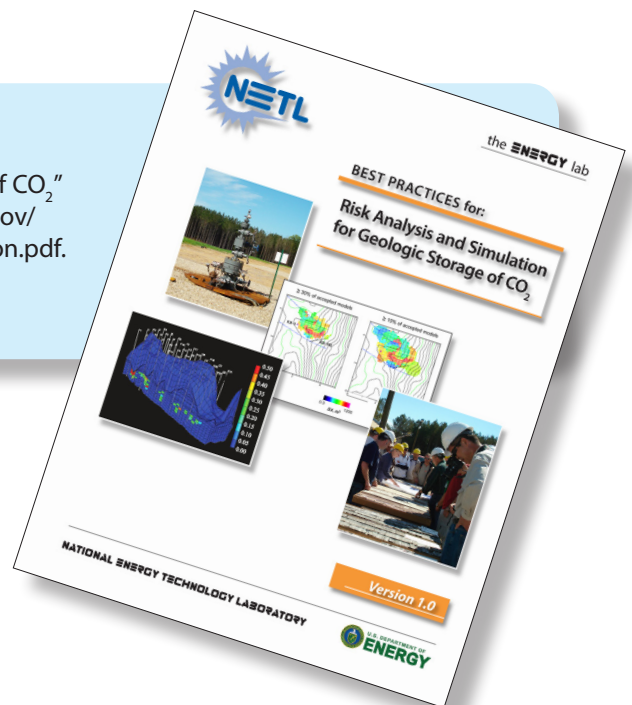
NATIONAL ENERGY TECHNOLOGY LABORATORY

1450 Queen Avenue SW
Albany, OR 97321-2198
541-967-5892

2175 University Avenue South,
Suite 201
Fairbanks, AK 99709
907-452-2559

3610 Collins Ferry Road
P.O. Box 880
Morgantown, WV 26507-0880
304-285-4764

626 Cochrans Mill Road
P.O. Box 10940
Pittsburgh, PA 15236-0940
412-386-4687

13131 Dairy Ashford,
Suite 225
Sugar Land, TX 77478
281-494-2516

WEBSITE: **www.netl.doe.gov**

CUSTOMER SERVICE: **1-800-553-7681**

U.S. DEPARTMENT OF ENERGY

March 2011